Control of DC Microgrids for Distributed Generation including Energy Storage

Daniel Zammit B.Eng.(Hons.), M.Sc.

Department of Industrial Electrical Power Conversion
Faculty of Engineering
University of Malta

Supervised by

Prof. Ing. Cyril Spiteri Staines B.Eng.(Hons), Ph.D.(Nott.).

Prof. Ing. Maurice Apap B.Eng.(Hons.), M.Sc., Ph.D.(Nott.)

Dr. Alexander Micallef B.Eng.(Hons), M.Sc., Ph.D.

A dissertation submitted in partial fulfilment of the requirements for the degree of Doctor of Philosophy in Engineering

March 2022

The research work disclosed in this publication is partially funded by the Tertiary Education Scholarships Scheme.

Copyright Notice

Acknowledgements

First and foremost, I would like to thank God for giving me the strength and knowledge to accomplish and finish this project successfully.

I would like to express my sincere gratitude to my supervisors, Prof. Ing. Cyril Spiteri Staines, Prof. Ing. Maurice Apap, and Dr. Alexander Micallef at the Department of Industrial Electrical Power Conversion, Faculty of Engineering, University of Malta. This research work would not have been possible without their constant guidance and support throughout this project.

I would also like to thank my family for their support and encouragement throughout this project.

Abstract

In recent years DC microgrids have attracted significant interest in research, with various literature published covering areas such as system design, control systems, and energy management. This interest can be attributed to the increase in use of DC energy generation systems, such as photovoltaics (PVs), and energy storage systems, such as battery banks.

The aims of this research were: (a) to build a laboratory-based DC microgrid system on which control algorithms can be developed, applied, and tested, (b) to implement and improve the primary control system, and (c) to develop a battery management system.

A lab-based 48V DC microgrid consisting of two 2.5kW Buck converters, a 1.5kW Bidirectional converter connected to a 24V battery bank, and a resistive load bank was built. Detailed modelling of the Buck and Boost converters was performed, deriving the small signal models and the transfer functions for both converters, which were needed to design the control systems. The two Buck converters and the Bidirectional converter were designed, built, and tested. The converters were connected in parallel and shared a common resistive load using droop control. Three droop control methods were implemented and tested: V-I droop, I-V droop, and a newly proposed method called Combined Voltage and Droop (CVD). A battery management system (BMS) was developed to provide high-level control to the Bidirectional converter.

The Buck and Bidirectional converters operated successfully both as standalone units and within a DC microgrid configuration. V-I droop control provided correct current sharing capability with good results, however its load sharing response was slower than CVD control. I-V droop control resulted to be unstable during practical implementation due to the high gain and bandwidth of the voltage control loop, which interacted with the bandwidth of the anti-aliasing filter in the voltage feedback path. The proposed CVD method solved the instability issues experienced by using I-V droop, making the control system work in a stable way by providing a means to adjust the bandwidth of the voltage control loop. Successful operation was also attained from the DC microgrid setup, which was operated in two scenarios: (1) with the two Buck converters and the Bidirectional converter (operated as a Boost converter) all sharing the resistive load among them, and (2) with the Bidirectional converter (operated as a

Buck converter) charging the battery bank and the two Buck converters supplying the load current and input current of the Bidirectional converter. The BMS was successfully tested with simulations, utilizing the load current and state of charge (SOC) of the battery bank to select the mode of operation of the Bidirectional converter among battery charging, load sharing/supplying, and idle modes.

Through this project, an experimental lab-based DC microgrid was built, serving as a valuable setup for further research on control algorithms of renewable energy conversion systems. By using the lab-based DC microgrid, the new CVD droop control method was developed, which offers advantages over the other droop methods. The BMS developed set up the basis for further development in the area. From this thesis there are two main contributions:

(1) the novel droop control method (Combined Voltage and Droop method) which offers an alternative to the standard I-V droop control system, and

(2) an algorithm for a BMS which provides simple but effective control of the Bidirectional converter and its storage system.

Table of Contents

List of Figures

List of Tables

List of Abbreviations

AAF	Anti-Aliasing Filter
AC	Alternating Current
ADC	Analogue-to-Digital Converter
AGM	Absorbent Glass Mat
BMS	Battery Management System
CAN	Controller Area Network
CCM	Continuous Conduction Mode
CHP	Combined Heat and Power
CLA	Control Law Accelerator
CPU	Central Processing Unit
CVD	Combined Voltage and Droop
DC	Direct Current
DCM	Discontinuous Conduction Mode
EMC	Electromagnetic Compatibility
EMF	Electro Motive Force
EMI	Electromagnetic Interference
EMS	Energy Management System
ESR	Equivalent Series Resistance
IDE	Integrated Development Environment
IGBT	Insulated-Gate Bipolar Transistor
ISR	Interrupt Service Routine
LBC	Low Bandwidth Communication
LDO	Low Dropout

LED	Light-Emitting Diode
LPF	Low Pass Filter
MCB	Miniature Circuit Breaker
MOSFET	Metal Oxide Semiconductor Field Effect Transistor
MPPT	Maximum Power Point Tracking
PCB	Printed Circuit Board
PCC	Point of Common Coupling
PI	Proportional Integral
PLL	Phase-Locked Loop
PV	Photovoltaic
PWM	Pulse Width Modulation
RAM	Random Access Memory
RES	Renewable Energy Source
SMD	Surface-Mounted Device
SOC	State Of Charge
SSR	Solid State Relay
UART	Universal Asynchronous Receiver-Transmitter
UC	Ultra-Capacitor
VRLA	Valve Regulated Lead-Acid

CHAPTER 1 Introduction

1.1 Overview

During the last decade renewable energy sources (RES) have attracted significant interest since these provide our energy needs without hazardous emissions. This interest called for more research on the various aspects of these types of energy sources. The growing amount of renewable energy sources connected to the grid contributed to the idea of distributed electrical power generation systems. Distributed generation means the introduction of various electrical energy sources connected to the electrical grid in addition to the traditional centralized power station.

Distributed electrical power generation systems, energy storage systems, and loads can be connected together to form microgrids. Microgrids can be AC, DC or a combination of both, depending on the particular application. The concept of a microgrid, including its architecture and functions was presented in literature [1] and [2]. Microgrids were presented as a cluster of distributed electrical power sources (photovoltaic (PV) systems, wind generation systems, combined heat and power (CHP) systems), and loads, which are connected together as a single entity. The microgrid system has gained popularity due to the increasing number of distributed power generation systems, as well as its ability to form a self-sustainable electrical grid system. In fact, a very attractive aspect of the microgrid is the ability to operate both in grid-connected mode as well as in islanded mode. In grid-connected mode, the microgrid is connected through a point of common coupling (PCC) to the electrical grid, while in islanded (also referred to as stand-alone) mode the microgrid is disconnected from the electrical grid and operates in an autonomous way. The islanded mode of operation provides the advantage of isolated operation in case of an electrical grid failure, thus offering higher local reliability [2]. In addition, this mode provides the means to supply electricity in remote, isolated, and rural areas, where the provision of an AC grid is difficult or highly unlikely to be achieved. A microgrid can also incorporate an energy storage solution within its architecture, which balances the power and energy requirements of the system.

An important aspect of microgrids is the control architecture, which takes care of load sharing between the energy sources and the energy storage systems within the

microgrid. The energy storage aspect is another important part of the microgrid architecture, especially when operated in the stand-alone mode. Electrical energy storage systems integrated within microgrids consist of batteries, super-capacitors, and flywheels. Energy storage within the microgrid provides energy and power balance when new loads come on-line. An energy storage management system takes care of the coordination of different energy storage units in the microgrid, and therefore it is important to guarantee electricity supply and stability of the system. Reviews of microgrid architectures and distributed energy sources can be read from literature [3] and [4].

Different scenarios call for different AC or DC microgrid configurations. Recently, DC microgrids have drawn particular attention due to the number of advantages they offer. A DC microgrid offers advantages such as lower conversion losses due to less conversion stages, no synchronisation, phase or frequency issues, and independence from voltage sags, dips, and other power quality issues that occur on the AC grid side. These advantages make the DC microgrid attractive for use with consumer electronics (generally the main circuitry is DC-operated), electric vehicle charging, telecommunication equipment, and military equipment. Figure 1.1 shows an example of a DC microgrid.

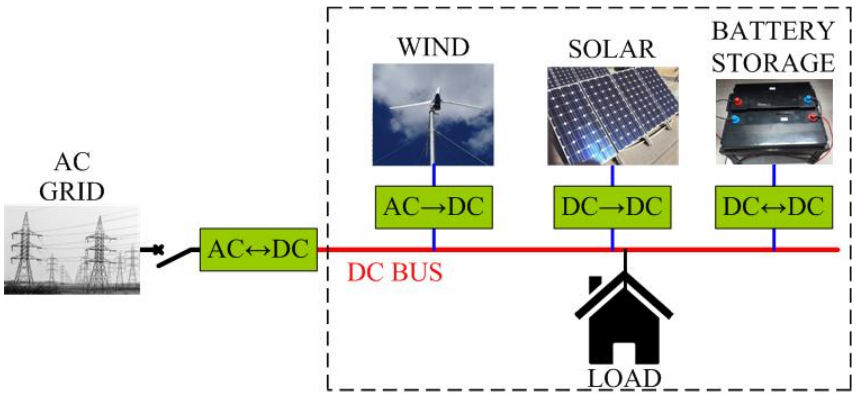

Figure 1.1: DC Microgrid

Control of voltage and current in a microgrid is very important to maintain power balance between energy supply and demand. The functionality of all energy sources and the energy storage system is governed by primary control algorithms that are local to each unit. These algorithms are normally based on droop control, which allows load sharing between distributed sources without communication. Secondary control

algorithms take care of any voltage deviations created by the droop control. An energy management system is utilised to integrate energy storage into the microgrid, with the aim to optimise energy generation from renewable sources, and enhance reliability and stability of the microgrid.

Research in the field of DC microgrids spans across a broad range of topics, ranging from control algorithms to improve load sharing between converters within the DC microgrid, energy management, to algorithms to reduce operational costs of the system. Researchers have also been working on trying to establish common standardization in the control systems of DC microgrids by reviewing control strategies, stabilization techniques, and standardization issues [5], [6]. Various works have also been conducted on different droop control methods. Gao et al. in [7] presented an analysis of a number of these droop control methods. Other reviews discussed power sharing, control, and voltage restoration techniques such as [8] and [9]. Energy management within DC microgrids is also a popular research topic, which can be divided into two aspects. One aspect of energy management focuses on the control of the converters to generate and use energy in the most efficient way possible [10], [11]. The other aspect focuses on energy management from a higher management level taking a more cost effective point of view, with considerations for power scheduling, running costs and/or maintenance costs [12], [13]. Ali et al. in [14] provided a review of energy management systems (EMS) for DC microgrids applied to residential applications.

1.2 Research Objectives

The objectives of this research were:

(a) to build a laboratory-based DC microgrid system on which control algorithms can be developed, applied, and tested,

(b) to implement and improve the primary control system, and

(c) to develop a battery management system (BMS).

In order to achieve the objectives, these were divided into a number of steps:

- Design converters for the DC microgrid, consisting of two 2.5kW Buck converters and a 1.5kW Bidirectional converter with a battery bank.
- Perform a detailed analysis and modelling of the Buck and Boost converters.

- Design control systems to operate the converters in parallel within a DC microgrid using the droop control method.
- Model and simulate the designed converters and their control system, including droop control and voltage restoration, in Simulink/Matlab.
- Build the two Buck converters and the Bidirectional converter prototypes.
- Perform experimental tests with the prototype converters on their own to test their operation, including the control system.
- Test and compare different droop control methods, identify any limitations and if identified formulate a droop method to mitigate or overcome the limitation.
- Develop a BMS, with the prospect of further development.
- Model and simulate the DC microgrid consisting of two Buck converters and a Bidirectional converter including the developed BMS, in Simulink/Matlab.
- Build the laboratory-based DC microgrid with the possibility of further development.
- Perform experimental tests with the laboratory-based DC microgrid.

1.3 Methodology

The methodology used in this research is presented in the form of a flowchart shown in Figure 1.2. A literature review in the field of DC microgrids was initially conducted to better understand the concept and function of a DC microgrid, and get an understanding of existing research. Special focus was given to converter modelling and design, and the control systems needed to operate converters within a DC microgrid. Three areas of interest were identified: converter modelling, droop control, and battery management.

An in-depth analysis of the Buck and Boost converters was carried out. The converter types to be used in setting up the DC microgrid were identified, namely the Buck converter and the Bidirectional converter which can operate as a Buck and as a Boost.

The Buck converters, the Bidirectional converter, and their control systems were designed, modelled, and simulated to confirm correct operation. Simulations were also performed with these converters connected in parallel, and sharing a common resistive load using droop control. Three droop control methods were used, namely V-I droop, I-V droop, and a newly proposed droop method called Combined Voltage and Droop (CVD).

The three converters were built and tested on their own and in a DC microgrid configuration. The three droop control methods were also tested with experimental tests.

A BMS was designed and tested with simulations, which provide high-level control to the Bidirectional converter, selecting its mode of operation.

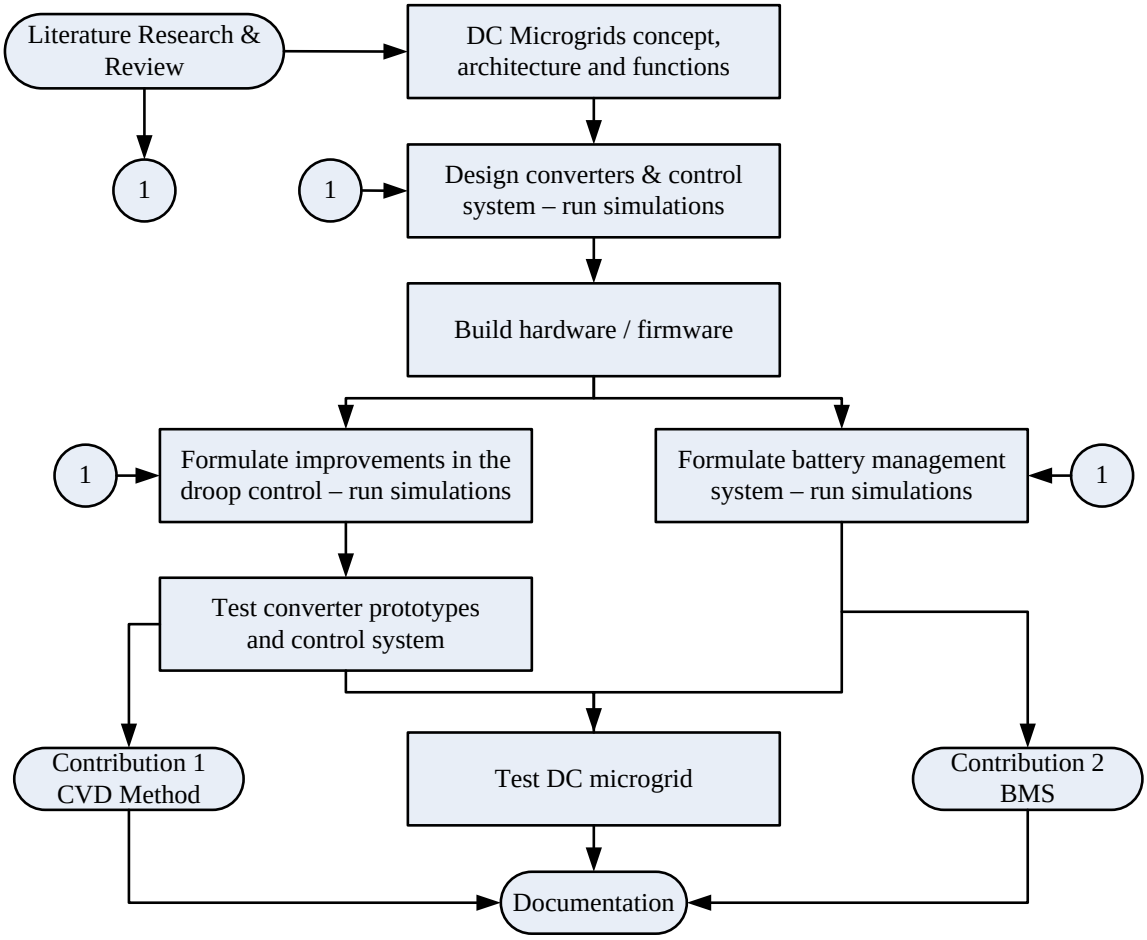

Figure 1.2: Research Methodology Flowchart

1.4 Research Contributions

The research work presented in this thesis provided two main contributions:

(1) A novel droop control method, which was named Combined Voltage and Droop (CVD) control. CVD is an alternative I-V droop-type control method which solved the issues encountered with the use of the standard I-V droop control method. As shall be presented and discussed in this thesis the I-V droop control can cause large transient oscillations and overshoots at the start up of converters. In addition it can also cause stability issues due to

interactions between the bandwidth of the voltage control loop and the bandwidth of other components in the control system, like the anti aliasing filter in the voltage feedback path. Both issues are solved with the proposed CVD control method as shall be presented in Chapter 5, with the simulation and experimental results shown and discussed in Chapter 7.

(2) An algorithm for a Battery Management System which provides simple but effective control to the Bidirectional converter. The BMS algorithm makes use of the load current and the state of charge (SOC) of the battery bank to select the mode of operation of the Bidirectional converter, selecting between load sharing, battery charging, and idle modes. The BMS algorithm shall be presented in Chapter 5, and the testing and simulation results shall be presented in Chapter 8.

1.5 Publications

The work carried out during this research was rewarded by a number of publications as listed below. A number of papers discussed the modelling of Buck and Boost converters, and the control system needed to operate within a DC microgrid. The newly proposed CVD method was also the subject of published literature, and a paper on the subject was selected to form part of a book chapter.

This research has the potential for further publications, which at the moment are being planned.

- D. Zammit, C. S. Staines, M. Apap, A. Micallef, ‘Paralleling of Buck Converters for DC Microgrid Operation’, IEEE International Conference on Control, Decision and Information Technologies (CoDIT'16), St Paul’s Bay, Malta, 6-8 April 2016.

- D. Zammit, C. S. Staines, M. Apap, A. Micallef, ‘Overview of Buck and Boost Converters Modelling and Control for Stand Alone DC Microgrid Operation’, Offshore Energy & Storage Symposium and Industry Connector Event (OSES 2016), Valletta, Malta, 13-15 July 2016.

- D. Zammit, C. S. Staines, M. Apap, A. Micallef, 'Control Of Buck and Boost Converters For Stand-Alone DC Microgrids', 8th International Symposium on Energy, Aberdeen, Scotland, UK, 6-9 August 2018.

- D. Zammit, C. S. Staines, M. Apap, A. Micallef, 'Alternative Droop Control Method using a Modified Lag Compensator for Paralleled Converters in DC Microgrids', IEEE 6th International Conference on Control, Decision and Information Technologies (CoDIT'19), Paris, France, 23-26 April 2019.

- D. Zammit, C. S. Staines, M. Apap, A. Micallef, 'Paralleling Converters in DC Microgrids with Modified Lag I-V Droop Control and Voltage Restoration', ELECTRIMACS 2019, Salerno, Italy, 21-23 May 2019.

- D. Zammit, C. S. Staines, M. Apap, A. Micallef, 'Paralleling Converters in DC Microgrids with Modified Lag I-V Droop Control and Voltage Restoration', Chapter in book ELECTRIMACS 2019 - Selected Papers - Volume 2, Springer, 2020.

1.6 Thesis Layout

Apart from the introduction provided in this chapter, this thesis is divided into the following chapters:

Chapter 2: Literature Research and Review

This chapter provides a literature review of publications covering research in areas of interest, namely hierarchical control and system design, load sharing using the droop control method, and energy management systems in DC microgrids.

Chapter 3: DC Microgrid System

The experimental DC microgrid built for this research includes two Buck converters and a Bidirectional converter. This chapter covers the theory and design of these converters.

Chapter 4: Converter Modelling

This chapter provides a detailed analysis and modelling of the Buck and Boost converters. The small signal models are derived, followed by the derivation of the transfer functions needed to design the control system for these converters. The analysis and modelling covers both the continuous conduction mode (CCM) and discontinuous conduction mode (DCM) of the Buck and Boost converters.

Chapter 5: Converter Control

This chapter covers the control systems for the Buck and Bidirectional converters, including the theory and design of primary and secondary control. Three types of droop control methods are presented: V-I droop, I-V droop, and the CVD method which is an innovative droop control method being proposed in this research. The BMS is also covered in this chapter.

Chapter 6: Experimental Setup

This chapter covers the design and construction of the hardware, including a description of the interface circuitry with the microcontroller. This chapter also covers the firmware and settings of the microcontroller that were used to implement the converters' control system.

Chapter 7: Simulation and Experimental Tests of the Paralleled Converters using Droop Control

This chapter presents the results obtained from the Simulink/Matlab simulations and experimental tests performed with the converters connected in parallel, to test and compare the three different droop control methods: V-I droop, I-V droop and the newly proposed CVD method.

Chapter 8: Simulation and Experimental Tests of the DC Microgrid

The simulation and practical results obtained from tests performed with the DC microgrid are presented in this chapter. The DC microgrid model composed of the two Buck converters, the Bidirectional converter, and a common resistive load was tested with simulations. These simulations also tested the BMS which controlled the mode of operation of the Bidirectional converter. This chapter also presented and discussed the practical results obtained from the experimental DC microgrid setup.

Chapter 9: Conclusion

Final conclusions on the research are discussed in this chapter. It provides a brief discussion on the work performed and the results obtained. It also includes future work suggestions for further research.

Appendix A: Buck and Bidirectional Converters Simulation Results

This chapter presents the results obtained from simulations performed with the Buck and Bidirectional converters modelled in Simulink/Matlab. Simulations were performed with the converters operating on their own to test their control system.

Appendix B: Buck and Bidirectional Converters Experimental Results

This chapter presents the results obtained from experimental tests performed with the Buck and Bidirectional converters, while operated on their own in order to test the converter prototypes and their control system.

Chapter 2 Literature Research and Review

This chapter presents a discussion and review of present and past research in the field of DC microgrids. The literature under review was grouped under three sections; those that are concerned with the control system and the design of the system, those that focus on load sharing using the droop method, and those that are concerned with energy management systems in DC microgrids.

2.1 Hierarchical Control and System Design

An area of study within the research field of DC microgrids is concerned with finding the optimal voltage levels at which DC microgrids will give best performance. However, this could result as a difficult task, since different DC microgrid applications would require different performance and parameters. One such research was conducted by Anand and Fernandes, and presented in [15]. The authors researched the optimal voltage in DC microgrids for residential and commercial facilities. A DC microgrid was taken into consideration consisting of photovoltaic (PV) and wind sources, battery storage, and various loads such as LED lighting, domestic appliances, computer, and other consumer electronics. Two AC systems, one residential and one commercial, were also taken into consideration consisting of similar items as the DC system. A study was made comparing the AC residential and commercial systems with the DC version, taking into consideration various factors like the voltage level, the power load needed, the types of converters needed and their efficiency, safety issues, and other factors. Loads like LED lighting and consumer electronics ultimately need DC to work, whilst PV systems generate DC power and wind turbine systems have the output converted to DC before being connected to an AC grid through an inverter. This leads to conversions from one form of electricity to another, which can cause substantial energy losses. The DC system taken under consideration achieved an improvement in operating efficiency of 15-22% for residential systems and 10-11% for commercial systems, over conventional AC systems. In addition, it was concluded by the authors that for residential use a DC system working at 48V gives the optimal performance, considering the lower power requirements, higher safety and efficiency. For commercial use a voltage of 400V offered the highest efficiency.

A very important research area involving DC microgrids is the control system, which takes care of the complete operation of the energy source converters and energy storage systems within the microgrid. The control system needs to control the current, voltage and power flow in the converters as well as in the microgrid, which can be divided into different levels of control. In [16], Guerrero et al. discussed in detail a hierarchical control system for microgrids consisting of three levels, shown in Figure 2.1. The first level (primary control) consists of current and voltage control, with droop control for common load sharing. The second level (secondary control) restores any deviations caused by droop in the primary control, while the third level (tertiary control) manages the power flow between the microgrid and external electrical distribution systems.

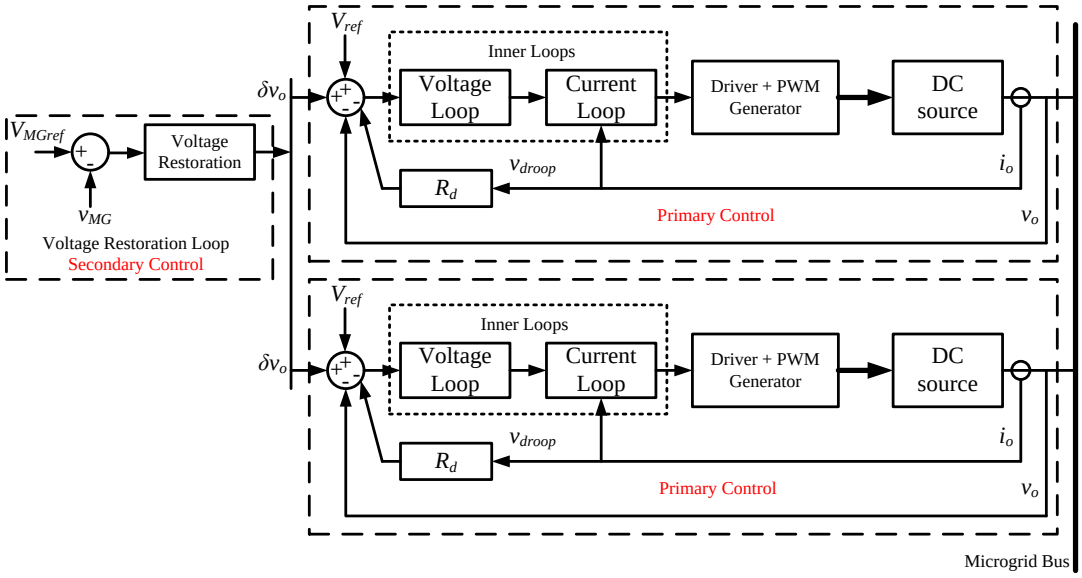

(a)

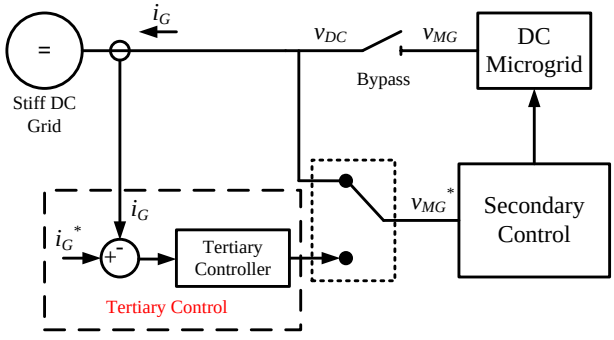

(b)

Figure 2.1: Hierarchical Control System for DC Microgrids [16]
(a) Primary and Secondary Control (b) Tertiary Control

The hierarchical control system proposed in [16] can be extended to multiple DC microgrids connected together, to regulate power flow among the microgrids, as well

as improve the overall stability of the connected systems, as was reported by Shafiee et al. in [17] and [18].

As stated earlier, part of this hierarchical control system is secondary control, which is employed to regulate voltage drops created by primary control. Secondary control is generally applied by a voltage controller common to all converters within the DC microgrid, and corrects any voltage deviations created by droop control, thus restoring the DC-bus voltage to the desired value. In [19] Peyghami et al., studied the effect of the secondary controller on voltage regulation in DC microgrids, and proposed a new voltage regulation strategy. In high capacity microgrids and long feeders with voltage drops on the line resistances, the conventional methods may not guarantee voltage regulation on load buses. Line resistances cause voltage drops on the lines feeding the DC-bus and the loads, which interfere with the load current sharing process between the converters in the microgrid and affects voltage regulation on the DC-bus. This is mostly observed in long feeder lines, which can be the case in practical applications. This raises the need to regulate the voltage on critical loads. In [19] the authors proposed a system which identifies buses which are the weakest and base the voltage compensation on these buses. A simplified DC microgrid system made up of two generation sources and five separate DC-buses was taken into consideration. The DC-buses were considered to be located at different distances between them. Following experimental tests on the DC microgrid system, the authors propose to compensate the weakest buses, which generally are the furthest buses from the sources. With their approach all the buses in the microgrid had their voltage compensated successfully to within +/-5%. However, in larger DC microgrid systems with a larger number of sections and/or longer feeders, the voltage compensation might not be within the +/-5% range. Thus, in this case there will be the need for the microgrid to be divided in sections and compensated accordingly.

2.2 Load Sharing using the Droop Control Method

Droop control is a method used to obtain load sharing between parallel-connected converters, and makes part of the primary control system within the hierarchical control system previously described. If two converters are connected in parallel while sharing a load without any control on the current being shared, any differences in the converters' output voltages will cause one converter to take over the supply of the load current. This would lead to an unwanted scenario, so ways were found to control

the load current sharing process. The most popular solution to obtain this current sharing is in fact droop control. Droop control works by creating a load dependent voltage deviation in the converter's output voltage, which causes a reduction in output current. In this way when two droop-controlled converters are connected in parallel, a balance is reached between the converters in sharing the load current. The 'conventional' droop method is the V-I droop, which is graphically presented in Figure 2.2. V-I droop is applied by introducing a loop with what is called a droop virtual resistance R_d which reduces the voltage reference to the inner control loops, with the reduction being based on the output current, as can be observed from Figure 2.2.

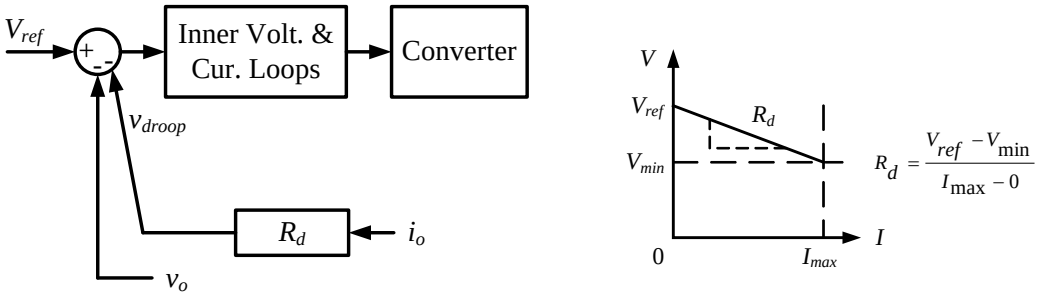

Figure 2.2: V-I Droop Control Method
V_{ref}: Reference Voltage, V_{min}: Minimum Permitted Voltage, v_{droop}: Droop Voltage Term, v_o: Output Voltage
I_{max}: Maximum Output Current, i_o: Output Current, R_d: Droop Virtual Resistance

Research was conducted to compare droop control with other current load sharing methods. Karlsson and Svensson in [20] investigated a DC distribution system for renewable energy sources. Two types of DC-bus voltage control schemes were introduced; the master-slave method and the droop control method. In the master-slave method a master converter takes care of the DC-bus voltage and distributes power references to the other converters, using fast communication between the source and load converters. The master-slave method is totally dependent on a fast communication system to operate, thus in the case of a communication failure the microgrid would trip. On the other hand, with droop control there is no communication required between the converters for the power sharing operation. In the droop control method the DC-bus voltage is measured at each source converter and all source converters contribute to provide the power required by the loads, and obtained equal load shared between the converters. Some droop control limitations are voltage deviations from the reference DC-bus voltage, limited transient response, and current sharing inaccuracies due to bus and line resistances.

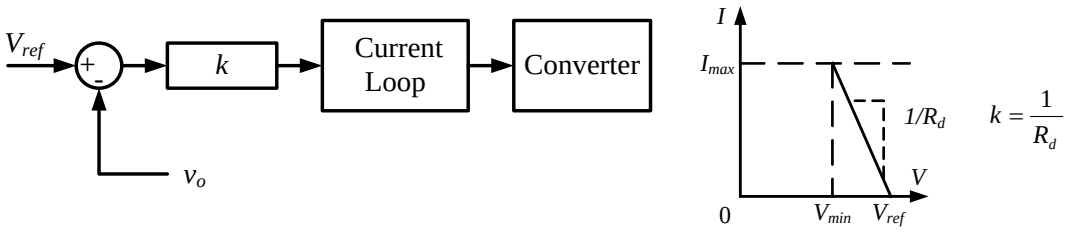

Figure 2.3: I-V Droop Control Method
V_{ref}: Reference Voltage, V_{min}: Minimum Permitted Voltage, v_o: Output Voltage, I_{max}: Maximum Output Current, R_d: Droop Virtual Resistance, k: Multiplier Term

Research on droop control has led to further droop control methods in addition to the conventional V-I droop control method. Jin et al., in [21] introduced what they called virtual inertia into the DC microgrid, with the aim to improve the transient response and stability of the microgrid. The concept of an RC droop was introduced, and this concept was applied to the V-I droop and I-V droop methods. The admittance-type I-V droop method was selected for the application of the RC droop method, since it was more effective in providing virtual inertia. I-V droop is another droop control method which replaces the voltage controller, generally a PI controller, with a multiplier term k, where $1/k$ would be equal to R_d, as shown in Figure 2.3. The authors modified the admittance-type I-V droop method to introduce virtual inertia with the equivalent circuit shown in Figure 2.4. The proposed system was verified with simulations and experiments, comparing admittance-type droop without and with the proposed RC-mode droop control. The simulation model in PLECS consisted of two droop-controlled Buck converters connected to a shared resistive load with a DC-bus voltage of 115V and resistive load of 28.75Ω. The experimental setup consisted of four Buck converters operating in a low voltage DC microgrid with a DC-bus voltage of 120V and a resistive load of 17Ω, and the control and data acquisition done in dSpace. The results show an effective improvement in the system inertial behaviour and transient response while the desired power sharing of the droop control was not affected. However the RC droop method resulted less effective in the impedance-type V-I droop. This was attributed mainly due to the significant interaction between the present inductive intrinsic impedance and the desired virtual capacitance. The interaction showed resonant behaviour and this further reduces the effective range of operation in the impedance-type V-I droop method.

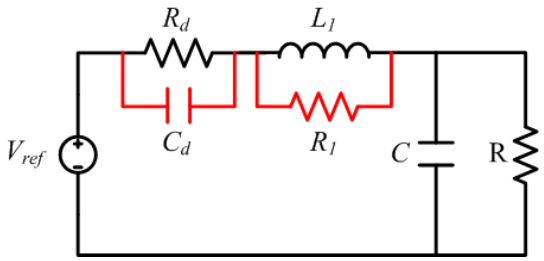

$$L_1 = \frac{R_d}{\omega_c}$$

$$R_1 = \omega_c C_d$$

Figure 2.4: Equivalent Circuit of RC Droop Method
(components introduced by proposed virtual inertia method are shown in red) [21]

Research on droop control has also led to adaptive droop methods to cater for discrepancies caused by line resistances as previously pointed out. One such droop control method was presented by Peyghami et al., in [22]. The authors presented an adaptive droop method, shown in Figure 2.5, which is based on superimposing a small AC voltage signal on the DC microgrid voltage to adapt the droop control to cater for sharing discrepancies due to line/feeder resistance issues. The frequency of the injected AC voltage is proportional to the output DC current of the converter. The AC voltage causes an AC current to flow, which would be proportional to the phase angle of the AC voltage and line impedances. These AC currents will contain the information of the voltage phases and line resistances. In this proposed DC microgrid system, the superimposed AC voltage signal of each DC converter reaches the same frequency by controlling the AC power. In low voltage systems the reactive power can be controlled by the frequency. Using this idea, current sharing between the DC microgrid converters is obtained by sharing reactive power between the converters to obtain the same superimposed AC voltage frequency. Therefore, the injected reactive power is utilized to adapt the conventional droop gains in order to achieve proportional load sharing. By adjusting the DC voltages based on the reactive power, the output DC current is controlled. A secondary controller locally estimates and compensates the voltage drop due to the droop controller. The proposed method mitigates the load sharing inaccuracies with conventional droop methods in low voltage DC microgrids when operating with sources having long feeder lines. While in conventional droop controlled microgrids communication is needed between the converters to improve this load sharing problem, with this proposed method there is no need for this extra communication. This improves reliability and stability. The proposed method was tested with simulations and experiments using a DC microgrid made up of two Boost converters, a resistive load, and a 4kW DC motor. A DC-bus voltage of 400V was used, and the superimposed AC voltage was set to 2.5V with a

frequency of 50Hz. The results showed improved load current sharing accuracy between the converters, when using the proposed method. Peyghami et al., in [23] and [24] continued to expand on the concept of superimposed frequency droop to obtain power sharing and management. A drawback with a control system like the one suggested by the authors is that, the control might get complicated with a larger microgrid system, possibly affecting reliability. In addition, the DC currents and voltages will have a 50Hz AC ripple superimposed on them.

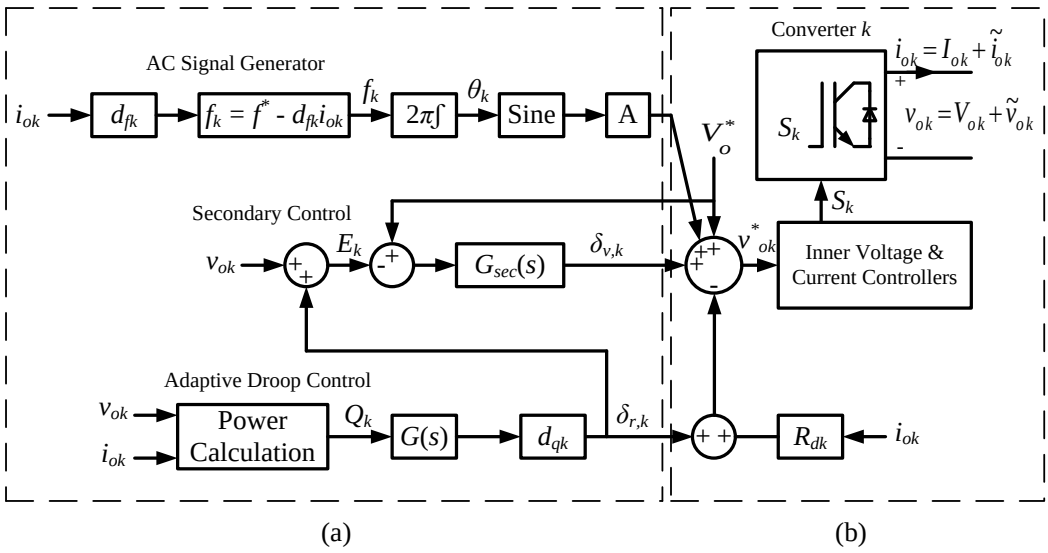

Figure 2.5: Adaptive Droop Method a) Adaptive Control b) Conventional Droop [22]

As already stated, droop control provides load sharing between paralleled converters by reducing the output voltage as the output current increases. This creates a deviation in the output voltage from the set DC-bus voltage. In addition the output voltage of the converters cannot be exactly the same due to different line resistances. Lu et al., in [25] proposed a control system to mitigate these effects. The authors presented a droop control method that makes use of low bandwidth communication (LBC), in order to improve the performance of the DC microgrid operation. The control system proposed does not have a centralized secondary controller, but makes use of a LBC network while using the local controllers. The LBC is used to exchange information between the converter units, exchanging the values of the DC voltage and current. Load sharing correction and voltage restoration are performed simultaneously, by varying the virtual droop resistance and correcting the voltage reference value to obtain the desired output voltage. The proposed system was tested by simulations and experimental implementation. The experimental setup consisted of two 2.2kW converters connected in parallel operating with a 700V DC-bus voltage and 100-200Ω load resistances. The line resistances for the two converters were unequally set to 1Ω

and to 4Ω. The authors tested the proposed system to obtain voltage restoration and better current sharing accuracy, mitigating the effects of the line resistances. Testing was also conducted with different communication delays of 1μs, 20ms, and 1s, to verify the system performance. It was noted that, with a communication delay of 20ms, overshoots and oscillations in the output voltage were larger than when a communication delay of 1μs was used. With a communication delay larger than 1s the system became oscillatory with oscillations in the output voltage. It can be noted that with communication delays longer than 1s the control system starts to become unstable. This instability resulted since voltage values which are communicated between the converters are used by the controllers in calculations performed locally by each converter. Thus the delay in communicating the voltage value from one converter results in inaccuracies in the calculations of the other converter. Thus, the authors validated their proposed control system with a low bandwidth communication with communication delays kept below 20ms.

Other control system approaches can be taken to mitigate the current sharing inaccuracies due to differences in the line resistances and converter parameters. L. Gao et al. in [26] proposed a DC droop control strategy based on integrator current-sharing. The idea behind the strategy is to eliminate current deviation by the use of an integrator function current-sharing term, to provide uniform power sharing between the different power generation units in the DC microgrid with reduced circulating currents between the units. The authors took into consideration the diagram shown in Figure 2.6 to formulate the current-sharing term, taking into consideration two power sources for simplification. The proposed DC droop control strategy with the integrator current sharing term was derived and is given by:

$$U_{dci} = U_{dc}^{*} - K_{di} I_{dci} + K_u \int \left[(U_{com}^{*} - U_{com}) - K_{pi} P_{dci} \right] dt \qquad (2.1)$$

where U_{dc}^{*} is the no-load voltage, U_{dci} is the output voltage of power source i, I_{dci} is the output current of power source i, K_{di} is the droop coefficient, U_{com}^{*} is the no-load voltage of the DC-bus, U_{com} is the actual voltage of DC-bus, K_{pi} is the current-sharing coefficient, K_u is the integrator coefficient, and P_{dci} is the output power.

The current-sharing coefficient is set according to the power source unit power capability, rationalizing the sources, and avoiding circulating currents. A challenge that might be encountered to apply this strategy would be to sample the DC-bus voltage, which might not be in the immediate vicinity.

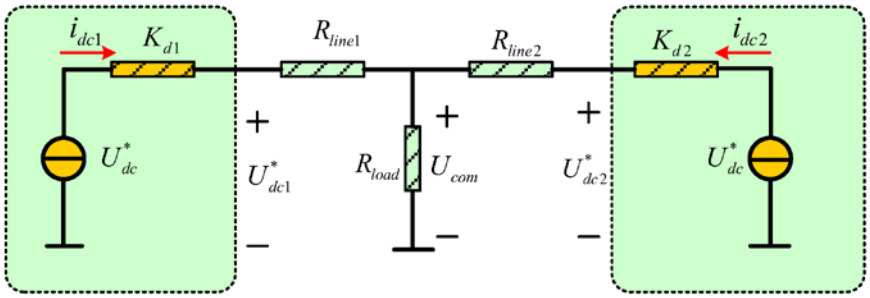

Figure 2.6: Paralleled Power Sources with Conventional Droop Method [26]
https://www.mdpi.com/1996-1073/10/8/1116

Research involving droop control covers a broad range of ideas and approaches, as can be noted by the selection of literature on the subject covered in this subsection. The various authors contributed in the area by proposing improvements to the droop control method and also mitigation measures to correct line resistance issues. The authors in [21] proposed an alternative I-V droop control method which improved the system inertial behaviour and transient response, however it resulted to be problematic when used with V-I droop. The authors in [22] to [26] utilized successfully various droop strategies to compensate for current sharing inaccuracies caused by line resistances and also compensate for droop voltage deviations, however these methods can be difficult to apply in practice due to control complexities. The area regarding droop control is still open for further improvements and contributions, and would surely be an area in which this research shall contribute.

2.3 Energy Management Systems in DC Microgrids

An energy management system (EMS) takes care of the various energy sources, energy storage, and loads forming the DC microgrid. The area of energy management covers different systems depending on the type of DC microgrid in use, and is quite a broad subject. Two main concerns of any EMS are generally the management of energy sources (like PVs) to use these sources in the best way possible, and the management of energy storage system (like battery banks).

One of the major challenges that needs to be catered for by an energy management system of a DC microgrid is battery management. The energy management system needs to perform decisions on when and how to use batteries and when to charge them. The management gets more complicated if more battery banks are added to the DC microgrid. One issue which has been researched a lot is that of balancing of state of charge (SOC) of multiple battery banks within the microgrid. There are a number

of research publications which propose ways to tackle this issue. One popular way is using an adaptive droop control method in order to take care of the SOCs of the batteries. One such publication is [27] authored by Dragicevic et al., which presented a supervisory control system for a DC microgrid with battery storage. An adaptive droop method was introduced in order to sustain the SOC of the batteries. The control system was made up of a double layer hierarchical control strategy, having the primary control layer and the supervisory control layer. The primary control layer is composed of adaptive droop aimed to regulate the common bus voltage and to keep the SOCs of batteries close to each other, together with a maximum power point tracking (MPPT) system. The supervisory control layer used a low bandwidth communication interface between a central controller and the energy sources in order to achieve the data needed for the calculation of the adaptive droop virtual resistances and for changing operating modes. Figure 2.7 shows the proposed control system for a single unit in the DC microgrid.

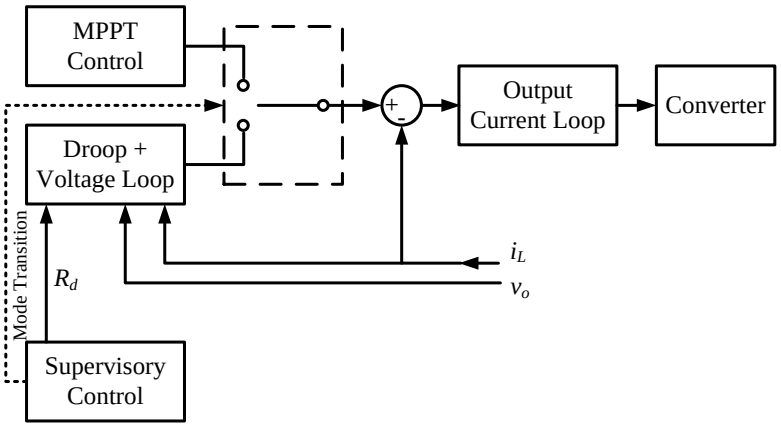

Figure 2.7: Primary and Supervisory Control System [27]

Another SOC-based adaptive droop control method was proposed by Lu et al. in [28], [29], and [30] in order to balance the SOC of each battery energy storage unit and reach power sharing between the different energy storage units. The control system is shown in Figure 2.8. In this method the droop coefficient is adaptively adjusted according to the SOC. By changing the value of the exponent *n*, the balancing of the SOC and the output power equalization speed could be regulated. In the battery charging process the droop coefficient was set to be proportional to the order n of the SOC (SOC^n), while in the discharge process the droop coefficient was set to be inversely proportional to the order n of the SOC. This SOC-based droop control method achieved SOC balancing and output power equalization in both charging and discharging modes.

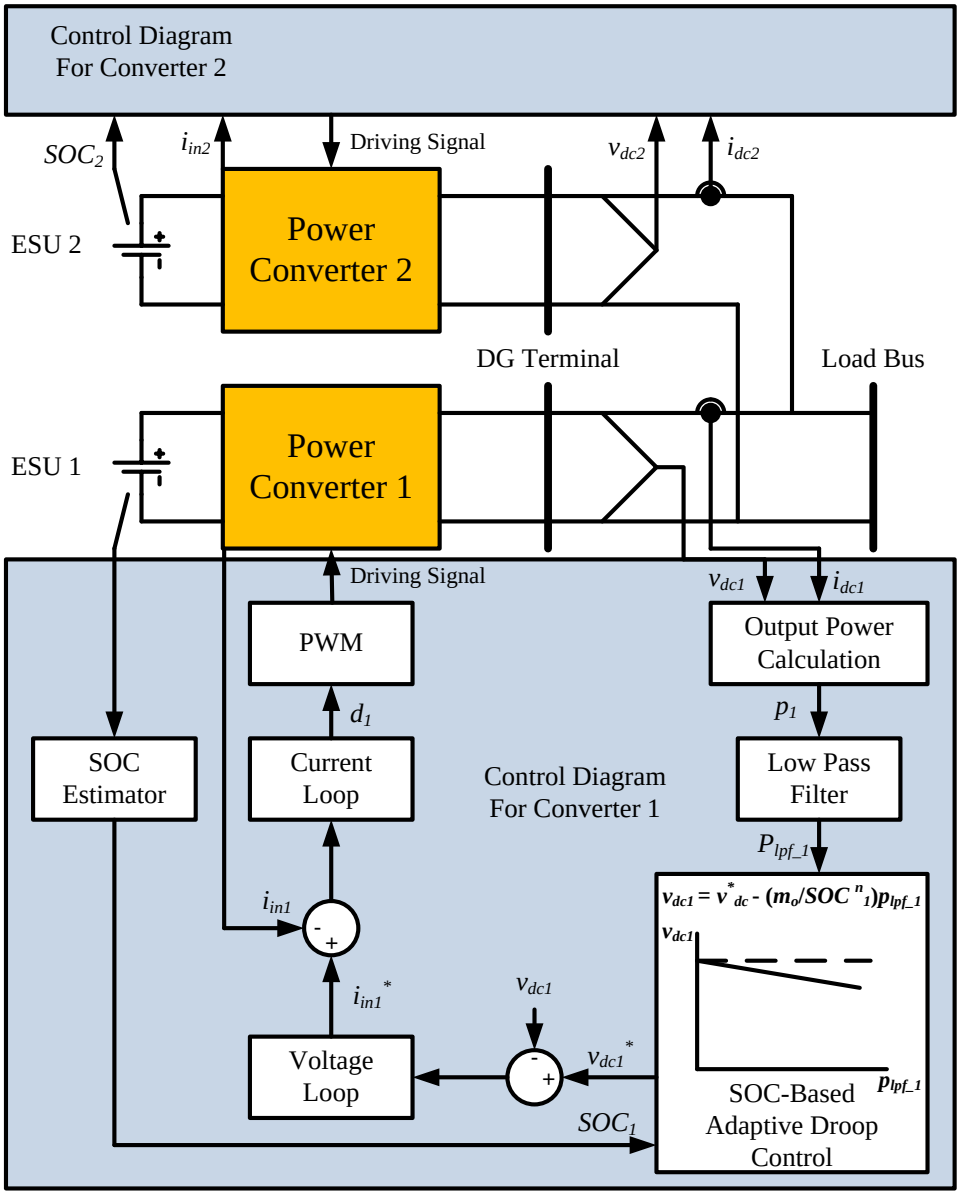

Figure 2.8: SOC-Based Adaptive Droop Control System [28]

Another adaptive droop-based energy management scheme for an autonomous DC microgrid was proposed by Subham et al. in [31]. The authors' aim was to overcome management issues with multiple batteries in a distributed DC network. The power system under consideration was made up of PV panels operated as a constant power source with MPPT and two battery energy storage systems. The energy management scheme controlled the battery energy storage systems to cooperate and balance the SOC of the two battery units, and perform constant voltage charging when the condition arises, which is handled by the adaptive droop control. The energy management system also took care of voltage regulation of the DC microgrid.

Another challenge with DC microgrids that an energy management system should take care of, is power quality issues created by load fluctuations and fast changes. These would result in transient spikes, dips, and swells in the DC-bus voltage and load currents. Research has been conducted to find mitigation measures for these issues. One of the papers that aims to mitigate transients caused by load changes is the paper authored by Bastos et al. in [32]. This paper presents a decentralized control strategy to manage storage units within a grid connected DC microgrid without any high bandwidth communication. Batteries and Ultracapacitors (UC) were utilized within the microgrid. The batteries were used to supply/absorb extra power in steady state and the ultracapacitors were used to take care of the power transients caused by variations in power due to power production or load changes. The proposed control strategy used only the DC-link voltage, SOC, and UC terminal voltage as inputs.

On a similar line of thought, Zhang et al. in [33] presented a power management strategy for a DC microgrid with a hybrid storage system. The hybrid storage system was made up of a battery storage unit and a supercapacitor unit. Supercapacitors are able to take care of fast load fluctuations more than batteries. Thus, the combination of the two types of storage can take better care of fast and slow power changes, which offers a very good advantage over microgrids using only battery storage.

Another energy management system for DC microgrids that made use of supercapacitors together with batteries to cater for better supply stability was presented by Jarrahi et al., in [34]. The DC microgrid setup taken into consideration by the authors was made up of a PV source, and two energy storage units; a battery bank source and a supercapacitor, together with loads. The control system used the supercapacitor to take care of fast load variations, while the batteries were used to provide longer power requirements.

The use of supercapacitors in the field of DC microgrids merit further investigation due to their potential in riding through disturbances in the microgrid caused by sudden large load changes.

2.4 Literature Review Conclusion

The papers discussed in this chapter show that current research on DC microgrids covers various aspects, from control design, stability of various converters, as well as, systems integrated into the DC microgrid. The reviewed papers also covered research on energy management within DC microgrids.

From the review three main areas of interest emerged: the area regarding the design of the control system needed to operate converters within a DC microgrid and converter modelling, the area of droop control, and the area of battery management systems.

The selection of the converters and the control systems in use is very important for proper operation of the DC microgrid. Thus, having proper understanding of the converters and the control system is a must. In these regards, it was felt that there was the need to model the DC-DC converters in detail to properly design the control system in order to integrate the converters in a DC microgrid. This detailed converter modelling and analysis is covered in Chapter 4.

Another area of interest in which further improvement could be obtained is that of droop control in DC microgrids. Many control systems include impedance or V-I droop, while others make use of admittance or I-V droop. I-V droop can offer higher bandwidth speeds that V-I droop, thus it can provide faster response to changes and transitions in the DC microgrid. However, I-V droop can be problematic to apply in practice due to bandwidth interactions with other parts in the control loop, like for example anti-aliasing filters and/or plant dynamics, as will be observed in Chapter 7. These interactions can lead to instability. Part of this research focused on an alternative modified I-V droop method that solved the issues with I-V droop, as can be observed in Chapter 7.

The third area of interest in which research work was carried out is concerned with battery management. The reviewed literature presented a number of power management systems that required complicated systems with communication between units within the microgrid. During this work a battery management system (BMS) was developed and implemented on the Bidirectional converter. This converter was selected to handle the operation of the battery bank. The developed BMS does not need any high bandwidth communication and provides simple but effective operation. The BMS algorithm is based on the load current and the SOC of the battery bank, and according to the value of these quantities the mode of operation of the Bidirectional converter is selected, changing between load sharing, battery charging, and idle modes. This BMS is open for further development and expansion. The BMS shall be presented in Chapters 5 and simulation results shall be presented in Chapter 8.

Chapter 3 DC Microgrid System

This chapter covers the theory and design of the converters forming part of the DC microgrid system. The selection of the converter's power levels were based on small to medium commercially available power converter sizes used with renewable energy sources. The laboratory-based DC microgrid was designed to consist of two 2.5kW Buck converters used as energy source converters and a 1.5kW Bidirectional converter for a battery storage system, connected together with resistive loads. The DC-bus voltage was selected to be 48V, an ideal voltage for domestic applications [15]. The two Buck converters operate from an input voltage within the range 70V – 120V and provide an output voltage of 48V. During tests the Buck converters were operated with a recommended input voltage of 100V. The Bidirectional converter operates between 24V on the battery bank side and 48V on the DC-bus side. The Bidirectional converter is controlled to operate as a Buck converter when charging the batteries and as a Boost converter when supplying load current to the DC-bus. Figure 3.1 shows a block diagram of the DC microgrid setup.

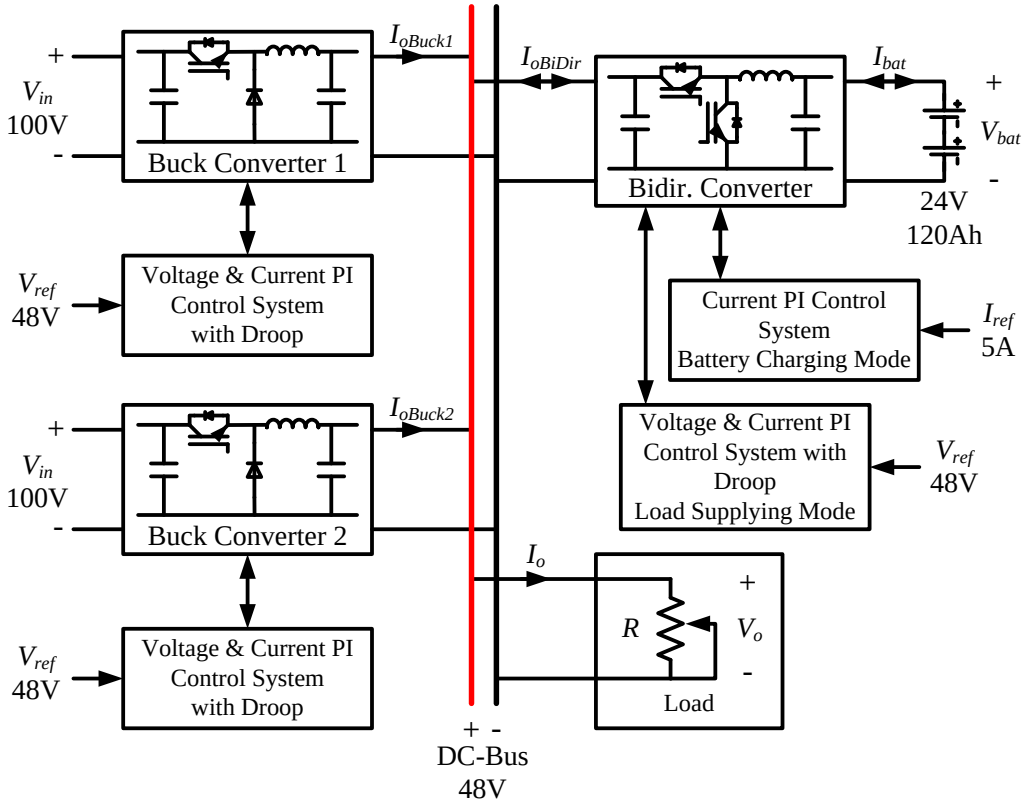

Figure 3.1: Block Diagram – Laboratory-Based DC Microgrid

3.1 DC-DC Converters

A DC-DC converter is a switching power electronic unit that converts a DC voltage to another DC voltage level. Two main DC-DC converter types are the Buck and Boost converters. These converters are a popular choice when connecting renewable energy sources (such as photovoltaics) in a DC microgrid, since these can convert DC output voltage from the source to the required DC microgrid voltage very efficiently.

3.1.1 Buck Converter

Figure 3.2 shows a Buck (step-down) converter, which is a switching converter that provides a lower average output voltage (V_o) than the DC input voltage (V_{in}).

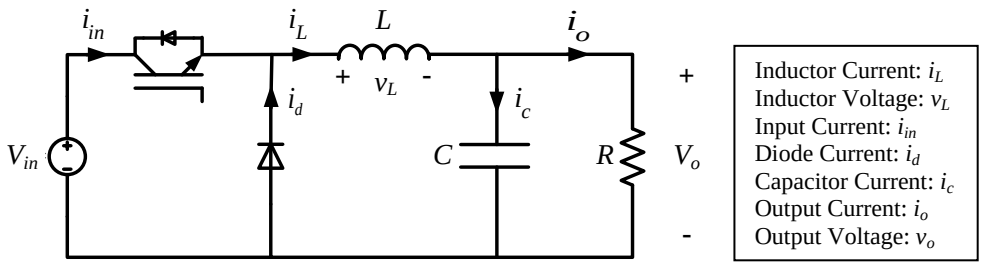

Figure 3.2: Buck Converter

The Buck converter reduces the input DC voltage by switching the IGBT or MOSFET at a specific frequency using pulse width modulation (PWM). The Buck converter can be operated in two modes: in the continuous conduction mode (CCM) and the discontinuous conduction mode (DCM). Operating in CCM means that the converter inductor current ripple never reaches zero current, while operating in DCM means that the converter is operated with a light load, which causes the inductor current ripple to reach zero current for part of the switching cycle.

Figures 3.3 and 3.4 show the inductor current, inductor voltage, and output voltage waveforms for the Buck converter operating in CCM and DCM, respectively. In CCM mode the converter operates in two states: when the IGBT (or MOSFET) is conducting and the diode is off (reverse biased), and when the IGBT is off and the diode is conducting (forward biased). A Buck converter using unidirectional switches and operating with a light load will have the ripple in the inductor current being more significant when compared to the average inductor current value. In this case the Buck converter is operating in DCM. In DCM mode the converter operates in three states: when the IGBT (or MOSFET) is conducting and the diode is off (reverse biased),

when the IGBT is off and the diode is conducting (forward biased), and when the IGBT and the diode are both off.

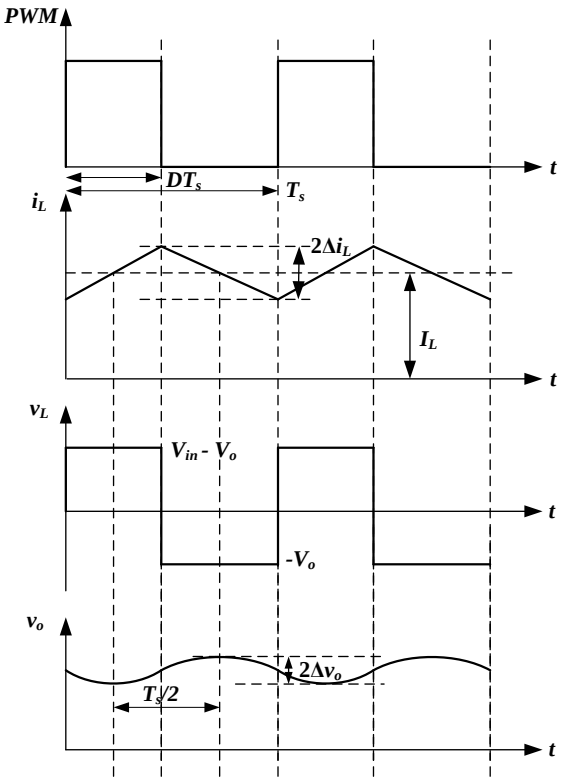

Figure 3.3: Current and Voltage Ideal Buck Converter Waveforms in CCM

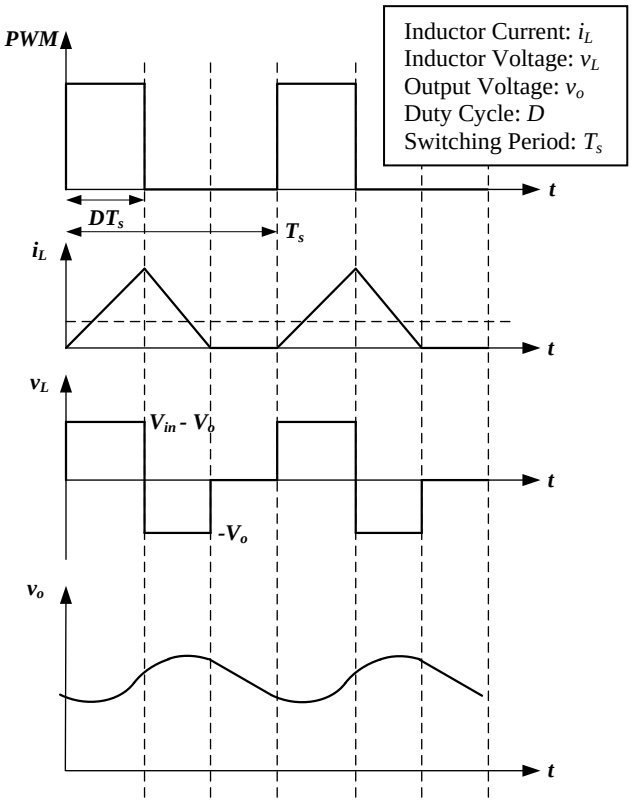

Figure 3.4: Current and Voltage Ideal Buck Converter Waveforms in DCM

For the Buck converter, the voltage conversion ratio of the input voltage V_{in} to the output voltage V_o, *M(D)*, while the converter is operating in CCM, is given by:

$$M(D) = \frac{V_o}{V_{in}} = D \tag{3.1}$$

where *D* is the duty cycle, which is the fraction of time the IGBT (or MOSFET) is on.

The value of the inductor *L* and the value of the output capacitor *C* set the peak ripple in the inductor current and output voltage, respectively. Equations were derived to obtain the values needed for the inductor and capacitor depending on the desired ripple [35].

The value for the Buck converter inductor *L* can be calculated by [35]:

$$L = \frac{(V_{in} - V_o)D}{2\Delta i_L f_s} \tag{3.2}$$

where Δi_L is the desired inductor current peak ripple, *D* is the duty cycle, and f_s is the switching frequency of the Buck converter.

The value for the Buck converter capacitor C can be calculated by [35]:

$$C = \frac{\Delta i_L}{8 \Delta v_o f_s} \tag{3.3}$$

where Δv_o is the desired output voltage peak ripple, Δi_L is the desired inductor current peak ripple, and f_s is the switching frequency of the Buck converter.

In DCM the input voltage to output voltage conversion ratio M becomes load dependent. Deriving the conversion ratio M gives [36]:

$$M = \frac{V_o}{V_{in}} = \frac{2}{1 + \sqrt{1 + \frac{4K}{D^2}}} \tag{3.4}$$

where D is the duty cycle, and K is a parameter that gives a measure of the tendency of the converter to operate in DCM. K is defined as:

$$K = \frac{2L}{RT_s} \tag{3.5}$$

where L is the Buck converter inductor, R is the load resistance, and T_s is the switching period.

Large K values lead to CCM operation, while small K values lead to DCM with certain duty cycles [36]. The boundary between the CCM and DCM modes is given by the critical K value K_{crit}. For a Buck converter, this is given by:

$$K_{crit}(D) = D' = 1 - D \tag{3.6}$$

The mode boundary can also be expressed in terms of the load resistance R, given by (3.7). When the load resistance R exceeds the critical load resistance value R_{crit} the converter enters DCM.

$$R_{crit}(D) = \frac{2L}{D'T_s} \tag{3.7}$$

3.1.2 Boost Converter

Figure 3.5 shows a Boost (step-up) converter, which is a switching converter that provides a higher average output voltage (V_o) than the DC input voltage (V_{in}).

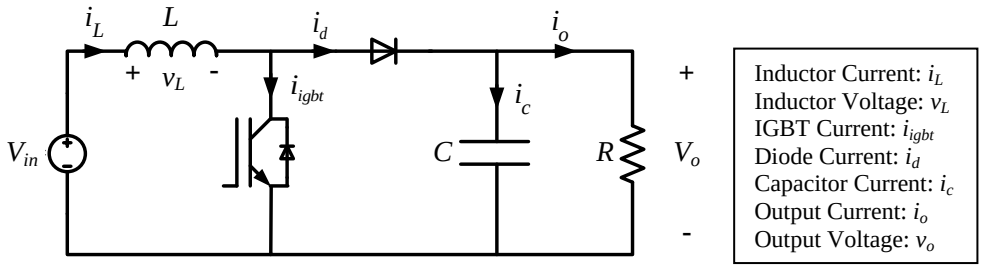

Figure 3.5: Boost Converter

The Boost converter steps-up the input DC voltage by switching the IGBT or MOSFET at a specific frequency using pulse width modulation (PWM). Similar to the Buck converter, the Boost converter can be operated in two modes: in the continuous conduction mode (CCM) and the discontinuous conduction mode (DCM). When operating in CCM, the converter inductor current ripple never reaches zero current, while when operating in DCM the converter is connected to a light load, which causes the inductor current ripple to reach zero current for part of the switching cycle.

Figure 3.6 and 3.7 show the inductor current, inductor voltage and output voltage waveforms for the Boost converter operating in CCM and DCM, respectively. In CCM mode the converter operates in two states: when the IGBT (or MOSFET) is conducting and the diode is off (reverse biased), and when the IGBT is off and the diode is conducting (forward biased). Similarly to the Buck converter, a Boost converter using unidirectional switches and operating with a light load, will have the ripple in the inductor current being more significant when compared to the average inductor current value. In this case the Boost converter is operating in DCM. In DCM mode the converter operates in three states: when the IGBT (or MOSFET) is conducting and the diode is off (reverse biased), when the IGBT is off and the diode is conducting (forward biased), and when the IGBT and the diode are both off.

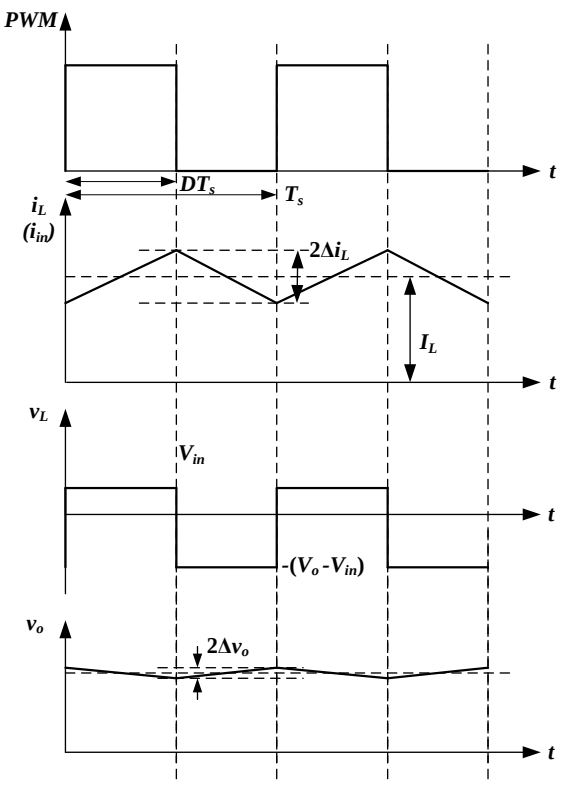

Figure 3.6: Current and Voltage Ideal Boost Converter Waveforms in CCM

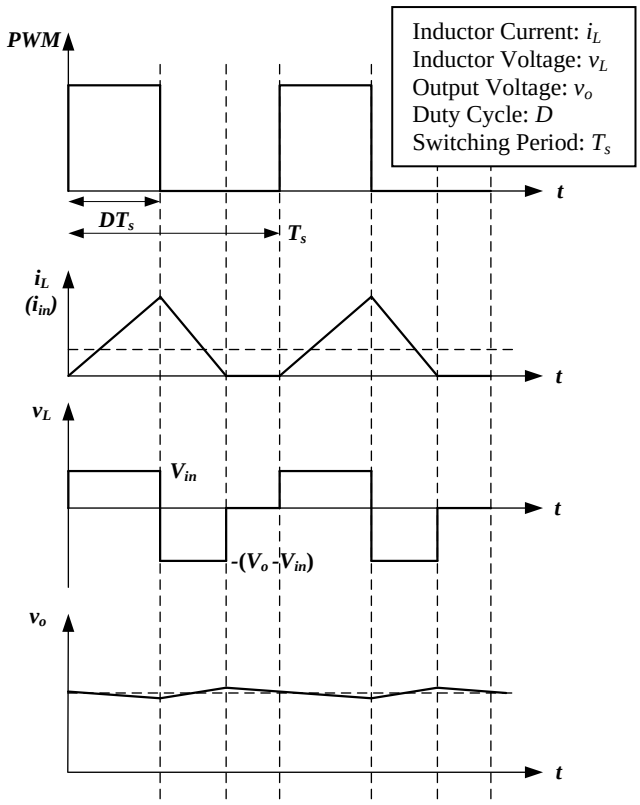

Figure 3.7: Current and Voltage Ideal Boost Converter Waveforms in DCM

For the Boost converter, the voltage conversion ratio of the input voltage V_{in} to the output voltage V_o, *M(D)*, while the converter is operating in CCM, is given by:

$$M = \frac{V_o}{V_{in}} = \frac{1}{1-D} \tag{3.8}$$

where D is the duty cycle, which is the fraction of time the IGBT (or MOSFET) is on.

The value of the inductor L and the value of the output capacitor C set the peak ripple in the inductor current and output voltage, respectively. Equations were derived to obtain the values needed for the inductor and capacitor depending on the desired ripple [35].

The value for the Boost converter inductor L can be calculated by [35]:

$$L = \frac{V_{in} D}{2\Delta i_L f_s} \tag{3.9}$$

where Δi_L is the desired inductor current peak ripple, D is the duty cycle, and f_s is the switching frequency of the Boost converter.

The value for the Boost converter capacitor C can be calculated by [35]:

$$C = \frac{V_o D}{2\Delta v_o R f_s} \tag{3.10}$$

where Δv_o is the desired output voltage peak ripple, R is the load resistance, and f_s is the switching frequency of the Boost converter.

In DCM the input voltage to output voltage conversion ratio M becomes load dependent. Deriving the conversion ratio M gives [36]:

$$M = \frac{V_o}{V_{in}} = \frac{1+\sqrt{1+\frac{4D^2}{K}}}{2} \tag{3.11}$$

where D is the duty cycle, and K is a parameter that gives a measure of the tendency of the converter to operate in DCM. K is defined as:

$$K = \frac{2L}{RT_s} \tag{3.12}$$

where L is the Buck converter inductor, R is the load resistance, and T_s is the switching period.

Large K values lead to CCM operation, while small K values lead to DCM with certain duty cycles [36]. The boundary between the CCM and DCM modes is given by the critical K value K_{crit}. For a Boost converter, this is given by:

$$K_{crit}(D) = DD'^2 = D(1-D)^2 \tag{3.13}$$

The mode boundary can also be expressed in terms of the load resistance R, given by (3.14). When the load resistance R exceeds the critical load resistance value R_{crit} the converter enters DCM.

$$R_{crit}(D) = \frac{2L}{DD'^2 T_s} \tag{3.14}$$

3.2 Converter Design

The experimental DC microgrid built for this research consists of two Buck converters and one Bidirectional converter connecting a battery bank to the DC microgrid. Designing these converters involved calculating the values for the inductors and capacitors, selecting the switching devices and calculating the heatsink required, and designing the sensing and control circuitry. In this section, only the

calculation of the inductors and capacitors is covered. Other design details are covered in Chapter 6.

3.2.1 Design of the Buck Converter Inductor and Output Capacitor

The two Buck converters were designed to operate with an input voltage in the range of 70V - 120V, and an output voltage of 48V. For the calculations and testing the input voltage was set to 100V. The Buck converter circuit diagram is shown in Figure 3.8.

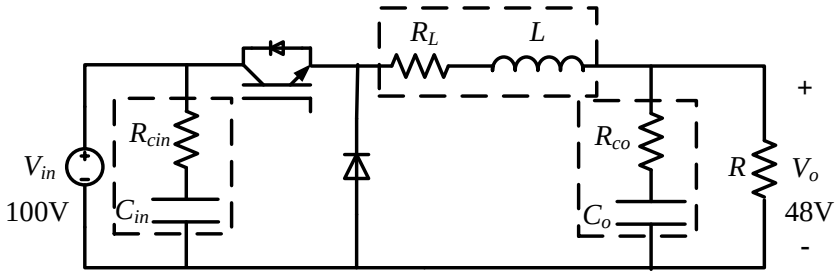

Figure 3.8: Buck Converter Circuit Diagram

Therefore, using (3.1), the Buck converters will have an average duty cycle D of 0.48.

Each Buck converter was designed for a maximum power of 2.5kW, and the switching frequency f_s of the IGBT was selected to be 10kHz, which offers a good trade-off between switching speed and losses.

The inductor was designed to have a maximum inductor current peak to peak ripple of 10% of the maximum converter current. For a maximum power of 2.5kW with an output voltage of 48V, the maximum output current is 52.1A. This leads to an average inductor current of 52.1A, and therefore, the inductor current peak to peak ripple results to be 5.21A. Using (3.2), the required inductance L was determined to be 479µH.

Following a procedure similar to the Colonel McLyman method [37], a suitable core was selected, and the number of turns and gap needed were calculated. The selected ferrite core was the Blinzinger R154x80x45-BFM8. The number of turns and the gap resulted to be 52 and 12mm, respectively. The number of turns were fine-tuned with experimental measurements once the ferrite core with the gap was available.
With this inductor, the Buck converter enters DCM when the load resistance R exceeds the critical load resistance R_{crit} of 18.4Ω, determined by (3.7).

The capacitor was calculated to have a maximum output voltage peak to peak ripple of 0.5% of the output voltage. For an output voltage of 48V, the output voltage peak to peak ripple results to be 0.24V. Using (3.3), the capacitance C_o was determined to be 271.25μF.

A Polypropylene DC-link capacitor from CDM Cornell Dubilier was selected, having a capacitance value of 270μF and a typical equivalent series resistance (ESR) of 2.1mΩ, with part number 947D271K112AEGSN.
Another Polypropylene DC-link capacitor from CDM Cornell Dubilier was selected to be installed on the input side of the Buck converters, having a capacitance value (C_{in}) of 130μF and a typical ESR of 1.9mΩ, with part number 947D131K132ACGSN.

The parameters for the Buck converters are presented in Table 3.1.

Set Parameters	
Input Voltage V_{in}	100V
Output Voltage V_o	48V
Switching Frequency f_s	10kHz
Converter Power P	2.5kW
Inductor current peak to peak percentage ripple $2\Delta i_L$	10%
Output voltage peak percentage ripple Δv_o	0.5%
Duty Cycle D	0.48
Inductor L	479μH
Inductor Resistance R_L	2mΩ
Capacitor C_o	270μF
ESR R_{co}	2.1mΩ
Capacitor C_{in}	130μF
ESR R_{cin}	1.9mΩ

Table 3.1: Buck Converter Parameters

3.2.2 Design of the Bidirectional Converter Inductor and Output Capacitor

A Synchronous Buck converter was used as the Bidirectional converter. This was designed to operate with a voltage of 48V on the higher-voltage-side and 24V on the lower-voltage-side. The 48V is the microgrid DC-bus voltage. The 24V is obtained from two 12V 120Ah batteries connected in series. The Synchronous Buck converter is a current-bidirectional converter, which means that it can conduct current from both sides. The converter works in Buck-mode when charging the 24V batteries from the microgrid 48V DC-bus, and in Boost-mode when supplying current from the 24V

batteries to the microgrid 48V DC-bus. The Bidirectional converter circuit diagram is shown in Figure 3.9.

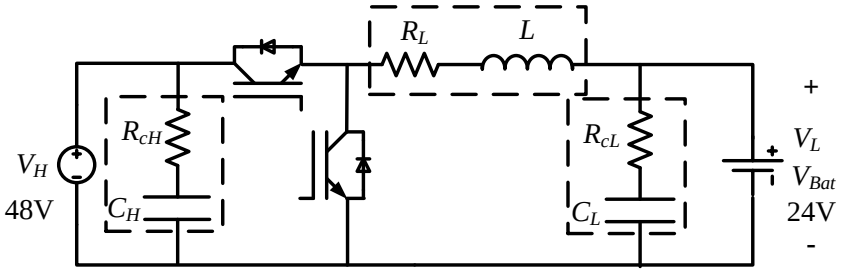

Figure 3.9: Bidirectional Converter Circuit Diagram

The values of the inductor and the higher-voltage-side capacitor were calculated by considering the converter operating as a Boost converter, while the value of the lower-voltage-side capacitor was calculated by considering the converter operating as a Buck converter.

Therefore, using (3.8), the Bidirectional converter operating as a Boost converter will have with an average duty cycle D of 0.5.

The Bidirectional converter was designed for a maximum power of 1.5kW, and the switching frequency f_s of the IGBT was selected to be 10kHz, which offers a good trade-off between switching speed and losses.

The inductor was designed to have a maximum inductor current peak to peak ripple of 10% of the maximum converter current. For a maximum power of 1.5kW with an output voltage of 48V (V_H) , the maximum output current (V_H-side current I_H) is 31.25A. With an average duty cycle of 0.5, this leads to an inductor current of 62.5A. Therefore, the inductor current peak to peak ripple results to be 6.25A. Using (3.9), the required inductance L was determined to be 192µH.

Following a procedure similar to the Colonel McLyman method [37], a suitable core was selected, and the number of turns and gap needed were calculated. The selected ferrite core was the Blinzinger R154x80x45-BFM8. The number of turns and the gap resulted to be 25 and 7mm, respectively. The number of turns were fine tuned with experimental measurements once the ferrite core with the gap was available.

The higher-voltage-side capacitor was calculated to have a maximum voltage peak to peak ripple of 1V for a higher-side voltage of 48V. Using (3.10), the capacitance C_H was determined to be 1562.5µF.

An aluminium electrolytic capacitor from Nichicon was selected, having a capacitance value of 1500μF and a measured ESR of 0.03Ω, with part number LNX2V152MSEF.

The lower-voltage-side capacitor was calculated to have a maximum voltage peak to peak ripple of 0.5% of the lower-side voltage. For a voltage of 24V, the voltage peak to peak ripple results to be 0.12V. Using (3.3), the capacitance C_L was determined to be 651.04μF.

An aluminium electrolytic capacitor from Nichicon was selected, having a capacitance value of 680μF and a measured ESR of 0.03Ω, with part number LNT2G681MSEF.

For both the higher-voltage-side capacitor and the lower-voltage-side capacitor the first preference was to use Polypropylene DC-link capacitors due to their low ESR. However there was a difficulty to source the required values and the space in the converters' enclosures to form the required values with multiple capacitors was limited for only two capacitors. Due to this aluminium electrolytic capacitors were used.

The parameters for the Bidirectional converter are presented in Table 3.2.

Set Parameters	
Lower-Side Voltage V_L	24V
Higher-Side Voltage V_H	48V
Switching Frequency f_s	10kHz
Converter Power P	1.5kW
Inductor current peak to peak percentage ripple $2\Delta i_L$	10%
Lower-voltage-side peak to peak percentage ripple Δv_L	0.5%
Higher-voltage-side peak to peak ripple Δv_H	1V
Duty Cycle D in Boost-mode	0.5
Duty Cycle D in Buck-mode	0.5
Inductor L	192μH
Inductor Resistance R_L	2mΩ
Lower-voltage-side Capacitor C_L	680μF
Lower-voltage-side Capacitor ESR R_{cL}	0.03Ω
Higher-voltage-side Capacitor C_H	1500μF
Higher-voltage-side Capacitor ESR R_{cH}	0.03Ω

Table 3.2: Bidirectional Converter Parameters

3.3 Conclusion

This chapter covered the theory and design of the converters forming part of the laboratory-based DC microgrid.

The equations required to calculate the inductors and capacitors for the converters were discussed. The theory covered the two modes of operation of these converters, namely the continuous conduction mode (CCM) and the discontinuous conduction mode (DCM). In CCM, the converter inductor current ripple never reaches zero current. On the other hand, DCM operation occurs when the converter is operating with a light load, causing the inductor current ripple to reach zero current for part of the switching cycle. DCM generally occurs in converters using current-unidirectional switches.

The experimental DC microgrid consists of two Buck converters and one Bidirectional converter, together with resistive loads. The two Buck converters were designed to operate with an input voltage in the range between 70V – 120V and an output voltage of 48V, while the Bidirectional converter was designed to operate with a DC-bus voltage of 48V and battery voltage of 24V. The Bidirectional converter works as a Buck converter when charging the 24V batteries from the microgrid's 48V DC-bus and as a Boost converter when supplying current from the 24V batteries to the microgrid's 48V DC-bus.

Chapter 4 Converter Modelling

4.1 DC-DC Converter Modelling

The selection and design of the converters and their control systems are very important for proper operation of the DC microgrid. In order to design correctly the control system a detailed converter model and analysis is required. Therefore, for this research work, effort was directed on modelling the Buck and Boost converters, deriving the small signal model, and deriving the transfer functions needed to design the control system for these converters, to be used within a DC microgrid.

The Buck and Boost converter topologies can be considered as the basis for other advanced converters. These two converter topologies are an attractive option for interfacing renewable energy sources, such as photovoltaic (PV) panels and wind turbine systems, with a DC microgrid infrastructure. This is because these converters can convert the DC output from the source to the required DC microgrid voltage with less conversion stages compared to other converter topologies. Both converters were modelled operating in the continuous conduction mode (CCM) and the discontinuous conduction mode (DCM). CCM means that the converter is operated with the inductor current ripple never reaching zero current. On the other hand, with DCM the converter is operated with a light load, causing the inductor current ripple to reach zero current for part of the switching cycle. The small signal models were derived for both Buck and Boost converters. These models were used to derive the transfer functions needed to design the control loops.

4.2 Averaged Equation Representation of Converters

To construct a model of a converter, the average equations representing the converter need to be derived. These equations are obtained by averaging currents and voltages in the converter over a time interval taken as the switching period. Averaging removes the switching ripples in the inductor current and capacitor voltage waveforms, and describes the variations in DC and low-frequency components of the waveforms. This method of converter modelling is valid when considering an inductor current with a linear ripple and with a small output voltage ripple.

The average value of a current or voltage variable $x(t)$ over a switching period T_s is obtained by:

$$\langle x(t)\rangle_{T_s} = \frac{1}{T_s}\int_{t}^{t+T_s} x(\tau)d\tau \tag{4.1}$$

The averaged equations are non-linear since these contain multiplications of time-varying quantities. This makes the use of circuit analysis techniques like Laplace Transform and other frequency-domain methods useless [36]. Therefore, linearization of the equations is needed to derive and construct the small signal model.

4.3 Buck Converter

4.3.1 Modelling the Buck Converter in CCM

The averaged equations representing the ideal Buck converter operating in CCM were derived, shown as equations (4.2), (4.3), and (4.4). These equations were obtained by considering the two states of operation of the Buck converter: when the IGBT (or MOSFET) is conducting and the diode is off (reverse biased), and when the IGBT is off and the diode is conducting (forward biased). If a non-ideal Buck converter is considered, by taking into consideration the inductor resistance R_L and the equivalent series resistance (ESR) of the capacitor R_C, the averaged equations (4.2) and (4.3) change to (4.5) and (4.6), respectively. Equation (4.4) remains the same. These equations describe DC and low-frequency AC variations in the inductor current, capacitor voltage, and input current.

$$\langle v_L(t)\rangle_{T_s} = L\frac{d\langle i_L(t)\rangle}{dt} = d(t)\langle v_{in}(t)\rangle - \langle v_o(t)\rangle \quad \text{(Ideal)} \tag{4.2}$$

$$\langle i_c(t)\rangle_{T_s} = C\frac{d\langle v_o(t)\rangle}{dt} = \langle i_L(t)\rangle - \frac{\langle v_o(t)\rangle}{R} \quad \text{(Ideal)} \tag{4.3}$$

$$\langle i_{in}(t)\rangle_{T_s} = d(t)\langle i_L(t)\rangle \tag{4.4}$$

$$\langle v_L(t)\rangle_{T_s} = L\frac{d\langle i_L(t)\rangle}{dt} = d(t)\langle v_{in}(t)\rangle - \langle i_L(t)\rangle R_L - \langle v_o(t)\rangle \quad \text{(Non-ideal)} \tag{4.5}$$

$$\langle i_c(t)\rangle_{T_s} = C\frac{d\langle v_c(t)\rangle}{dt} = \langle i_L(t)\rangle - \frac{\langle v_o(t)\rangle}{R} \quad \text{(Non-ideal)} \tag{4.6}$$

where $\langle i_L(t)\rangle$, $\langle i_c(t)\rangle$, $\langle i_{in}(t)\rangle$, $\langle v_L(t)\rangle$, $\langle v_{in}(t)\rangle$, $\langle v_o(t)\rangle$, $\langle v_c(t)\rangle$, and $d(t)$ represent the average values of the inductor current, capacitor current, input current, inductor

voltage, input voltage, output voltage, capacitor voltage, and duty cycle, respectively. *L*, *C*, and *R* are the Buck converter inductor, the Buck converter capacitor, and the load resistance, respectively.

The linearized small signal mathematical equations for the ideal Buck converter in CCM were derived from the averaged equations, giving equations (4.7), (4.8) and (4.9). For a non-ideal Buck converter, the CCM linearized small signal mathematical equations (4.7) and (4.8) change to (4.10) and (4.11), respectively. Equation (4.9) remains the same.

$$L\frac{d\hat{i}_L(t)}{dt} = D\hat{v}_{in}(t) + \hat{d}(t)V_{in} - \hat{v}_o(t) \qquad \text{(Ideal)} \qquad (4.7)$$

$$\hat{i}_c(t) = C\frac{d\hat{v}_o(t)}{dt} = \hat{i}_L(t) - \frac{\hat{v}_o(t)}{R} \qquad \text{(Ideal)} \qquad (4.8)$$

$$\hat{i}_{in}(t) = D\hat{i}_L(t) + \hat{d}(t)I_L \qquad (4.9)$$

$$L\frac{d\hat{i}_L(t)}{dt} = D\hat{v}_{in}(t) + \hat{d}(t)V_{in} - \hat{i}_L(t)R_L - \hat{v}_o(t) \qquad \text{(Non-ideal)} \qquad (4.10)$$

$$\hat{i}_c(t) = C\frac{d\hat{v}_c(t)}{dt} = \hat{i}_L(t) - \frac{\hat{v}_o(t)}{R} \qquad \text{(Non-ideal)} \qquad (4.11)$$

where $\hat{i}_L(t)$, $\hat{i}_c(t)$, $\hat{i}_{in}(t)$, $\hat{d}(t)$, $\hat{v}_{in}(t)$, $\hat{v}_o(t)$, and $\hat{v}_c(t)$ are small AC variations around the quiescent values for the inductor current, capacitor current, input current, duty cycle, input voltage, output voltage, and capacitor voltage, respectively. I_L is the average inductor current, L is the Buck converter inductor, R_L is the inductor resistance, C is the Buck converter capacitor, R_C is the equivalent series resistance (ESR) of the capacitor, D is the duty cycle, and R is the load resistance.

From the linearized small signal mathematical equations, the CCM small signal equivalent models of the ideal and non-ideal Buck converters were obtained, shown in Figures 4.1 and 4.2, respectively. In Figures 4.1 and 4.2, the switches are represented using dependent sources. The CCM small signal model can also be built using the ideal transformer method instead of the dependent sources, as shown in Figures 4.3 and 4.4.

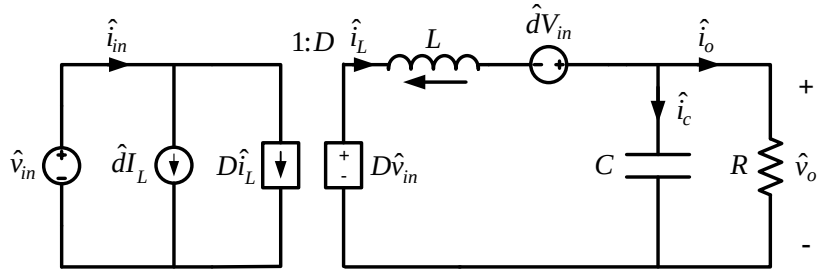

Figure 4.1: Buck Converter Small Signal Equivalent Circuit (Ideal) using Dependent Sources in CCM

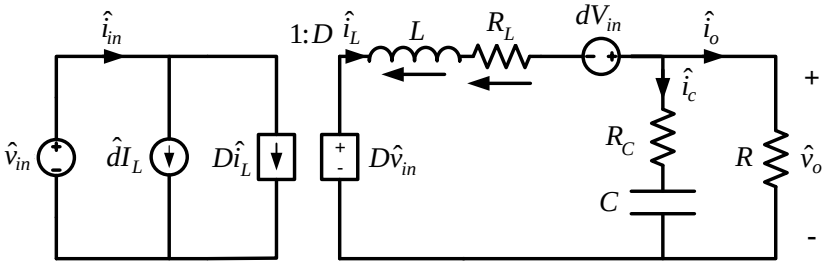

Figure 4.2: Buck Converter Small Signal Equivalent Circuit (with R_L and R_C) using Dependent Sources in CCM

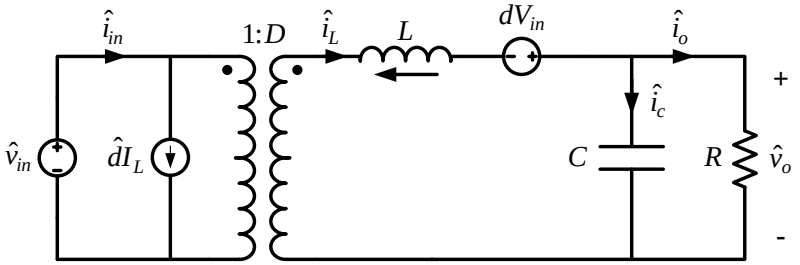

Figure 4.3: Buck Converter Small Signal Equivalent Circuit (Ideal) using Ideal Transformer

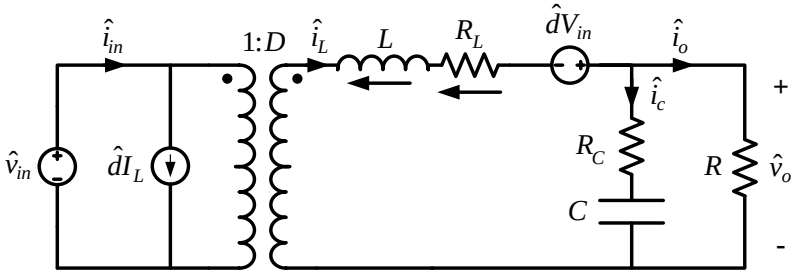

Figure 4.4: Buck Converter Small Signal Equivalent Circuit (with R_L and R_C) using Ideal Transformer

If the small AC variations around the quiescent value of the input voltage are considered as negligible ($\hat{v}_{in}(t) \rightarrow 0$), the equivalent circuits in Figures 4.3 and 4.4 can be simplified to obtain the versions shown in Figures 4.5 and 4.6, which are more intuitive to obtain the required transfer functions.

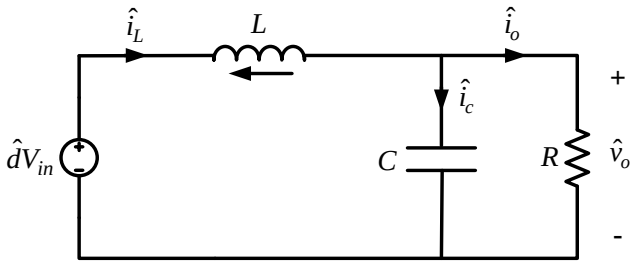

Figure 4.5: Buck Converter Simplified Small Signal Equivalent Circuit (Ideal)

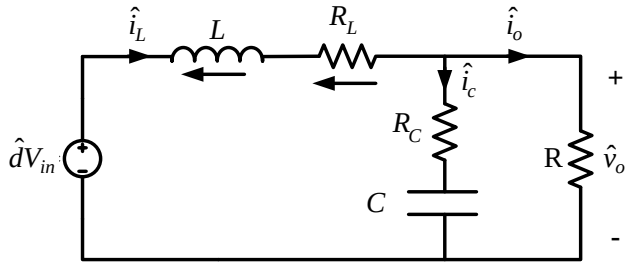

Figure 4.6: Buck Converter Simplified Small Signal Equivalent Circuit (with R_L and R_C)

By transforming the small signal mathematical model equations to the s-domain and using the small signal equivalent circuit, the transfer functions of the duty cycle to the inductor current G_{id}(s), (4.12) and (4.15), the inductor current to the output voltage G_{vi}(s), (4.13) and (4.16), and the duty cycle to the output voltage G_{vd}(s), (4.14) and (4.17), can be obtained as follows:

For the ideal CCM Buck converter:

$$G_{id}(s) = \frac{\hat{i}_L(s)}{\hat{d}(s)} = \frac{V_{in}(sCR+1)}{s^2CLR + sL + R} \tag{4.12}$$

$$G_{vi}(s) = \frac{\hat{v}_o(s)}{\hat{i}_L(s)} = \frac{R}{sCR+1} \tag{4.13}$$

$$G_{vd}(s) = \frac{\hat{v}_o(s)}{\hat{d}(s)} = \frac{V_{in}R}{s^2CLR + sL + R} \tag{4.14}$$

For the non-ideal (including R_L and R_C) CCM Buck converter:

$$G_{id}(s) = \frac{\hat{i}_L(s)}{\hat{d}(s)} = \frac{V_{in}(s(CR+CR_C)+1)}{s^2(CLR+CLR_C) + s(L+CRR_L+CR_CR_L+CR_CR) + R_L + R} \tag{4.15}$$

$$G_{vi}(s) = \frac{\hat{v}_o(s)}{\hat{i}_L(s)} = \frac{sCRR_C + R}{s(CR+CR_C)+1} \tag{4.16}$$

$$G_{vd}(s) = \frac{\hat{v}_o(s)}{\hat{d}(s)} = \frac{V_{in}(sCRR_C + R)}{s^2(CLR + CLR_C) + s(L + CRR_L + CR_CR_L + CR_CR) + R_L + R} \quad (4.17)$$

4.3.2 Modelling the Buck Converter in DCM

In DCM mode, the converter operates in three states: when the IGBT (or MOSFET) is conducting and the diode is off (reverse biased), when the IGBT is off and the diode is conducting (forward biased), and when the IGBT and the diode are both off.

In DCM mode a model for the Buck converter can be built using the loss-free resistor and dependent power source model.

4.3.2.1 Loss-free Resistor and Dependent Power Source Model

In the discontinuous conduction mode, the IGBT (or MOSFET) average current and voltage follow a linear behaviour, so it can be modelled using an effective resistance R_e. The diode average current and voltage follow a power source characteristic, with the power value being the power dissipated in R_e, which result in the diode being modelled as a dependent power source p [36]. The model for the switching elements of the Buck converter is shown in Figure 4.7.

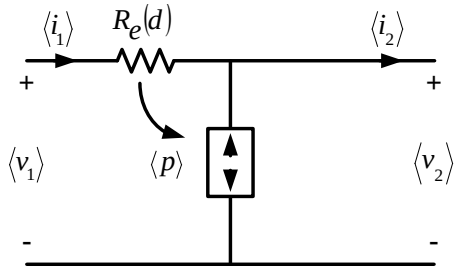

Figure 4.7: Averaged Model of the Switching Elements in a Buck Converter – Loss-Free Resistor and Dependent Power Source Method

The effective resistance R_e for the Buck converter can be obtained by:

$$R_e(d) = \frac{2L}{d^2 T_s} \quad (4.18)$$

where L is the Buck converter inductor, d is the duty cycle (ON state), and T_s is the switching period.

Deriving the averaged equations representing the switching elements of the Buck converter operating in DCM give equations (4.19) and (4.20):

$$\langle i_1(t) \rangle_{T_s} = \frac{\langle v_1(t) \rangle}{R_e(d)} - \frac{\langle v_2(t) \rangle}{R_e(d)} \quad (4.19)$$

$$\langle i_2(t)\rangle_{T_s} = \frac{\langle v_1(t)\rangle^2}{\langle v_2(t)\rangle R_e(d)} - \frac{\langle v_1(t)\rangle}{R_e(d)} \tag{4.20}$$

where $\langle i_1(t)\rangle$, $\langle i_2(t)\rangle$, $\langle v_1(t)\rangle$, and $\langle v_2(t)\rangle$ represent the average values of the input port current, output port current, input port voltage, and output port voltage, respectively. $R_e(d)$ is the effective resistance.

The averaged model for the Buck converter in DCM using the loss-free resistor and dependent power source model is shown in Figure 4.8.

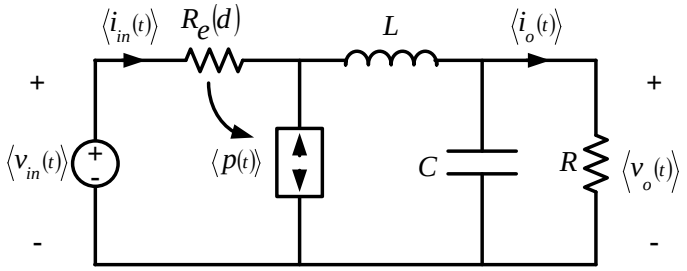

Figure 4.8: Averaged Model of the Buck Converter in DCM – Loss-Free Resistor and Dependent Power Source Method

The linearized small signal mathematical equations for the switching elements of the Buck converter operating in DCM were derived from the averaged equations, giving equations (4.21) and (4.22):

$$\hat{i}_1(t) = \hat{v}_1(t)\frac{1}{r_1} + \hat{v}_2(t)g_1 + \hat{d}(t)\,j_1 \tag{4.21}$$

where $r_1 = R_e$,

$$g_1 = -\frac{1}{R_e},$$

$$j_1 = \frac{2(V_1 - V_2)}{DR_e} = \frac{2(1-M)V_1}{DR_e}$$

$$\hat{i}_2(t) = \hat{v}_2(t)\left(-\frac{1}{r_2}\right) + \hat{v}_1(t)g_2 + \hat{d}(t)\,j_2 \tag{4.22}$$

where $-\frac{1}{r_2} = -\frac{V_1^2}{V_2^2 R_e} = -\frac{1}{M^2 R_e}$ => $r_2 = M^2 R_e$,

$$g_2 = \frac{2V_1}{V_2 R_e} - \frac{1}{R_e} = \frac{2-M}{MR_e},$$

$$j_2 = \frac{2V_1^2}{DR_e V_2} - \frac{2V_1}{DR_e} = \frac{2(1-M)V_1}{MDR_e}$$

where $\hat{i}_1(t)$, $\hat{i}_2(t)$, $\hat{d}(t)$, $\hat{v}_1(t)$, and $\hat{v}_2(t)$ are small AC variations around the quiescent values for the input port current, output port current, duty cycle, input port voltage, and output port voltage, respectively. R_e is the effective resistance, V_1 is the input port voltage, V_2 is the output port voltage, D is the duty cycle, and M is the conversion ratio (V_2/V_1).

The conversion ratio M can be derived in terms of the effective resistance R_e, given by (4.23) for an ideal Buck converter in DCM and by (4.24) if the inductor resistance R_L is included:

$$M = \frac{V_o}{V_{in}} = \frac{2}{1+\sqrt{1+\frac{4R_e}{R}}} \tag{4.23}$$

$$M = \frac{V_o}{V_{in}} = \frac{R}{(R_L+R)} \frac{2}{\left(1+\sqrt{1+\frac{4R_e}{R_L+R}}\right)} \tag{4.24}$$

where R_L is the inductor resistance, R is the load resistance, R_e is the effective resistance, V_{in} is the input voltage, and V_o is the output voltage.

Using the linearized small signal mathematical equations, the DCM small signal equivalent models of the ideal and non-ideal Buck converters were obtained, shown in Figures 4.9 and 4.10, respectively, using dependent sources.

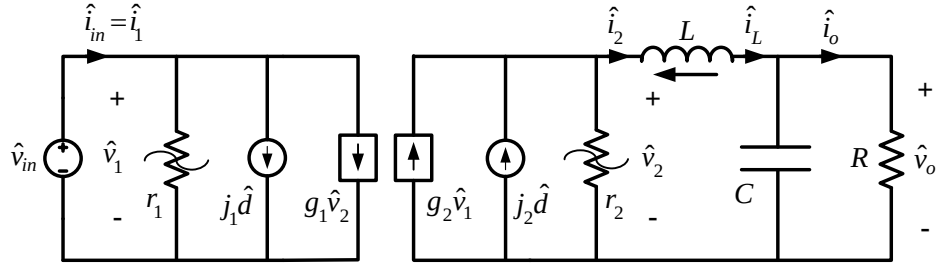

Figure 4.9: Buck Converter Small Signal Equivalent Circuit (Ideal) using Dependent Sources in DCM

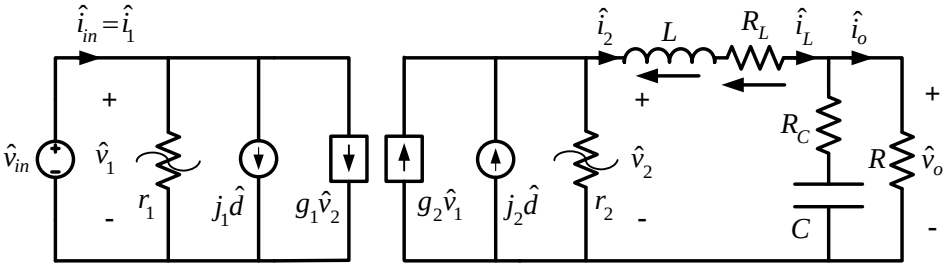

Figure 4.10: Buck Converter Small Signal Equivalent Circuit (with R_L and R_C) using Dependent Sources in DCM

$\hat{i}_L(t)$, $\hat{i}_{in}(t)$, $\hat{d}(t)$, $\hat{v}_{in}(t)$, and $\hat{v}_o(t)$ are small AC variations around the quiescent values for the inductor current, input current, duty cycle, input voltage, and output voltage, respectively. L is the Buck converter inductor, R_L is the inductor resistance, C is the Buck converter capacitor, R_C is the equivalent series resistance (ESR) of the capacitor, and R is the load resistance.

Using the small signal mathematical model equations and the small signal equivalent circuit, the transfer functions of the duty cycle to the inductor current G_{id}(s), (4.25) and (4.28), the inductor current to the output voltage G_{vi}(s), (4.26) and (4.29), and the duty cycle to the output voltage G_{vd}(s), (4.27) and (4.30), can be obtained:

For the ideal DCM Buck converter:

$$G_{id}(s) = \frac{\hat{i}_2(s)}{\hat{d}(s)} = \frac{\hat{i}_L(s)}{\hat{d}(s)} = \frac{sCRr_2 j_2 + r_2 j_2}{s^2 CLR + s(CRr_2 + L) + r_2 + R} \tag{4.25}$$

$$G_{vi}(s) = \frac{\hat{v}_o(s)}{\hat{i}_2(s)} = \frac{\hat{v}_o(s)}{\hat{i}_L(s)} = \frac{R}{sCR + 1} \tag{4.26}$$

$$G_{vd}(s) = \frac{\hat{v}_o(s)}{\hat{d}(s)} = \frac{Rr_2 j_2}{s^2 CLR + s(CRr_2 + L) + r_2 + R} \tag{4.27}$$

For the non-ideal (including R_L and R_C) DCM Buck converter:

$$G_{id}(s) = \frac{\hat{i}_2(s)}{\hat{d}(s)} = \frac{\hat{i}_L(s)}{\hat{d}(s)} = \frac{sC(R + R_C)r_2 j_2 + r_2 j_2}{s^2 CL(R + R_C) + s(L + C(R + R_C)R_L + C(R + R_C)r_2 + CRR_C) + r_2 + R_L + R} \tag{4.28}$$

$$G_{vi}(s) = \frac{\hat{v}_o(s)}{\hat{i}_2(s)} = \frac{\hat{v}_o(s)}{\hat{i}_L(s)} = \frac{sCRR_C + R}{sC(R + R_C) + 1} \tag{4.29}$$

$$G_{vd}(s) = \frac{\hat{v}_o(s)}{\hat{d}(s)} = \frac{sCRR_C r_2 j_2 + Rr_2 j_2}{s^2 CL(R + R_C) + s(L + C(R + R_C)R_L + C(R + R_C)r_2 + CRR_C) + r_2 + R_L + R} \tag{4.30}$$

4.4 Boost Converter

4.4.1 Modelling the Boost Converter in CCM

The averaged equations representing the ideal Boost converter operating in CCM were derived, shown as equations (4.31), (4.32), and (4.33). These equations were obtained by considering the two states of operation of the Boost converter: when the IGBT (or MOSFET) is conducting and the diode is off (reverse biased), and when the IGBT is off and the diode is conducting (forward biased). If a non-ideal Boost converter is considered, by taking into consideration the inductor resistance R_L and the equivalent series resistance (ESR) of the capacitor R_C, the averaged equations (4.31) and (4.32) change to (4.34) and (4.35), respectively. Equation (4.33) remains the same. These equations describe DC and low-frequency AC variations in the inductor current, capacitor voltage, and input current.

$$\left\langle v_L(t)\right\rangle_{T_s} = L\frac{d\left\langle i_L(t)\right\rangle}{dt} = \left\langle v_{in}(t)\right\rangle - d'(t)\left\langle v_o(t)\right\rangle \qquad \text{(Ideal)} \qquad (4.31)$$

$$\left\langle i_c(t)\right\rangle_{T_s} = C\frac{d\left\langle v_o(t)\right\rangle}{dt} = -\frac{\left\langle v_o(t)\right\rangle}{R} + d'(t)\left\langle i_L(t)\right\rangle \qquad \text{(Ideal)} \qquad (4.32)$$

$$\left\langle i_{in}(t)\right\rangle_{T_s} = \left\langle i_L(t)\right\rangle \qquad (4.33)$$

$$\left\langle v_L(t)\right\rangle_{T_s} = L\frac{d\left\langle i_L(t)\right\rangle}{dt} = \left\langle v_{in}(t)\right\rangle - \left\langle i_L(t)\right\rangle R_L - d'(t)\left\langle v_o(t)\right\rangle \quad \text{(Non-ideal)} \qquad (4.34)$$

$$\left\langle i_c(t)\right\rangle_{T_s} = C\frac{d\left\langle v_c(t)\right\rangle}{dt} = -\frac{\left\langle v_o(t)\right\rangle}{R} + d'(t)\left\langle i_L(t)\right\rangle \qquad \text{(Non-ideal)} \qquad (4.35)$$

where $\left\langle i_L(t)\right\rangle$, $\left\langle i_c(t)\right\rangle$, $\left\langle i_{in}(t)\right\rangle$, $\left\langle v_L(t)\right\rangle$, $\left\langle v_{in}(t)\right\rangle$, $\left\langle v_o(t)\right\rangle$, $\left\langle v_c(t)\right\rangle$, and $d(t)$ represent the average values of the inductor current, capacitor current, input current, inductor voltage, input voltage, output voltage, capacitor voltage, and duty cycle, respectively. L, C, and R are the Boost converter inductor, the Boost converter capacitor, and the load resistance, respectively.

Also, $\quad d'(t) = 1 - d(t) \qquad (4.36)$

The linearized small signal mathematical equations for the ideal Boost converter in CCM were derived from the averaged equations, giving equations (4.37), (4.38) and (4.39). For a non-ideal Boost converter, the CCM linearized small signal mathematical equations (4.37) and (4.38) change to (4.40) and (4.41), respectively. Equation (4.39) remains the same.

$$L\frac{d\hat{i}_L(t)}{dt} = \hat{v}_{in}(t) - D'\hat{v}_o(t) + \hat{d}(t)V_o \qquad \text{(Ideal)} \qquad (4.37)$$

$$\hat{i}_c(t) = C\frac{d\hat{v}_o(t)}{dt} = -\frac{\hat{v}_o(t)}{R} + D'\hat{i}_L(t) - \hat{d}(t)I_L \qquad \text{(Ideal)} \qquad (4.38)$$

$$\hat{i}_{in}(t) = \hat{i}_L(t) \qquad (4.39)$$

$$L\frac{d\hat{i}_L(t)}{dt} = \hat{v}_{in}(t) - \hat{i}_L(t)R_L - D'\hat{v}_o(t) + \hat{d}(t)V_o \qquad \text{(Non-ideal)} \qquad (4.40)$$

$$\hat{i}_c(t) = C\frac{d\hat{v}_c(t)}{dt} = -\frac{\hat{v}_o(t)}{R} + D'\hat{i}_L(t) - \hat{d}(t)I_L \qquad \text{(Non-ideal)} \qquad (4.41)$$

where $\hat{i}_L(t)$, $\hat{i}_c(t)$, $\hat{i}_{in}(t)$, $\hat{d}(t)$, $\hat{v}_{in}(t)$, $\hat{v}_o(t)$, and $\hat{v}_c(t)$ are small AC variations around the quiescent values for the inductor current, capacitor current, input current, duty cycle, input voltage, output voltage, and capacitor voltage, respectively. I_L is the average inductor current, L is the Boost converter inductor, R_L is the inductor resistance, C is the Boost converter capacitor, R_C is the equivalent series resistance (ESR) of the capacitor, D is the duty cycle, and R is the load resistance.

Also, $D' = 1 - D$ (4.42)

From the linearized small signal mathematical equations, the CCM small signal equivalent models of the ideal and non-ideal Boost converters were obtained, shown in Figures 4.11 and 4.12, respectively. In Figures 4.11 and 4.12, the switches are represented using dependent sources. The CCM small signal model can also be built using the ideal transformer method instead of the dependent sources, as shown in Figures 4.13 and 4.14.

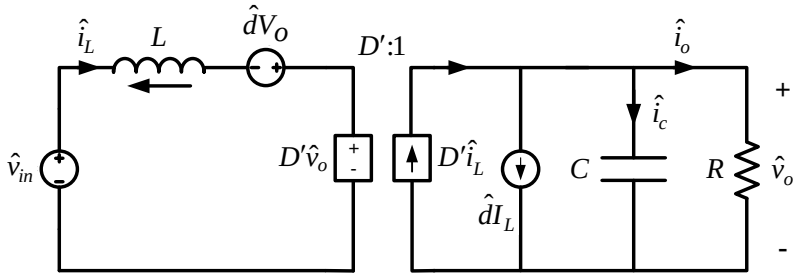

Figure 4.11: Boost Converter Small Signal Equivalent Circuit (Ideal) using Dependent Sources in CCM

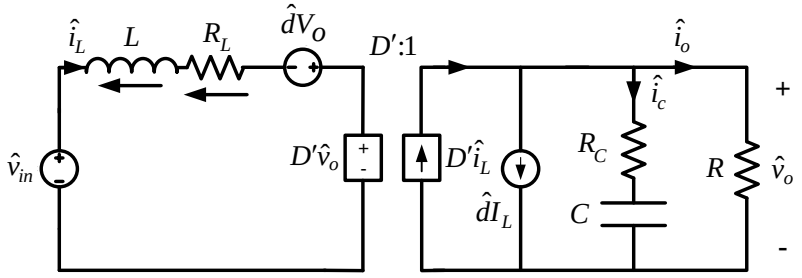

Figure 4.12: Boost Converter Small Signal Equivalent Circuit (with R_L and R_C) using Dependent Sources in CCM

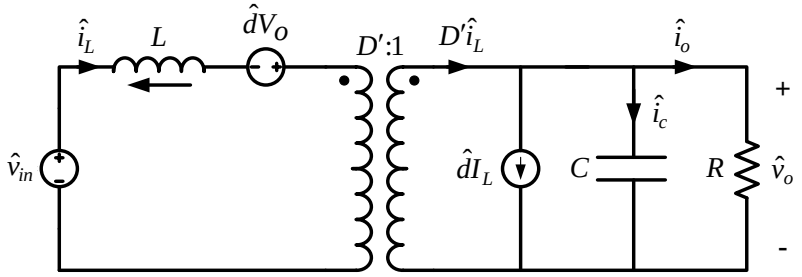

Figure 4.13: Boost Converter Small Signal Equivalent Circuit (Ideal) using Ideal Transformer

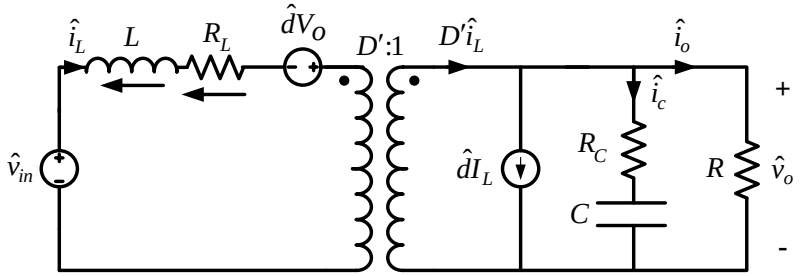

Figure 4.14: Boost Converter Small Signal Equivalent Circuit (with R_L and R_C) using Ideal Transformer

If the small AC variations around the quiescent value of the input voltage are considered as negligible ($\hat{v}_{in}(t) \rightarrow 0$), the equivalent circuits in Figures 4.13 and 4.14 can be simplified to obtain the versions shown in Figures 4.15 and 4.16, which are more intuitive to obtain the required transfer functions.

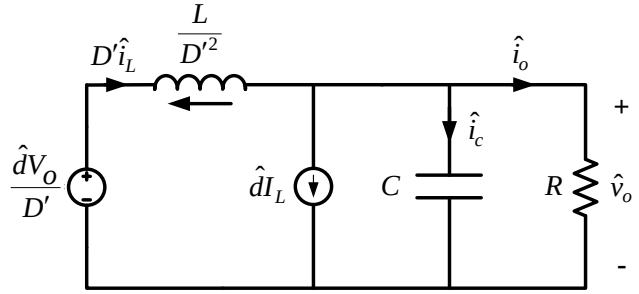

Figure 4.15: Boost Converter Simplified Small Signal Equivalent Circuit (Ideal)

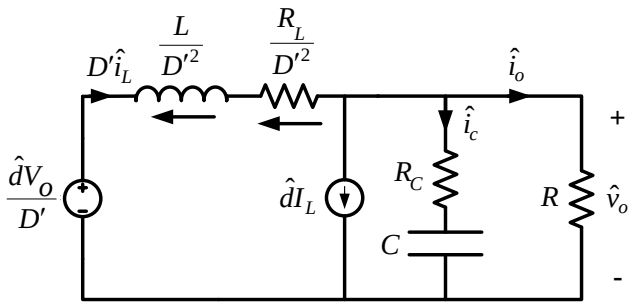

Figure 4.16: Boost Converter Simplified Small Signal Equivalent Circuit (with R_L and R_C)

By transforming the small signal mathematical model equations to the s-domain and using the small signal equivalent circuit, the transfer functions of the duty cycle to the inductor current G_{id}(s), (4.43) and (4.46), the inductor current to the output voltage G_{vi}(s), (4.44) and (4.47), and the duty cycle to the output voltage G_{vd}(s), (4.45) and (4.48), can be obtained as follows:

For the ideal CCM Boost converter:

$$G_{id}(s) = \frac{\hat{i}_L(s)}{\hat{d}(s)} = \frac{sCRV_o + V_o + I_L RD'}{s^2 CLR + sL + RD'^2} \tag{4.43}$$

$$G_{vi}(s) = \frac{\hat{v}_o(s)}{\hat{i}_L(s)} = \frac{-sLRI_L + D'V_o R}{sCRV_o + V_o + I_L RD'} \tag{4.44}$$

$$G_{vd}(s) = \frac{\hat{v}_o(s)}{\hat{d}(s)} = \frac{-sLRI_L + D'V_o R}{s^2 CLR + sL + RD'^2} \tag{4.45}$$

For the non-ideal (including R_L and R_C) CCM Boost converter:

$$G_{id}(s) = \frac{\hat{i}_L(s)}{\hat{d}(s)}$$

$$= \frac{sC(RV_o + R_C V_o + R_C RD'I_L) + V_o + I_L RD'}{s^2 CL(R + R_C) + s(L + CRR_L + CR_C R_L + CR_C RD'^2) + R_L + RD'^2} \tag{4.46}$$

$$G_{vi}(s) = \frac{\hat{v}_o(s)}{\hat{i}_L(s)}$$

$$= \frac{-s^2 CLR_C RI_L + s(CR_C RD'V_o - LRI_L - CR_C R_L RI_L) - R_L RI_L + D'V_o R}{sC(RV_o + R_C V_o + R_C RD'I_L) + V_o + I_L RD'} \tag{4.47}$$

$$G_{vd}(s) = \frac{\hat{v}_o(s)}{\hat{d}(s)}$$

$$= \frac{-s^2 CLR_C RI_L + s(CR_C RD'V_o - LRI_L - CR_C R_L RI_L) - R_L RI_L + D'V_o R}{s^2 CL(R + R_C) + s(L + CRR_L + CR_C R_L + CR_C RD'^2) + R_L + RD'^2} \tag{4.48}$$

4.4.2 Modelling the Boost Converter in DCM

In DCM mode, the converter operates in three states: when the IGBT (or MOSFET) is conducting and the diode is off (reverse biased), when the IGBT is off and the diode is conducting (forward biased), and when the IGBT and the diode are both off.

In DCM mode a model for the Boost converter can be built using the loss-free resistor and dependent power source model.

4.4.2.1 Loss-free Resistor and Dependent Power Source Model

In the discontinuous conduction mode, the IGBT (or MOSFET) average current and voltage follow a linear behaviour, so it can be modelled using an effective resistance R_e. The diode average current and voltage follow a power source characteristic, with the power value being the power dissipated in R_e, which result in the diode being modelled as a dependent power source p [36]. The model for the switching elements of the Boost converter is shown in Figure 4.17.

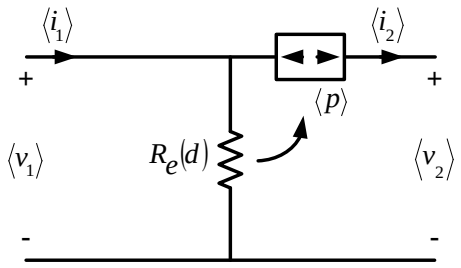

Figure 4.17: Averaged Model of the Switching Elements in a Boost Converter – Loss-Free Resistor and Dependent Power Source Method

The effective resistance R_e for the Boost converter can be obtained by:

$$R_e(d) = \frac{2L}{d^2 T_s} \tag{4.49}$$

where, L is the Boost converter inductor, d is the duty cycle (ON state), and T_s is the switching period.

Deriving the averaged equations representing the switching elements of the Boost converter operating in DCM give equations (4.50) and (4.51):

$$\left\langle i_1(t)\right\rangle_{T_s} = \frac{\left\langle v_1(t)\right\rangle}{R_e(d)} - \frac{\left\langle v_1(t)\right\rangle^2}{\left(\left\langle v_2(t)\right\rangle - \left\langle v_1(t)\right\rangle\right)R_e(d)} \tag{4.50}$$

$$\left\langle i_2(t)\right\rangle_{T_s} = \frac{\left\langle v_1(t)\right\rangle^2}{\left(\left\langle v_2(t)\right\rangle - \left\langle v_1(t)\right\rangle\right)R_e(d)} \tag{4.51}$$

where $\langle i_1(t)\rangle$, $\langle i_2(t)\rangle$, $\langle v_1(t)\rangle$, and $\langle v_2(t)\rangle$ represent the average values of the input port current, output port current, input port voltage, and output port voltage, respectively. $R_e(d)$ is the effective resistance.

The averaged model for the Boost converter in DCM using the loss-free resistor and dependent power source model is shown in Figure 4.18.

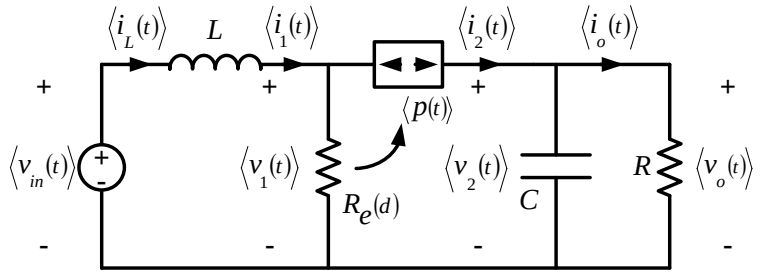

Figure 4.18: Averaged Model of the Boost Converter in DCM – Loss-Free Resistor and Dependent Power Source Method

The linearized small signal mathematical equations for the switching elements of the Boost converter operating in DCM were derived from the averaged equations, giving equations (4.52) and (4.53):

$$\hat{i}_1(t) = \hat{v}_1(t)\frac{1}{r_1} + \hat{v}_2(t)g_1 + \hat{d}(t)\,j_1 \qquad (4.52)$$

where $r_1 = \dfrac{R_e(M-1)^2}{M^2}$,

$g_1 = -\dfrac{1}{R_e(M-1)^2}$,

$j_1 = \dfrac{2V_1M}{R_eD(M-1)}$

$$\hat{i}_2(t) = \hat{v}_2(t)\left(-\frac{1}{r_2}\right) + \hat{v}_1(t)g_2 + \hat{d}(t)\,j_2 \qquad (4.53)$$

where $-\dfrac{1}{r_2} = -\dfrac{V_1^2}{R_e(V_2-V_1)^2} = -\dfrac{1}{R_e(M-1)^2} \Rightarrow r_2 = R_e(M-1)^2$,

$g_2 = \dfrac{2M-1}{R_e(M-1)^2}$,

$$j_2 = \frac{2V_1}{R_e D(M-1)}$$

where $\hat{i}_1(t)$, $\hat{i}_2(t)$, $\hat{d}(t)$, $\hat{v}_1(t)$, and $\hat{v}_2(t)$ are small AC variations around the quiescent values for the input port current, output port current, duty cycle, input port voltage, and output port voltage, respectively. R_e is the effective resistance, V_1 is the input port voltage, V_2 is the output port voltage, D is the duty cycle, and M is the conversion ratio (V_2/V_1).

The conversion ratio M can be derived in terms of the effective resistance R_e, given by (4.54) for an ideal Boost converter in DCM and by (4.55) if the inductor resistance R_L is included:

$$M = \frac{V_o}{V_{in}} = \frac{1+\sqrt{1+\frac{4R}{R_e}}}{2} \tag{4.54}$$

$$M = \frac{V_o}{V_{in}} = \left(\frac{1+\sqrt{1+\frac{4R}{R_e}}}{2}\right) - \frac{R_L I_L}{V_{in}}\left(\frac{1+\sqrt{1+\frac{4R}{R_e}}}{2}\right) \tag{4.55}$$

where R_L is the inductor resistance, R is the load resistance, R_e is the effective resistance, I_L is the inductor current, V_{in} is the input voltage, and V_o is the output voltage.

Using the linearized small signal mathematical equations, the DCM small signal equivalent models of the ideal and non-ideal Boost converters were obtained, shown in Figures 4.19 and 4.20, respectively, using dependent sources.

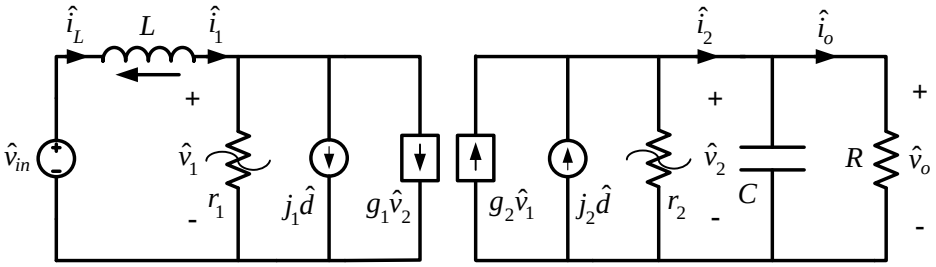

Figure 4.19: Boost Converter Small Signal Equivalent Circuit (Ideal) using Dependent Sources in DCM

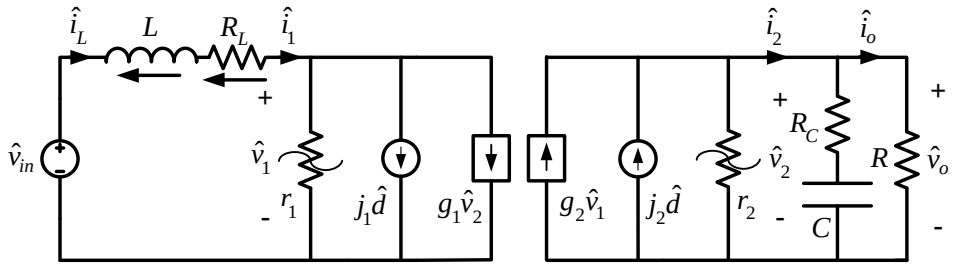

Figure 4.20: Boost Converter Small Signal Equivalent Circuit (with R_L and R_C) using Dependent Sources in DCM

$\hat{i}_L(t)$, $\hat{i}_o(t)$, $\hat{d}(t)$, $\hat{v}_{in}(t)$, and $\hat{v}_o(t)$ are small AC variations around the quiescent values for the inductor current, output current, duty cycle, input voltage, and output voltage, respectively. $\hat{i}_1(t)$, $\hat{i}_2(t)$, $\hat{v}_1(t)$, and $\hat{v}_2(t)$ are small AC variations around the quiescent values for the input port current, output port current, input port voltage, and output port voltage of the switching elements, respectively.

L is the Boost converter inductor, R_L is the inductor resistance, C is the Boost converter capacitor, R_C is the equivalent series resistance (ESR) of the capacitor, and R is the load resistance.

Using the small signal mathematical model equations and the small signal equivalent circuit, the transfer functions of the duty cycle to the inductor current G_{id}(s), (4.56) and (4.59), the inductor current to the output voltage G_{vi}(s), (4.57) and (4.60), and the duty cycle to the output voltage G_{vd}(s), (4.58) and (4.61), can be obtained:

For the ideal DCM Boost converter:

$$G_{id}(s) = \frac{\hat{i}_1(s)}{\hat{d}(s)} = \frac{\hat{i}_L(s)}{\hat{d}(s)} = \frac{sCRr_1r_2j_1 + Rr_1r_2j_2g_1 + Rr_1j_1 + r_1r_2j_1}{s^2CLRr_2 + s(CRr_1r_2 + LR + Lr_2 + LRr_1r_2g_1g_2) + Rr_1 + r_1r_2} \tag{4.56}$$

$$G_{vi}(s) = \frac{\hat{v}_2(s)}{\hat{i}_1(s)} = \frac{\hat{v}_o(s)}{\hat{i}_L(s)} = \frac{sLR(r_2j_2 - r_1r_2j_1g_2) + Rr_1r_2j_2}{sCRr_1r_2j_1 + Rr_1r_2g_1j_2 + Rr_1j_1 + r_1r_2j_1} \tag{4.57}$$

$$G_{vd}(s) = \frac{\hat{v}_o(s)}{\hat{d}(s)} = \frac{sLR(r_2j_2 - r_1r_2j_1g_2) + Rr_1r_2j_2}{s^2CLRr_2 + s(CRr_1r_2 + LR + Lr_2 + LRr_1r_2g_1g_2) + Rr_1 + r_1r_2} \tag{4.58}$$

For the non-ideal (including R_L and R_C) DCM Boost converter:

$$G_{id}(s) = \frac{\hat{i}_1(s)}{\hat{d}(s)} = \frac{\hat{i}_L(s)}{\hat{d}(s)}$$
$$= \frac{sC(RR_C r_1 j_1 + Rr_1 r_2 j_1 + R_C r_1 r_2 j_1 + RR_C r_1 r_2 j_2 g_1) + Rr_1 j_1 + Rr_1 r_2 j_2 g_1 + r_1 r_2 j_1}{\begin{aligned} &s^2 CL(RR_C + Rr_2 + R_C r_2 + RR_C r_1 r_2 g_1 g_2) \\ &+ s(CRR_C r_1 + CRr_1 r_2 + CR_C r_1 r_2 + CRR_C R_L + CRR_L r_2 + CR_C R_L r_2 \\ &+ CRR_C R_L r_1 r_2 g_1 g_2 + LR + LRr_1 r_2 g_1 g_2) \\ &+ RR_L + Rr_1 + R_L r_2 + RR_L r_1 r_2 g_1 g_2 + r_1 r_2 \end{aligned}} \quad (4.59)$$

$$G_{vi}(s) = \frac{\hat{v}_2(s)}{\hat{i}_1(s)} = \frac{\hat{v}_o(s)}{\hat{i}_L(s)}$$
$$= \frac{\begin{aligned} &s^2 CLRR_C(r_2 j_2 - r_1 r_2 j_1 g_2) \\ &+ sR(CR_C r_1 r_2 j_2 + CR_C R_L r_2 j_2 - CR_C R_L r_1 r_2 j_1 g_2 + Lr_2 j_2 - Lr_1 r_2 j_1 g_2) \\ &+ Rr_1 r_2 j_2 + RR_L r_2 j_2 - RR_L r_1 r_2 j_1 g_2 \end{aligned}}{sC(RR_C r_1 j_1 + Rr_1 r_2 j_1 + R_C r_1 r_2 j_1 + RR_C r_1 r_2 j_2 g_1) + Rr_1 j_1 + Rr_1 r_2 j_2 g_1 + r_1 r_2 j_1} \quad (4.60)$$

$$G_{vd}(s) = \frac{\hat{v}_o(s)}{\hat{d}(s)}$$
$$= \frac{\begin{aligned} &s^2 CLRR_C(r_2 j_2 - r_1 r_2 j_1 g_2) \\ &+ sR(CR_C r_1 r_2 j_2 + CR_C R_L r_2 j_2 - CR_C R_L r_1 r_2 j_1 g_2 + Lr_2 j_2 - Lr_1 r_2 j_1 g_2) \\ &+ Rr_1 r_2 j_2 + RR_L r_2 j_2 - RR_L r_1 r_2 j_1 g_2 \end{aligned}}{\begin{aligned} &s^2 CL(RR_C + Rr_2 + R_C r_2 + RR_C r_1 r_2 g_1 g_2) \\ &+ s(CRR_C r_1 + CRr_1 r_2 + CR_C r_1 r_2 + CRR_C R_L + CRR_L r_2 + CR_C R_L r_2 \\ &+ CRR_C R_L r_1 r_2 g_1 g_2 + LR + LRr_1 r_2 g_1 g_2) \\ &+ RR_L + Rr_1 + R_L r_2 + RR_L r_1 r_2 g_1 g_2 + r_1 r_2 \end{aligned}} \quad (4.61)$$

4.5 Conclusion

This chapter presented the modelling of the Buck and Boost converters. Both converters were modelled operating in the continuous conduction mode (CCM) and the discontinuous conduction mode (DCM). The small signal models of both converters were derived, which were used to derive the transfer functions needed to design the control loops. The CCM and DCM transfer functions of the duty cycle to the inductor current G_{id}(s), the inductor current to the output voltage G_{vi}(s), and the duty cycle to the output voltage G_{vd}(s) were derived and presented for both Buck and Boost converters. The next chapter will use the transfer functions derived here to design the control loops for the converters.

Chapter 5 Converter Control

This chapter presents the control systems for the Buck and Bidirectional converters, including the theory and design of primary and secondary control. Three types of droop control methods are investigated, which are the V-I droop (impedance droop), I-V droop (admittance droop), and the newly proposed combined voltage and droop (CVD) method. This chapter also presents a battery management system (BMS) designed to provide high-level control to the Bidirectional converter by selecting the mode of operation between charging mode and load supplying/sharing mode.

5.1 DC-DC Converter Control System

The main control system for a DC-DC converter generally consists of nested current and voltage loops, to control the inductor current and the output voltage of the converter. When the converters are connected in parallel within a DC microgrid, the droop control method is utilized to obtain load sharing between the converters. Since the droop control method causes voltage deviations from the desired DC microgrid voltage, another outer loop called the voltage restoration loop is included to correct these voltage deviations.

The control system described above forms the primary and secondary control levels as proposed by Guerrero et al. in [16], which suggested a three-level hierarchical control system for microgrids. The hierarchical control system consists of primary control including current control, voltage control, and droop, secondary control which restores deviations caused by the primary control, and tertiary control which handles the power flow between the microgrid and the electrical distribution system.

Figure 5.1 shows a block diagram of the control system with nested current and voltage loops. The inner current loop controls the inductor current, while the outer voltage loop controls the output voltage of the converter. The inner current control loop should be faster than the outer voltage control loop to minimize interaction between the two loops and therefore, prevent instability. Proportional Integral (PI) controllers are used to control the inductor current and output voltage.

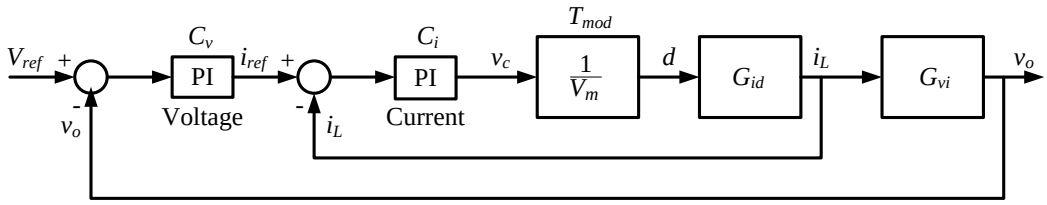

Figure 5.1: Block Diagram of the Control System with Current and Voltage Control Loops

The current and voltage PI controllers, C_i(s) and C_v(s), are of the form:

$$C(s) = K_p + \frac{K_I}{s} \tag{5.1}$$

where K_P is the Proportional Gain term and K_I is the Integral Gain term.

The plant transfer function P_i(s) that is used with the current PI controller is obtained by:

$$P_i(s) = T_{mod} \times G_{id}(s) \tag{5.2}$$

where T_{mod} is the transfer function representing the pulse width modulation stage, and $G_{id}(s)$ is the transfer function of the relationship between the duty cycle and the inductor current, which was derived in Chapter 4.

The pulse width modulation stage produces the duty cycle d that is proportional to the control voltage v_c. V_m is the peak-to-peak amplitude of the carrier used by the pulse width modulation stage, with a frequency corresponding to the desired converter switching frequency f_s. The pulse width modulation stage can be modelled by the transfer function T_{mod} given by:

$$T_{mod} = \frac{1}{V_m} \tag{5.3}$$

The transfer function $P_{iCL}(s)$ of the current closed loop is given by:

$$P_{iCL}(s) = \frac{C_i(s)P_i(s)}{1 + C_i(s)P_i(s)} \tag{5.4}$$

The plant transfer function $P_v(s)$ that is used with the voltage PI controller is obtained by:

$$P_v(s) = \frac{C_i(s)P_i(s)}{1 + C_i(s)P_i(s)} \times G_{vi}(s) \tag{5.5}$$

where $G_{vi}(s)$ is the transfer function of the relationship between the inductor current and the output voltage, which was derived in Chapter 4.

The transfer function of the voltage closed loop $P_{vCL}(s)$ is given by:

$$P_{vCL}(s) = \frac{C_v(s)P_v(s)}{1 + C_v(s)P_v(s)} \tag{5.6}$$

5.2 Droop Control

In a DC microgrid operated in stand-alone or islanded mode, and even in certain cases in grid-connected mode, load sharing between parallel-connected energy source converters is generally achieved using the droop control method. This method prevents circulating currents between the parallel-connected converters, which would result if there are any differences in the converter's output voltages. Droop control achieves this by adjusting the converter's voltage and current control loops references.

There are two main types of droop control methods: the impedance droop method, which is also referred to as V-I droop, and the admittance droop method, which is also referred to as I-V droop.

5.2.1 V-I Droop Control

The V-I or Impedance Droop method can be considered as the traditional droop control method. V-I droop is used with a control system consisting of nested current and voltage loops using Proportional Integral (PI) controllers. The block diagram in Figure 5.2 shows the control system for a converter including the V-I droop loop. The control system consists of two nested PI controllers, one controlling the inductor current and the other controlling the output voltage.

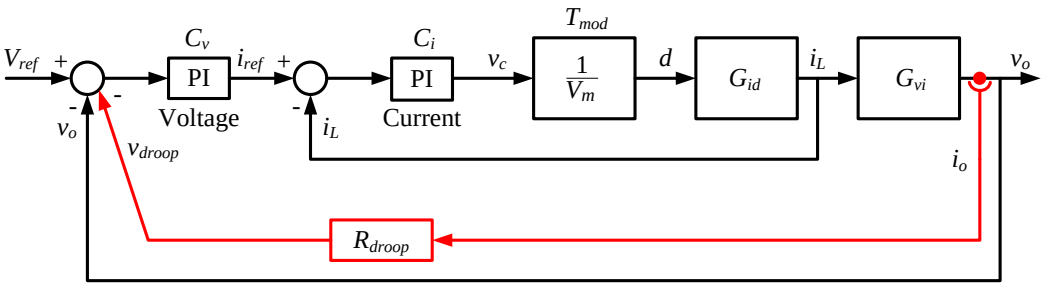

Figure 5.2: Block Diagram of the Control System with Current and Voltage Control including V-I Droop

V-I droop is applied by inserting an additional loop containing a virtual resistance R_{droop} as shown in Figure 5.2. The product of the inductor current and the droop virtual resistance is subtracted from the voltage reference. This causes a load dependent deviation in the output voltage of the converter, achieving a load sharing behaviour between the parallel-connected converters. The value of R_{droop} is calculated using (5.7). This is graphically represented in Figure 5.3.

$$R_{droop} = \frac{V_{ref} - V_{\min}}{I_{\max} - 0} \tag{5.7}$$

where V_{min} is the converter's minimum output voltage permitted, V_{ref} is the no load output voltage reference, and I_{max} is the converter maximum current.
Equation (5.7) can also be expressed as:

$$R_{droop} = \frac{\varepsilon_v}{i_{o\_\max}} \tag{5.8}$$

where i_{o_max} is the maximum output current and ε_v is the maximum permissible voltage deviation calculated by:

$$\varepsilon_v = V_{ref} - V_{min} \tag{5.9}$$

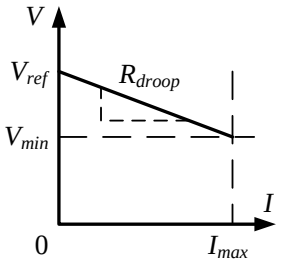

Figure 5.3: V-I Droop - Graphical Representation

Therefore, the converter output voltage v_o can be expressed as:

$$v_o = V_{ref} - R_{droop} i_o \tag{5.10}$$

where i_o is the output current.

In the case of a Buck converter where the average inductor current and output current are approximately equal, the inductor current i_L can be used instead of i_o in the control loop, therefore:

$$v_o = V_{ref} - R_{droop} i_L \tag{5.11}$$

The transfer function of the voltage closed loop $P_{vCL}(s)$, with the droop resistance now becomes:

$$P_{vCL}(s) = \frac{C_v(s)P_v(s)}{1 + C_v(s)P_v(s)(1 + \frac{R_{droop}}{G_{vi}(s)})} \quad (5.12)$$

5.2.2 I-V Droop Control

I-V or Admittance Droop is another droop control method used in DC microgrids. In this droop control method the voltage PI controller is replaced with a multiplier term as a proportional-type controller, denoted by a constant value *k*, which effectively is the inverse of the droop virtual resistance R_{droop} as shown by (5.13). The multiplier term *k* is multiplied to the difference between the voltage reference and the actual output voltage to obtain the current reference for the current PI controller. I-V droop is graphically represented in Figure 5.4. The block diagram in Figure 5.5 shows the control system for a converter using I-V droop.

$$k = \frac{1}{R_{droop}} \quad (5.13)$$

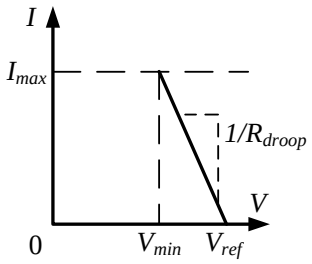

Figure 5.4: I-V Droop - Graphical Representation

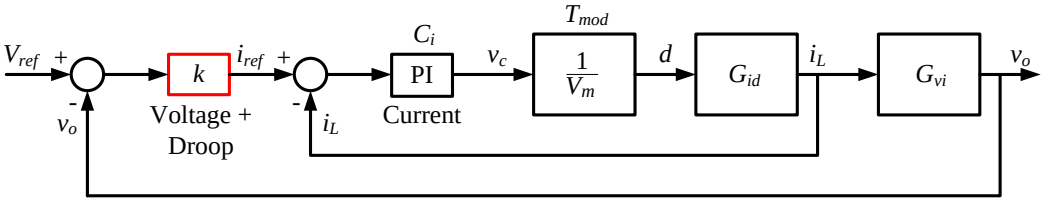

Figure 5.5: Block Diagram of the Control System with Current and Voltage Control including I-V Droop

The plant transfer functions, P_i(s) that is used with the current PI controller, and P_v(s) that is used with the multiplier term *k* are the same transfer functions shown in (5.2) and (5.5), respectively.

The transfer function of the voltage closed loop $P_{vCL}(s)$, with the multiplier term k becomes:

$$P_{vCL}(s) = \frac{kP_v(s)}{1 + kP_v(s)} \tag{5.14}$$

Compared to the V-I droop control method, the I-V droop control method achieves a simpler control system, due to the replacement of the PI voltage controller with the multiplier term. However, a drawback with the I-V droop control method is that overshoots or transient oscillations may occur during the start-up of the converters, as is documented in Chapter 7, which shows results from simulations and experimental tests.

In this research an alternative I-V droop control method is proposed in order to reduce or eliminate these overshoots.

5.2.3 Combined Voltage and Droop Control

The proposed Combined Voltage and Droop (CVD) control method is an alternative I-V droop-type control method which makes use of a lag-type compensator. A lag compensator is generally used to reduce the steady state error, however it does not remove it completely. In the proposed droop control method the steady state error is used to provide the droop voltage deviation to obtain load sharing. Additionally, the lag compensator also offers stabilisation of the system by eliminating any start-up overshoots and oscillations. With the proposed droop control method based on a 'modified' lag compensator, voltage control and droop are combined. In addition, any start-up oscillations can be eliminated by adjusting the bandwidth of the voltage controller.

With the conventional lag compensator, the DC gain is used to set the bandwidth of the loop, and the pole is placed before the zero within the lag compensator [37]. In the proposed CVD method, the DC gain of the lag-type compensator is set by the multiplier term k, and the pole and zero are used to set the bandwidth.

The CVD controller transfer function is presented by:

$$C_{CVD}(s) = k\frac{\left(1 + s/\omega_z\right)}{\left(1 + s/\omega_p\right)} \tag{5.15}$$

where the value *k*, representing the DC gain, is the same value as the I-V droop multiplier term found by (5.8) and (5.13). ω_z and ω_p are the frequency locations in rad/s for the zero and pole, respectively.

Transfer function (5.15) can also be expressed as:

$$C_{CVD}(s) = k\frac{(1+T_Z s)}{(1+T_P s)} \tag{5.16}$$

where *k* is the DC gain term, and T_Z and T_P are the inverse of the frequency locations ω_z and ω_p for the zero and pole, respectively.

The block diagram in Figure 5.6 shows the control system for a converter using the proposed droop method with the CVD controller.

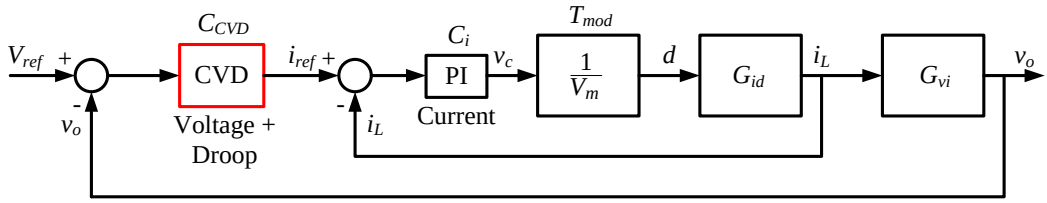

Figure 5.6: Block Diagram of the Control System with Current and Voltage Control including CVD

The plant transfer functions, P_i(s) that is used with the current PI controller and P_v(s) that is used with the CVD controller are the same transfer functions shown in (5.2) and (5.5), respectively.

The transfer function of the CVD closed loop $P_{CVDCL}(s)$, is given by:

$$P_{CVDCL}(s) = \frac{C_{CVD}(s)P_v(s)}{1+C_{CVD}(s)P_v(s)} \tag{5.17}$$

5.3 Voltage Restoration

The droop control loop permits sharing of a common load between paralleled converters, however it causes a load dependent output voltage deviation. The voltage deviation problem can be solved by the application of another controller which restores the microgrid voltage to the desired level. This controller forms another outer control loop common to all the converters/sources in the microgrid as shown in Figure 5.7. In this control loop the microgrid voltage is compared with the desired voltage, and the PI compensator of the loop generates the needed value for correct

voltage restoration that is required for the primary control loops of each converter in the microgrid.

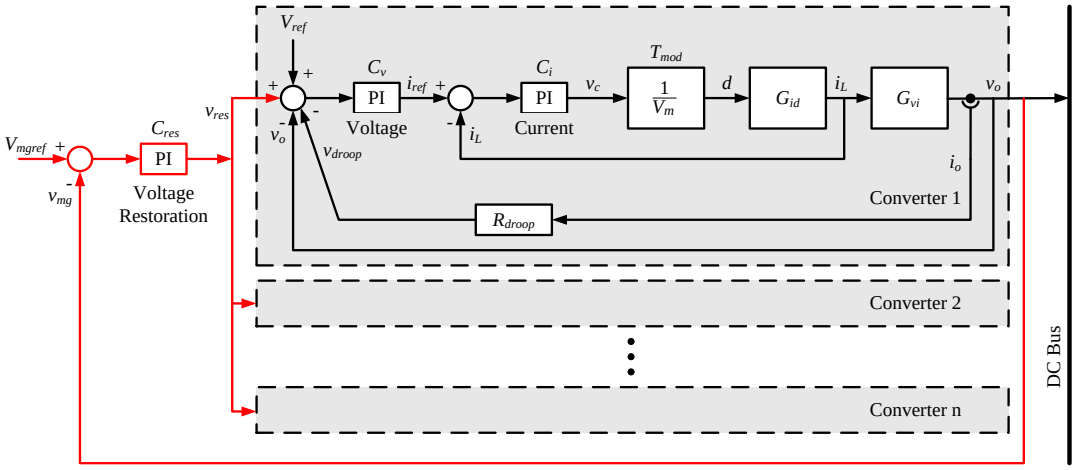

Figure 5.7: Block Diagram of the Voltage Restoration Control Loop including V-I Droop

The voltage restoration PI controller C_{res} transfer function is shown in (5.18). The demanded value of the voltage restoration loop V_{mgref} is set to the desired DC microgrid voltage. The actual DC-bus microgrid voltage v_{mg} is measured and fed back to this loop for the controller to generate the required restoration voltage v_{res}, as shown in Figure 5.7. The value of v_{res} should be restricted within limits to prevent it from exceeding the maximum allowed voltage deviation.

$$C_{res}(s) = K_p + \frac{K_I}{s} \tag{5.18}$$

where K_P is the Proportional Gain term and K_I is the Integral term.

When using the V-I droop method, the output voltage v_o equation (5.11) has to be modified to include the restoration voltage as follows:

$$v_o = V_{ref} + v_{res} - R_{droop} i_o \tag{5.19}$$

When using the V-I droop method, the plant transfer function P_{res}(s) that is used with the voltage restoration PI controller is obtained by:

$$P_{res}(s) = \frac{C_v(s)P_v(s)}{1 + C_v(s)P_v(s)(1 + \frac{R_{droop}}{G_{vi}(s)})} \tag{5.20}$$

When using the I-V droop method, the plant transfer function $P_{res}(s)$ that is used with the voltage restoration PI controller is obtained by:

$$P_{res}(s) = \frac{kP_v(s)}{1 + kP_v(s)} \tag{5.21}$$

When using the proposed CVD method, the plant transfer function $P_{res}(s)$ that is used with the voltage restoration PI controller is obtained by:

$$P_{res}(s) = \frac{C_{CVD}(s)P_v(s)}{1 + C_{CVD}(s)P_v(s)} \tag{5.22}$$

A block diagram of the control system with the voltage restoration loop, including I-V droop or the proposed CVD method is shown in Figure 5.8.

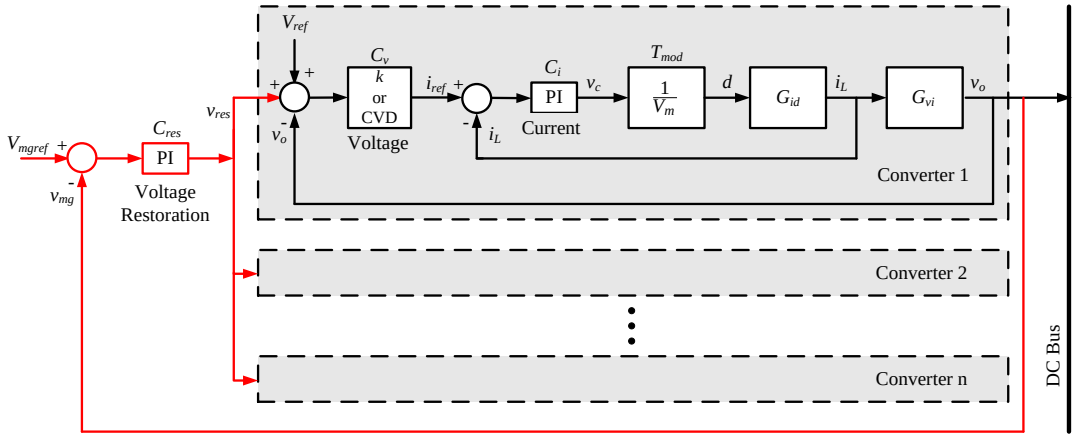

Figure 5.8: Block Diagram of the Voltage Restoration Control Loop including I-V Droop or CVD

5.4 Controller Design

The transfer functions which were derived from the small signal models of the converters covered in Chapter 4, were needed to design the controllers covered in this section. The controllers were designed using SISOTool, which is part of Matlab.

5.4.1 Buck Converter Controller Design

The two Buck converters built for the DC microgrid setup, are controlled by the droop control method. Three control systems were designed, one for each method of droop: V-I droop, I-V droop, and CVD. These control systems were eventually compared by simulations and experimental results.

5.4.1.1 Buck Converter Current Controller

The current controller was designed and used for all the three different droop control methods. The current controller is a PI controller represented by transfer function (5.1). The plant transfer function $P_i(s)$ used for designing the current PI controller is shown in (5.2).

Using the Buck converter inductor (L = 479µH, R_L = 2mΩ) and capacitor (C = 271.25µF, R_c = 2.1mΩ) values calculated in Chapter 3, and a load resistance for maximum output power (R = 0.9216Ω for 2.5kW with 48V, 52.08A), the transfer function of the duty cycle to the inductor current $G_{id}(s)$ is given by:

$$G_{id}(s) = \frac{\hat{i}_L(s)}{\hat{d}(s)} = \frac{V_{in}(s(CR + CR_C) + 1)}{s^2(CLR + CLR_C) + s(L + CRR_L + CR_C R_L + CR_C R) + R_L + R} = \frac{0.02506\ \mathrm{s} + 100}{1.2 \times 10^{-7}\mathrm{s}^2 + 0.00048\ \mathrm{s} + 0.9236} \quad (5.23)$$

The peak-to-peak amplitude of the carrier V_m for the PWM generation was set to be 100V, the maximum input voltage seen by the Buck converter. Therefore, the transfer function for the pulse width modulation stage T_{mod} is given by:

$$T_{mod} = \frac{1}{V_m} = \frac{1}{100} \quad (5.24)$$

The plant transfer function $P_i(s)$ needed to design the current PI controller is given by:

$$P_i(s) = T_{\mathrm{mod}} \times G_{id}(s) = \frac{0.0002506\ \mathrm{s} + 1}{1.2 \times 10^{-7}\mathrm{s}^2 + 0.00048\ \mathrm{s} + 0.9236} \quad (5.25)$$

The bandwidth of the current closed loop varies according to the load, with maximum bandwidth when the load current is at its maximum. The current controller was designed to obtain a current closed loop bandwidth of around 130Hz at the converter's full load current (52.1A). (This bandwidth was verified to be less than the anti-aliasing filter's frequency by a factor greater than 10).

This resulted in a current PI controller having a proportional gain term of 1.14 and an integral gain term of 880, as shown by:

$$C_i(s) = K_p + \frac{K_I}{s} = 1.14 + \frac{880}{s} \quad (5.26)$$

The closed loop transfer function of the current loop was obtained using (5.4), resulting in:

$$P_{iCL}(s) = \frac{C_i(s)P_i(s)}{1 + C_i(s)P_i(s)} = \frac{2388\,\mathrm{s}^2 + 1.137\times10^7\,\mathrm{s} + 7.332\times10^9}{\mathrm{s}^3 + 6388\,\mathrm{s}^2 + 1.906\times10^7\,\mathrm{s} + 7.332\times10^9} \qquad (5.27)$$

Using the current PI controller (5.26), the current closed loop bandwidth range for 10% to 100% load current (5.21A – 52.1A) varies between 11.83Hz to 133.42Hz with settling times in the range of 51ms to 6.9ms. The bandwidth of the current closed loop was kept relatively low to reduce the effect of the zero due to the load present in the current closed loop transfer function P_{iCL}(s). Since the load can vary this zero varies accordingly.

The Phase Margin of the system obtained with 10% to 100% load current varies in the range between 83.9deg at a frequency of 4225.7rad/s (672.5Hz) to 105.5deg at a frequency of 3069.2rad/s (488.5Hz).

5.4.1.2 Buck Converter Voltage Controller

The voltage PI controller is represented by transfer function (5.1). The plant transfer function $P_v(s)$ used for designing the voltage PI controller is shown in (5.5).

Using the Buck converter inductor (L = 479µH, R_L = 2mΩ) and capacitor (C = 271.25µF, R_c = 2.1mΩ) values calculated in Chapter 3, and a load resistance for maximum output power (R = 0.9216Ω for 2.5kW with 48V, 52.08A), the transfer function of the inductor current to the output voltage $G_{vi}(s)$ is given by:

$$G_{vi}(s) = \frac{\hat{v}_o(s)}{\hat{i}_L(s)} = \frac{sCRR_C + R}{s(CR + CR_C) + 1} = \frac{5.25\times10^{-7}s + 0.9216}{0.0002506s + 1} \qquad (5.28)$$

The plant transfer function $P_v(s)$ needed to design the voltage PI controller is given by:

$$P_v(s) = \frac{C_i(s)P_i(s)}{1 + C_i(s)P_i(s)} \times G_{vi}(s) = \frac{5.004\,\mathrm{s}^2 + 8.789\times10^6\,\mathrm{s} + 6.758\times10^9}{\mathrm{s}^3 + 6388\,\mathrm{s}^2 + 1.906\times10^7\,\mathrm{s} + 7.332\times10^9} \qquad (5.29)$$

The bandwidth of the voltage closed loop varies according to the load, with maximum bandwidth when the load current is at its minimum. The voltage controller was designed to obtain a voltage closed loop bandwidth of around 6Hz at 10% (5.21A) of the converter's full load current.

This resulted in a voltage PI controller having a proportional gain term of 0.064 and an integral gain term of 4.6, as shown by:

$$C_v(s) = K_p + \frac{K_I}{s} = 0.064 + \frac{4.6}{s} \tag{5.30}$$

The closed loop transfer function of the voltage loop was obtained using (5.6), resulting in:

$$P_{vCL}(s) = \frac{C_v(s)P_v(s)}{1 + C_v(s)P_v(s)} = \frac{0.3223\,\mathrm{s}^3 + 5.66\times10^5\,\mathrm{s}^2 + 4.756\times10^8\,\mathrm{s} + 3.108\times10^{10}}{\mathrm{s}^4 + 6388\,\mathrm{s}^3 + 1.963\times10^7\,\mathrm{s}^2 + 7.808\times10^9\,\mathrm{s} + 3.108\times10^{10}} \tag{5.31}$$

Using the voltage PI controller (5.30), the voltage closed loop bandwidth for 10% to 100% load current (5.21A – 52.1A) varies between 6.46Hz to 0.64Hz with settling times in the range of 95ms to 0.96s. The design of the voltage PI controller took into account the variations of the voltage closed loop bandwidth and the current closed loop bandwidth with load current, and it was designed to limit any interaction between the two control loops.

The Phase Margin of the system obtained with 10% to 100% load current varies in the range between 92.50deg at a frequency of 42.45rad/s (6.76Hz) to 93.09deg at a frequency of 4.25rad/s (0.68Hz).

5.4.1.3 V-I Droop Control Design

The V-I droop virtual resistance was calculated for a maximum percentage output voltage deviation (ε_v) of 10%. This results in a reduced output voltage of 43.2V at a maximum output current (i_{o_max}) of 52.1A. Therefore, using (5.8):

$$R_{droop} = \frac{\varepsilon_v}{i_{o\_\max}} = \frac{4.8}{52.1} = 0.092\Omega \tag{5.32}$$

The closed loop transfer function of the voltage loop including the droop virtual resistance was obtained using (5.12), resulting in:

$$\begin{aligned} P_{vCL}(s) &= \frac{C_v(s)P_v(s)}{1 + C_v(s)P_v(s)(1 + \frac{R_{droop}}{G_{vi}(s)})} \\ &= \frac{0.3223\,\mathrm{s}^3 + 5.66\times10^5\,\mathrm{s}^2 + 4.756\times10^8\,\mathrm{s} + 3.108\times10^{10}}{\mathrm{s}^4 + 6403\,\mathrm{s}^3 + 1.97\times10^7\,\mathrm{s}^2 + 7.856\times10^9\,\mathrm{s} + 3.419\times10^{10}} \end{aligned} \tag{5.33}$$

When including V-I droop and using the voltage PI controller (5.30), the voltage closed loop bandwidth for 10% to 100% load current (5.21A – 52.1A) varies between 6.52Hz to 0.7Hz with settling times in the range of 94.4ms to 0.876s.

The Phase Margin of the system obtained with 10% to 100% load current varies in the range between 92.58deg at a frequency of 42.88rad/s (6.82Hz) to 93.4deg at a frequency of 4.67rad/s (0.74Hz).

5.4.1.4 I-V Droop Control Design

For the I-V droop method, the droop multiplier value *k* was calculated using (5.13):

$$k = \frac{1}{R_{droop}} = \frac{1}{0.092}\Omega \tag{5.34}$$

The plant transfer function $P_v(s)$ that is used with the *k* multiplier is found by (5.5) and the resulting transfer function is given by (5.29).

The closed loop transfer function of the voltage loop with the droop multiplier value *k* was obtained using (5.14), resulting in:

$$P_{vCL}(s) = \frac{kP_v(s)}{1 + kP_v(s)} = \frac{54.3\,s^2 + 9.536\times10^7\,s + 7.332\times10^{10}}{s^3 + 6442\,s^2 + 1.144\times10^8\,s + 8.066\times10^{10}} \tag{5.35}$$

The voltage closed loop bandwidth for 10% to 100% load current (5.21A – 52.1A) varies between 2449Hz to 2416Hz with settling times in the range of 3.8ms to 1.4ms. From the resulting bandwidth it can be noted that stability issues are expected due to interaction with the 2.5kHz bandwidth of the anti-aliasing filter in voltage feedback loop.

5.4.1.5 Buck Converter CVD Controller

The CVD controller is represented by transfer function (5.16). The plant transfer function $P_v(s)$ used for designing the CVD controller is obtained by (5.5) and the resulting transfer function is given by (5.29).

The bandwidth of the voltage closed loop varies according to the load, with maximum bandwidth when the load current is at its minimum. The CVD controller was designed to obtain a voltage closed loop bandwidth of around 28Hz at 10% (5.21A) of the converter's full load current.

This resulted in a CVD controller having a proportional gain term of $1/0.092$ and inverse frequency locations for the zero and pole; T_Z of 0.0023 and T_P of 0.4, as shown by:

$$C_{CVD}(s) = k\frac{(1+T_Z s)}{(1+T_P s)} = \frac{1}{0.092}\frac{(1+0.0023s)}{(1+0.4s)} \tag{5.36}$$

The closed loop transfer function of the CVD loop was obtained using (5.17), resulting in:

$$P_{CVDCL}(s) = \frac{C_{CVD}(s)P_v(s)}{1+C_{CVD}(s)P_v(s)} = \frac{0.3122\,\mathrm{s}^3 + 5.485\times10^5\,\mathrm{s}^2 + 6.6\times10^8\,\mathrm{s} + 1.833\times10^{11}}{\mathrm{s}^4 + 6391\,\mathrm{s}^3 + 1.963\times10^7\,\mathrm{s}^2 + 8.04\times10^9\,\mathrm{s} + 2.016\times10^{11}} \tag{5.37}$$

Using the CVD controller (5.36), the voltage closed loop bandwidth for 10% to 100% load current (5.21A – 52.1A) varies between 28.47Hz to 4.26Hz with settling times in the range of 58.9ms to 144.8ms.

The Phase Margin of the system obtained with 10% to 100% load current varies in the range between 54.17deg at a frequency of 128.47rad/s (20.45Hz) to 97.16deg at a frequency of 24.89rad/s (3.96Hz).

5.4.2 Voltage Restoration Controller Design

The voltage restoration controller is common to all converters within the DC microgrid. For this reason the voltage restoration PI controller was designed to obtain a voltage restoration closed loop with a narrow bandwidth, having dominant poles, and thus being the slowest in operation.

For the design of the voltage restoration PI controller, two parallel-connected Buck converters were considered to be sharing a common load with the V-I droop method. The plant transfer function $P_{res}(s)$ (5.20) was used to design the voltage restoration PI controller.

The voltage restoration PI controller was designed to obtain a closed loop bandwidth of around 0.05Hz. Being a control loop common to all converters, the voltage restoration loop was designed to obtain a slow dominant loop, with all control loops within the converters having higher bandwidths.

This resulted in a voltage restoration PI controller having a proportional gain term of 0.0056 and an integral gain term of 0.33, as shown by:

$$C_{res}(s) = K_p + \frac{K_I}{s} = 0.0056 + \frac{0.33}{s} \tag{5.38}$$

The closed loop transfer function of the voltage restoration loop is given by:

$$P_{resCL}(s) = \frac{C_{res}(s)P_{res}(s)}{1 + C_{res}(s)P_{res}(s)} \tag{5.39}$$

where $P_{res}(s)$ is the plant transfer function used for designing the voltage restoration PI controller.

The voltage restoration loop has a closed loop bandwidth of 0.05Hz and a settling time of approximately 12s. Both the bandwidth and settling time do not vary much with load since the voltage restoration loop was designed with dominant poles and the slowest loop in operation.

5.4.3 Bidirectional Converter Controller Design

The Bidirectional converter was built to connect a battery bank to the DC microgrid setup. The control system for the Bidirectional converter was designed to consist of two parts: one part takes care of the battery charging process, and the other part takes care of the current sharing process, when sharing current with the other converters in the DC microgrid. The control system used to charge the batteries is made up of a current controller, while the control system that connects the Bidirectional converter in parallel to the other converters is made up of nested current and voltage controllers with droop control. This control system was eventually tested by simulations and experimental tests. A block diagram of the control system for the Bidirectional converter is shown in Figure 5.9. Figure 5.9 (a) is the control system concerned with the battery charging, while (b) is the control system concerned with the load sharing process using droop control.

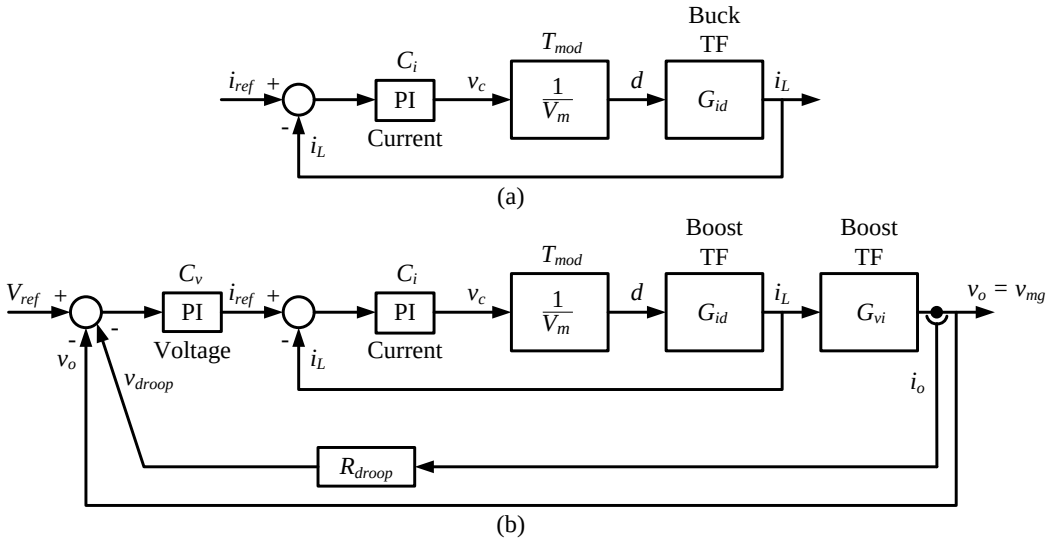

Figure 5.9: Block Diagram of the Control System for the Bidirectional Converter: (a) Battery Charging (b) Load Sharing

5.4.3.1 Bidirectional Converter Current Controller – Battery Charging Mode

When in battery charging mode, the Bidirectional converter, which effectively is a Synchronous Buck converter, operates as a Buck converter. This means that the converter has an input voltage of approximately 48V supplied from the DC-bus and an output voltage of approximately 24V applied to the batteries. The current controller was designed by considering the Bidirectional converter as a Buck converter operating in the battery charging mode.

The current controller is a PI controller represented by transfer function (5.1). The plant transfer function $P_i(s)$ used for designing the current PI controller is represented by (5.2).

Using the Bidirectional converter inductor (L = 192µH, R_L = 2mΩ) and low-voltage-side capacitor (C = 680µF, R_c = 0.03Ω) values calculated in Chapter 3, the transfer function of the duty cycle to the inductor current $G_{id}(s)$ can be obtained.

Since in this case the load is a 24V battery bank, the transfer function $G_{id}(s)$ can be given by:

$$G_{id}(s) = \frac{\hat{i}_L(s)}{\hat{d}} = \frac{V_{in}}{sL + R_L} = \frac{48}{0.000192\,\mathrm{s} + 0.002} \tag{5.40}$$

The peak-to-peak amplitude of the carrier V_m for PWM generation was set to be 48V, the maximum possible input voltage seen by the converter from the DC microgrid

bus. Therefore, the transfer function for the pulse width modulation stage T_{mod} is given by:

$$T_{mod} = \frac{1}{V_m} = \frac{1}{48} \tag{5.41}$$

The plant transfer function $P_i(s)$ needed to design the current PI controller is given by:

$$P_i(s) = T_{\text{mod}} \times G_{id}(s) = \frac{1}{0.000192\,\text{s} + 0.002} \tag{5.42}$$

The current PI controller was designed to obtain a closed loop bandwidth of around 800Hz. For this converter, a higher bandwidth than the one designed for in the Buck converters was desired, so as to obtain faster response and mitigate back flow current from the battery bank to the input side when the converter is starting up.

This resulted in a current PI controller having a proportional gain term K_P of 0.76 and an integral gain term K_I of 871, as shown by:

$$C_i(s) = K_p + \frac{K_I}{s} = 0.76 + \frac{871}{s} \tag{5.43}$$

The closed loop transfer function of the current loop was obtained using (5.4), resulting in:

$$P_{iCL}(s) = \frac{C_i(s)P_i(s)}{1 + C_i(s)P_i(s)} = \frac{3947\,\text{s} + 4.536 \times 10^6}{\text{s}^2 + 3957\,\text{s} + 4.536 \times 10^6} \tag{5.44}$$

The current loop has a closed loop bandwidth of 800Hz, with a settling time of 2.5ms. The Phase Margin of the system obtained is 74.48deg at a frequency of 4099rad/s (652Hz).

5.4.3.2 Bidirectional Converter Current Controller – Load Sharing/Supplying Mode

When in the load sharing/supplying mode, the Bidirectional converter operates as a Boost converter, and it shares the DC microgrid load together with the other converters. The 24V from the batteries is taken as the input voltage and boosted up to an output voltage of around 48V required by the DC microgrid bus. The current controller for this mode of operation was designed by considering the converter as a Boost converter.

The current controller is a PI controller represented by transfer function (5.1). The plant transfer function $P_i(s)$ used for designing the current PI controller is represented by (5.2).

Using the Bidirectional converter inductor (L = 192µH, R_L = 2mΩ) and high-voltage-side capacitor (C = 1500µF, R_c = 0.03Ω) values calculated in Chapter 3, and a load resistance for maximum output power of 1.5kW (R = 1.536Ω for 1.5kW with 48V, 31.25A), a numerical value of the transfer function of the duty cycle to the inductor current $G_{id}(s)$ can be obtained:

$$G_{id}(s) = \frac{\hat{i}_L(s)}{\hat{d}} == \frac{sC(RV_o + R_C V_o + R_C RD' I_L) + V_o + I_L RD'}{s^2 CL(R + R_C) + s(L + CRR_L + CR_C R_L + CR_C RD'^2) + R_L + RD'^2}$$
$$= \frac{0.1149\,\mathrm{s} + 96}{4.51\times10^{-7}\,\mathrm{s}^2 + 0.000214\,\mathrm{s} + 0.386} \tag{5.45}$$

The peak-to-peak amplitude of the carrier V_m for PWM generation was set to be 48V, the maximum possible voltage seen by the converter from the DC microgrid bus. Therefore, the transfer function for the pulse width modulation stage T_{mod} is given by:

$$T_{mod} = \frac{1}{V_m} = \frac{1}{48} \tag{5.46}$$

The plant transfer function $P_i(s)$ needed to design the current PI controller is given by:

$$P_i(s) = T_{\mathrm{mod}} \times G_{id}(s) = \frac{0.002394\,\mathrm{s} + 2}{4.51\times10^{-7}\,\mathrm{s}^2 + 0.000214\,\mathrm{s} + 0.386} \tag{5.47}$$

The bandwidth of the current closed loop varies according to the load, with maximum bandwidth when the load current is at its maximum. However, it results that in this case the bandwidth is less affected by the load than in the case of the Buck converter. The current PI controller was designed to obtain a current closed loop bandwidth of around 700Hz at the converter's full load current (31.25A).

This resulted in a current PI controller having a proportional gain term of 0.64 and an integral gain term of 378, as shown by:

$$C_i(s) = K_p + \frac{K_I}{s} = 0.64 + \frac{378}{s} \tag{5.48}$$

The closed loop transfer function of the current loop was obtained using (5.4), resulting in:

$$P_{iCL}(s) = \frac{C_i(s)P_i(s)}{1 + C_i(s)P_i(s)} = \frac{3411\,\mathrm{s}^2 + 4.856\times10^6\,\mathrm{s} + 1.676\times10^9}{\mathrm{s}^3 + 3885\,\mathrm{s}^2 + 5.712\times10^6\,\mathrm{s} + 1.676\times10^9} \qquad (5.49)$$

Using the current PI controller (5.48), the current closed loop bandwidth range for 10% to 100% load current (3.13A – 31.25A) varies between 652Hz to 708Hz with settling times in the range of 47.4ms to 6.7ms.

The Phase Margin of the system obtained with 10% to 100% load current varies in the range between 81.01deg at a frequency of 3635rad/s (579Hz) to 76.15deg at a frequency of 3736rad/s (595Hz).

5.4.3.3 Bidirectional Converter Voltage Controller – Load Sharing/Supplying Mode

The Bidirectional converter operates as a Boost converter when operated in load sharing/supplying mode. The 24V from the batteries is boosted up to an output voltage of around 48V for the DC microgrid bus. The voltage controller for this mode of operation was designed by considering the converter as a Boost converter.

The voltage PI controller is represented by transfer function (5.1). The plant transfer function $P_v(s)$ used for designing the voltage PI controller is shown by (5.5).

Using the Bidirectional converter inductor (L = 192µH, R_L = 2mΩ) and high-voltage-side capacitor (C = 1500µF, R_c = 0.03Ω) values calculated in Chapter 3, and a load resistance for maximum output power of 1.5kW (R = 1.536Ω for 1.5kW with 48V, 31.25A), a numerical value of the transfer function of the inductor current to the output voltage $G_{vi}(s)$ can be obtained:

$$G_{vi}(s) = \frac{\hat{v}_o(s)}{\hat{i}_L(s)} = \frac{-s^2CLR_CRI_L + s(CR_CRD'V_o - LRI_L - CR_CR_LRI_L) - R_LRI_L + D'V_oR}{sC(RV_o + R_CV_o + R_CRD'I_L) + V_o + I_LRD'}$$

$$= \frac{-8.294\times10^{-7}\,\mathrm{s}^2 - 0.01678\,\mathrm{s} + 36.67}{0.1149\,\mathrm{s} + 96} \qquad (5.50)$$

The plant transfer function $P_v(s)$ needed to design the voltage PI controller is given by:

$$P_v(s) = \frac{C_i(s)P_i(s)}{1 + C_i(s)P_i(s)} \times G_{vi}(s) = \frac{-0.02462\,s^3 - 512.6\,s^2 + 7.955\times10^5\,s + 6.403\times10^8}{s^3 + 3885\,s^2 + 5.712\times10^6\,s + 1.676\times10^9} \tag{5.51}$$

The bandwidth of the voltage closed loop varies according to the load, with maximum bandwidth when the load current is at its minimum. The voltage controller was designed to obtain a voltage closed loop bandwidth of around 30Hz at 10% (3.13A) of the converter's full load current.

This resulted in a voltage PI controller having a proportional gain term of 0.72 and an integral gain term of 80, as shown by:

$$C_v(s) = K_p + \frac{K_I}{s} = 0.72 + \frac{80}{s} \tag{5.52}$$

The closed loop transfer function of the voltage loop was obtained using (5.6), resulting in:

$$\begin{aligned} P_{vCL}(s) &= \frac{C_v(s)P_v(s)}{1 + C_v(s)P_v(s)} \\ &= \frac{-0.01805\,s^4 - 377.8\,s^3 + 5.414\times10^5\,s^2 + 5.341\times10^8\,s + 5.215\times10^{10}}{s^4 + 3578\,s^3 + 6.356\times10^6\,s^2 + 2.241\times10^9\,s + 5.215\times10^{10}} \end{aligned} \tag{5.53}$$

Using the voltage PI controller (5.52), the voltage closed loop bandwidth for 10% to 100% load current (3.13A – 31.25A) varies between 32.87Hz to 4.18Hz with settling times in the range of 37.7ms to 146ms.

The Phase Margin of the system obtained with 10% to 100% load current varies in the range between 81.7deg at a frequency of 185.42rad/s (29.51Hz) to 102.01deg at a frequency of 31.72rad/s (5.05Hz).

5.4.3.4 Bidirectional Converter V-I Droop Design – Load Sharing/Supplying Mode

The Bidirectional converter was set to share load equally with the other two Buck converters in the DC microgrid. Hence, the V-I droop virtual resistance was set to be equal to the value calculated for the Buck converters:

$R_{droop} = 0.092\Omega$

The only difference between the application of the V-I droop method to the Bidirectional converter and the application of the V-I droop method to the Buck converters is that for the former, the current fed back for the droop is the output current i_o instead of the inductor current i_L. The reason for this is that the Bidirectional converter is operating as a Boost converter in this mode, and a Boost converter does not have the average inductor current approximately equal to the output current, as in the case of the Buck converter. Thus, for V-I droop control the output current should be used. This can be observed in the control system block diagram in Figure 5.9.

5.5 Discretization of the Controllers

The controllers covered in the previous sections were presented and designed in the s-domain. To implement these controllers using a microcontroller, discretization of the controllers is required. The discretization method used was the Bilinear Transform where the s term is expressed and substituted by:

$$s = f(z) = \frac{2}{T_s}\frac{(z-1)}{(z+1)} \tag{5.54}$$

where T_s is the sampling time given by $1/f_s$. f_s is the sampling frequency.

The discretized transfer function of the controller becomes:

$$C(z) = \frac{U_z}{E_z} \tag{5.55}$$

where U_z is the output from the controller and E_z is the error input.

From (5.55), the controller can be expressed in a difference equation of the form:

$$U(z) = (A)E(z) - (B)E(z)(z^{-1}) + U(z)(z^{-1}) \tag{5.56}$$

where A and B are constant values depending on the controller, and the term z^{-1} means that the previous sample is used in the mathematical expression.

Using the Bilinear Transform, all the controllers were transformed from the s-domain to the z-domain using a sampling frequency of 10kHz (T_s = 100μs). This was the sampling frequency selected for the ADCs, and controllers were designed to provide a closed loop bandwidth lower than the sampling frequency by a factor of 10. Table 5.1 lists the difference equation for each controller. Before practical implementation simulations were performed with these discrete controllers to confirm correct operation, taking also into consideration a delay of one sample.

Buck Converter Controllers	
Current PI Controller	
$C_i(s) = K_p + \frac{K_I}{s} = 1.144 + \frac{880}{s}$	U(z) = (1.188)E(z) – (1.1)E(z)(z^{-1}) + U(z)(z^{-1})
Voltage PI Controller	
$C_v(s) = K_p + \frac{K_I}{s} = 0.0644 + \frac{4.6}{s}$	U(z) = (0.06463)E(z) – (0.06417)E(z)(z^{-1}) + U(z)(z^{-1})
CVD Controller	
$C_{CVD}(s) = k\frac{(1+T_Z s)}{(1+T_P s)}$ $= \frac{1}{0.09216}\frac{(1+0.0023s)}{(1+0.4s)}$	U(z) = (0.06374)E(z) – (0.061027)E(z)(z^{-1}) + (0.99975)U(z)(z^{-1})
Bidirectional Converter Controllers	
Current PI Controller – Buck Mode – Battery Charging Mode	
$C_i(s) = K_p + \frac{K_I}{s} = 0.75777 + \frac{871}{s}$	U(z) = (0.80132)E(z) – (0.71422)E(z)(z^{-1}) + U(z)(z^{-1})
Current PI Controller – Boost Mode – Load Sharing/Supplying Mode	
$C_i(s) = K_p + \frac{K_I}{s} = 0.6426 + \frac{378}{s}$	U(z) = (0.6615)E(z) – (0.6237)E(z)(z^{-1}) + U(z)(z^{-1})
Voltage PI Controller – Boost Mode – Load Sharing/Supplying Mode	
$C_v(s) = K_p + \frac{K_I}{s} = 0.72 + \frac{80}{s}$	U(z) = (0.724) E(z) – (0.716)E(z)(z^{-1}) + U(z)(z^{-1})
Voltage Restoration PI Controller	
$C_{res}(s) = K_p + \frac{K_I}{s} = 0.00561 + \frac{0.33}{s}$	U(z) = (0.0056265)E(z) – (0.0055935)E(z)(z^{-1}) + U(z)(z^{-1})

Table 5.1: List of Controllers' Difference Equations

5.6 Battery Management System (BMS) Design

The battery management system (BMS) was designed to provide high-level control to the Bidirectional converter, by controlling the mode of operation between battery charging mode and load sharing/supplying mode. Figure 5.10 shows a block diagram of the DC Microgrid setup with the BMS connected to the Bidirectional converter.

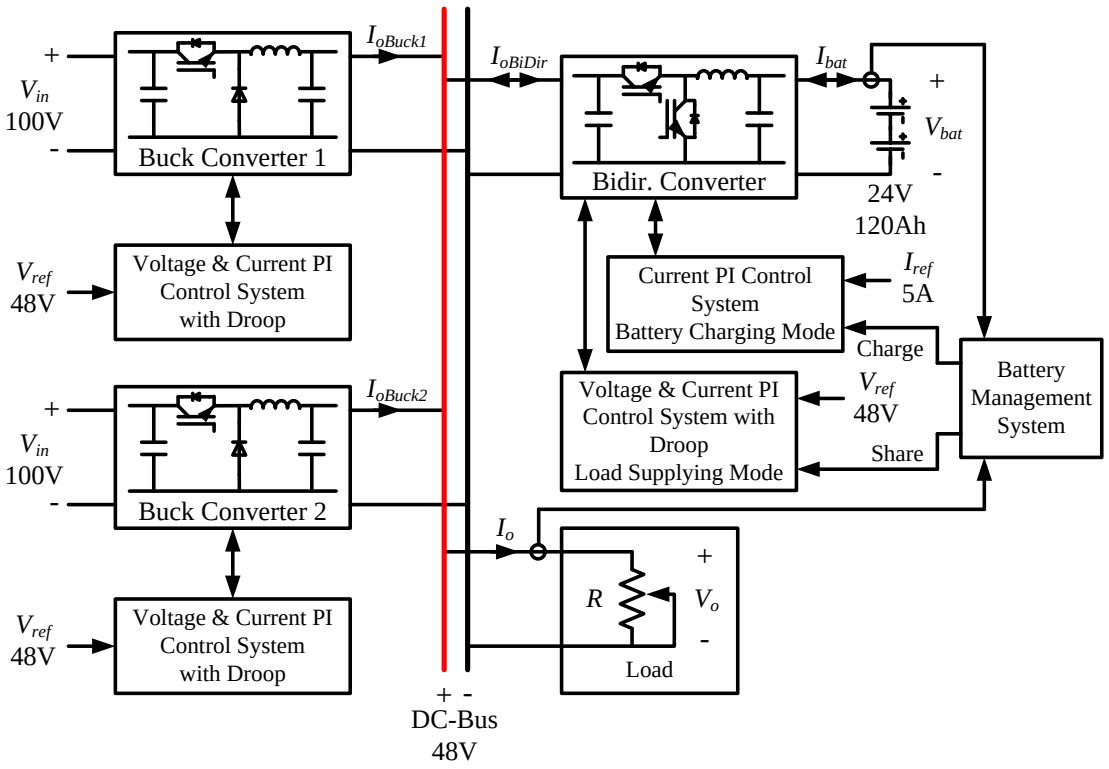

Figure 5.10: Block Diagram of the DC Microgrid Setup with BMS

The BMS algorithm uses the load current and the state of charge (SOC) of the battery bank to select amongst four possible output states/modes: State/Mode 0 – Idle (fully charged battery), State/Mode 1 – Battery Charging, State/Mode 2 – Sharing, and State/Mode 3 – Idle (fully discharged battery). A flowchart of the BMS algorithm is shown in Figure 5.11. The BMS algorithm uses hysteresis to prevent fast changeover between states. Fast changeovers can damage the converter and create disturbances in the DC microgrid, which can in turn damage other connected units. A lock period (time hysteresis) after a state change is also applied to keep the converter operating in the new state for at least 1 minute before changing to another state, again to prevent disturbances in the DC microgrid.

At start-up, the high SOC threshold (HSOCT) and low SOC threshold (LSOCT) variables are initialized, together with the variables for the time hysteresis (lock, n, ChargeLock, ShareLock). HSOCT and LSOCT are initialized to 82% and 20%, respectively. The load current and battery current are sampled by the ADCs within the microcontroller. The battery current is used to estimate the SOC of the battery bank. The state/mode is selected according to the values of the load current (I_{load}) and SOC.

The BMS has two state/modes when the Bidirectional converter is idle, namely when the battery bank is fully charged with an SOC equal or over 82% and a load current

under 20A, and when the battery bank is discharged with an SOC under 18% and a load current equal or over 18A.

When the BMS enters the fully charged idle state/mode, the HSOCT variable is modified to 80% to prevent oscillatory state changeover between this idle state/mode and the charging state/mode.

When the BMS enters the fully discharged idle state/mode, the LSOCT variable is modified to 20% to prevent oscillatory state changeover between this idle state/mode and the sharing state/mode.

When the load current increases over or equal to 20A and the SOC is greater or equal to 20%, the Bidirectional converter enters the load sharing/supplying mode. When the sharing state/mode is entered, the LSOCT variable is modified to 18% to continue sharing until the SOC decreases below 18%. This threshold change prevents oscillatory changeover between this state/mode and the fully discharged idle state/mode. Also, the HSOCT variable is modified to 80%.

When the load current decreases under 18A and the SOC is smaller than 80%, the Bidirectional converter enters the battery charging mode. When the charging state/mode is entered the HSOCT variable is modified to 82% to charge up to a SOC of 82%. This threshold change prevents oscillatory changeover between this state/mode and the fully charged idle state/mode.

Similarly, a hysteresis structure is also used between the load current thresholds to prevent any oscillatory changeovers between states. For this reason another flow path was added in the algorithm to keep the Bidirectional converter on its current state/mode in the case the load current value is between 18A and 20A.

Once the state/mode is selected, the algorithm checks if a state/mode change has occurred. In the case that a state/mode change occurred a time hysteresis or lock period is applied, which locks the BMS control outputs (Charge, Share) to their previous state until 1 minute has passed. This prevents very short mode changeovers in the Bidirectional converter operation.

A finite state machine for the BMS algorithm is shown in Figure 5.12.

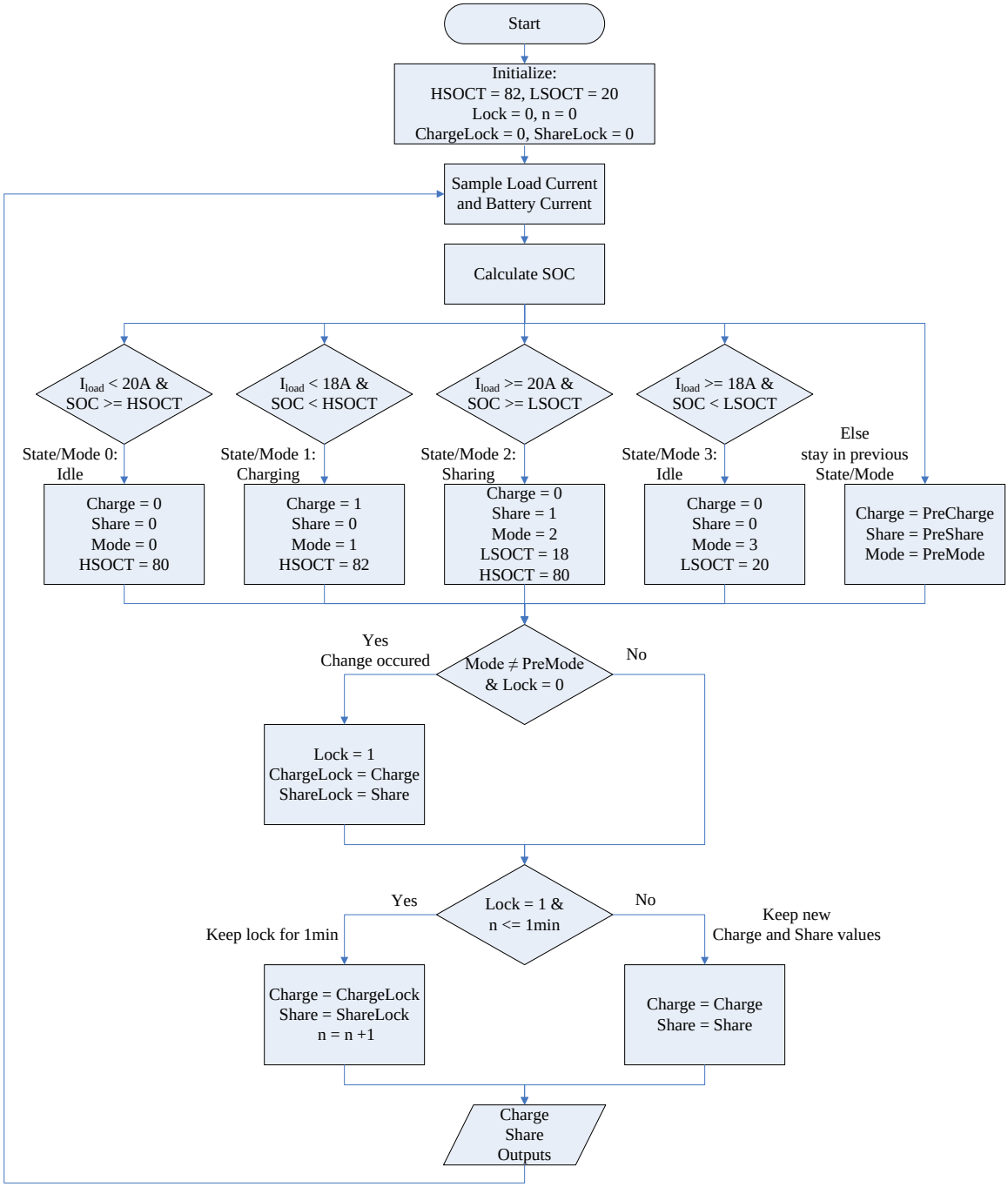

Figure 5.11: Flowchart for the BMS Algorithm

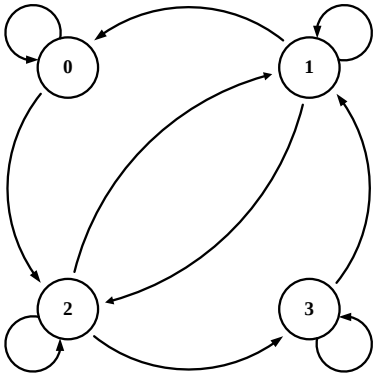

Figure 5.12: Finite State Machine Diagram for the BMS Algorithm

The SOC was estimated using the Coulomb Counting Method, which is one of the most common techniques to estimate the SOC of a battery [38].

This method integrates the battery current over time to provide an estimate of the SOC. The mathematical expression is given by:

$$SOC = SOC(t_0) + \frac{1}{C_{rated}} \int_{t_0}^{t_0+\tau} I_{bat}\, dt \qquad (5.57)$$

where $SOC(t_0)$ is the initial SOC, C_{rated} is the rated capacity in Ah, and I_{bat} is the battery current.

The mathematical expression for the Coulomb counting method is applied using a microcontroller by the expression given by:

$$SOC = SOC(t-1) + \left(\frac{I_{bat}}{C_{rated}} \Delta t \right) 100 \qquad (5.58)$$

where $SOC(t\text{-}1)$ is the previously estimated SOC value and Δt is the time sample in hours.

Although this method of SOC estimation is one of the most popular, it is worth noting that there are a number of factors that affect the accuracy. Such factors include temperature, battery cycle life, and other charging/discharging losses [38-41]. These factors were not a point of concern at this stage of this particular research work.

5.7 Conclusion

This chapter covered the theory and design of the control systems for the Buck converters and the Bidirectional converter. The design of the battery management system was also covered.

The theory section covered the control system of the voltage and current loops in both the Buck and the Boost converters. The control system consists of nested current and voltage control loops that control the inductor current and output voltage, respectively. The droop control method is used to obtain load sharing between the converters when connected in parallel within a DC microgrid while sharing a common load. Three droop control methods were presented: the ‘conventional’ V-I droop, the I-V droop, and the proposed combined voltage and droop (CVD) method. The voltage restoration control loop was also covered. The voltage restoration control loop is an outer loop common to all converters within the DC microgrid. It is used to correct any

voltage deviations created by droop control, adjusting the microgrid's DC-bus voltage to the desired value.

This chapter also covered the design of the control systems for both the Buck converters and the Bidirectional converter.

The control system for the Buck converters consists of nested current and voltage control loops with droop control. For the Buck converters the current closed loop bandwidth range for 10% to 100% load current (5.21A – 52.1A) varies between 11.83Hz to 133.42Hz with settling times in the range of 51ms to 6.9ms, while the voltage closed loop bandwidth varies between 6.46Hz to 0.64Hz with settling times in the range of 95ms to 0.96s. When using V-I droop, the voltage closed loop bandwidth for 10% to 100% load current (5.21A – 52.1A) varies between 6.52Hz to 0.7Hz with settling times in the range of 94.4ms to 0.876s. In the case of I-V droop the voltage closed loop bandwidth for the same load current range varies between 2449Hz to 2415.7Hz with settling times in the range of 3.8ms to 1.4ms. Using the CVD method, the voltage closed loop bandwidth for the same load current range varies between 28.47Hz to 4.26Hz with settling times in the range of 58.9ms to 144.8ms. The voltage restoration closed loop has got a bandwidth of 0.05Hz.

The control system for the Bidirectional converter consists of two parts: one part takes care of the battery charging process, and the other part takes care of the load current supplying/sharing process. For the Bidirectional converter operating as a Buck converter, the current loop has a closed loop bandwidth of 800Hz, with a settling time of 2.5ms. For the Bidirectional converter operating as a Boost converter, the current closed loop bandwidth range for 10% to 100% load current (3.13A – 31.25A) varies between 652Hz to 708Hz with settling times in the range of 47.4ms to 6.7ms, while the voltage closed loop bandwidth varies between 32.87Hz to 4.18Hz with settling times in the range of 37.7ms to 146ms.

This chapter also presented the BMS which was designed to provide high-level control to the Bidirectional converter, controlling the operation between battery charging mode and load sharing/supplying mode. The BMS algorithm uses the load current in the DC microgrid and the SOC of the battery bank to select amongst four possible output states/modes: State/Mode 0 – Idle (fully charged battery), State/Mode 1 – Battery Charging, State/Mode 2 – Sharing, and State/Mode 3 – Idle (fully discharged battery).

Chapter 6 Experimental Setup

This chapter covers the hardware and the firmware coding performed to build and control the converters, used to set up an experimental laboratory-based DC Microgrid. The experimental setup consists of two 2.5kW Buck converters used as energy source converters and a 1.5kW Bidirectional converter for a battery storage system, which together with loads form a DC microgrid test setup. The common microgrid DC-bus voltage was chosen to be 48V. The two Buck converters convert a source voltage within the range of 70V – 120V (recommended input voltage 100V - selected for design and testing) to the DC-bus voltage of 48V, while the Bidirectional converter operates between 24V on the battery-bank-side and 48V on the DC-bus-side. Each converter is controlled by its control system applied using the TI microcontroller TMS320F28379D. A battery management system (BMS) controls the Bidirectional converter on a higher level, controlling the mode of operation between load supplying/sharing mode and battery charging mode. A block diagram of the experimental DC microgrid setup is shown in Figure 6.1.

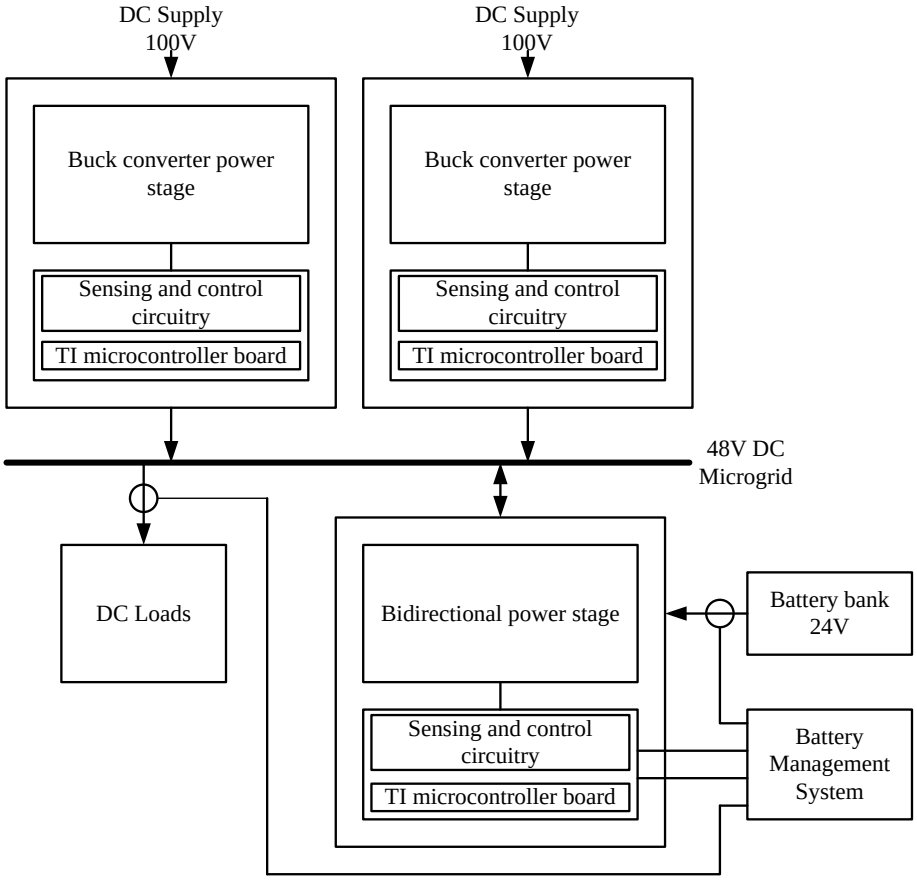

Figure 6.1: Block Diagram of Experimental DC Microgrid

6.1 Converter Unit Design

Each converter is housed within its own enclosure, making it easy to add converter units to the DC microgrid, and also makes future expansion easier. Each converter can be divided in two parts: the power stage, and the sensing and control circuitry. The power stage includes the power converter itself made up of the switching module, the inductor, and the input/output capacitors, and also of the contactors, the inrush current limiting power resistors, the start-up power resistor, and the circuit breakers. The sensing and control circuitry includes the current and voltage sensing circuit PCBs, the control circuit PCB, the IGBT driver PCB, and the power supply units for the circuitry.

6.1.1 Buck Converter Hardware Design

Figure 6.2 shows one of the Buck converter prototypes; external view and internal view.

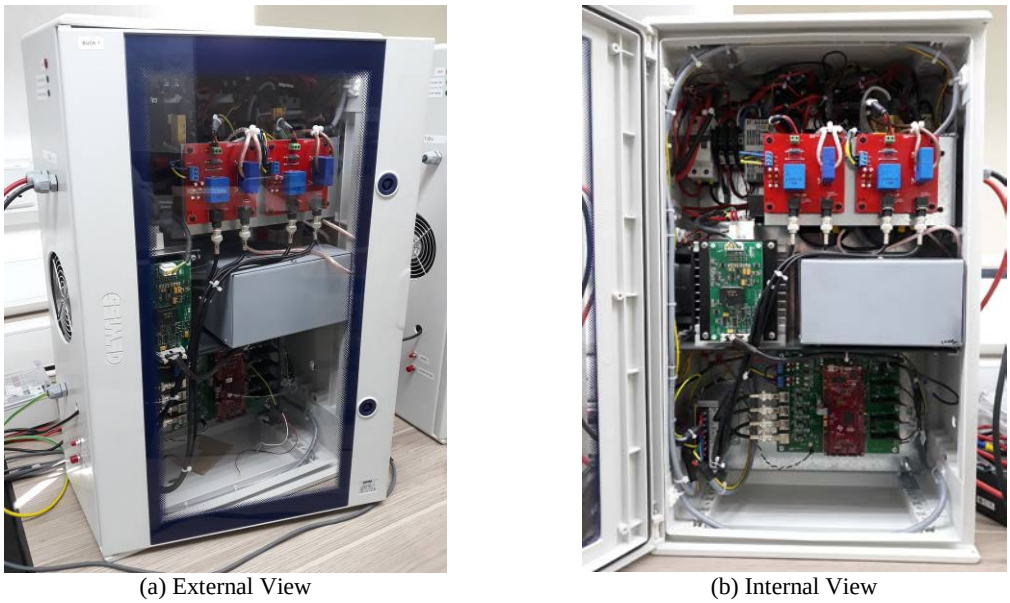

(a) External View (b) Internal View

Figure 6.2: Buck Converter Prototype

6.1.1.1 Buck Converter Power Stage

Figure 6.3 shows the circuit diagram for the power stage of the two Buck converters.

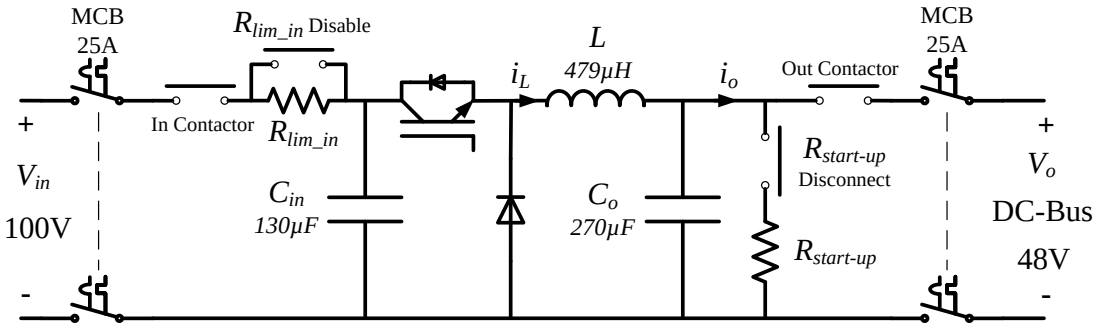

Figure 6.3: Buck Converter Power Stage – Circuit Diagram

6.1.1.1.1 Buck Converter Inductors and Capacitors

The design and value calculations for the inductor and capacitors for the Buck converters were covered in Chapter 3. A table summarising the data for the inductor and capacitors for the Buck converters is shown as Table 6.1. The inductor in both Buck converters was enclosed in an earthed metal housing to reduce EMI emissions. Figure 6.4 shows the inductor in the metal housing and the location of the input and output capacitors.

Buck Converters		
Inductor	Output Capacitor	Input Capacitor
479µH Core: Blinzinger R154x80x45-BFM8	270µF CDM Cornell Dubilier Polypropylene DC-link capacitor 947D271K112AEGSN	130µF CDM Cornell Dubilier Polypropylene DC-link capacitor 947D131K132ACGSN

Table 6.1: Summary of Buck Converter Inductor and Capacitor Data

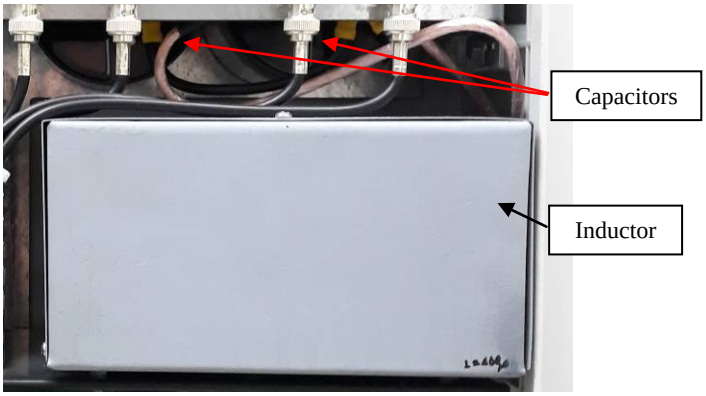

Figure 6.4: Buck Converter Inductor and Capacitors

6.1.1.1.2 IGBT Module for the Buck Converters

The Buck converters use the SKM150GAR12T4 IGBT module from Semikron, consisting of a leg made up of an IGBT with parallel-connected diode and a diode, as shown in Figure 6.5.

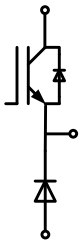

Figure 6.5: SKM150GAR12T4 module – Circuit Diagram

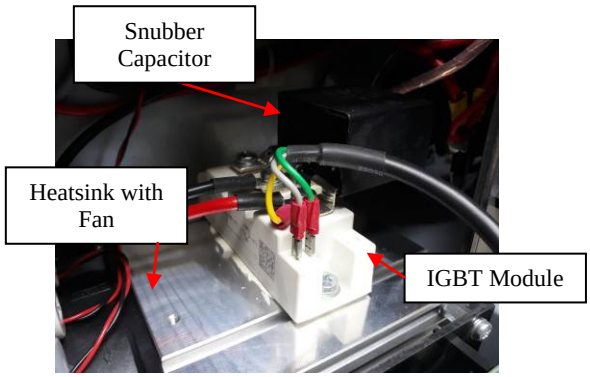

Figure 6.6: SKM150GAR12T4 module mounted on the Heatsink

The IGBT modules were mounted on Semikron P3/120 heatsinks with added 24V DC cooling fan, giving a heatsink to ambient thermal resistance R_{thha} of 0.167K/W. The cooling fan is protected by a 500mA fuse installed in a DIN rail mounted fuse holder.

A 3.3µF snubber capacitor was mounted on each IGBT module, fixed across the IGBT / diode combination on the SKM150GAR12T4 module. The snubber capacitor selected for the applications was the Vishay Metallized Polypropylene Film Capacitor 3.3µF MKP386M Snubber. Figure 6.6 shows the IGBT module mounted on the heatsink.

6.1.1.1.3 MCBs used in the Buck Converters

The Buck converters have miniature circuit breakers (MCBs) on both input and output sides to provide overload and short circuit protection, as well as provide a means to manually disconnect the unit in case there is the need for isolation. These MCBs are located as shown in Figure 6.7. The MCBs are all C-type 25A double pole, and rated for DC operation. The MCBs are not the only means of protection against overload and short circuit protection, since these type of devices would not be fast enough for certain short circuit faults. Therefore, there is also protection circuitry in the control PCB, which is explained in an upcoming section.

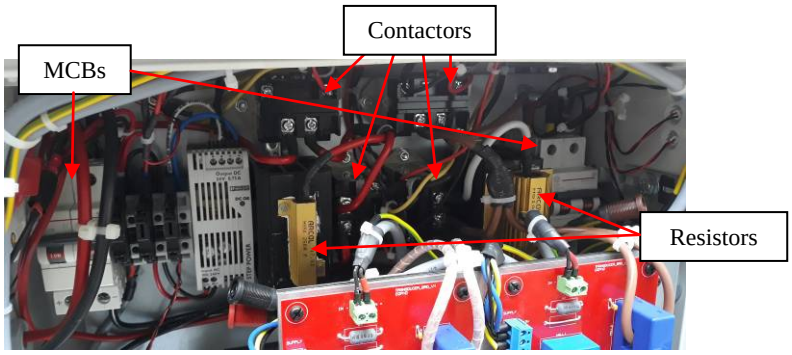

Figure 6.7: MCBs, Contactors, and Power Resistors in Buck Converter

6.1.1.1.4 Contactors and Power Resistors used in the Buck Converters

Contactors were used to control the connection and disconnection of the converter to the supply source and to the DC-bus. These contactors are labelled in the diagram in Figure 6.3 as In_Contactor and Out_Contactor.

The Buck converters are equipped with a 50Ω 100W start-up resistor, to enable the converter to operate and build-up the output voltage before closing the output-side contactor and connecting to the DC-bus. This serves to obtain a similar output voltage value to the DC-bus voltage value before connecting to an already energized DC-bus,

which reduces a spike in current caused by the charging of capacitors at the moment of connection to the DC-bus. This start-up resistor is labelled in Figure 6.3 as $R_{start\text{-}up}$ and can be disconnected from the circuit when not needed by a contactor labelled $R_{start\text{-}up}$_Disconnect. The Buck converters are also equipped with an inrush current limiting resistor, to limit current spikes due to the charging of the input capacitor at the moment of connection to the supply source. This resistor has a value of 250Ω 50W. This resistor is labelled in Figure 6.3 as R_{lim_in}, and is shorted out after a specific time following the connection to the supply source using the contactor labelled R_{lim_in}_Disable.

The contactors used are Omron G7L-1A-BUBJ-CB-DC24, operated by a 24V DC coil, and the switching contacts are rated for 20A operation. A diode was connected in reverse bias across each coil to protect the contactor's driving circuits against back EMF. The power resistors are the aluminium-housing type by Arcol, from the HS50 and HS100 ranges. The power resistors are mounted on heatsinks with DIN rail attachment. The contactors and power resistors are located as shown in Figure 6.7. Panel mount LEDs serve as indicators for the contactors, indicating if the contactors are on or off. These LEDs are shown in Figure 6.8. Other panel mount LEDs indicate the presence of the 100V input voltage and the 48V output voltage, which are also shown in Figure 6.8.

(a) Input Side (b) Output Side

Figure 6.8: Panel Mount Indicator LEDs – Buck Converter

6.1.1.2 Buck Converter Sensing and Control Circuitry

Figure 6.9 shows a general block diagram for the sensing and control circuitry of the Buck converters, with the green block representing the two voltage and current sensing PCBs, the blue blocks representing the control PCB, the yellow block

represent the IGBT driver PCB, and the orange blocks represent the power supplies. The white blocks represent items from the power stage.

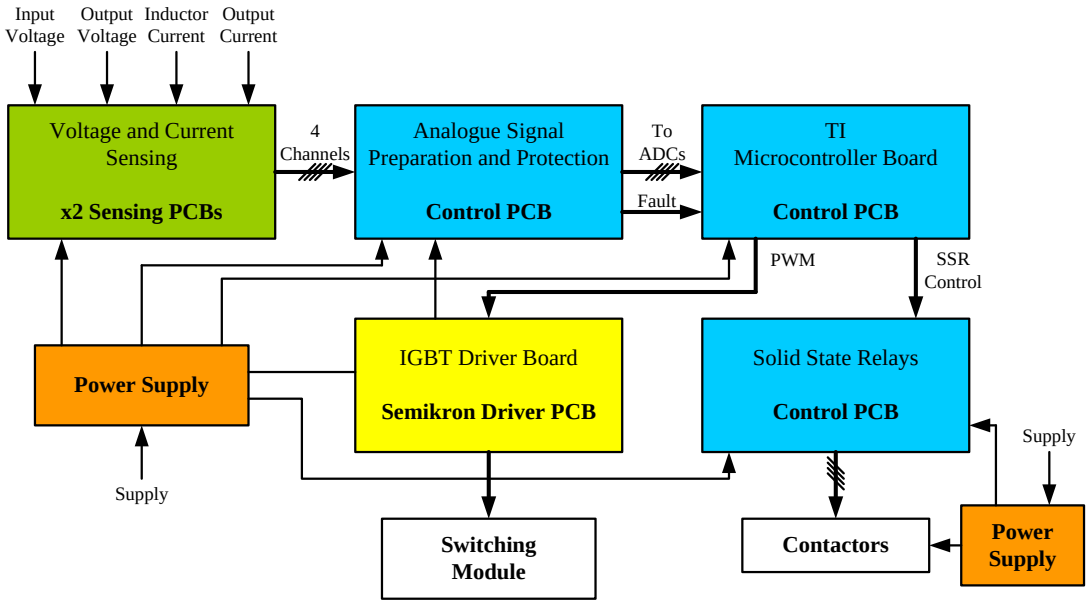

Figure 6.9: Block Diagram of the Buck Converter Sensing and Control Circuitry

6.1.1.2.1 Power Supplies used in the Buck Converters

Two switch-mode power supplies are used in each Buck converter. One power supply supplies the PCBs and another one supplies the contactor coils and heatsink fan. Both power supplies are protected by a 500mA fuse installed in a DIN rail mounted fuse holder on the input side. These power supplies are shown in Figures 6.10 and 6.11.

The power supplies used for the Buck converters are:

- Mean Well RQ-50C used to supply the PCBs, operated from an input voltage of 100V DC, to obtain output voltages of 15V, -15V, 5V, and -5V DC.
- Phoenix Contact Step Power 2868622 DIN rail-type power supply used to supply the contactor coils and heatsink fan, operated from an input voltage of 100V DC, to obtain an output voltage of 24V DC.

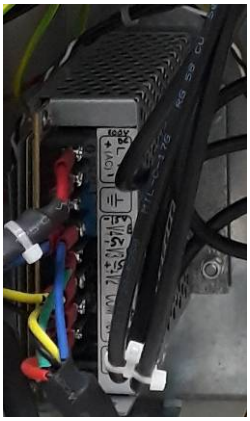

Figure 6.10: Mean Well RQ-50C
- Supplies the PCBs for the Buck Converter

Figure 6.11: Phoenix Contact Step Power 2868622
- Supplies the Contactor Coils and the Heatsink Fan for the Buck Converter

6.1.1.2.2 Buck Converter Voltage and Current Sensing Circuits

Voltage and current sensing in each Buck converter is achieved by two PCBs, each containing two circuits; one for the voltage and one for the current. Voltage sensing is obtained by a Hall Effect voltage transducer LV25-P from LEM [42]. Current sensing is obtained by a Hall Effect current transducer LA55-P/SP1 from LEM [43]. The transducers operate with supply voltages of +15V and -15V. Figure 6.12 show the two transducer PCBs.

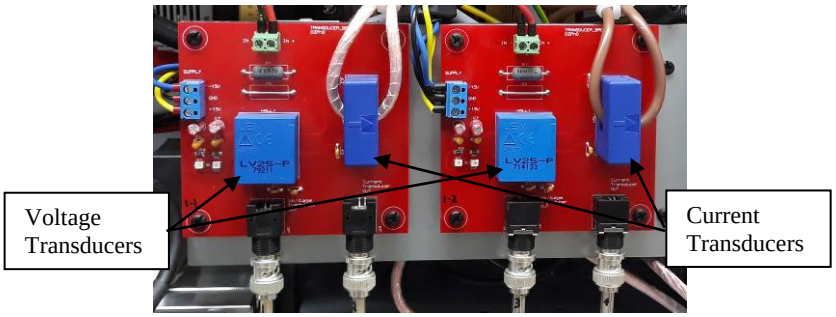

Figure 6.12: Transducer PCBs in the Buck Converter

In the Buck converters the voltage and current sensing circuits on the first PCB sense the input voltage (V_{in}) and the inductor current (i_L), and the voltage and current sensing circuits on the second PCB sense the output voltage (V_o) (DC-bus side) and output current (i_o). (See Figure 6.3)

Figures 6.13 and 6.14 show an internal representation of the LEM voltage and current transducers, respectively, with the external components needed for operation.

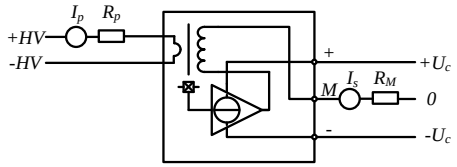

Figure 6.13: Representation of the LEM LV25-P Voltage Transducer

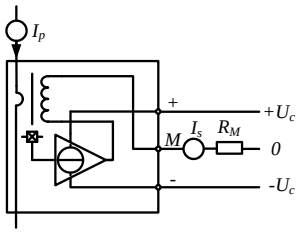

Figure 6.14: Representation of the LEM LV55-P/SP1 Voltage Transducer

The voltages measured by the LV25-P transducers are the input voltage (V_{in}) of 100V and the output voltage (V_o) of 48V. The higher voltage between the two was considered for the calculation of the primary resistance to consider the maximum value, therefore using the same calculated resistance value for both voltage transducers. The primary resistance (R_p) was calculated to obtain a primary current (I_p) of 10mA with a measured voltage of 100V. Therefore, the primary resistance needed was 10kΩ with a power dissipation capability of 1W. The resistor selected was the Riedon UBN-5C of value 10kΩ with 5W power capability, non inductive, and with 1% tolerance. The LV25-P transducer has a conversion ratio of 2500:1000. Therefore, with a primary current (I_p) of 10mA the secondary current (I_s) would be 25mA. The voltage across the secondary resistance (R_M) was desired to be 5V for the recommended value of the measured voltage (100V). This corresponds to a secondary current (I_s) of 25mA with a primary current (I_p) of 10mA, therefore a secondary resistor (R_M) of 200Ω with a power dissipation capability of 0.125W was needed. The selected resistor was a 200Ω resistor from the E192 (0.1% Tolerance) series with 0.25W power capability.

The currents measured by the LA55-P/SP1 transducers for the Buck converters are the inductor current (i_L) with a maximum peak value of 54.68A (Inductor current average I_L of 52.08A + ripple peak of 2.6A) and the output current (I_o) with a value of 52.08A. Since both currents are similar, a maximum current of 60A was considered as the primary current (I_p). The LA55-P/SP1 transducer has a conversion ratio of 1:2000. Therefore, with a primary current (I_p) of 60A the secondary current (I_s) would be 30mA. The voltage across the secondary resistance (R_M) was desired to be 6V for the maximum value of the measured current (60A). This corresponds to a secondary current (I_s) of 30mA with a primary current (I_p) of 60A, therefore a secondary resistor (R_M) of 200Ω with a power dissipation capability of 0.18W was needed. The selected

resistor was a 200Ω resistor from the E192 (0.1% Tolerance) series with 0.25W power capability.

The secondary resistor (R_M) for all transducers was not placed on the voltage and current sensing PCBs, but instead it was placed on the control PCBs. This was done to conduct the signals from the voltage and current sensing PCBs to the control PCBs as a current signal and not a voltage signal. This prevented a voltage drop issue on the cable connecting the PCBs. The secondary/output current from the transducers is conducted to the control PCBs using coax cable and BNC connectors to reduce EMI effects. The transducers were calibrated using precise voltage and current sources, and calibration factors were applied in the firmware.

6.1.1.2.3 Buck Converter Signal Preparation Circuits

The signal preparation circuits prepare the analogue output signals obtained from the voltage and current transducers, to be sampled by the ADCs within the microcontroller.

For the Buck converter the signal preparation circuits consist of four identical circuits/channels, one for each sensed signal; the input voltage, the output voltage, the inductor current, and the output current. Figure 6.15 shows the four channels on the control PCB.

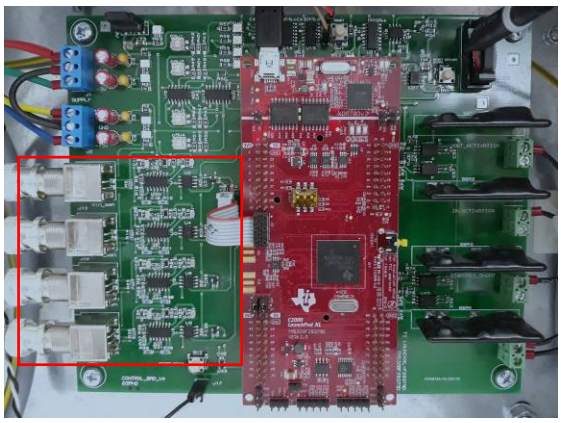

Figure 6.15: Buck Converter Signal Preparation Circuit – Four Channels

Each channel can be divided in seven parts: the input circuit, a voltage follower/buffer, an Anti-Aliasing filter, a scaling/attenuation circuit, another voltage follower/buffer, an output voltage limiter, and a low pass filter. Figure 6.16 show a simplified circuit diagram representation of the signal preparation circuit.

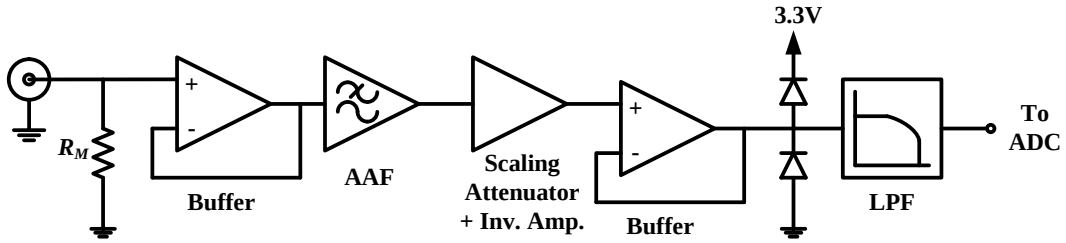

Figure 6.16: Simplified Circuit Diagram – Buck Converter Signal Preparation Circuit – Four Channels

The input circuit receives the sensed signal from the transducer via a coax cable. The current signal from the secondary of the transducer is received and converted to a voltage signal by the secondary resistor (R_M). A voltage follower provides a buffer between the LEM transducer output and the following circuitry. This voltage follower is followed by an anti-aliasing filter (AAF), which is used to prevent aliasing of the sampled signals. The anti-aliasing filter is implemented by a second order non-inverting active low pass filter using the Sallen-Key filter implementation and a Butterworth design. The anti-aliasing filter was designed for a cut-off frequency of 2.5kHz.

The ADC microcontroller inputs can handle voltages in the range of 0 up to 3V, however for better accuracy the voltage signal from the transducer secondary resistor (R_M) was set to be in the range 0 up to 5V. Therefore, the voltage signal needed scaling down to the appropriate range of 0 to 3V before sampling by the ADC, which is performed by the scaling circuit. The scaling circuit scales down the signal by a factor of two. However the scaled output signal is inverted when compared to the input, therefore an inverting amplifier with a gain of 1 was included within the scaling circuit to invert the scaled voltage signal to the original polarity.

Another voltage follower buffers the signal from the rest of the circuit, before sampling takes place. This is followed by a voltage limiter circuit made up of two diodes connected between the +3.3V supply and ground, which provides protection for the microcontroller ADC inputs in the case that the voltage signal tries to go beyond 3.3V, keeping the microcontroller input in the range 0 to 3.3V. At the input of the microcontroller ADCs a low pass filter (LPF) with a cut-off frequency of approximately 100kHz was applied to clean the sensed signal from any noise which is picked up by the circuit.

6.1.1.2.4 Buck Converter Protection Circuit

The protection circuit monitors against over-voltages and over-currents. The protection circuit monitors the input voltage, output voltage, inductor current, and output current signals from the signal preparation circuits. If these exceed a certain limit, the protection circuit outputs a fault/trip signal to the microcontroller which switches of the PWM output thus switching off the converter IGBT. The protection circuit also takes another input from the IGBT driver board. The IGBT driver board provides an error signal in case of IGBT short circuit or supply under-voltage. This error signal is monitored by the protection circuit, which outputs a fault signal to the microcontroller. Once a fault occurs, the protection circuit and the microcontroller stay in the tripped state until the fault is cleared, and both the protection circuit and the microcontroller are reset. Each type of fault is indicated by a red LED (five fault indicator LEDs). Figure 6.17 shows the protection circuit on the control PCB. Figure 6.18 show a simplified circuit diagram representation of the protection circuit.

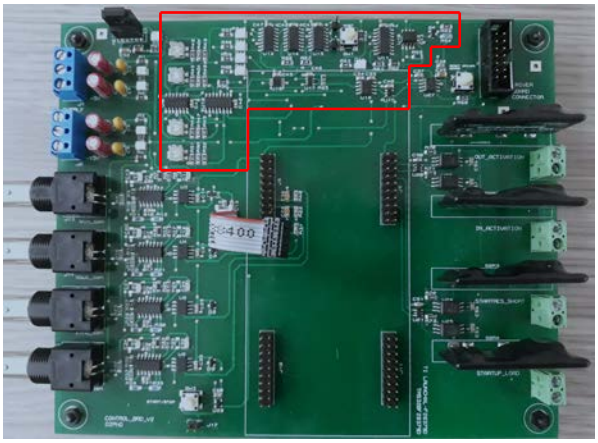

Figure 6.17: Buck Converter Protection Circuit

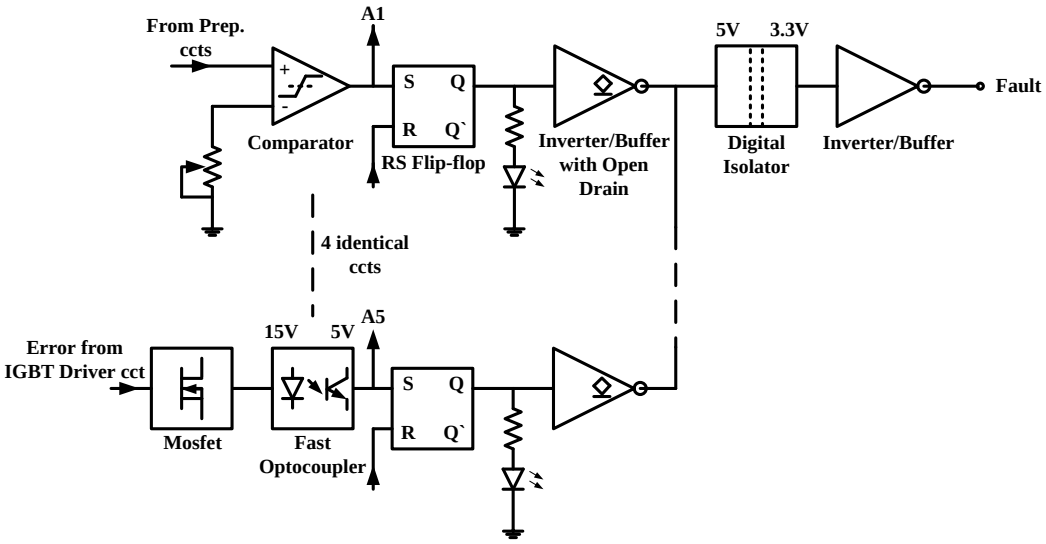

Figure 6.18: Simplified Circuit Diagram – Buck Converter Protection Circuit

The four signals from within the signal preparation circuit; for the input voltage, output voltage, inductor current, and output current, are compared to set threshold values using comparator circuits, one for each signal. The threshold values are set using 10kΩ preset potentiometers, and were set for a threshold voltage of 2.8V on the comparator input pin.

The comparator is followed by an RS flip-flop which holds the fault state until the fault is cleared and it is reset. The output of the each RS flip-flop switches on the indicator LED according to the type of fault. The output of the each RS flip-flop also feeds into an inverter-buffer with open drain output. The four inverter-buffer outputs are connected in an OR configuration, with the common point fed to a digital isolator to have a 5V input level and provide a 3.3V output level. The 3.3V output level from the digital isolator is fed through an inverter-buffer to connect to the microcontroller pin.

The error signal from the IGBT driver board has a slightly different circuit since it is a 15V levelled signal. This error signal, being a high logic error, is fed to an N-channel MOSFET circuit which controls a high speed optocoupler with a 5V levelled output. The output of the optocoupler is connected to an RS flip-flop. The output of the RS flip-flop switches on the indicator LED to indicate a driver board error, and feeds to an inverter-buffer with open drain output. The inverter-buffer output is then connected with the other inverter-buffer outputs in OR configuration to continue the circuit as described above.

The RS flip-flops must not reset with a fault still present, so a logic circuit was designed to only permit reset when the fault is cleared. The RS flip-flop reset logic circuit uses standard AND, OR, and inverter gates. The RS flip-flops are reset by a push button switch, which is shown within the highlighted area in Figure 6.17. Figure 6.19 show a simplified circuit representation of the reset circuit. Another push button switch serves to reset the IGBT driver board, which is discussed in the driver board section.

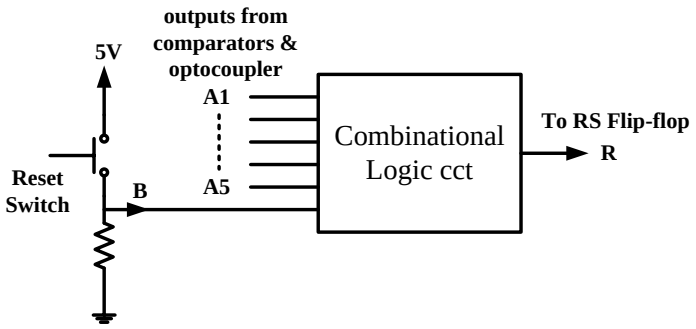

Figure 6.19: Simplified Circuit Diagram – Buck Converter Protection Reset Circuit

6.1.1.2.5 Buck Converter PWM Circuit

The PWM circuit connects the PWM output from the microcontroller to the IGBT driver board. The PWM output signal from the microcontroller is at a 3.3V voltage level, while the IGBT driver board PWM input is at a 15V voltage level. A gate driver IC was used to perform the voltage level conversion, operating from a 3.3V PWM input to provide a 15V PWM output signal. The gate driver IC used is the ADUM3123ARZ from Analog Devices. This gate driver IC has a disable feature input, which was connected to the fault signal coming from the protection circuit. In case of a fault the signal goes to logic high which puts the gate driver output to low. This is another layer of protection, in addition to the microcontroller PWM output going low in the case of a fault. The PWM circuit is indicated on Figure 6.20. Figure 6.21 shows a simplified circuit representation for the PWM circuit.

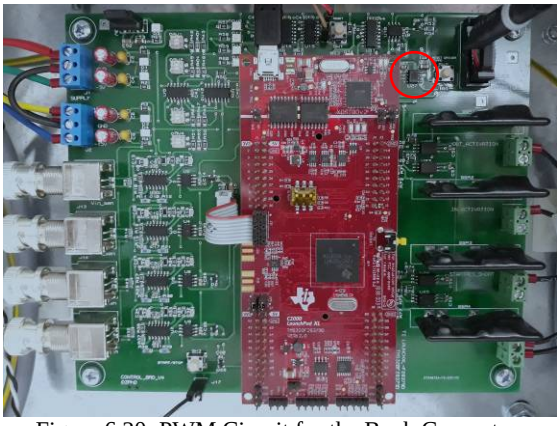

Figure 6.20: PWM Circuit for the Buck Converter – Connects a 3.3V PWM output from the microcontroller to the 15V PWM input of the IGBT driver PCB

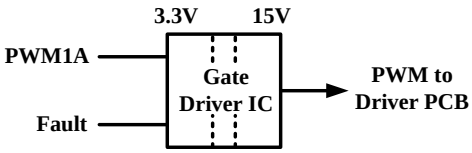

Figure 6.21: Simplified Circuit Diagram – PWM Circuit for the Buck Converter

6.1.1.2.6 Buck Converter Solid State Relay (SSR) Circuit

The solid state relay (SSR) circuit switches on/off the contactors as controlled by the microcontroller. The circuit contains four SSRs, one for each contactor in the Buck converter. The switch control signal from the microcontroller at 3.3V is fed to an inverter-buffer with an open drain output, which switches a logic compatible

optocoupler. The optocoupler provides a 5V output to switch on the SSR. This circuit is repeated for each of the four contactors. The SSR circuit is highlighted in Figure 6.22. Figure 6.23 show a simplified circuit representation of the SSR circuit.

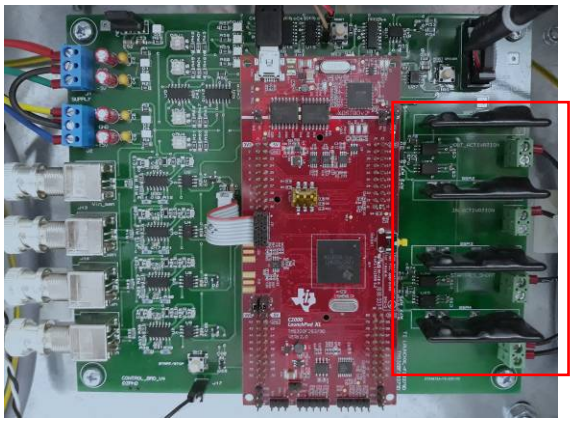

Figure 6.22: SSR Circuit for the Buck Converter

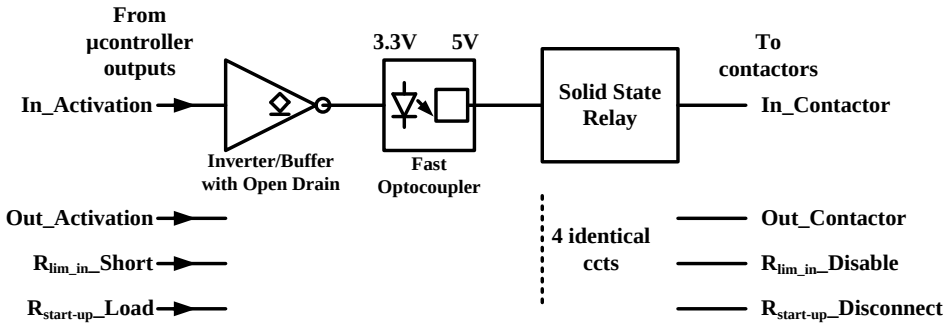

Figure 6.23: Simplified Circuit Diagram – SSR Circuit for the Buck Converter

6.1.1.2.7 Other Features on the Buck Converter PCBs

The voltage and current sensing PCBs operate from supplies of +15V, and -15V. The control PCB operates from supplies of +15V, -15V, +5V, and -5V. The supplies to these PCBs are provided by the Mean Well RQ-50C power supply. All supply inputs on the PCBs are connected to a capacitor combination of a 1µF Electrolytic capacitor and a 1µF Tantalum capacitor, providing more stable and cleaner voltages from any noise that can be picked up by the supply wires. SMD LEDs were used as voltage presence indicators. Figure 6.24 and 6.25 show the location of these circuits on the control PCB and on the Voltage and Current Sensing PCBs, respectively.

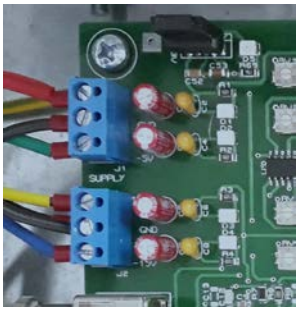

Figure 6.24: Supply Connectors on the Buck Converter Control PCB

Figure 6.25: Supply Connector on the Buck Converter Voltage and Current Sensing PCBs

The TI microcontroller development board and subsequently some support circuitry needs a +3.3V supply. The +3.3V supply is achieved using a linear 3.3V LDO regulator BA033ST from ROHM. The regulator is supplied from the +5V supply. The +3.3V supply has an SMD LED as a supply indicator. The location of the regulator is shown in Figure 6.24.

The Buck converters have start/stop push button switches, to start/stop the operation of the converters. Two switches performing the same operation were installed; one on the control PCB and another panel mounted. A Maxim MAX6816 switch debouncer was used to prevent spurious switching due to mechanical bouncing when pressing the switch. Figures 6.26 and 6.27 show the locations of these switches.

Figure 6.26: Start/Stop Push Button Switch on the Buck Converter Control PCB

Figure 6.27: Panel Mount Start/Stop Push Button Switch on the Buck Converter

6.1.1.2.8 IGBT Driver PCB

The IGBT driver PCB used for the Buck converters is the Semikron Semidriver SKHI 10/12 (R), shown in Figure 6.28. The IGBT driver PCB was mounted on the heatsink to be at the shortest distance possible to the IGBT module, to keep resistance, stray inductances, and interference in the cable between the driver board and the IGBT, to the minimum possible.

Figure 6.28: IGBT Driver PCB for the Buck Converter

The SKHI 10/12 is a single IGBT driver which is capable to switch a high current IGBT module or several paralleled IGBTs. It has galvanic isolation between the primary and the secondary sides, which provides protection to the control board.

The SKHI 10/12 IGBT driver board operates with a voltage of +15V. This supply voltage is supplied from the control PCB.

The SKHI 10/12 IGBT driver board can operate with PWM input signals of 5V or 15V voltage levels, which is set by an input level selector on the PCB. The 15V voltage level is the preferred setting for applications with possible high switching noise [44], therefore it was used for the Buck converter application. The IGBT driver board has a short circuit protection feature by measuring the V_{ce} of the IGBT. Another protection feature is monitoring of the primary supply voltage V_s against any malfunction. Both failure cases generate an error signal to the control PCB through an open collector transistor. This error signal from the driver board is monitored by the protection circuit which outputs a fault signal to the microcontroller in case of a fault, as previously discussed in section 6.1.1.2.5 (Buck Converter Protection Circuit). Error conditions in the IGBT driver board are reset, once the fault is cleared, using a push button switch on the control PCB shown in Figure 6.29.

Figure 6.29 shows the location of the connector on the Buck converter control PCB used to connect the control PCB with the IGBT driver board. Figure 6.30 shows the pinout of the IGBT driver board connector. A shielded ribbon cable was used to connect the two PCBs.

Figure 6.29: IGBT Driver Connector on the Buck Converter Control PCB

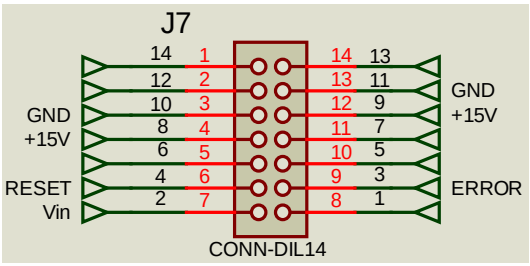

Figure 6.30: IGBT Driver Connector Pinout on the Buck Converter Control PCB

6.1.2 Bidirectional Converter Hardware Design

Figure 6.31 shows the Bidirectional converter prototypes; external view and internal view.

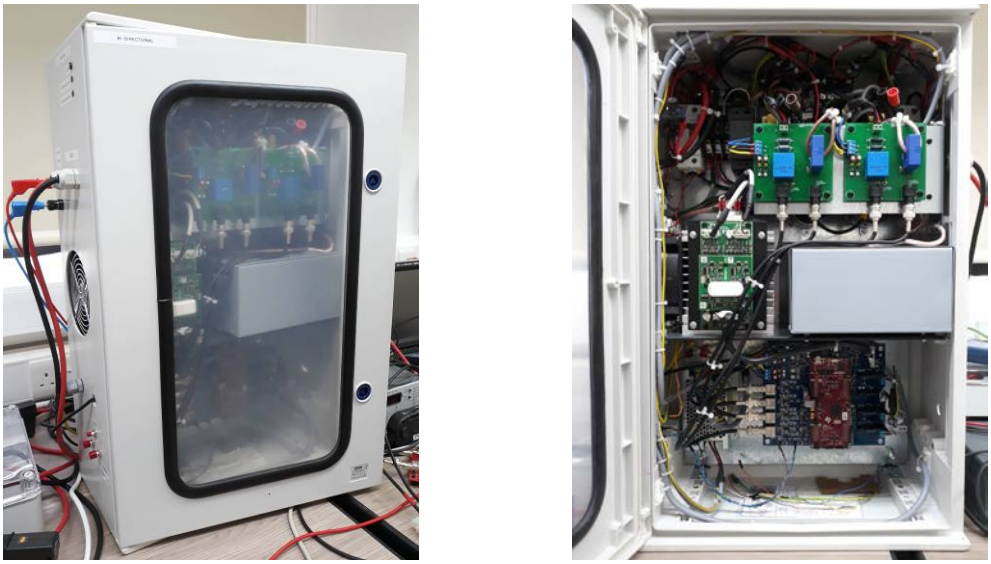

(a) External View (b) Internal View

Figure 6.31: Bidirectional Converter Prototype

6.1.2.1 Bidirectional Converter Power Stage

Figure 6.32 shows the circuit diagram for the power stage of the Bidirectional converter.

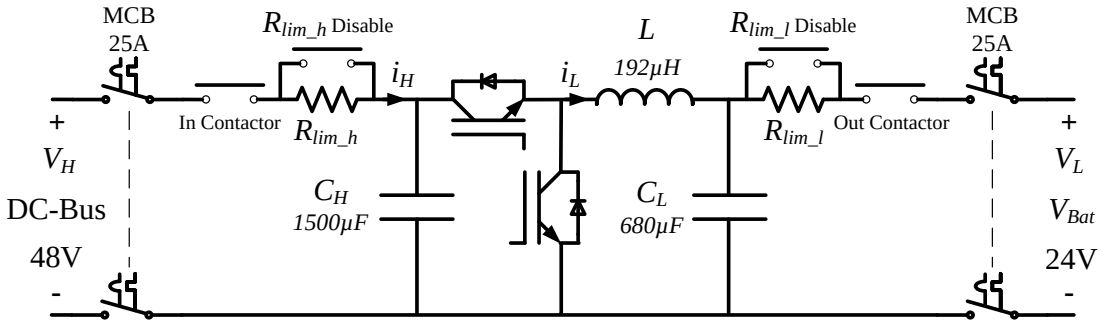

Figure 6.32: Bidirectional Converter Power Stage – Circuit Diagram

6.1.2.1.1 Bidirectional Converter Inductors and Capacitors

The design and value calculations for the inductors and capacitors for the Bidirectional converter were covered in Chapter 3. A table summarising the data for the inductor and capacitors for the Bidirectional converter is shown as Table 6.2. The inductor in the Bidirectional converter was enclosed in an earthed metal housing to reduce EMI emissions. Figure 6.33 shows the inductor in the metal housing and the location of the input and output capacitors.

Bidirectional Converter		
Inductor	Higher-Voltage-Side Capacitor	Lower-Voltage-Side Capacitor
192µH Core: Blinzinger R154x80x45-BFM8	1500µF Nichicon Aluminium Electrolytic Capacitor LNX2V152MSEF	680µF Nichicon Aluminium Electrolytic Capacitor LNT2G681MSEF

Table 6.2: Summary of Bidirectional Converter Inductor and Capacitor Data

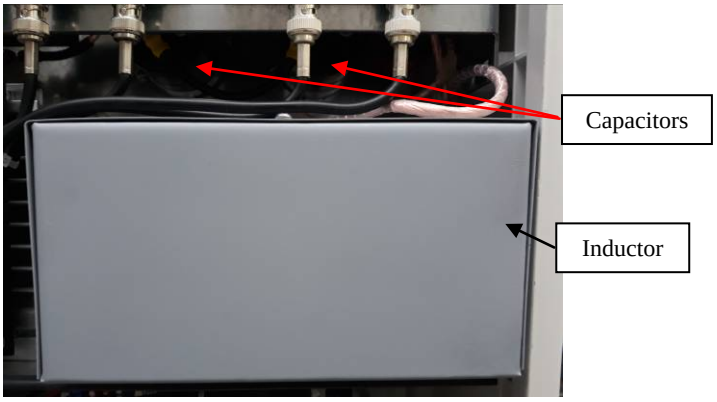

Figure 6.33: Bidirectional Converter Inductor and Capacitors

6.1.2.1.2 IGBT Module for the Bidirectional Converter

The Bidirectional converter uses the SKM100GB063D IGBT module from Semikron, consisting of a half bridge leg made up of two IGBTs, each with parallel-connected diode, as shown in Figure 6.34.

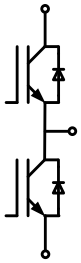

Figure 6.34: SKM100GB063D module – Circuit Diagram

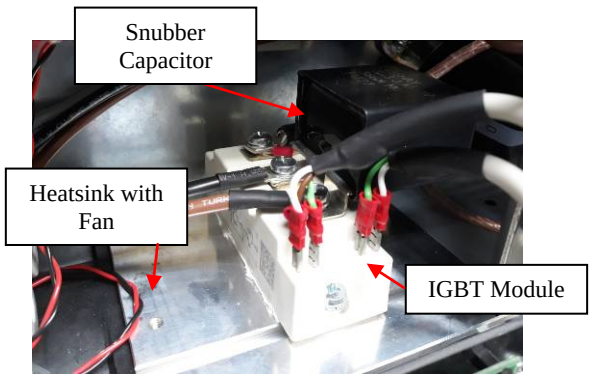

Figure 6.35: SKM100GB063D module mounted on the Heatsink

The IGBT module was mounted on Semikron P3/120 heatsinks with added 24V DC cooling fan, giving a heatsink to ambient thermal resistance R_{thha} of 0.167K/W. The cooling fan is protected by a 500mA fuse installed in a DIN rail mounted fuse holder.

A 3.3µF snubber capacitor was mounted on the IGBT module, fixed across the two IGBTs on the SKM100GB063D module. The snubber capacitor selected for the applications was the Vishay Metallized Polypropylene Film Capacitor 3.3µF MKP386M Snubber. Figure 6.35 shows the IGBT module mounted on the heatsink.

6.1.2.1.3 MCBs used in the Bidirectional Converter

The Bidirectional converter has miniature circuit breakers (MCBs) on both input and output sides to provide overload and short circuit protection, as well as provide a means to manually disconnect the unit in case there is the need for isolation. These MCBs are located as shown in Figure 6.36. The MCBs are all C-type 25A double pole, and rated for DC operation. The MCBs are not the only means of protection against overload and short circuit protection, since these type of devices would not be fast enough for certain short circuit faults. Therefore, there is also protection circuitry in the control PCB, which is explained in an upcoming section.

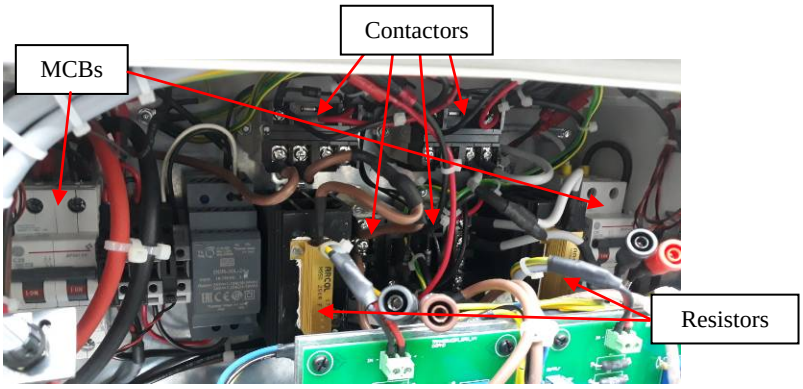

Figure 6.36: MCBs, Contactors, and Power Resistors in Bidirectional Converter

6.1.2.1.4 Contactors and Power Resistors used in the Bidirectional Converter

Similar to the Buck converters, in the Bidirectional converter contactors were used to control the connection and disconnection of the converter to the supply/battery source and to the DC-bus. These contactors are labelled in the diagram in Figure 6.32 as In_Contactor and Out_Contactor.

The Bidirectional converter is equipped with two inrush current limiting resistors, to limit current spikes due to the charging of capacitors at the moment of connection to the supply/battery source or DC-bus. These resistors have a value of 250Ω 50W. The

two inrush current limiting resistors, are placed one on the DC-bus-side and another on the battery-bank-side, and are labelled in Figure 6.32 as R_{lim_h} and R_{lim_l}, respectively. These are shorted out after a specific time following the connection to the supply source using the contactors labelled R_{lim_h}_Disable and R_{lim_l}_Disable, respectively.

The contactors used are Omron G7L-1A-BUBJ-CB-DC24, operated by a 24V DC coil, and the switching contacts are rated for 20A operation. A diode was connected in reverse bias across each coil to protect the contactor's driving circuits against back EMF. The power resistors are the aluminium-housing type by Arcol, from the HS50 range. The power resistors were mounted on heatsinks with DIN rail attachment. The contactors and power resistors are located as shown in Figure 6.36. Panel mount LEDs serve as indicators for the contactors, indicating if the contactors are on or off. These LEDs are shown in Figure 6.37. Other panel mount LEDs indicate the presence of the 48V DC-bus voltage and the 24V battery voltage, which are also shown in Figure 6.37.

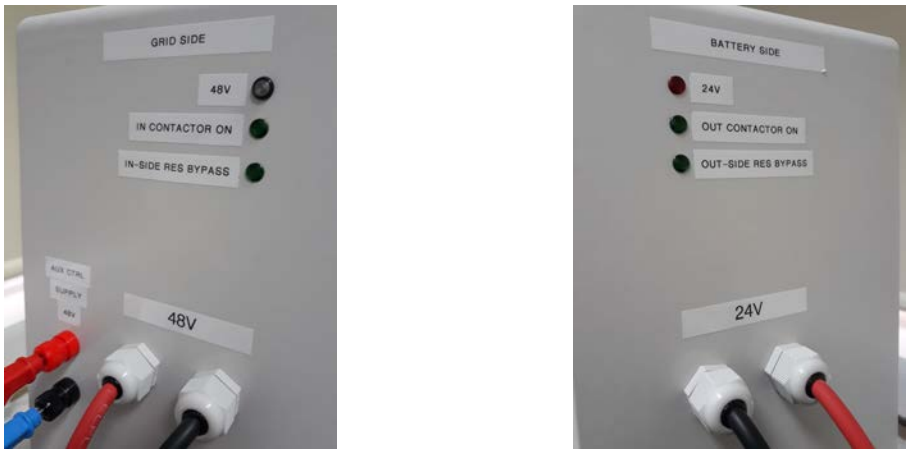

(a) Higher-Voltage-Side (DC-Bus Side) (b) Lower-Voltage-Side (Battery Side)

Figure 6.37: Panel Mount Indicator LEDs – Bidirectional Converter

6.1.2.2 Bidirectional Converter Sensing and Control Circuitry

Figure 6.38 shows a general block diagram for the sensing and control circuitry of the Bidirectional converter, with the green block representing the two voltage and current sensing PCBs, the blue blocks representing the control PCB, the yellow block represent the IGBT driver PCB, and the orange blocks represent the power supplies. The white blocks represent items from the power stage.

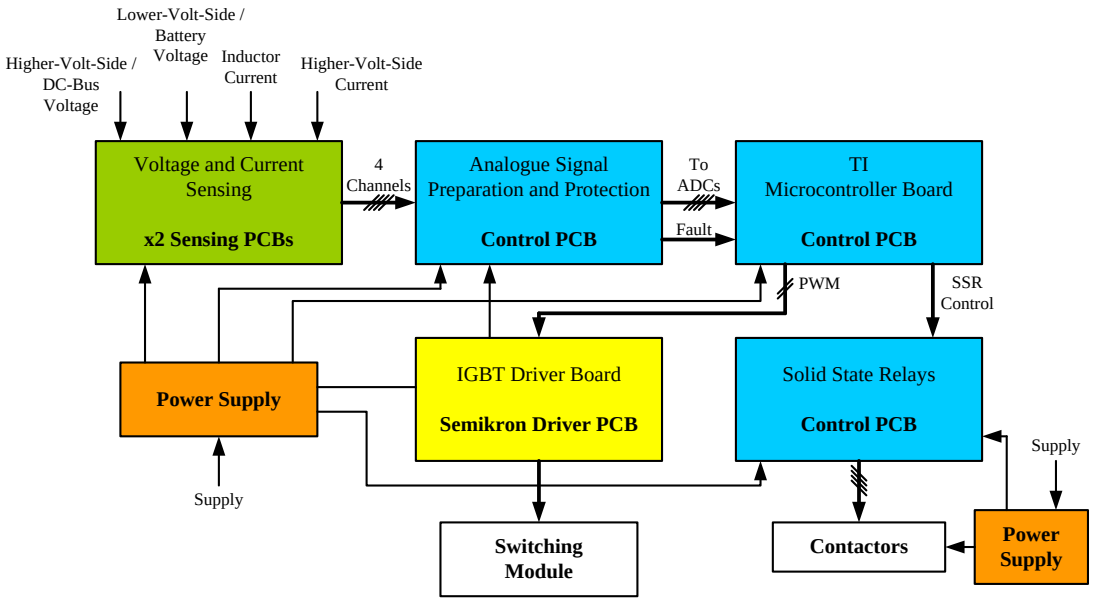

Figure 6.38: Block Diagram of the Bidirectional Converter Sensing and Control Circuitry

6.1.2.2.1 Power Supplies used in the Bidirectional Converter

Similar to the Buck converters, two switch-mode power supplies are used in the Bidirectional converter. One power supply supplies the PCBs and another one supplies the contactor coils and heatsink fan. Both power supplies are protected by a 500mA fuse installed in a DIN rail mounted fuse holder on the input side. These power supplies are shown in Figures 6.39 and 6.40.

The power supplies used for the Bidirectional converters are:

- Integrated Power Designs DC4-70-4005 CHCO used to supply the PCBs, operated from an input voltage of 48V DC, to obtain output voltages of 15V, -15V, 5V, and -5V DC.

- Mean Well DDR-30L-24 DIN rail-type power supply used to supply the contactor coils and heatsink fan, operated from an input voltage of 48V DC, to obtain an output voltage of 24V DC.

Figure 6.39: Integrated Power Designs DC4-70-4005 - Supplies the PCBs for the Bidirectional Converter

Figure 6.40: Mean Well DDR-30L-24 - Supplies the Contactor Coils and the Heatsink Fan for the Bidirectional Converter

6.1.2.2.2 Bidirectional Converter Voltage and Current Sensing Circuits

Voltage and current sensing in the Bidirectional converter is achieved by two PCBs, each containing two circuits; one for the voltage and one for the current. Voltage sensing is obtained by a Hall Effect voltage transducer LV25-P from LEM [42]. Current sensing is obtained by a Hall Effect current transducer LA55-P/SP1 from LEM [43]. The transducers operate with supply voltages of +15V and -15V. Figure 6.41 show the two transducer PCBs.

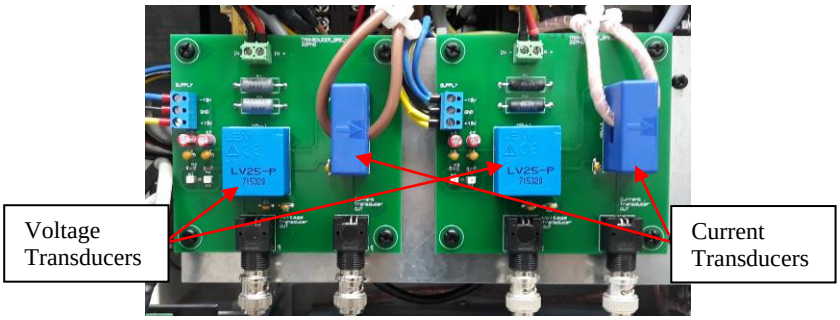

Figure 6.41: Transducer PCBs in the Bidirectional Converter

Internal representations of the LEM voltage and current transducers are shown in Figures 6.13 and 6.14 (section 6.1.1.2.3), respectively, with the external components needed for operation.

In the Bidirectional converter the voltage and current sensing circuits on the first PCB sense the higher voltage V_H (DC-bus-side) and the higher-voltage-side current i_H, and the voltage and current sensing circuits on the second PCB sense the lower voltage V_L (battery voltage V_{bat}) and inductor current i_L. (See Figure 6.32)

The voltages measured by the LV25-P transducers for the Bidirectional converter are the higher/DC-bus voltage (V_H) of 48V and the lower/battery voltage (V_L *or* V_{bat}) of 24V. The higher voltage between the two was considered for the calculation of the primary resistance to consider the maximum value, therefore using the same calculated resistance value for both voltage transducers. The primary resistance (R_p) was calculated to obtain a primary current (I_p) of 10mA with a measured voltage of 48V. Therefore, the primary resistance needed was 4.8kΩ with a power dissipation capability of 0.48W. To obtain this primary resistance of 4.8kΩ, two 2.4kΩ resistors connected in series were used. The resistors selected were the Riedon UBN-5C of value 2.4kΩ with 5W power capability, non inductive, and with 1% tolerance. The LV25-P transducer has a conversion ratio of 2500:1000. Therefore, with a primary

current (I_p) of 10mA the secondary current (I_s) would be 25mA. The voltage across the secondary resistance (R_M) was desired to be 5V for the maximum value of the measured voltage (48V). This corresponds to a secondary current (I_s) of 25mA with a primary current (I_p) of 10mA, therefore a secondary resistor (R_M) of 200Ω with a power dissipation capability of 0.125W was needed. The selected resistor was a 200Ω resistor from the E192 (0.1% Tolerance) series with 0.25W power capability.

The currents measured by the LA55-P/SP1 transducers for the Bidirectional converter are the inductor current (i_L) with a maximum peak value of 65.63A (Inductor current average I_L of 62.5A + ripple peak of 3.13A) and the higher-voltage-side/DC-bus-side current (I_H) with a value of 31.25A. A maximum current of 70A was considered as the primary current (I_p), for both current transducers. The LA55-P/SP1 transducer has a conversion ratio of 1:2000. Therefore, with a primary current (I_p) of 70A the secondary current (I_s) would be 35mA. The output voltage across the secondary resistance (R_M) was desired to be below 6V for the maximum value of the measured current (70A). Using a secondary resistor (R_M) of 169Ω with a secondary current (I_s) of 35mA gives a voltage across the secondary resistor (R_M) of 5.915V. Therefore, a secondary resistor (R_M) of 169Ω with a power dissipation capability of 0.21W was needed. The selected resistor was a 169Ω resistor from the E192 (0.1% Tolerance) series with 0.25W power capability.

Similar to the Buck converters, the secondary resistor (R_M) for all transducers was placed on the control PCB, to conduct the signals from the voltage and current sensing PCBs to the control PCB as a current signal and not a voltage signal. This prevented a voltage drop issue on the cable connecting the PCBs. The secondary/output current from the transducers is conducted to the control PCB using coax cable and BNC connectors to reduce EMI effects. The transducers were calibrated using precise voltage and current sources, and calibration factors were applied in the firmware.

6.1.2.2.3 Bidirectional Converter Signal Preparation Circuits

The signal preparation circuits prepare the analogue output signals from the voltage and current transducers, to be sampled by the ADCs within the microcontroller.

For the Bidirectional converter the signal preparation circuit is made up of four circuits / channels. These channels are divided in two different sets; two identical

channels for the higher voltage (DC-bus voltage) and the lower voltage (battery voltage), and another two identical channels for the inductor current and the higher-voltage-side current. The two channels used for the voltages can handle only a positive signal, while the channels used for the currents can handle a bidirectional signal (both +ve and –ve). Figure 6.42 shows the four channels on the control PCB.

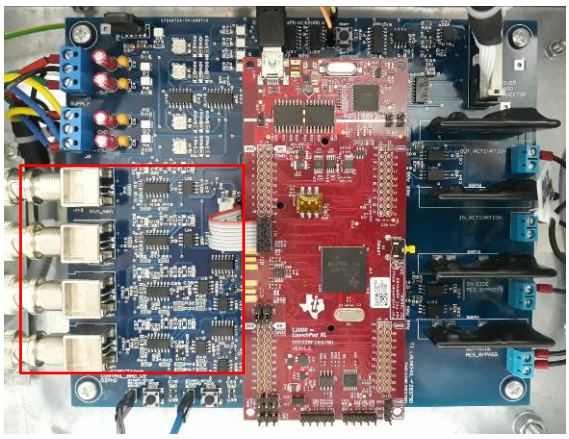

Figure 6.42: Bidirectional Converter Signal Preparation Circuit – Four Channels

The two channel used for the voltages can be divided in seven parts: the input circuit, a voltage follower/buffer, an Anti-Aliasing filter, a scaling/attenuation circuit, another voltage follower/buffer, an output voltage limiter, and a low pass filter.

The two channels used for the currents can be divided in eight parts: the input circuit, a voltage follower/buffer, an Anti-Aliasing filter, a scaling/attenuation circuit, a summing amplifier / level shifter, another voltage follower/buffer, an output voltage limiter, and a low pass filter. Figure 6.43 show a simplified circuit diagram representation of the signal preparation circuit.

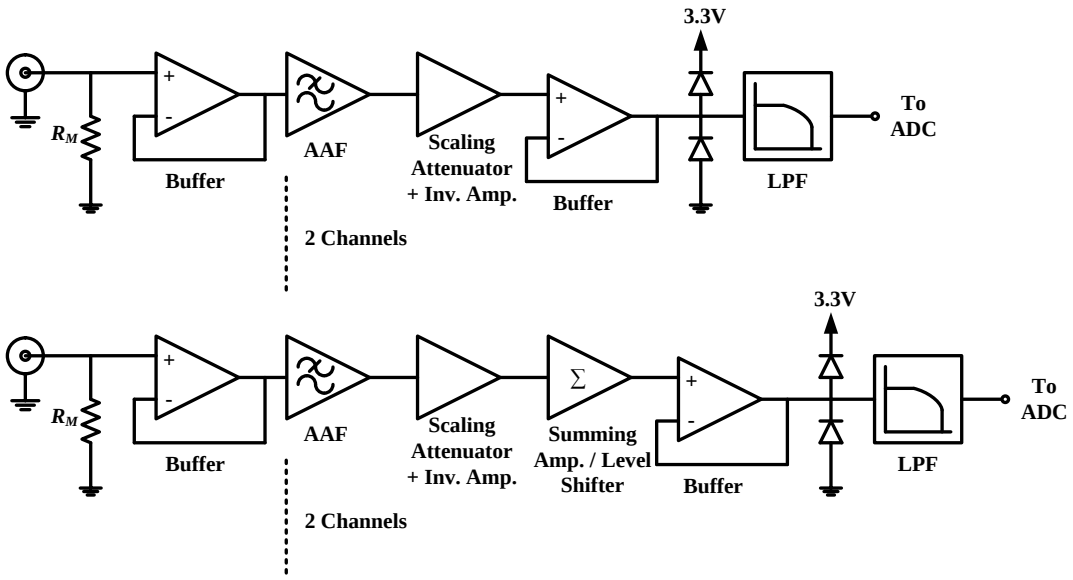

Figure 6.43: Simplified Circuit Diagram – Bidirectional Converter Signal Preparation Circuit

The input circuit receives the sensed signal from the transducer via a coax cable. The current signal from the secondary of the transducer is received and converted to a voltage signal by the secondary resistor (R_M). A voltage follower provides a buffer between the LEM transducer output and the following circuitry. This voltage follower is followed by an anti-aliasing filter, which is used to prevent aliasing of the sampled signals. The anti-aliasing filter implemented is a second order non-inverting active low pass filter using the Sallen-Key filter implementation and a Butterworth design. The anti-aliasing filter was designed for a cut-off frequency of 2.5kHz.

The ADC microcontroller inputs can handle voltages in the range of 0 up to 3V, however for better accuracy the voltage signal from the transducer secondary resistor (R_M) was set to be in the range 0 up to 5V for the two voltage sensing channels and in the range -5.915V up to 5.915V for the two current sensing channels. Therefore, the voltage signal needed scaling down to the appropriate range of 0 to 3V before sampling by the ADC.

For the channels used for the voltages, the scaling circuit scaled down the signal by a factor of two. However the scaled output signal is invert when compared to the input, therefore an inverting amplifier with a gain of 1 was included within the scaling circuit to invert the scaled voltage signal to the original polarity.

For the channels used for the currents, the scaling circuit scaled down the signal by four, and then followed by the inverting amplifier with a gain of 1 to obtain the original signal polarity. Since the signals for these channels represented bidirectional currents with both positive and negative values, the signal was shifted up to vary between 3V and 0. A summing amplifier / level shifter circuit was used to shift the signal by 1.5V.

For each four channels, another voltage follower buffers the signal from the rest of the circuit, before sampling takes place. This is followed by a voltage limiter circuit made up of two diodes, which provides protection for the microcontroller ADC inputs in the case that the voltage signal tries to go beyond 3V, keeping the microcontroller input in the range 0 to 3V. At the input of the microcontroller ADCs a low pass filter (LPF) with a cut-off frequency of approximately 100kHz was applied to clean the sensed signal from any noise which is picked up by the circuit.

6.1.2.2.4 Bidirectional Converter Protection Circuit

The protection circuit monitors against over-voltages and over-currents. The protection circuit monitors the DC-bus-side voltage, battery voltage, inductor current, and DC-bus-side current signals from the signal preparation circuits. If these exceed a certain limit, the protection circuit outputs a fault/trip signal to the microcontroller which switches of the PWM output thus switching off the converter IGBTs. The protection circuit also takes another input from the IGBT driver board. The IGBT driver board provides an error signal in case of IGBT short circuit or supply under-voltage. This error signal is monitored by the protection circuit, which outputs a fault signal to the microcontroller. Once a fault occurs, the protection circuit and the microcontroller stay in the tripped state until the fault is cleared, and both the protection circuit and the microcontroller are reset. Each type of fault is indicated by a red LED (five fault indicator LEDs). Figure 6.44 shows the protection circuit on the control PCB. Figure 6.45 show a simplified circuit diagram representation of the protection circuit.

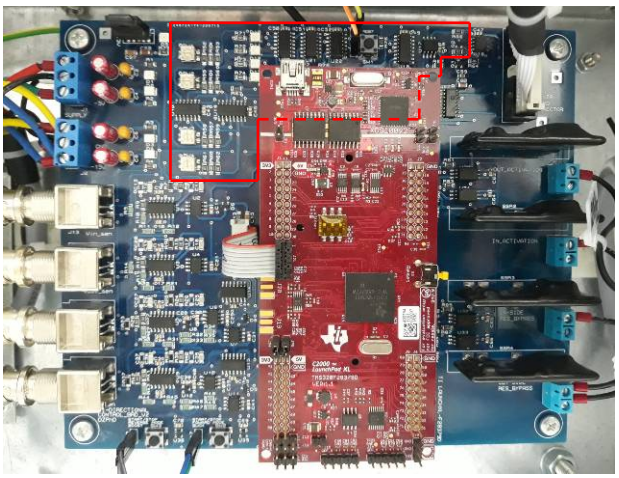

Figure 6.44: Bidirectional Converter Protection Circuit

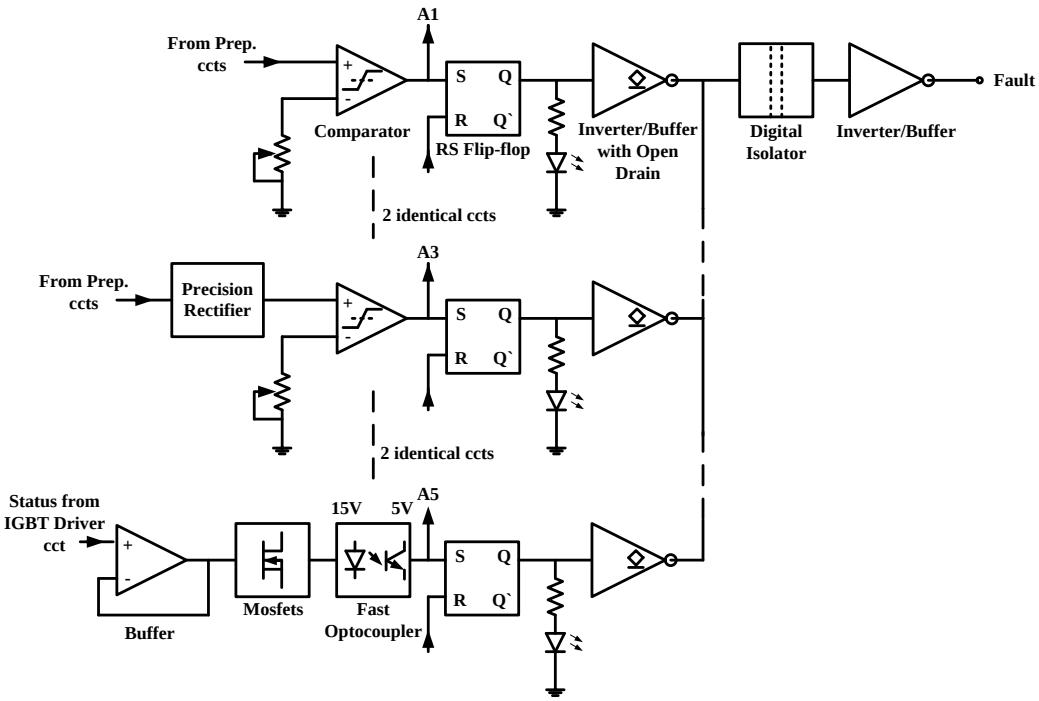

Figure 6.45: Simplified Circuit Diagram – Bidirectional Converter Protection Circuit

The four signals from within the signal preparation circuit, for the DC-bus-side voltage, battery voltage, inductor current, and DC-bus-side current are compared to set threshold values using comparator circuits, one for each signal.

The protection circuitry for the two signals representing the currents defer from the protection circuitry for the two signals representing the voltages. Being bidirectional currents and therefore resulting in bidirectional signals, a precision full wave rectifier for each signal representing the currents was used to rectify the signal, making it easier to compare with the threshold voltage. In the case of the two signals representing the voltages, being always positive signals, were fed directly to the comparators. The threshold values were set using 10kΩ preset potentiometers, and were set for a threshold voltage of 2.8V on the comparator input pin.

The comparator is followed by an RS flip-flop which holds the fault state until the fault is cleared and it is reset. The output of the each RS flip-flop switches on the indicator LED according to the type of fault and feeds to an inverter-buffer with open drain output. The four inverter-buffer outputs are connected in an OR configuration, with the common point fed to a digital isolator to have a 5V input level and provide a 3.3V output level. The 3.3V output level from the digital isolator is fed through an inverter-buffer to connect to the microcontroller pin.

The error signal from the IGBT driver board has a slightly different circuit since it is a 15V levelled signal. This error signal, being a low logic error, is fed to a voltage follower/buffer, followed by two N-channel MOSFET circuits. The first MOSFET inverts the signal, and the second MOSFET controls a high speed optocoupler with a 5V levelled output. The output of the optocoupler is connected to an RS flip-flop. The output of the RS flip-flop switches on the indicator LED to indicate a driver board error, and feeds to an inverter-buffer with open drain output. The inverter-buffer output is then connected with the other inverter-buffer outputs in OR configuration to continue the circuit as described above.

The RS flip-flops must not reset with a fault still present, so a logic circuit was designed to only permit reset when the fault is cleared. The RS flip-flop reset logic circuit uses standard AND, OR, and inverter gates. The RS flip-flops are reset by pressing a push button switch, which is shown within the highlighted area in Figure 6.44. A simplified circuit representation of the reset circuit is shown in Figure 6.19, since it is the same as the one used for the Buck converters.

6.1.2.2.5 Bidirectional Converter PWM Circuit

The PWM circuit connects the two PWM outputs from the microcontroller to the IGBT driver board. The PWM output signals from the microcontroller are at a 3.3V voltage level, while the IGBT driver board PWM inputs are at a 15V voltage level. A gate driver IC was used to perform the voltage level conversion, operating from the two 3.3V PWM inputs to provide a 15V PWM output signals. The gate driver IC used is the ADUM3223ARZ from Analog Devices. This gate driver IC has a disable feature input, which was connected to the fault signal coming from the protection circuit. In case of a fault the signal goes to logic high which puts the gate driver output to low. This is another layer of protection, in addition to the microcontroller PWM output going low in the case of a fault. The PWM circuit is indicated on Figure 6.46. Figure 6.47 shows a simplified circuit representation for the PWM circuit.

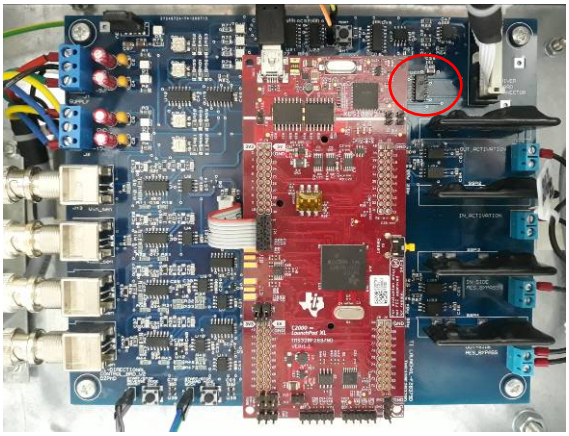

Figure 6.46: PWM Circuit for the Bidirectional Converter – Connects the two 3.3V PWM outputs from the microcontroller to the 15V PWM inputs of the IGBT driver PCB

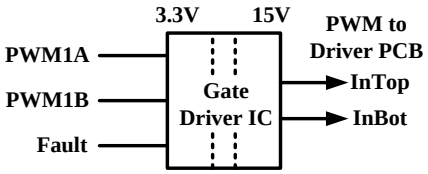

Figure 6.47: Simplified Circuit Diagram – PWM Circuit for the Bidirectional Converter

6.1.2.2.6 Bidirectional Converter Solid State Relay (SSR) Circuit

The solid state relay (SSR) circuit switches on/off the contactors as controlled by the microcontroller. The circuit contains four SSRs, one for each contactor in the Bidirectional converter. The switch control signal from the microcontroller at 3.3V is fed to an inverter-buffer with an open drain output, which switches a logic compatible optocoupler. The optocoupler provides a 5V output to switch on the SSR. This circuit is repeated for each of the four contactors. The SSR circuit is highlighted in Figure 6.48. Figure 6.49 show a simplified circuit representation of the SSR circuit.

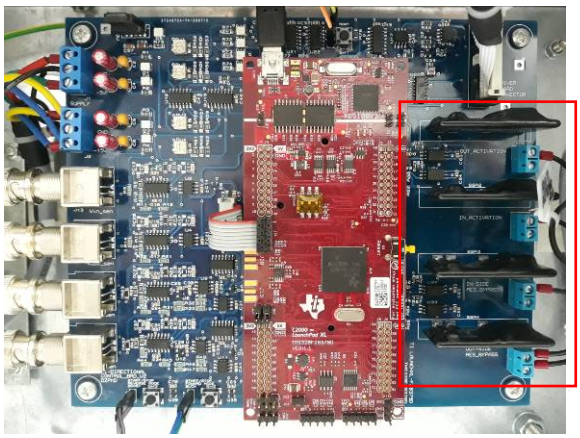

Figure 6.48: SSR Circuit for the Bidirectional Converter

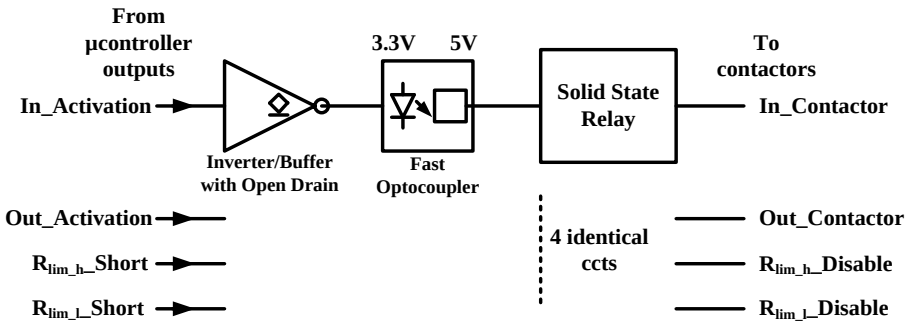

Figure 6.49: Simplified Circuit Diagram – SSR Circuit for the Bidirectional Converter

6.1.2.2.7 Other Features on the Bidirectional Converter PCBs

The voltage and current sensing PCBs operate from supplies of +15V, and -15V. The control PCB operates from supplies of +15V, -15V, +5V, and -5V. The supplies to these PCBs are provided by the Integrated Power Designs DC4-70-4005 power supply. All supply inputs on the PCBs are connected to a capacitor combination of a 1µF Electrolytic capacitor and a 1µF Tantalum capacitor, providing more stable and cleaner voltages from any noise that can be picked up by the supply wires. SMD LEDs were used as voltage presence indicators. Figure 6.50 and 6.51 show the location of these circuits on the control PCB and on the Voltage and Current Sensing PCBs, respectively.

The power supply for the voltage and current sensing PCBs and the control PCB takes its 48V input voltage from the DC-bus. This created the situation that the Bidirectional converter cannot operate on its own, supplying a load from the battery bank, if there is no voltage source already connected to the DC-bus. For this reason the power supply for the PCBs in the Bidirectional converter was wired to operate from two supply source options; from the 48V DC-bus as the main supply source and from a 48V auxiliary input source. The selection of input source for this power supply is made from a rotary switch, shown in Figure 6.52, with the source options labelled ‘m’ for main and ‘a’ for auxiliary. The auxiliary input connections are shown in Figure 6.53. By connecting an auxiliary 48V supply and selecting the auxiliary supply option, the Bidirectional converter can be operated on its own in load sharing/supplying (Boost) mode.

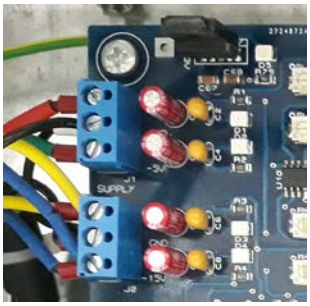

Figure 6.50: Supply Connectors on the Bidirectional Converter Control PCB

Figure 6.51: Supply Connector on the Bidirectional Converter Voltage and Current Sensing PCBs

Figure 6.52: Selector Rotary Switch for the 48V Input Source to the Power Supply for the PCBs in the Bidirectional Converter

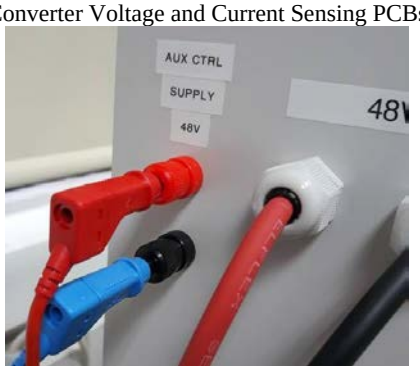

Figure 6.53: Auxiliary 48V Supply Connector for the PCBs' Power Supply

The TI microcontroller development board and subsequently some support circuitry needs a +3.3V supply. The +3.3V supply is achieved using a linear 3.3V LDO regulator BA033ST from ROHM. The regulator is supplied from the +5V supply. The +3.3V supply has an SMD LED as a supply indicator. The location of the regulator is shown in Figure 6.50.

The Bidirectional converter has two start/stop push button switches on the control PCB. One switch starts or stops the converter operating in battery charging (Buck) mode and another switch starts or stops the converter operating in load sharing/supplying (Boost) mode. Each start/stop push button switch has another switch with the same function mounted externally on the enclosure. Maxim MAX6816 switch debouncers were used to prevent spurious switching due to mechanical bouncing when pressing the switches. Figures 6.54 and 6.55 show the locations of these switches.

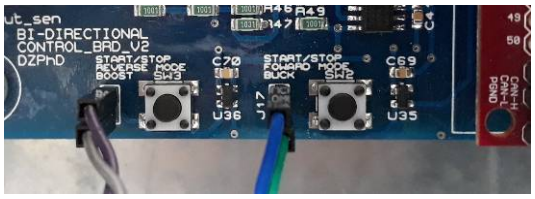

Figure 6.54: Start/Stop Push Button Switches on the Bidirectional Converter Control PCB

Figure 6.55: Panel Mount Start/Stop Push Button Switches on the Bidirectional Converter

6.1.2.2.8 IGBT Driver PCB

The IGBT driver PCB used for the Bidirectional converter is the Semikron Skyper 32 Pro R with its adapter board, shown in Figure 6.56. The IGBT driver PCB was mounted on the heatsink to be at the shortest distance possible to the IGBT module, to keep resistance, stray inductances, and interference in the cable between the driver board and the IGBTs, to the minimum possible.

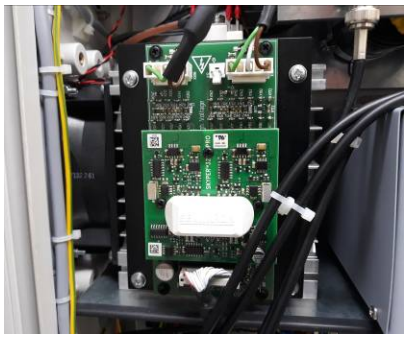

Figure 6.56: IGBT Driver PCB for the Bidirectional Converter

The Skyper 32 Pro R is a half bridge driver, thus it can drive two IGBTs. It has galvanic isolation between the primary and the secondary sides, which provides protection to the control board. The IGBT driver board operates with a supply voltage of +15V, which is supplied from the control PCB.

The Skyper 32 Pro R IGBT driver board operates with 15V PWM input signals. The IGBT driver board has a short circuit protection feature by measuring the V_{ce} of the IGBT. Another protection feature is under-voltage detection of the primary and secondary voltages. Both failure cases generate an error signal to the control PCB through an open collector transistor. This error signal from the driver board is monitored by the protection circuit which outputs a fault signal to the microcontroller

in case of a fault, as previously discussed in section 6.1.2.2.5 (Bidirectional Converter Protection Circuit).

The dead time between the switching of the two IGBTs can be adjusted on the IGBT driver board by connecting appropriate pads to ground according to the datasheet [45] [46]. The default setting of 3.3µs was selected as the dead time value for the IGBTs in the Bidirectional converter.

Figure 6.57 shows the location of the connector on the Bidirectional converter control PCB used to connect the control PCB with the IGBT driver board. Figure 6.58 shows the pinout of the IGBT driver board connector. A shielded ribbon cable was used to connect the two PCBs.

Figure 6.57: IGBT Driver Connector on the Bidirectional Converter Control PCB

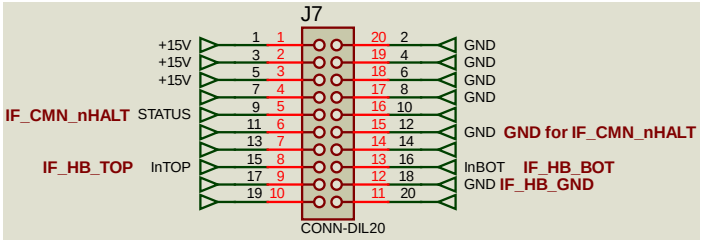

Figure 6.58: IGBT Driver Connector Pinout on the Bidirectional Converter Control PCB

6.1.2.2.9 Battery Bank

The battery bank connected to the Bidirectional converter consists of two 12V 120Ah batteries connected in series, obtaining a 24V 120Ah source. The batteries are PBQ L 120 – 12 VRLA AGM type. Figure 6.59 shows the battery bank.

Figure 6.59: 24V 120Ah Battery Bank

6.2 DC Microgrid Setup

The two Buck converters and the Bidirectional converter were connected to a common bus, together with a resistive load bank. The point of coupling was formed by two bus-bars. The converters and the resistive loads connect to the bus-bars using

Anderson Power connectors. This way the units are modular and can be easily connected or disconnected. The bus-bars forming the common DC-bus are shown in Figure 6.60 and the resistive load bank is shown in Figure 6.61.

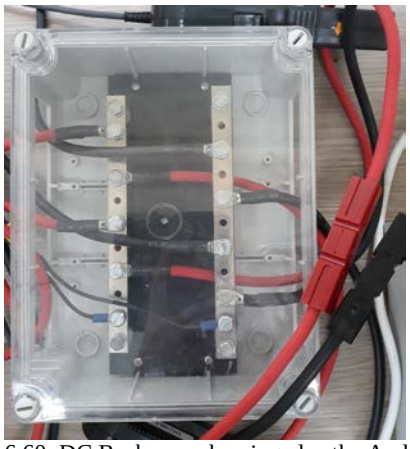

Figure 6.60: DC Busbars – showing also the Anderson Power Connectors used to connect up the converters and loads to the busbars

Figure 6.61: Resistive Load Bank

Figure 6.62 shows the DC microgrid setup while testing, including the two Buck converters, the Bidirectional converter, and the resistive load bank.

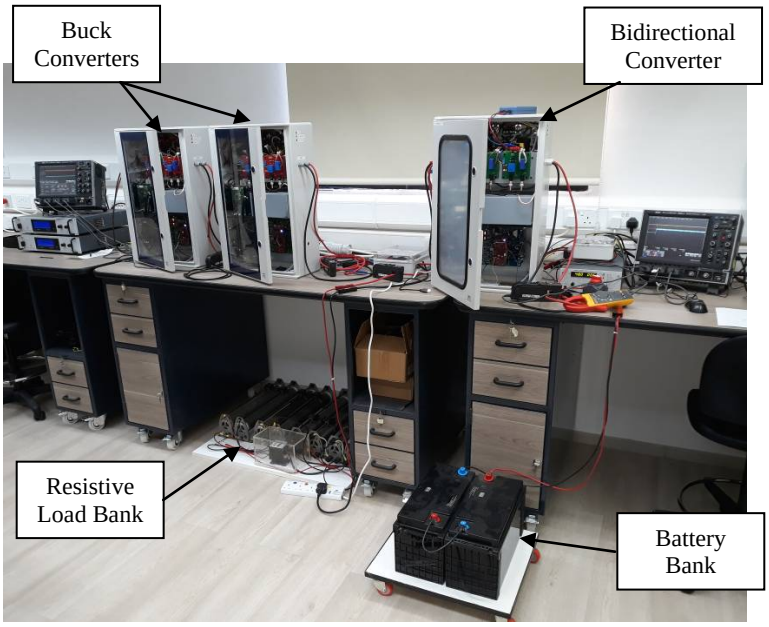

Figure 6.62: Experimental DC Microgrid Setup

6.3 Battery Management System

The battery management system (BMS) was designed to control the mode of operation of the Bidirectional converter within the DC microgrid. The hardware for the BMS consists of the main controller PCB and two current sensing PCBs.

The current sensing PCBs are similar to the ones shown in Figure 6.12. These are used to sense the resistive load current and the battery current. The main controller

PCB consists of two signal preparation channels as discussed in section 6.1.2.2.3, and the microcontroller with the development board. The signal preparation channels consist of one unidirectional channel for the load current sensed signal and one bidirectional channel for the battery current sensed signal. These two signals are sampled by the ADCs internal to the microcontroller, and are used by the BMS algorithm. The BMS algorithm was presented in Chapter 5, and is implemented using the TMS320F28379D microcontroller.

Figure 6.63 show the BMS controller board. The experimental setup for the BMS consists of both hardware and firmware implementation, followed by a testing phase. During this thesis the hardware part was partially completed, however more time was needed for the complete implementation and testing. Therefore, due to time restrictions the BMS was only implemented and tested by simulations. Eventually the idea is to build the proposed BMS system, which provides a simple but effective control of the Bidirectional converter.

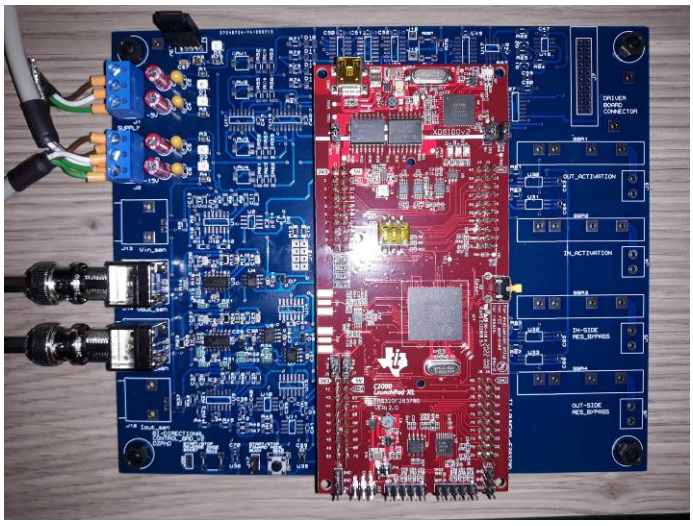

Figure 6.63: BMS Controller Board

6.4 Firmware Code Implementation

This section presents the microcontroller, the settings, and initialization functions for the different modules and features of the microcontroller used for the converters' control firmware.

The microcontroller used for the control of the converters is the TMS320F28379D with the LaunchPad LAUNCHXL-F28379D development board from Texas Instruments, shown in Figure 6.64. The TMS320F28379D is a dual core 32 bit

microcontroller which makes part of the C2000 Delfino microcontroller family. The debugging and programming of the microcontroller was carried out using the Code Composer Studio integrated development environment (IDE).

The TMS320F28379D microcontroller has several features which made it an ideal choice for this specific application. It features two 32 bit CPUs with an operation speed of up to 200MHz, two programmable control law accelerators (CLAs), 1MB of on-chip flash memory, 204kB of on-chip RAM, four analogue-to-digital converters (ADCs) with 12 bit or 16 bit modes, twenty four pulse width modulation (PWM) channels, a large number of configurable general purpose input/output pins, and a number of communication peripherals like UART and CAN amongst other features.

Figure 6.64: TI LaunchPad LAUNCHXL-F28379D Development Board with TMS320F28379D microcontroller

6.4.1 Firmware Flowchart

For the Buck converters the microcontroller is programmed to sample the input voltage, the output voltage, the inductor current, and the output current using the integrated ADCs. For the Bidirectional converter the microcontroller is programmed to sample the higher-voltage-side (DC-bus-side) voltage, the lower-voltage-side (battery-side) voltage, the inductor current, and the higher-voltage-side (DC-bus-side) current. The control law accelerator (CLA) directly reads the ADC results registers, and through a CLA task it carries out the controller algorithms, generating the duty cycle control value. Using the duty cycle control value the PWM register value is calculated, which is then passed to the PWM module. The PWM module then generates the PWM output waveform to control the switching of the IGBT/s. The firmware code flowchart is shown in Figure 6.65.

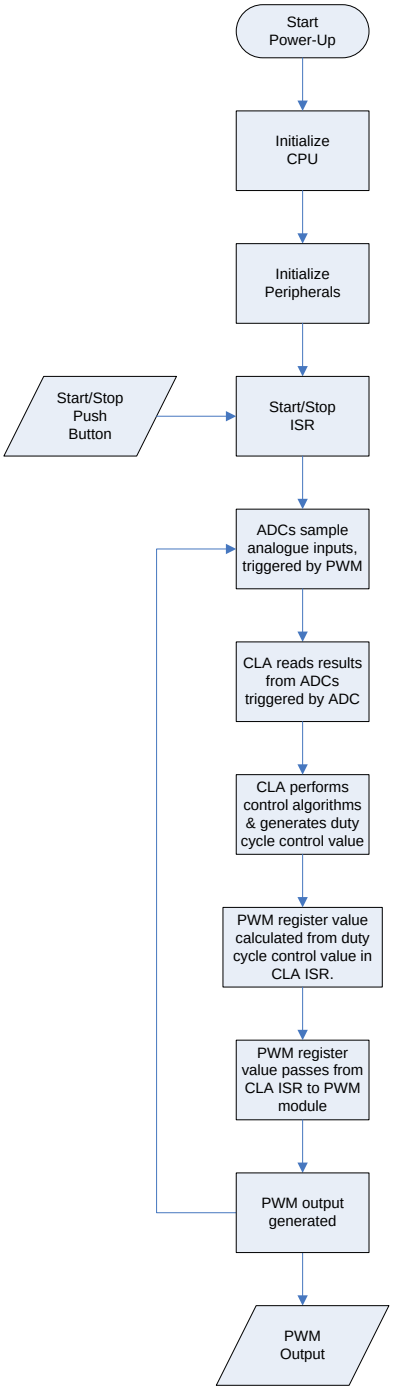

Figure 6.65: Firmware Code Flowchart

6.4.2 Device Configuration and System Initialization

At power-up the CPU gets initialized, which includes the initialization of the oscillator and PLL clock module, the watchdog timer, the general purpose digital input/outputs, and external interrupts. The flash memory is also initialized.

For the three converters only one core (CPU1) of the dual core microcontroller was used for the control system.

Four clock sources are available; two internal oscillators INTOSC1 and INTOSC2, an external oscillator XTAL, and an auxiliary clock input AUXCLKIN. For this firmware internal oscillator INTOSC2 was used. Using INTOSC2 and the PLL the system clock frequency was set to 200MHz.

The TMS320F28379D uses a multiplexing scheme to setup and enable input/output pins. The microcontroller pins can be set as general purpose inputs or outputs (GPIOs), and also as peripheral controlled pins (eg. PWM pins). The pins were set as shown in Table 6.3 for the Buck and Bidirectional converters.

Buck Converters		**Bidirectional Converter**	
GPIO0	PWM1A	GPIO0	PWM1A
		GPIO1	PWM1B
ADCINA0	Inductor Current I_L	ADCINA0	Inductor Current I_L
ADCINB2	Output Voltage V_o	ADCINB2	Output Voltage (Battery-Side) V_o (V_{bat})
ADCINC2	Output Current I_o	ADCINC2	Input Current (DC-Bus-Side) I_{in}
ADCIND0	Input Voltage V_{in}	ADCIND0	Input Voltage (DC-Bus-Side) V_{in}
GPIO32	Input – Fault Trip Zone TZ1	GPIO32	Input – Fault Trip Zone TZ1
GPIO34	Output – Flashing Red LED – Run Indicator	GPIO34	Output – Flashing Red LED – Run Indicator
GPIO31	Output – Blue LED – Status Indicator	GPIO31	Output – Blue LED – Status Indicator
GPIO67	Start/Stop ISR	GPIO67	Buck Mode Start/Stop ISR
		GPIO111	Boost Mode Start/Stop ISR
GPIO61	Output – Out Contactor	GPIO61	Output – Out (Battery-Side) Contactor
GPIO122	Output – R_{lim_in} Disable Contactor	GPIO122	Output – R_{lim_h} Disable Contactor
GPIO123	Output – In Contactor	GPIO123	Output – In (DC-Bus-Side) Contactor
GPIO124	Output – $R_{start\text{-}up}$ Disconnect Contactor	GPIO124	Output – R_{lim_l} Disable Contactor

Table 6.3: Microcontroller Input/Output Pins used for the Converters

The TMS320F28379D has 5 external interrupt signals: XINT1 up to XINT5. External interrupts were used to perform the start/stop function for the converters, using push buttons switches as covered in sections 6.1.1.2.8 and 6.1.2.2.8 for the Buck and Bidirectional converters, respectively. External interrupt XINT3 was used to perform the start/stop function whenever the Start/Stop push button is pressed on the Buck converter. External interrupt XINT3 was used to perform the Buck mode start/stop function whenever the Buck Mode Start/Stop push button is pressed on the Bidirectional converter, while external interrupt XINT4 was used to perform the Boost mode start/stop function whenever the Boost Mode Start/Stop push button is pressed. Each push button when pressed runs the function starting or stopping the converter, depending on its operating state. In the case of the Bidirectional converter, once it is running in a mode, it has to be stopped from that mode before pressing the other mode Start/Stop button, otherwise the converter remains operating in the original mode. This interlock was done as a safety feature.

6.4.3 Peripheral Configuration and Initialization

Following the CPU and flash initialization, peripherals like the ADCs, PWM, and CLA modules need to be initialized.

The TMS320F28379D has 4 independent ADC modules, configurable to 16 bit or 12 bit resolution. Each ADC module has a single sample and hold circuit. The ADC modules can be used together to have simultaneous sampling or independent operation. The ADC with 16 bit resolution operates in differential signal mode with a performance of 1.1 MSPS, providing 4.4 MSPS for the device. The ADC with 12 bit resolution operates in single signal mode with a performance of 3.5 MSPS, providing 14 MSPS for the device.

For all the converters, 4 ADC modules were used, operated with simultaneous sampling, with 12 bit resolution single signal mode. All 4 ADC modules were set to be triggered for start of conversion by PWM2 running at 10kHz.

For the Buck converters the 4 ADCs sample the input voltage V_{in}, the output voltage V_o, the inductor current i_L, and the output current i_o.

For the Bidirectional converter the 4 ADCs sample the higher-voltage-side (DC-bus-side) voltage V_H, the lower-voltage-side (battery-side) voltage V_L, the inductor current i_L, and the higher-voltage-side (DC-bus-side) current i_H.

The TMS320F28379D has two CLAs, one for each CPU. The Control Law Accelerator (CLA) is a 32 bit floating point math hardware accelerator which can perform real-time control algorithms, working in parallel to the CPU. Each CLA has 8 tasks, which can be triggered by peripherals and software.

In the Buck converters, CLA1 Task 1 was used to perform the control system, and CLA1 Task 8 was used to initialize variables. When the Start/Stop push button is pressed, the start/stop ISR (external interrupt XINT3) is entered, starting the converter. CLA1 Task 1 is triggered by ADC_A. The 4 ADC results are read by CLA1 where through Task 1 the control algorithm is performed. The duty cycle control value is calculated within the task. Then CLA1 generates an interrupt to the CPU, and in the CLA1_1 ISR the PWM register value is calculated according to the duty cycle control value. The PWM register value is then passed from the CLA1_1 ISR to the PWM module where the switching PWM1A output is generated. CLA1 Task 8 is triggered by code during the initialization procedure to initialize variables in

use by the CLA1 tasks, and also when entering the start/stop ISR (external interrupt XINT3) to stop the converter after pressing the Start/Stop push button, to reset the variables to their original values.

In the Bidirectional converter, CLA1 Task 1 and Task 2 were used to perform the control system, and CLA1 Task 8 was used to initialize variables. When the Buck Mode Start/Stop push button is pressed, the Buck mode start/stop ISR (external interrupt XINT3) is entered, starting the converter to operate in Buck mode. CLA1 Task 1 is triggered by ADC_A. The 4 ADC results are read by CLA1 where through Task 1 the control algorithm is performed. The duty cycle control value is calculated within the task. Then CLA1 generates an interrupt to the CPU, and in the CLA1_1 ISR the PWM register value is calculated according to the duty cycle control value. The PWM register value is then passed from the CLA1_1 ISR to the PWM module where the switching PWM1A and PWM1B outputs are generated. In the case when the Boost Mode Start/Stop push button is pressed, the Boost mode start/stop ISR (external interrupt XINT4) is entered, starting the converter to operate in Boost mode. CLA1 Task 2 is triggered by ADC_A. The 4 ADC results are read by CLA1 where through Task 2 the control algorithm is performed. The duty cycle control value is calculated within the task. Then CLA1 generates an interrupt to the CPU, and in the CLA1_2 ISR the PWM register value is calculated according to the duty cycle control value. The PWM register value is then passed from the CLA1_2 ISR to the PWM module where the switching PWM1A and PWM1B outputs are generated. CLA1 Task 8 is triggered by code during the initialization procedure to initialize variables in use by the CLA1 tasks, and also when entering the start/stop ISRs of both modes (external interrupt XINT3 and XINT4) to stop the converter after pressing the Start/Stop push buttons, to reset the variables to their original values.

The TMS320F28379D has 12 PWM modules, where each module has two PWM outputs EPWMxA and EPWMxB. For all converters, two PWM modules were used: ePWM1 to generate the switching PWM outputs and ePWM2 to trigger the ADCs. The input clock for the PWM modules was set to be 100MHz in all converters.

For the Buck converters, PWM1A was used to provide the PWM output waveform to the driver circuit to switch the IGBT. For the Bidirectional converter, PWM1A and PWM1B were used to provide the PWM output waveforms to the driver circuit to switch the two IGBTs. In all converters, the PWM switching frequency was set to

10kHz using the period register, and the time-base counter was set to up-count mode. The compare register CMPA was used to generate the switched PWM output. Therefore, the value calculated in the CLA1 ISRs, which was based on the duty cycle control value, was passed to the CMPA register. Figure 6.66 shows the PWM switching waveforms for the Buck and Bidirectional converters.

The Bidirectional converter, having two IGBTs, was the only converter which required dead time. However, the dead time through code was disabled, since the dead time value was set through hardware from the IGBT driver board.

In all converters the fault signal generated by the protection circuitry, covered in subsections 6.1.1.2.4 and 6.1.2.2.4, was used as an external trip signal, connected to trip zone signal TZ1 which was set as a one shot trip source. The PWM output pins were set to be forced low in case of a trip.

As stated earlier the PWM module ePWM2 was used to trigger the ADCs, at a frequency of 10kHz set by the period register, and the time-base counter was set to up-count mode. These settings were set the same for all converters.

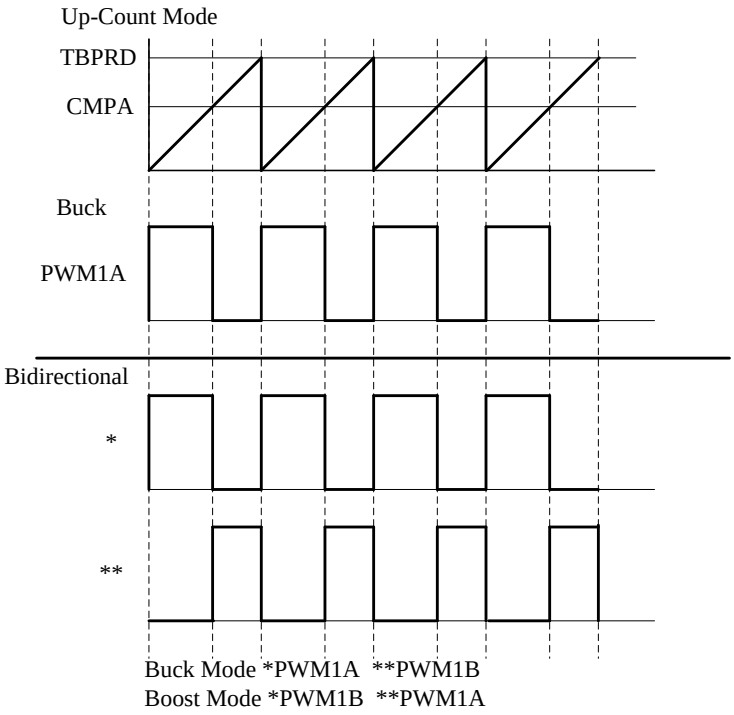

Figure 6.66: PWM Switching Waveform – Up-Count Mode

6.5 Conclusion

This chapter covered in detail the hardware setup used for the experimental laboratory-based DC Microgrid. The hardware and the firmware of the converters were discussed. The various parts making up the converters were divided into sections and explained. The firmware was also explained and the settings discussed.

The experimental DC microgrid setup consists of two 2.5kW Buck converters used as energy source converters and a 1.5kW Bidirectional converter for a battery storage system, together with resistive loads. The two Buck converters operate from an input source voltage in the range of 70V – 120V, and provide an output voltage of 48V. The Buck converters were designed for a recommended input voltage of 100V. The Bidirectional converter operates between 24V on the battery-bank-side and 48V on the DC-bus-side. The DC-bus voltage for the DC microgrid was set to 48V. The battery bank connected to the Bidirectional converter consists of two 12V 120Ah batteries connected in series, obtaining a 24V 120Ah source.

Each converter was housed within its own enclosure so as to be operated as standalone units, and to make it easier to add additional units and expand the DC microgrid setup. This leaves the setup open to further development and expansion. Each converter was divided in two parts: the power stage and the sensing and control circuitry. The power stage includes the power converter itself consisting of the switching module, the inductor, and the input/output capacitors, and also includes the contactors, the inrush current limiting power resistors, the start-up power resistor, and the circuit breakers. The sensing and control circuitry includes the current and voltage sensing circuit PCBs, the control circuit PCB, the IGBT driver PCB, and the power supply units for the circuitry.

The control system for each converter was applied using the TI microcontroller TMS320F28379D. The modules and features used within the microcontroller were discussed, including the setting up of the modules and sub-modules.

The hardware for the battery management system (BMS) was also presented. The BMS provides high level control to the Bidirectional converter, by controlling the mode of operation of the Bidirectional converter, selecting between load supplying/sharing mode and battery charging mode. The hardware for the BMS consists of the main controller PCB and two current sensing PCBs. The sensing PCBs utilize current transducers to sense the load current and the battery current, which are used by the BMS algorithm. The BMS algorithm is implemented using the

TMS320F28379D microcontroller. The BMS implementation consists in both hardware and firmware which take time to implement. During this thesis the hardware part was partially completed, however more time was needed for the complete implementation and testing. Therefore, due to time restrictions the proposed BMS was only implemented and tested by simulations. However, the BMS shall be built as further research, providing a setup that is open for further development and expansion.

Chapter 7 Simulations and Experimental Tests of the Paralleled Converters using Droop Control

This chapter presents the simulations and experimental results obtained when the converters were operated in paralleled, sharing a common resistive load using droop control.

The designed converters were modelled in Simulink/Matlab to test and simulate their functionality and operation. The Buck and Bidirectional converters were initially simulated on their own to test the operation of their respective control system. These simulations and the results are presented and discussed in Appendix A. Experimental tests were performed individually on the two Buck converters and the Bidirectional converter to test their operation. The experimental results obtained from these tests are presented in Appendix B.

Once it was confirmed that the converters were operating successfully, simulations and experimental tests were performed with converters connected in parallel, while sharing a common resistive load using droop control. These simulations and experimental tests were performed to test the operation of the converters using three different droop control methods:

- V-I droop,
- I-V droop, and
- the proposed Combined Voltage and Droop (CVD) method.

Additional simulations were then performed to test the voltage restoration loop.

7.1 Simulations of Paralleled Converters using Droop Control

The droop method was used to connect the converters in parallel while sharing a common resistive load. Simulations were performed to test the paralleled converters with three different droop control methods: V-I droop, I-V droop, and CVD. The simulations tested the load sharing performance during converter start-ups and during load changes. This section presents the results obtained from these simulations. The simulation model consisted of two converters connected in parallel as shown in Figure 7.1. Simulations were performed in the continuous time domain and in the discrete time domain. Having obtained similar results in both domains, only the simulations in the continuous time domain are presented here. Table 7.1 lists the parameters used in the Buck and Bidirectional converters simulation model.

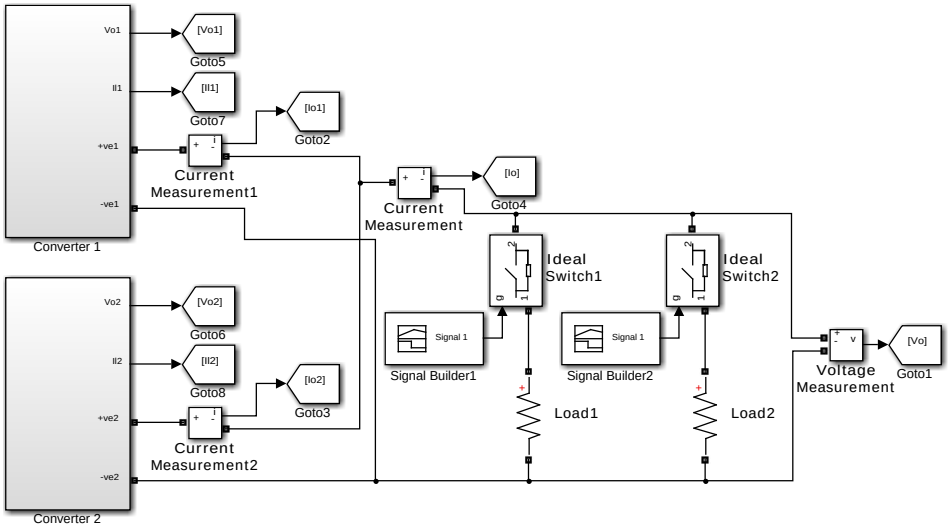

Figure 7.1: Paralleled Converters – Load Sharing

Buck Converters		Bidirectional Converter	
Input Voltage V_{in}	100V	Lower-Side Voltage V_L	24V
Output Voltage V_o	48V	Higher-Side Voltage V_H	48V
Switching Frequency f_s	10kHz	Switching Frequency f_s	10kHz
Inductor L	479µH	Inductor L	192µH
Inductor Resistance R_L	2mΩ	Inductor Resistance R_L	2mΩ
Capacitor C	270µF	Lower-voltage-side Capacitor C_L	680µF
ESR R_c	2.1mΩ	Lower-voltage-side Capacitor ESR R_{cL}	0.03Ω
Current PI K_P	1.14	Higher-voltage-side Capacitor C_H	1500µF
Current PI K_I	880	Higher-voltage-side Capacitor ESR R_{cH}	0.03Ω
Voltage PI K_P	0.064	Buck-Mode Current PI K_P	0.76
Voltage PI K_I	4.6	Buck-Mode Current PI K_I	871
		Boost-Mode Current PI K_P	0.64
		Boost-Mode Current PI K_I	378
		Boost-Mode Voltage PI K_P	0.72
		Boost-Mode Voltage PI K_I	80

Table 7.1: Buck and Bidirectional Converters - Simulation Parameters

7.1.1 V-I Droop Simulations

7.1.1.1 Two Paralleled Buck Converters with V-I Droop

The first simulation with V-I droop was performed with two paralleled Buck converters to test load sharing between the converters. The control system of the Buck converters consisted in nested current and voltage PI controllers with the V-I droop loop, as shown in Figure 7.2. The droop resistance R_d was set to 0.092Ω for both Buck converters to obtain equal load sharing (see Chapter 5 subsection 5.4.1.3). The reference voltage for the voltage loop was set to 48V.

Initially at t = 0s only one converter was switched on, supplying a resistive load of 0.92Ω (52.1A at 48V for 2.5kW). At t = 3s the second converter was connected in parallel with the first converter, and started sharing the resistive load. When the two

Buck converters were operating in parallel, the droop loop of each converter adjusted the output voltage of each converter to obtain load current sharing. At t = 25s a load change occurred, decreasing the total resistive load to 0.8Ω, causing a 15.2% change in load current. At t = 40s the resistive load was changed back to 0.92Ω.

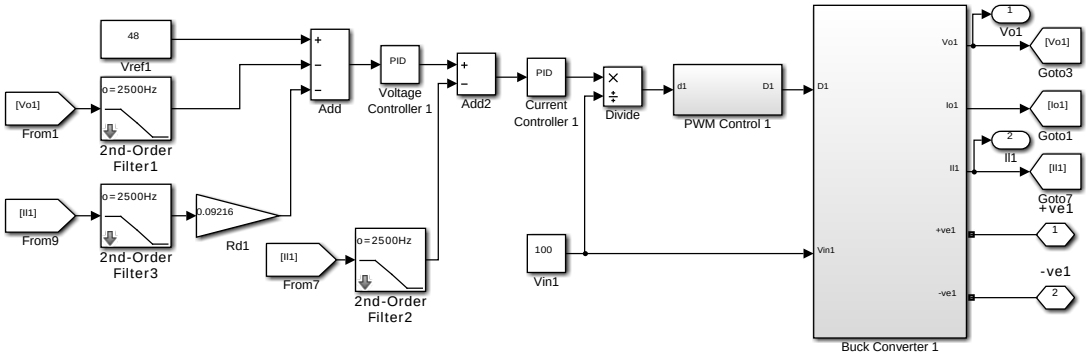

Figure 7.2: Buck Converter with Current and Voltage PI Controllers including V-I Droop in s-Domain

Figures 7.3 to 7.6 show the results from the simulation performed with the paralleled Buck converters using V-I droop control. Figure 7.3 shows the output current from each converter (I_{o1} and I_{o2}) and the total output/load current (I_o), during start-up and during the load sharing process. Figure 7.4 shows the output voltage (V_o) during start-up and during the load sharing process, while Figures 7.5 and 7.6 show the output currents and output voltage, respectively, for the complete simulation with load changes between 0.92Ω and 0.8Ω.

Load sharing between the two Buck converters took approximately 13s to reach steady state, as can be noted from Figure 7.3. Due to droop the total output voltage increased from approximately 43.64V to 45.71V, thus increasing the total output current from approximately 47.35A to 49.6A, as can be observed from Figures 7.3 and 7.4. As stated earlier, the droop resistance R_d was set to 0.092Ω for both converters. Increasing the droop resistance will make sharing faster, however it would increase the output voltage deviation from the desired value. Therefore, a compromise must be found between sharing speed and output voltage regulation. The 15.2% step load changes at t = 25s and t = 40s caused a dip of approximately 5V and a swell of approximately 5.4V in the output voltage, as can be observed from Figure 7.6. These disturbances are caused by the slowness in response of the voltage control loop. The disturbances in the output voltage also affected the output current, causing spikes at the load change transitions, as can be observed from Figure 7.5. In fact the larger the load change the larger the disturbances, as can be observed from the following simulations.

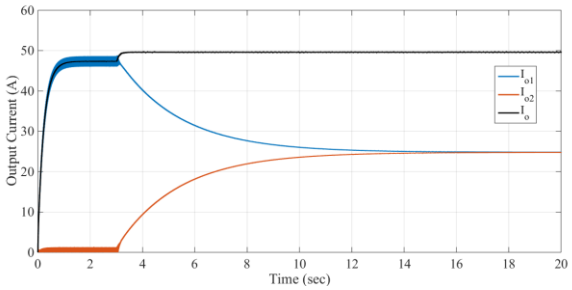

Figure 7.3: Output Currents – Load Sharing – V-I Droop – Two Buck Converters

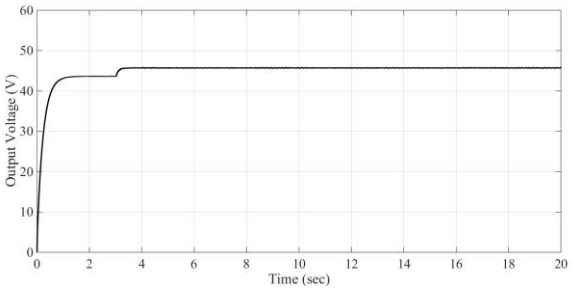

Figure 7.4: Output Voltage – Load Sharing – V-I Droop – Two Buck Converters

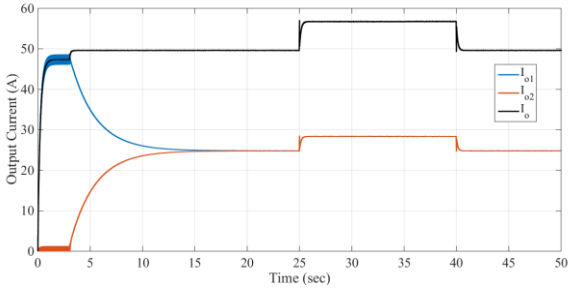

Figure 7.5: Output Currents – V-I Droop – Two Buck Converters – Load Changes 0.92Ω - 0.8Ω

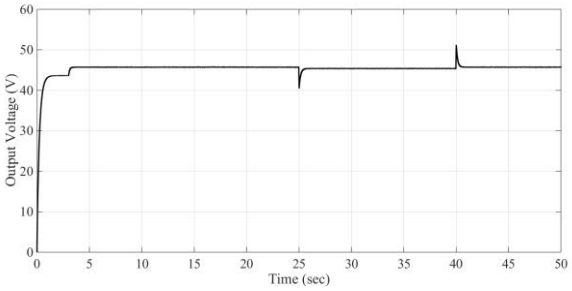

Figure 7.6: Output Voltage – V-I Droop – Two Buck Converters – Load Changes 0.92Ω - 0.8Ω

Another simulation was performed using the same model and following the same procedure, however with different resistive load values. The resistive load at t = 0s was set to 2.4Ω, at t = 25s it was decreased to 1.2Ω, and at t = 40s the resistive load was changed back to 2.4Ω, to simulate a larger load step change of 100%.

Figures 7.7 and 7.10 show the output currents and output voltage, respectively, for the complete simulation with the load step changes of 2.4Ω to 1.2Ω, and vice-versa. In this case the dip at t = 25s is of approximately 16V and the swell at t = 40s is of approximately 29V, caused by the 100% step change in load. As stated earlier, these disturbances are the result of the dynamics of the system, and the slow response of the voltage control loop. There is a limit on the bandwidth of the outer voltage control loop, since it has to be slower than the inner current control loop. The bandwidth of the voltage control loop is also limited by the anti-aliasing filter in the output voltage feedback path. The upward spikes can be mitigated by introducing anti-windup on the PI controllers. This same simulation was repeated with anti-windup introduced and the results are shown in Figures 7.9 and 7.10. The anti-windup saturation limits were set to 50V and 56A for the current and voltage PI controllers, respectively.

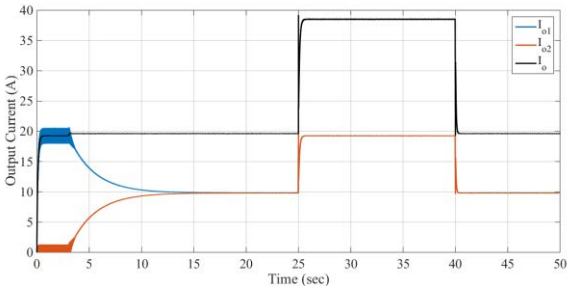

Figure 7.7: Output Currents – V-I Droop – Two Buck Converters – Load Changes 2.4Ω – 1.2Ω

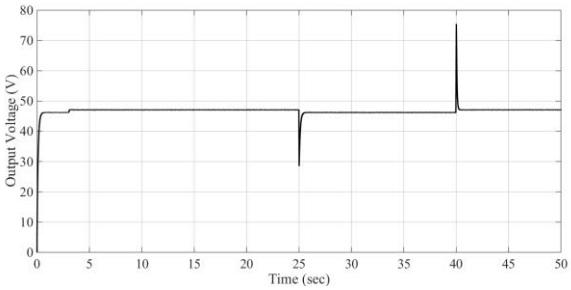

Figure 7.8: Output Voltage – V-I Droop – Two Buck Converters – Load Changes 2.4Ω – 1.2Ω

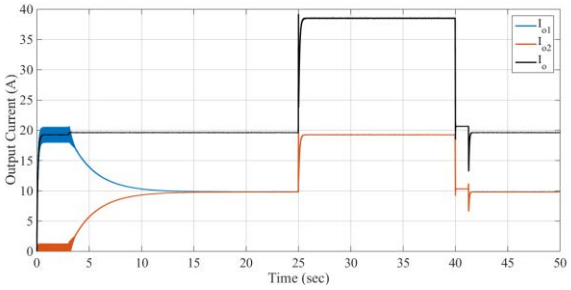

Figure 7.9: Output Currents – V-I Droop – Two Buck Converters – Load Changes 2.4Ω – 1.2Ω with Anti-Windup

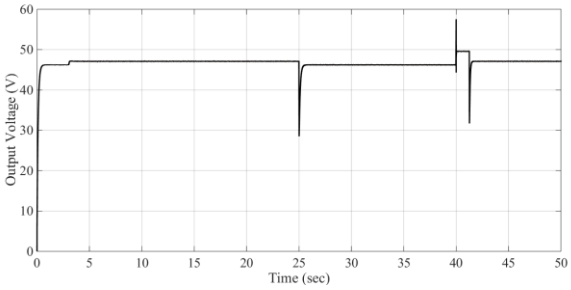

Figure 7.10: Output Voltage – V-I Droop – Two Buck Converters – Load Changes 2.4Ω – 1.2Ω with Anti-Windup

7.1.1.2 Paralleled Buck and Bidirectional Converters with V-I Droop

Another simulation with the V-I droop method was performed with the Buck converter connected in parallel with the Bidirectional converter operating as a Boost converter, to test load sharing between them. The control system for both converters consisted in nested current and voltage PI controllers with the V-I droop loop. The droop resistance R_d was set to 0.092Ω for both converters to obtain equal load sharing (see Chapter 5 subsection 5.4.1.3). The reference voltage for the voltage loop was set to 48V. Figure 7.11 shows the control system of the Bidirectional converter. The control system of the Buck converter remained as shown in Figure 7.1. The difference between the control systems for the Buck and Bidirectional converters is the current fed-back for the droop loop; for the Buck converter the inductor current I_L was fed-back, while for the Bidirectional converter the output current I_o was fed-back.

The simulation followed a similar profile as the one described in subsection 7.3.1.1, starting at t = 0s with only the Buck converter supplying a load resistance of 0.92Ω. At t = 3s the Bidirectional converter was connected in parallel, and started sharing the resistive load. At t = 25s the resistive load was decreased to 0.8Ω, causing a 15.2% change in load current, and at t = 40s the resistive load was changed back to 0.92Ω.

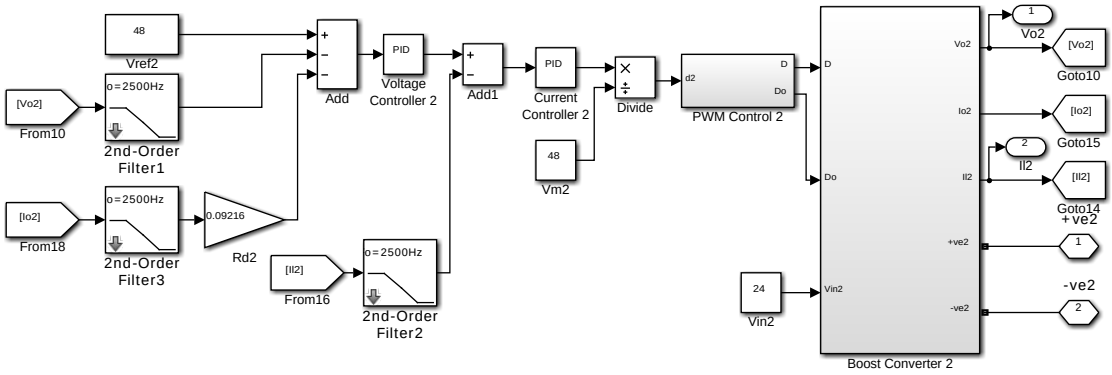

Figure 7.11: Bidirectional Converter (Boost Mode) with Current and Voltage PI Controllers including V-I Droop in s-Domain

Figures 7.12 to 7.15 show the results from the simulation performed with the paralleled Buck and Bidirectional (Boost) converters using V-I droop control. Figure 7.12 shows the output current from the Buck converter (I_{o1}), the Bidirectional converter (I_{o2}), and the total output/load current (I_o), during start-up and during the load sharing process. Figure 7.13 shows the output voltage (V_o) during start-up and during the load sharing process, while Figures 7.14 and 7.15 show the output currents and output voltage, respectively, for the complete simulation with load changes between 0.92Ω and 0.8Ω.

In this case the response obtained from the converters is different from the response obtained from the previous simulations, due to the different dynamics and control loop bandwidths of the converters. The current and voltage closed loop bandwidths of the control system in the Bidirectional converter were designed faster than the Buck converter control loops (see Chapter 5), thus the faster response, as can be observed at t = 25s and t = 40s. The load sharing transition took approximately 10s for the two converters to reach steady state, as can be observed from Figure 7.12. Due to droop the total output voltage increased from approximately 43.64V to 45.71V, thus increasing the total output current from approximately 47.35A to 49.6A, as can be observed from Figures 7.12 and 7.13. The ripple in the two converters' output currents and voltage increased when the two converters were operating in parallel. This resulted due to changes in the dynamics of the system, where the plant seen by each control system is practically changed with every converter connected in parallel.

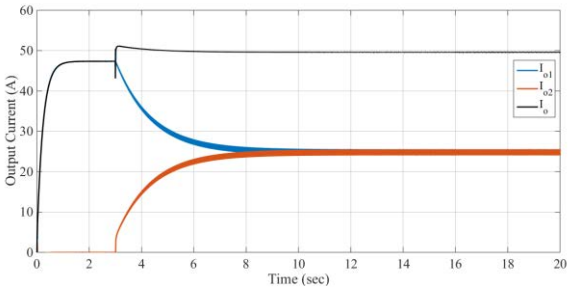

Figure 7.12: Output Currents – Load Sharing – V-I Droop – Buck and Bidirectional Converters

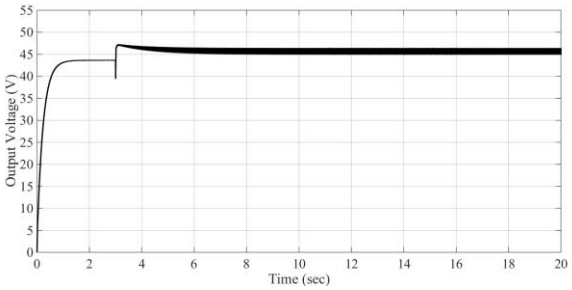

Figure 7.13: Output Voltage – Load Sharing – V-I Droop – Buck and Bidirectional Converters

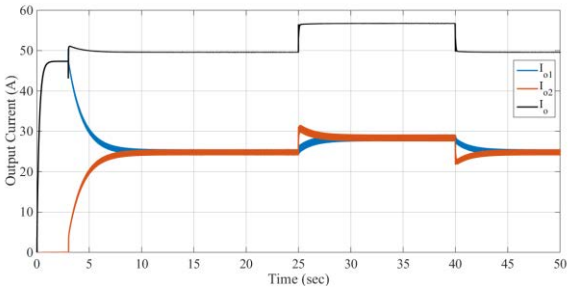

Figure 7.14: Output Currents – V-I Droop – Buck and Bidirectional Converters – Load Changes 0.92Ω - 0.8Ω

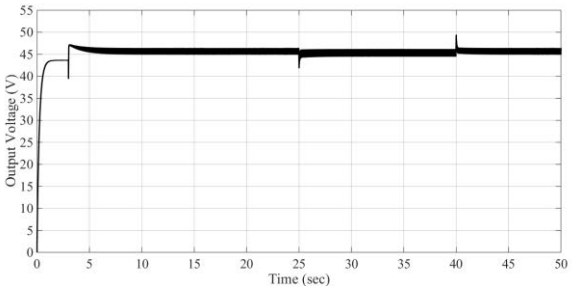

Figure 7.15: Output Voltage – V-I Droop – Buck and Bidirectional Converters – Load Changes 0.92Ω - 0.8Ω

The simulation was repeated using different resistive load values, to simulate the paralleled converters while undergoing a larger load step change. In this case, at t = 0s the resistive load was set to 2.4Ω, at t = 25s it was decreased to 1.2Ω, and at t = 40s the resistive load was changed back to 2.4Ω, simulating a step change in load of 100%. Figures 7.16 and 7.17 show the output currents and output voltage, respectively, for the complete simulation with load changes between 2.4Ω and 1.2Ω, and vice-versa. One can note that the spikes generated at the load step changes are smaller than those generated by the two paralleled Buck converter with the same load change shown in Figures 7.7 and 7.8. In this case the dip at t = 25s is of approximately 9.7V and the swell at t = 40s is of approximately 15.3V. This reduction is due to the Bidirectional converter having a faster response time than the Buck converters, thus having better ability to recover faster after a load change.

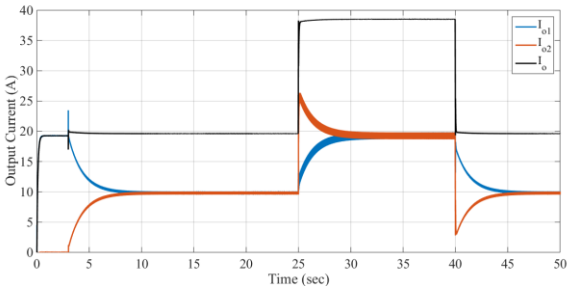

Figure 7.16: Output Currents – V-I Droop – Buck and Bidirectional Converters – Load Changes 2.4Ω – 1.2Ω

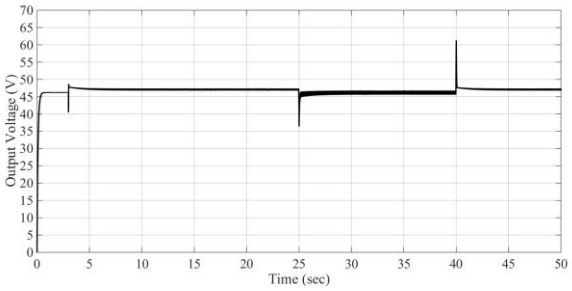

Figure 7.17: Output Voltage – V-I Droop – Buck and Bidirectional Converters – Load Changes 2.4Ω – 1.2Ω

7.1.2 I-V Droop Simulations

7.1.2.1 Two Paralleled Buck Converters with I-V Droop

Simulations were also performed with I-V droop, using two paralleled Buck converters, to test load sharing between the converters. Figure 7.18 shows the control system of one of the Buck converters with the I-V droop multiplier and the current PI controller. The droop multiplier term *k* was set to 1/0.092 for both Buck converters to obtain equal load sharing (see Chapter 5 subsection 5.4.1.4). The reference voltage for the voltage loop was set to 48V.

It should be noted that since the outer voltage loop has a bandwidth of approximately 2.42kHz, which is comparable to the 2.5kHz anti-aliasing filter, this filter in the output voltage feedback path had to be removed. If the filter is not removed it interferes with the voltage loop, making the system unstable. This provides challenges in practice, since the anti-aliasing filter is needed before sampling the output voltage when the control system is implemented using a microcontroller. This stability issue can be observed also in the experimental results presented in subsection 7.3.2.

The simulation carried out in this section followed the same profile used for V-I droop. Initially at t = 0s only one converter was switched on, supplying a resistive load of 0.92Ω (52.1A at 48V for 2.5kW). At t = 3s the second converter was connected in parallel with the first converter, and started sharing the resistive load. At t = 25s the load resistance was changed to 0.8Ω, causing a 15.2% change in load current. At t = 40s the resistive load was changed back to 0.92Ω.

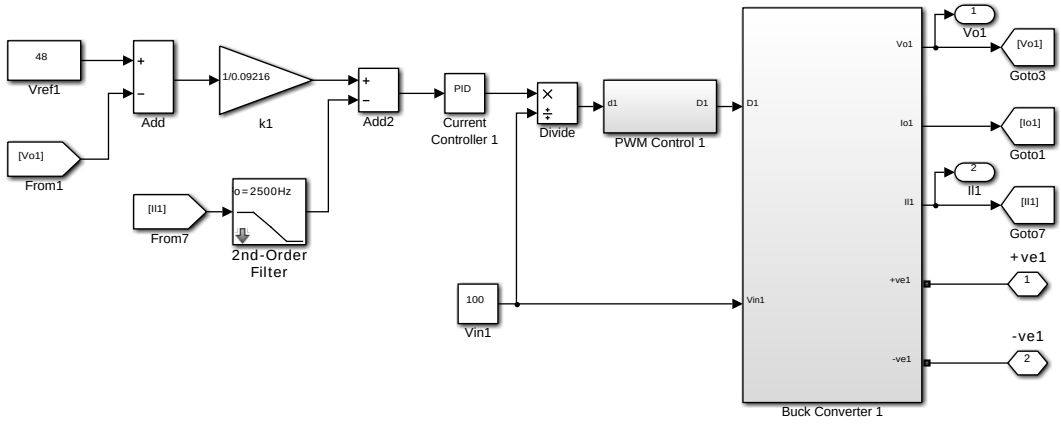

Figure 7.18: Buck Converter with Current PI Controller including I-V Droop in s-Domain

Figures 7.19 to 7.24 show the results from the simulation performed with the paralleled Buck converters using I-V droop control. Figure 7.19 shows the output current from each converter (I_{o1} and I_{o2}) and the total output/load current (I_o), during start-up and during the load sharing process. Figure 7.20 shows the output

voltage (V_o) during start-up and during the load sharing process, while Figures 7.21 and 7.22 show the output currents and output voltage, during the complete simulation, including the load changes between 0.92Ω and 0.8Ω.

Due to droop the total output voltage increased from approximately 43.64V to 45.71V, as can be seen in Figure 7.20, while the total output current increased from approximately 47.35A to 49.6A, as can be observed from Figure 7.19.

In this case, the disturbance in voltage during load changes is minimal, due to the high bandwidth of the voltage control loop, as can be observed from Figures 7.21 and 7.22. The voltage controller in this case is effectively a proportional gain term equal to the droop multiplier *k* (1/0.092), therefore the closed loop bandwidth of the voltage loop, being approximately 2.42kHz, depends on this droop multiplier. However, large oscillations during start-up resulted due to the large proportional gain term (~10.85). These oscillations can be seen in Figures 7.23 and 7.24 for the currents and voltage, respectively. These oscillations were mitigated by the proposed CVD droop method.

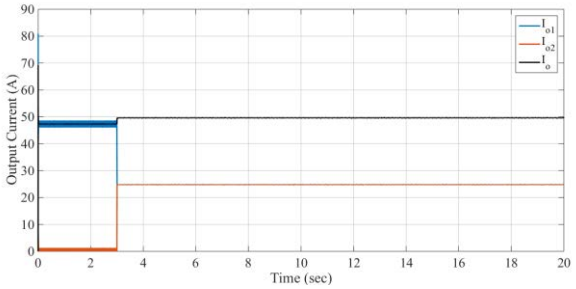

Figure 7.19: Output Currents – Load Sharing – I-V Droop – Two Buck Converters

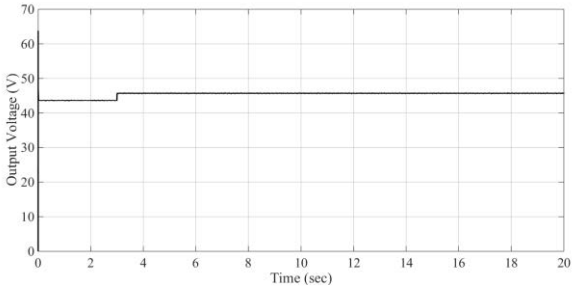

Figure 7.20: Output Voltage – Load Sharing – I-V Droop – Two Buck Converters

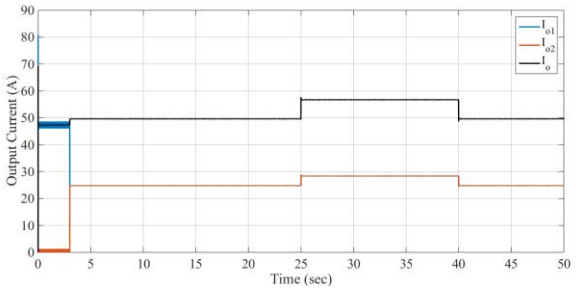

Figure 7.21: Output Currents – I-V Droop – Two Buck Converters – Load Changes 0.92Ω - 0.8Ω

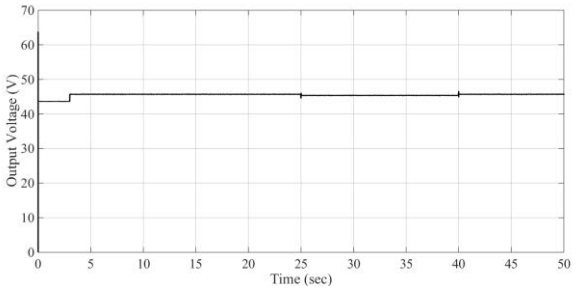

Figure 7.22: Output Voltage – I-V Droop – Two Buck Converters – Load Changes 0.92Ω - 0.8Ω

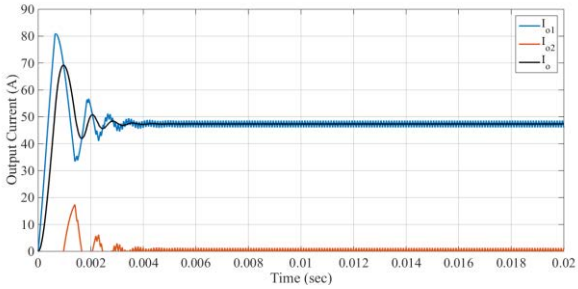

Figure 7.23: Output Currents – Start-Up Oscillations – I-V Droop – Two Buck Converters

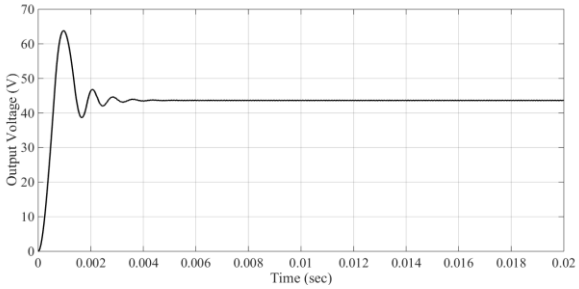

Figure 7.24: Output Voltage – Start-Up Oscillations – I-V Droop – Two Buck Converters

7.1.3 Combined Voltage and Droop Method Simulations

7.1.3.1 Two Paralleled Buck Converters with CVD

Simulations were also performed with the combined voltage and droop (CVD) method, using two paralleled Buck converters, to test load sharing between them. Figure 7.25 shows the control system of one of the Buck converters with the CVD controller and the current PI controller. The gain term *k* was set to 1/0.092 for both Buck converters to obtain equal load sharing (see Chapter 5 subsection 5.4.1.5). The reference voltage for the voltage loop was set to 48V.

Initially at t = 0s only one converter was switched on, supplying a resistive load of 0.92Ω (52.1A at 48V for 2.5kW). At t = 3s the second converter was connected in parallel with the first converter, and started sharing the resistive load. At t = 25s the load resistance was changed to 0.8Ω, causing a 15.2% change in load current. At t = 40s the resistive load was changed back to 0.92Ω.

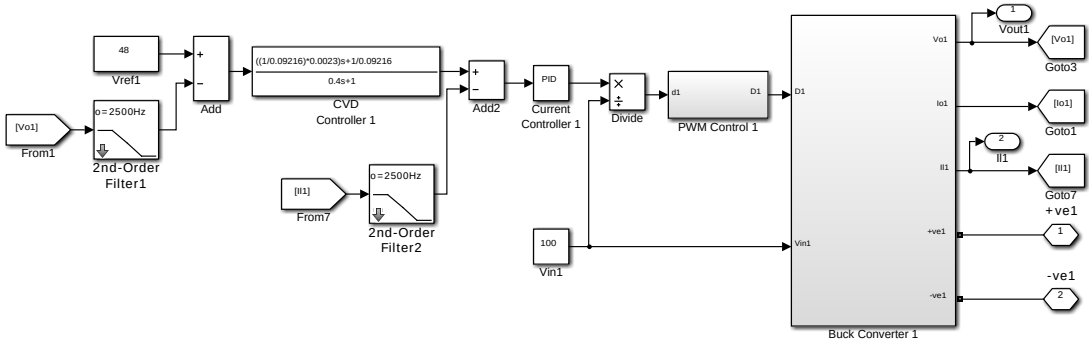

Figure 7.25: Buck Converter with Current PI Controller and CVD in s-Domain

Figures 7.26 to 7.31 show the results from the simulation performed with the paralleled Buck converters using the CVD method. Figure 7.26 shows the output current from each converter (I_{o1} and I_{o2}) and the total output/load current (I_o), during start-up and during the load sharing process. Figure 7.27 shows the output voltage (V_o) during start-up and during the load sharing process, while Figures 7.28 and 7.29 show the output currents and output voltage, during the complete simulation, including the load changes between 0.92Ω and 0.8Ω.

The load sharing transition took approximately 3s for the two Buck converters to reach steady state, as can be noted from Figure 7.26. Due to droop the total output voltage increased from approximately 43.64V to 45.71V, as can be seen in Figure 7.27, while the total output current increased from approximately 47.35A to 49.6A, as can be observed from Figure 7.26. From the simulation results obtained using CVD it can be observed that no oscillations occurred during start-up, as shown in Figures 7.30 and 7.31. Figures 7.30 and 7.31 show the output currents and output

voltage, respectively. This is due to the ability to adjust the bandwidth of the voltage control loop using the pole and zero of the CVD controller (see Chapter 5 subsection 5.2.3).

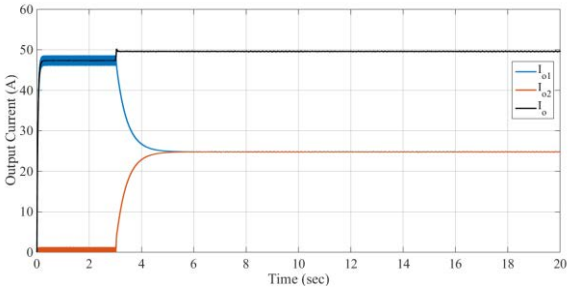

Figure 7.26: Output Currents – Load Sharing – CVD – Two Buck Converters

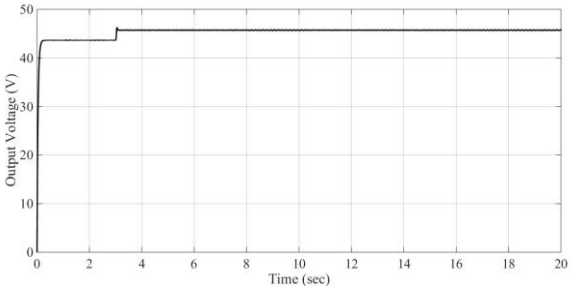

Figure 7.27: Output Voltage – Load Sharing – CVD – Two Buck Converters

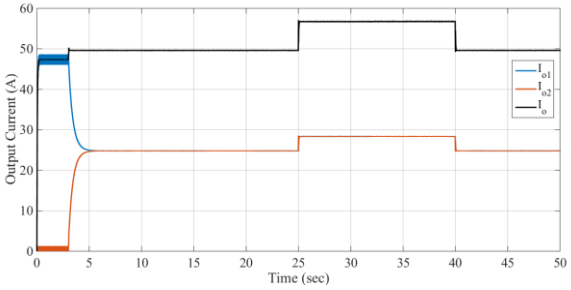

Figure 7.28: Output Currents – CVD – Two Buck Converters – Load Changes 0.92Ω - 0.8Ω

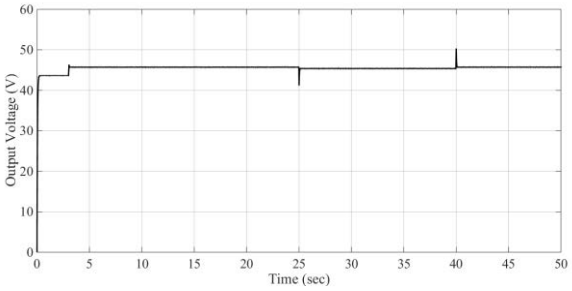

Figure 7.29: Output Voltage – CVD – Two Buck Converters – Load Changes 0.92Ω - 0.8Ω

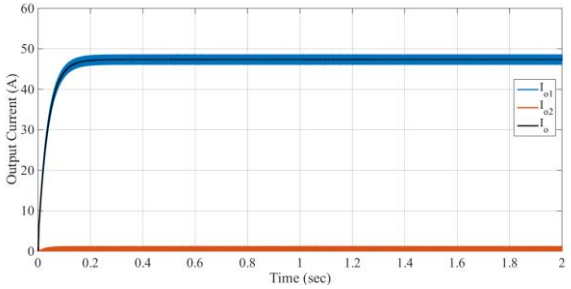

Figure 7.30: Output Currents – Start-Up – CVD – Two Buck Converters

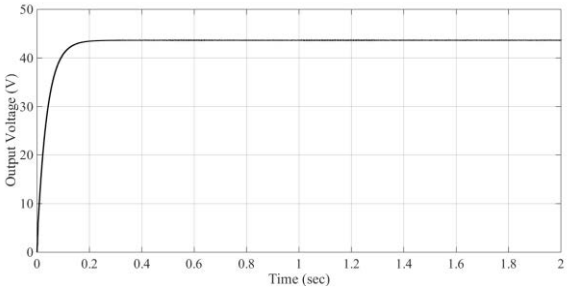

Figure 7.31: Output Voltage – Start-Up – CVD – Two Buck Converters

7.1.4 Comparison between Droop Control Methods by Simulations

The three droop control methods tested by simulations in this section, namely V-I droop, I-V droop, and CVD, all utilized the same droop coefficient; R_d = 0.092Ω for the V-I droop method and k = 1/0.092 for both I-V droop and CVD. Therefore, all methods caused the same droop voltage deviations in the output voltage, allowing the three droop methods to be compared to each other.

From the results obtained, all the three droop methods offered correct current sharing capabilities. As can be observed from the results obtained, the I-V droop method offered faster sharing response when compared with V-I droop. The load sharing process between the two paralleled Buck converters with a resistive load of 0.92Ω

using V-I droop control took ≈13s, while the load sharing process between the Buck converter and the Bidirectional converter took ≈10s for the same load. With I-V droop control the load sharing process could be taken as instant. Also, the disturbance in voltage during load changes is minimal when using I-V droop. This is due to the high bandwidth of the voltage control loop. The voltage controller in the I-V droop case is effectively a proportional gain term equal to the droop multiplier k (1/0.092), providing a voltage closed loop bandwidth of approximately 2.42kHz at the specific load. However, this large proportional gain term (~10.85) causes large oscillations during start-up. Another issue with I-V droop is the interaction with the anti-aliasing filter in the output voltage feedback path. The anti-aliasing filter, which was designed at 2.5kHz, is needed in practice to prevent aliasing when sampling by an ADC to implement the control system using a microcontroller. In fact for the simulation with I-V droop to run successfully, the anti-aliasing filter in the output voltage feedback path had to be removed from the control system model. If the filter is not removed the control system becomes unstable. This instability can also be observed in the experimental results presented in subsection 7.3.2. This means that the large voltage closed loop bandwidth in I-V droop is problematic for practical implementation. The start-up oscillations were mitigated by the proposed CVD droop method. The CVD method provides the ability to adjust the bandwidth of the voltage loop by the use of the pole and zero of the CVD controller. In fact the voltage closed loop bandwidth with the CVD controller was set to 4.26Hz, which eliminated the start-up oscillations, provided stability and very good response. Load sharing between the two paralleled Buck converters with a resistive load of 0.92Ω using the CVD method was obtained in less than 3s.

7.2 Voltage Restoration Simulations

The voltage restoration loop is used to restore the DC microgrid bus voltage to the desired voltage level by correcting any voltage deviations created by droop control. The voltage restoration loop is common to all converters connected within the DC microgrid. Simulations were performed to test the voltage restoration loop, with the simulation model consisting of parallel-connected converters with a shared resistive load. The simulations with voltage restoration were performed with the converters using V-I droop, I-V droop, and CVD. Figure 7.32 shows the Simulink model used to test the voltage restoration control loop. The control systems of the Buck converters

and the Bidirectional converter were modified to accommodate the voltage restoration controller. This involved adding an additional term at the voltage summing point. This additional voltage restoration term V_{res} can be observed in Figure 7.33, which shows the V-I droop control system for the Buck converters. Similarly, the additional voltage restoration term V_{res} was added to the control system for the Bidirectional converter, and for the Buck converters using I-V droop and the CVD method.

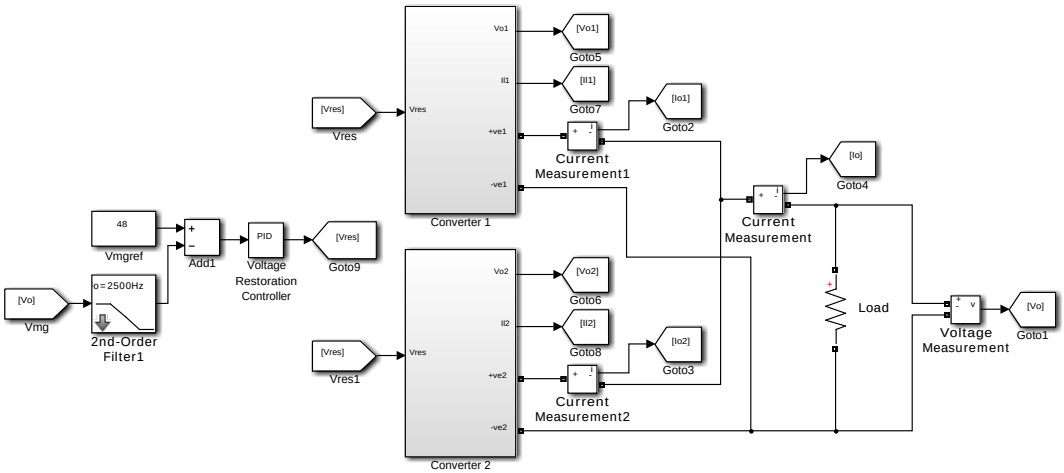

Figure 7.32: Paralleled Converters and Voltage Restoration Control Loop

7.2.1 Voltage Restoration with Two V-I Droop Controlled Buck Converters

The first simulation carried out to test the voltage restoration loop was performed using two paralleled Buck converters with V-I droop control. The control system with the additional voltage restoration term V_{res} and V-I droop for the Buck converters is shown in Figure 7.33. The reference for the voltage restoration loop was set to 48V.

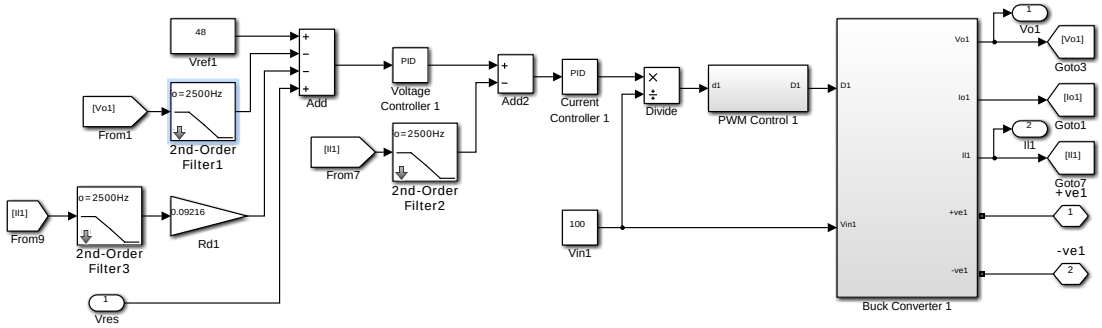

Figure 7.33: Buck Converter with Current and Voltage PI Controllers including V-I Droop and Voltage Restoration in s-Domain

Initially at t = 0s only one converter was switched on, supplying a resistive load of 0.92Ω (52.1A at 48V). At t = 3s the second converter was connected in parallel with the first converter, and started sharing the resistive load. At t = 25s the voltage restoration controller was switched on, restoring the DC-bus voltage to the desired 48V.

Figures 7.34 and 7.35 show the results from the simulation performed with the paralleled Buck converters using V-I droop and the voltage restoration loop. Figure 7.34 shows the output current from each converter (I_{o1} and I_{o2}) and the total output/load current (I_o), showing the start-up of both converters, the load sharing process, and the increase in current due to voltage correction. Figure 7.35 shows the output voltage (V_o), showing the start-up of both converters, and voltage correction starting at t = 25s. The voltage restoration controller successfully corrected the droop-reduced output voltage of the converters from approximately 45.68V to the desired 48V in approximately 20s (t = 45s), as can be observed from Figure 7.35. The voltage correction subsequently increased the converters' output currents, increasing the total output/load current from approximately 49.57A to the desired 52.08A, as shown in Figure 7.34.

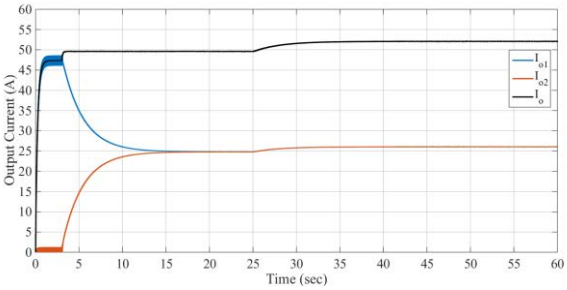

Figure 7.34: Output Currents – Load Sharing and Voltage Restoration – V-I Droop – Two Buck Converters

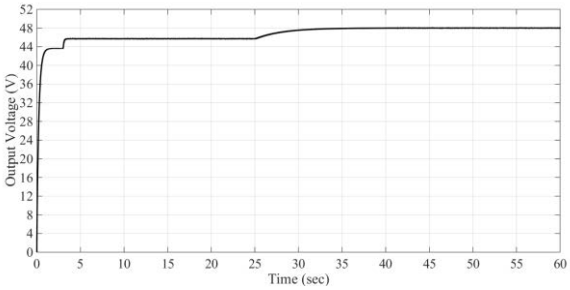

Figure 7.35: Output Voltage – Load Sharing and Voltage Restoration – V-I Droop – Two Buck Converters

7.2.2 Voltage Restoration with V-I Droop Controlled Buck and Bidirectional Converters

The second simulation was carried out to test the voltage restoration loop using the Buck converter and the Bidirectional converter (Boost mode) connected in parallel with V-I droop control. Similar to the Buck converter control system, the control system for the Bidirectional converter with V-I droop was modified to include the voltage restoration term at the voltage summing block, as shown in Figure 7.36. The reference for the voltage restoration loop was set to 48V. The simulation followed the same profile as the one in subsection 7.2.1. Initially at t = 0s only one converter was switched on, supplying a resistive load of 0.92Ω (52.1A at 48V). At t = 3s the second converter was connected in parallel with the first converter, and started sharing the resistive load. At t = 25s the voltage restoration controller was switched on, restoring the DC-bus voltage to the desired 48V.

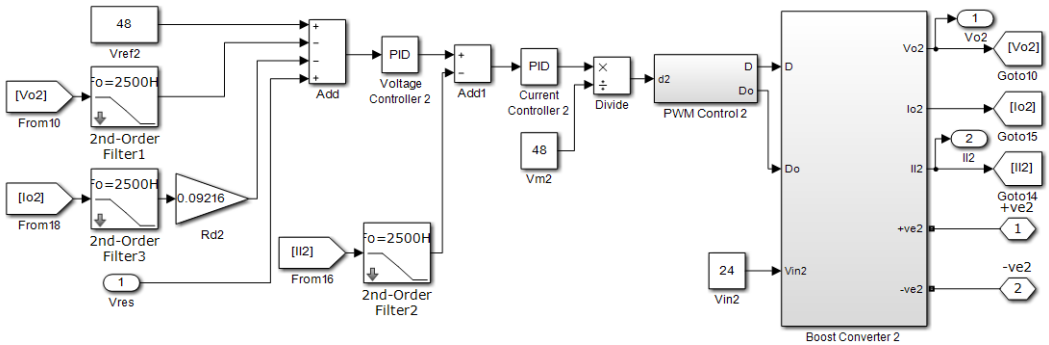

Figure 7.36: Bidirectional Converter (Boost Mode) with Current and Voltage PI Controllers including V-I Droop and Voltage Restoration in s-Domain

Figures 7.37 and 7.38 show the results from the simulation performed with the paralleled Buck and Bidirectional converters using V-I droop and the voltage restoration loop. Figure 7.37 shows the output current from the Buck converter (I_{o1}), the Bidirectional converter (I_{o2}), and the total output/load current (I_o), showing the start-up of both converters, the load sharing process, and the increase in current due to voltage correction. Figure 7.38 shows the output voltage (V_o), showing the start-up of both converters, and voltage correction starting at t = 25s. Similar to the previous simulation, the voltage restoration controller successfully corrected the droop-reduced output voltage of the converters from approximately 45.68V to the desired 48V in approximately 20s (t = 45s), as can be observed from Figure 7.38. The voltage correction subsequently increased the converters' output currents, increasing the total output/load current from approximately 49.57A to the desired 52.08A, as shown in Figure 7.37.

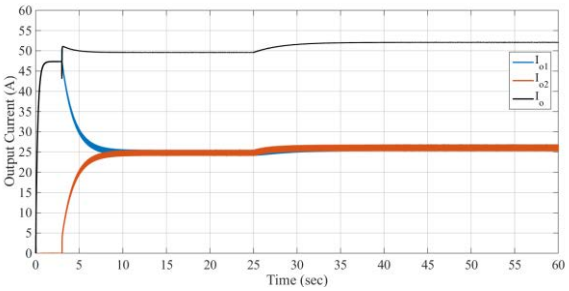

Figure 7.37: Output Currents – Load Sharing and Voltage Restoration – V-I Droop – Buck and Bidirectional Converters

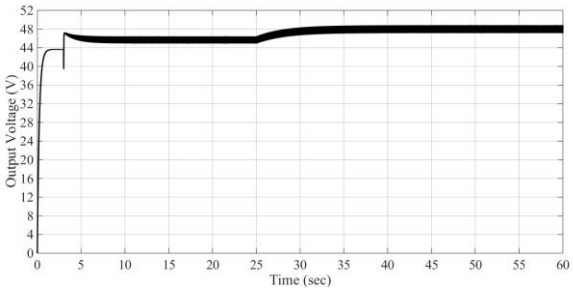

Figure 7.38: Output Voltage – Load Sharing and Voltage Restoration – V-I Droop – Buck and Bidirectional Converters

7.2.3 Voltage Restoration with Two I-V Droop Controlled Buck Converters

Another simulation was carried out to test the voltage restoration loop using two paralleled Buck converters with I-V droop. The control system for the Buck converter with I-V droop was modified to include the voltage restoration term at the voltage summing block, as shown in Figure 7.39. The reference for the voltage restoration

loop was set to 48V. The simulation followed the same profile as the ones in the previous subsections. At t = 0s only one converter was switched on, supplying a resistive load of 0.92Ω (52.1A at 48V). At t = 3s the second converter was connected in parallel with the first converter, and started sharing the resistive load. At t = 25s the voltage restoration controller was switched on, restoring the DC-bus voltage to the desired 48V.

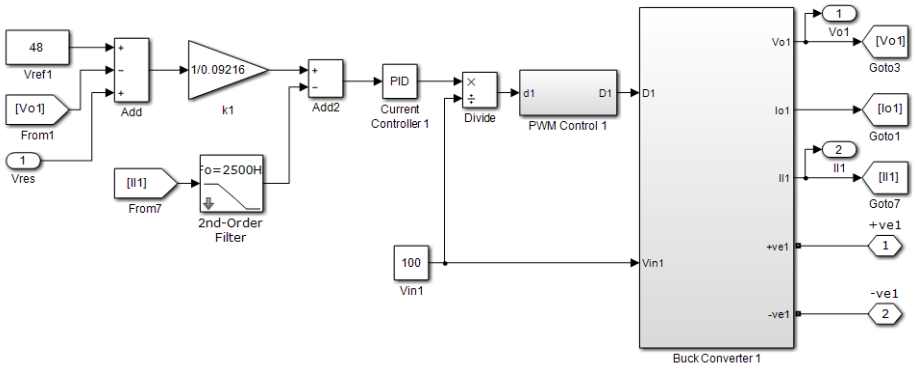

Figure 7.39: Buck Converter with Current PI Controller including I-V Droop and Voltage Restoration in s-Domain

Figure 7.40 and 7.41 show the results from the simulation performed with the paralleled Buck converters using I-V droop and the voltage restoration loop. Figure 7.40 shows the output current from each converter (I_{o1} and I_{o2}) and the total output/load current (I_o), showing the start-up of both converters, the load sharing process, and the increase in current due to voltage correction. Figure 7.41 shows the output voltage (V_o), showing the start-up of both converters, and voltage correction starting at t = 25s. As for the previous simulations with the voltage restoration loop, the voltage restoration controller corrected the droop-reduced output voltage of the converters from approximately 45.68V to the desired 48V in approximately 20s (t = 45s), as can be observed from Figure 7.41. The voltage correction subsequently increased the converters' output currents, increasing the total output/load current from approximately 49.57A to the desired 52.08A, as shown in Figure 7.40.

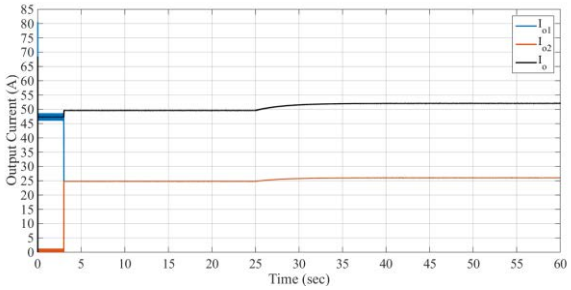

Figure 7.40: Output Currents – Load Sharing and Voltage Restoration – I-V Droop

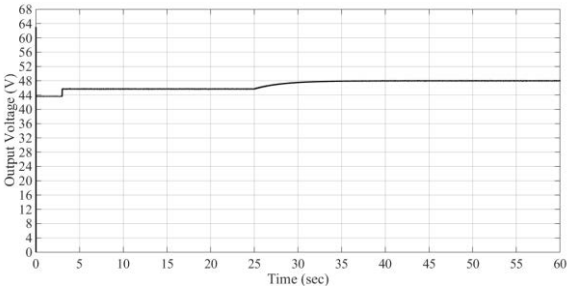

Figure 7.41: Output Voltage – Load Sharing and Voltage Restoration – I-V Droop

7.2.4 Voltage Restoration with Two CVD Controlled Buck Converters

The voltage restoration loop was also tested by simulation using two paralleled Buck converters with the CVD method. The control system for the Buck converter with CVD was modified to include the voltage restoration term at the voltage summing block, as shown in Figure 7.42. The reference for the voltage restoration loop was set to 48V. Following the same profile as the previous ones; the simulation started at t = 0s with only one converter switched on, supplying a resistive load of 0.92Ω (52.1A at 48V). At t = 3s the second converter was connected in parallel with the first converter, and started sharing the resistive load. The voltage restoration controller was switched on at t = 25s, restoring the DC-bus voltage to the desired 48V.

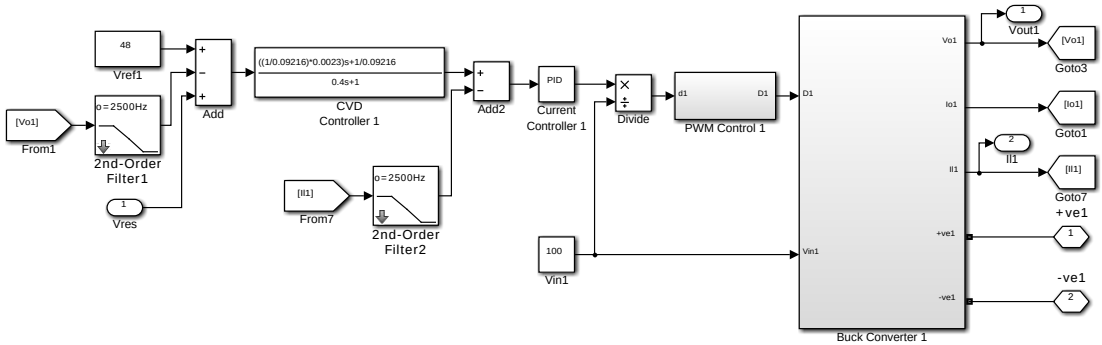

Figure 7.42: Buck Converter with Current PI Controller including CVD and Voltage Restoration in s-Domain

Figure 7.43 and 7.44 show the results from the simulation performed with the paralleled Buck converters using the CVD method and the voltage restoration loop. Figure 7.43 shows the output current from each converter (I_{o1} and I_{o2}) and the total output/load current (I_o), showing the start-up of both converters, the load sharing process, and the increase in current due to voltage correction. Figure 7.44 shows the output voltage (V_o), showing the start-up of both converters, and voltage correction starting at t = 25s. As for the previous simulations with the voltage restoration loop, the voltage restoration controller corrected the droop-reduced output voltage of the converters from approximately 45.68V to the desired 48V in approximately 20s (t = 45s), as can be observed from Figure 7.44. This voltage correction subsequently increased the converters' output currents, increasing the total output/load current from approximately 49.57A to the desired 52.08A, as shown in Figure 7.43.

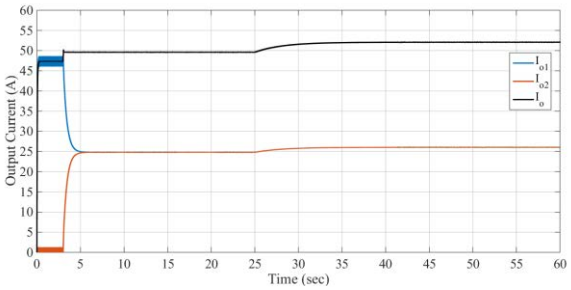

Figure 7.43: Output Currents – Load Sharing and Voltage Restoration – CVD

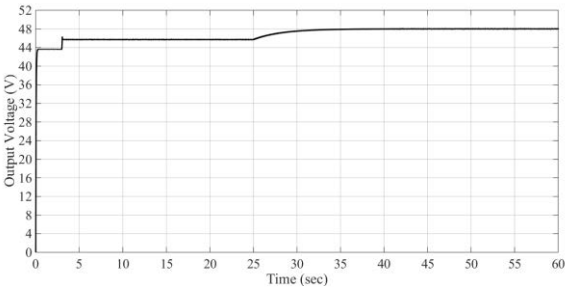

Figure 7.44: Output Voltage – Load Sharing and Voltage Restoration – CVD

7.2.5 Summary of Voltage Restoration Simulations

Having tested the voltage restoration loop with the three droop control methods, from the results obtained it can be concluded that voltage restoration was successfully attained with all the droop methods. In all simulations the load resistance was set to 0.92Ω to obtain a load current of 52.1A at 48V. Designing the voltage restoration loop with a small bandwidth of 0.05Hz and thus with dominant poles (see Chapter 5 subsection 5.4.2), provided a consistent response, reaching the corrected voltage of 48V in approximately 20s with all the three droop control systems.

7.3 Experimental Testing of Paralleled Converters using Droop Control

The converters were tested operating in parallel while sharing a common resistive load. The droop method was used to obtain output current sharing between the converters. The output voltage of each converter is adjusted by the droop loop to obtain load sharing. The three different droop control methods shown in the simulations were also tested with the experimental setup. The three different droop control methods were:

- the V-I droop (see Figure 5.2),
- the I-V droop (see Figure 5.5), and
- the proposed CVD method (see Figure 5.6).

Each droop method was implemented experimentally, and the load sharing performance of the converters was tested while supplying a common resistive load. This section presents the experimental tests and the results obtained from these tests. Figure 7.45 shows a block diagram representing the test setup used for experimental testing with the different droop methods.

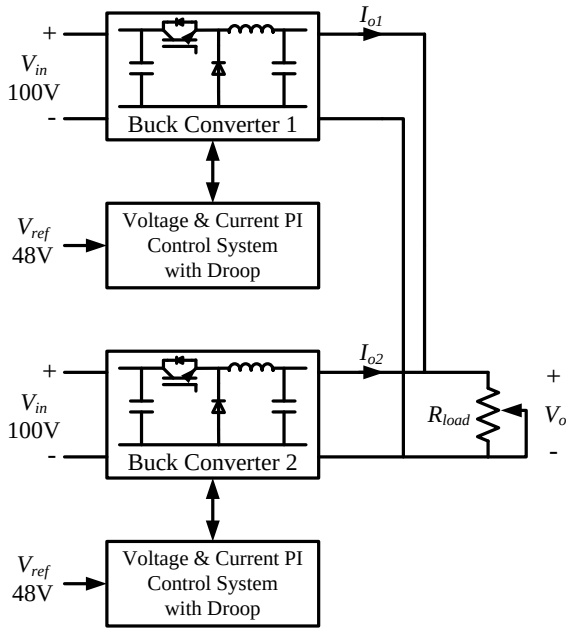

Figure 7.45: Block Diagram – Test Setup – Parallel Converters – with Droop Control

7.3.1 V-I Droop Tests

Experimental testing with V-I droop control was performed with two Buck converters connected in parallel as shown in Figure 7.45. For both Buck converters the droop resistance R_d was set to 0.092Ω (Chapter 5 subsection 5.4.1.3), to obtain equal load sharing. The control system consisted of nested current and voltage PI controllers with the V-I droop loop, as presented in Chapter 5 (see Figure 5.2). The current and voltage PI controllers controlled the inductor current and output voltage, respectively. The voltage reference for the voltage controller was set to 48V.

The test procedure was as follows: Buck converter 1 was switched on, supplying a resistive load of 9.6Ω. After a few seconds, Buck converter 2 was switched on, and started to share the load current with Buck converter 1. After some time Buck converter 2 was switched off, followed by the switching off of Buck converter 1. The same procedure was repeated with a resistive load of 2.4Ω.

Figures 7.46 to 7.49 show the experimental results obtained when the Buck converters were operated using V-I droop control with a load resistance of 9.6Ω, while Figures 7.50 to 7.53 show the results with the resistive load changed to 2.4Ω. The traces in the figures are the output current of Buck 1 (I_{o1}), the output current of Buck 2 (I_{o2}), the load current (I_o), and the load/output voltage (V_o).

Figure 7.46 shows the moment when Buck 1 was switched on, supplying the load resistance of 9.6Ω, while Figure 7.47 shows the moment when Buck 2 was switched on and started sharing the load current with Buck 1. Both converters reach steady state

operation with the load current shared between them in less than approximately 8s. Figure 7.48 shows the moment when Buck 2 was switched off, with Buck 1 returning to supply the total load current, while Figure 7.49 shows the moment when Buck 1 was switched off. The same procedure was followed with the resistive load of 2.4Ω, and the results are shown in Figures 7.50 to 7.53.

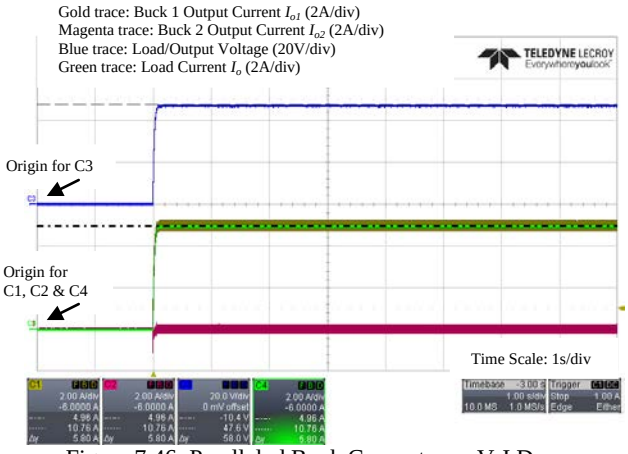

Figure 7.46: Paralleled Buck Converters – V-I Droop – Buck 1 Switching On – Resistive Load R_{load} = 9.6Ω

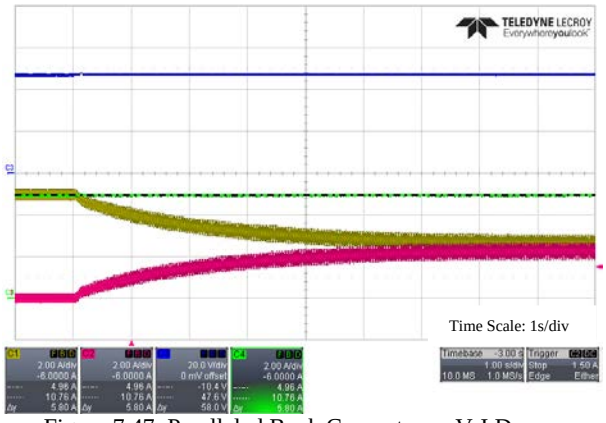

Figure 7.47: Paralleled Buck Converters – V-I Droop – Buck 1 Operating → Buck 2 Switching On – Resistive Load R_{load} = 9.6Ω

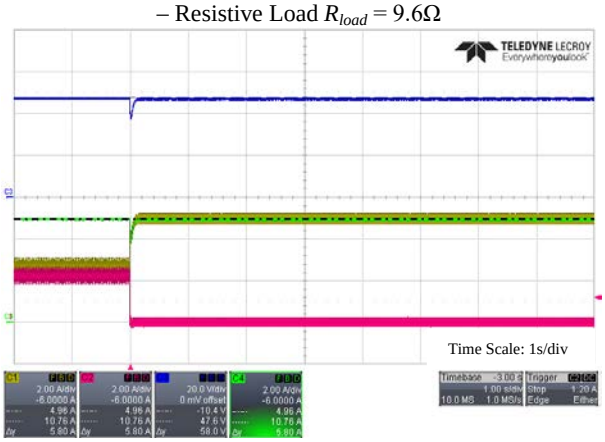

Figure 7.48: Paralleled Buck Converters – V-I Droop – Buck 1 and Buck 2 Operating → Buck 2 Switching Off – Resistive Load R_{load} = 9.6Ω

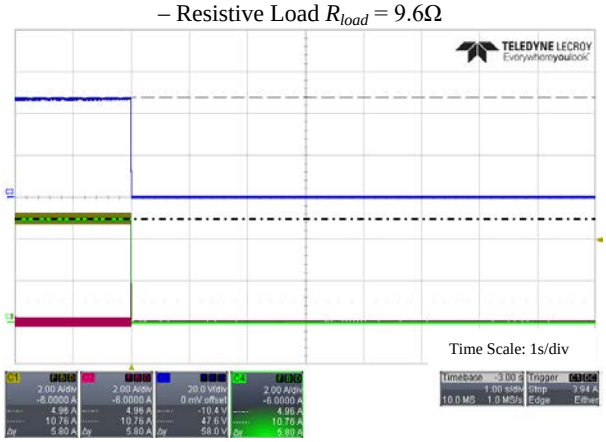

Figure 7.49: Paralleled Buck Converters – V-I Droop – Buck 1 Switching Off – Resistive Load R_{load} = 9.6Ω

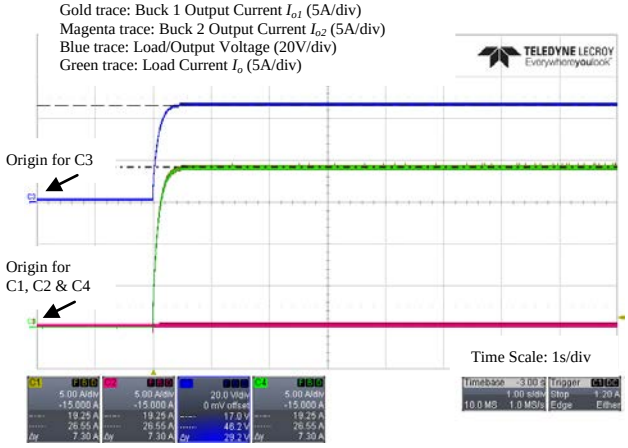

Figure 7.50: Paralleled Buck Converters – V-I Droop – Buck 1 Switching On – Resistive Load R_{load} = 2.4Ω

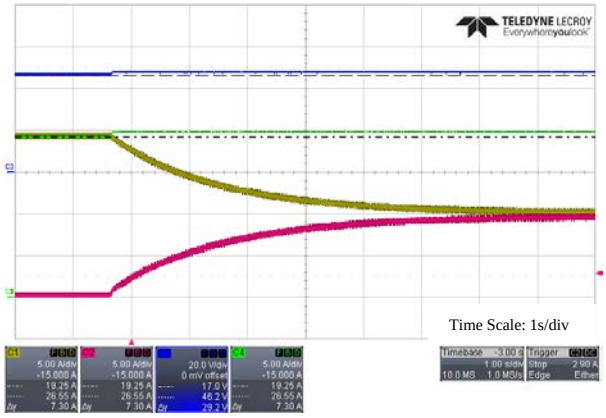

Figure 7.51: Paralleled Buck Converters – V-I Droop – Buck 1 Operating → Buck 2 Switching On – Resistive Load R_{load} = 2.4Ω

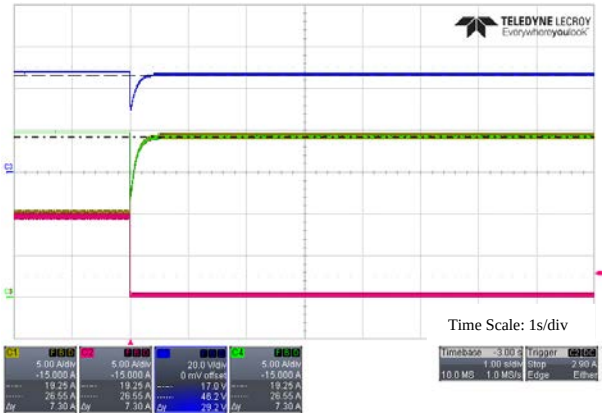

Figure 7.52: Paralleled Buck Converters – V-I Droop – Buck 1 and Buck 2 Operating → Buck 2 Switching Off – Resistive Load R_{load} = 2.4Ω

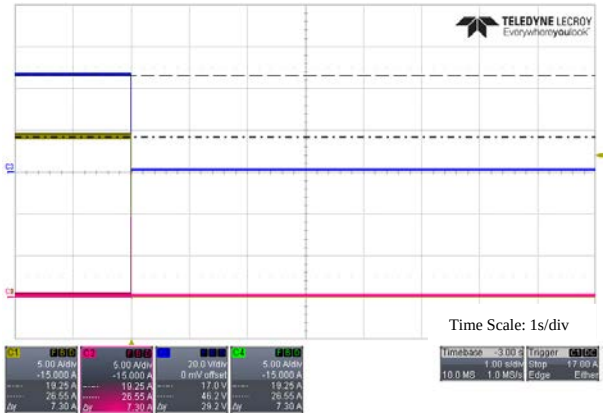

Figure 7.53: Paralleled Buck Converters – V-I Droop – Buck 1 Switching Off – Resistive Load R_{load} = 2.4Ω

Table 7.2 lists the results obtained from the experimental tests performed with two parallel-connected Buck converters sharing a common resistive load using V-I droop control. The input voltage V_{in} for both Buck converters was 100V and the voltage reference V_{ref} for the voltage controller was set to 48V. Tests were conducted with load resistances of 9.6Ω and 2.4Ω.

R_d = 0.092Ω for both Buck Converters								
R_{load}	**Expected I_{out} (I_{load}) Total**	**Expected I_{out} Buck 1**	**Expected I_{out} Buck 2**	**Expected V_{out}**	**V_{out}**	**I_{out} Buck 1**	**I_{out} Buck 2**	**I_{out} (I_{load}) Total**
9.6Ω	4.98A	2.49A	2.49A	47.77V	47.17V	2.68A	2.25A	4.93A
2.4Ω	19.62A	9.81A	9.81A	47.1V	47.87V	10.12A	9.68A	19.22A
Measurements taken from LeCroy Oscilloscope using differential voltage probe and current probes.								

Table 7.2: V-I Droop Results

The results demonstrated very good current sharing performance. With a 9.6Ω resistive load, the individual Buck converters' output currents resulted to be around the expected 2.49A, for a total load current of 4.98A at 47.77V. Similarly good results were also obtained with a 2.4Ω resistive load, where the output currents from the Buck converters were around the expected 9.81A for each converter, for a total load current of 19.62A at 47.1V. Small differences in the output currents were expected to result, which are mainly due to differences between the two converters. In both cases, the load current was successfully shared in less than 8s for both load resistances of 9.6Ω and 2.4Ω. This compares well with the simulation results documented in subsection 7.1.1.1. The simulation was performed using a load resistance of 0.92Ω to obtain the full load current of the Buck converter (2.5kW with 48V, 52.1A), which reached load sharing steady state in ≈13s. This meant that according to simulation the maximum expected sharing time between the two Buck converters was 13s. In practice the experimental results show that current sharing for load resistances of

9.6Ω and 2.4Ω was obtained in less than 8s, which is well within the maximum expected sharing time, demonstrating correct operation of the V-I droop control loop.

7.3.2 I-V Droop Tests

Experimental tests were also performed with I-V droop control, using two paralleled Buck converters set up as shown in Figure 7.45 to test the load sharing performance. For both Buck converters, the droop multiplier term *k* was set to 1/0.092 (Chapter 5 subsection 5.4.1.4), to obtain equal load sharing. The control system consisted of a voltage controller made up of the multiplier term *k* and a current PI controller, as presented in Chapter 5 (see Figure 5.5). The voltage reference for the voltage controller was set to 48V.

The tests planned with the I-V droop method were identical to those performed with the V-I droop method. As was noted during the simulations (subsection 7.1.2.1), testing with I-V droop proved to be problematic. During the analysis of the simulations it was observed that the outer voltage loop of the I-V droop control system, which has a bandwidth of around 2.42kHz, interacted with the bandwidth of the 2.5kHz anti-aliasing filter. It was shown in the simulations that for I-V droop control to operate successfully, the anti-aliasing filter in the output voltage feedback path had to be removed. This was not possible in the practical test setup, resulting in unstable operation of the Buck converters. When the first Buck converter (Buck 1) using I-V droop control with a *k* value of 1/0.092 and a resistive load of 9.6Ω was switched on, large oscillations were present during start-up and the operation was unstable. This can be observed from the results shown in Figures 7.54 and 7.55. In other cases the protection circuit operated due to high currents, shutting down the converter switching. The second Buck converter (Buck 2) was never switched on.

For testing purposes the *k* value was reduced by a factor of 10 to 1/0.92, and the resistive load was set to 2.4Ω. This time when the first Buck converter (Buck 1) was switched on large oscillations were present during start-up, and steady state was not always reached in subsequent switch on operations of the converter. Some results are shown in Figures 7.56, 7.57, and 7.58. Again, due to the instabilities in recurring switch on of Buck 1, no attempts to switch on Buck 2 were made.

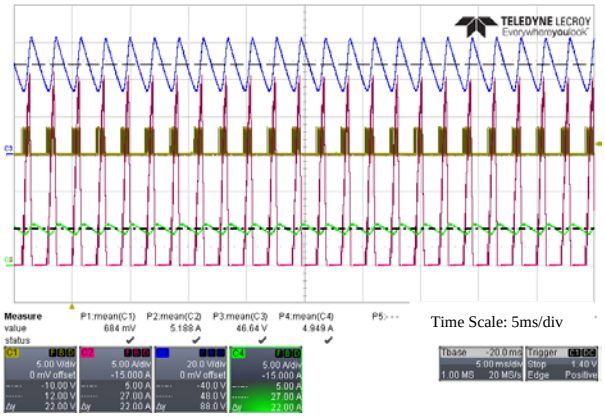

Figure 7.54: Paralleled Buck Converters – I-V Droop – Buck 2 Instability, k = 1/0.092, R_{load} = 9.6Ω

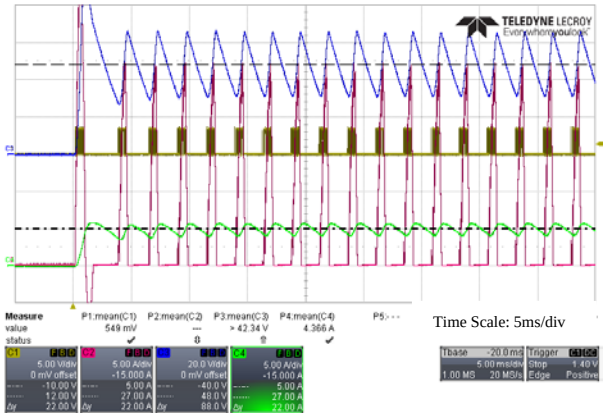

Figure 7.55: Paralleled Buck Converters – I-V Droop – Buck 2 Switching On, k = 1/0.092, R_{load} = 9.6Ω

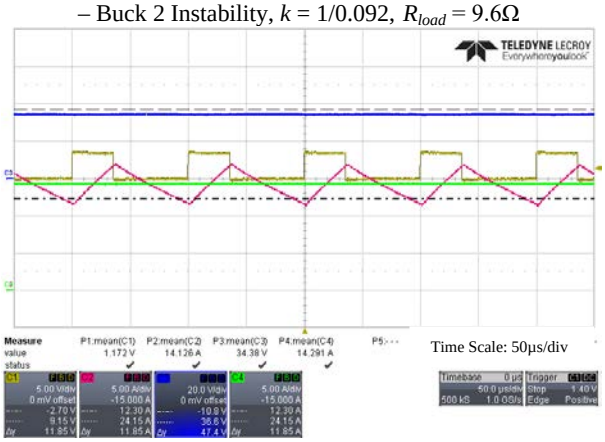

Figure 7.56: Paralleled Buck Converters – I-V Droop – Buck 1 Steady State, k = 1/0.92, R_{load} = 2.4Ω

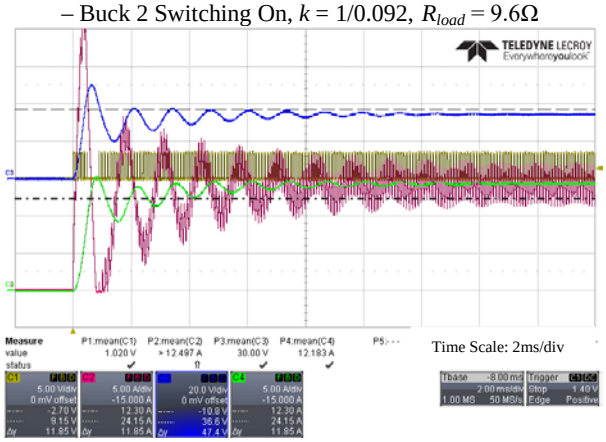

Figure 7.57: Paralleled Buck Converters – I-V Droop – Buck 1 Switching On (1), k = 1/0.92, R_{load} = 2.4Ω

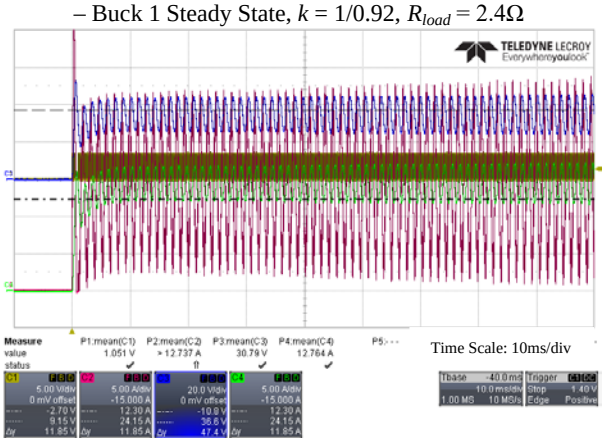

Figure 7.58: Buck Converter – I-V Droop – Buck 1 Switching On (2), k = 1/0.92, R_{load} = 2.4Ω

Gold trace: PWM from µcontroller IGBT (PWM1A) (5V/div)
Magenta trace: Inductor Current I_L (5A/div)
Blue trace: Load/Output Voltage V_o (20V/div)
Green trace: Load/Output Current I_o (5A/div)

7.3.3 Combined Voltage and Droop Method Tests

Experimental tests were also performed with the proposed CVD method, using the same setup as before with two paralleled Buck converters set up as shown in Figure 7.45. Both Buck converters were set to use the same k value of 1/0.092 (Chapter 5 subsection 5.4.1.5), for the CVD controller to obtain equal load sharing. The control system consisted of a voltage controller made up of the CVD method and a current PI controller, as presented in Chapter 5 (see Figure 5.6). The voltage

reference for the voltage controller was set to 48V. The proposed CVD method mitigates the oscillations experienced by the I-V droop control method.

The same test procedure as the one used for V-I droop was used; Buck converter 1 was switched on, supplying a resistive load of 9.6Ω. After a few seconds, Buck converter 2 was switched on and started to share the resistive load. After some time Buck converter 2 was switched off, followed by the switching off of Buck converter 1. The same procedure was repeated with a resistive load of 2.4Ω.

Figures 7.59 to 7.62 show the experimental results obtained when the Buck converters were operated using the CVD method, with the resistive load of 9.6Ω, while Figures 7.63 to 7.66 show the results when the resistive load was changed to 2.4Ω. The traces in the figures are the output current of Buck 1 (I_{o1}), the output current of Buck 2 (I_{o2}), the load current (I_o), and the load/output voltage (V_o).

Figure 7.59 shows the moment when Buck 1 was switched on, supplying the load resistance of 9.6Ω, while Figure 7.60 shows the moment when Buck 2 was switched on and started sharing the load current with Buck 1. Both converters reach steady state operation with the load current shared between them in slightly more than 1s. Figure 7.61 shows the moment when Buck 2 was switched off, with Buck 1 returning to supply the total load current, while Figure 7.62 shows the moment when Buck 1 was switched off. The same procedure was followed with the resistive load of 2.4Ω, and the results are shown in Figures 7.63 to 7.66.

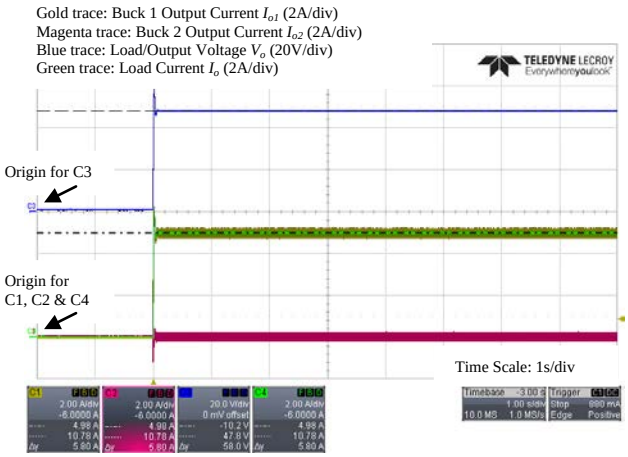

Figure 7.59: Paralleled Buck Converters – CVD
– Buck 1 Switching On
– Resistive Load R_{load} = 9.6Ω

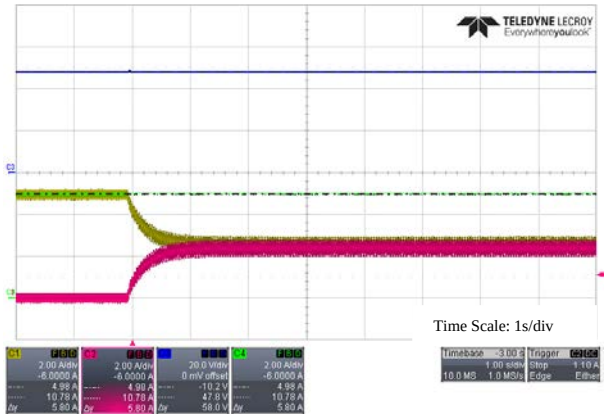

Figure 7.60: Paralleled Buck Converters – CVD
– Buck 1 Operating → Buck 2 Switching On
– Resistive Load R_{load} = 9.6Ω

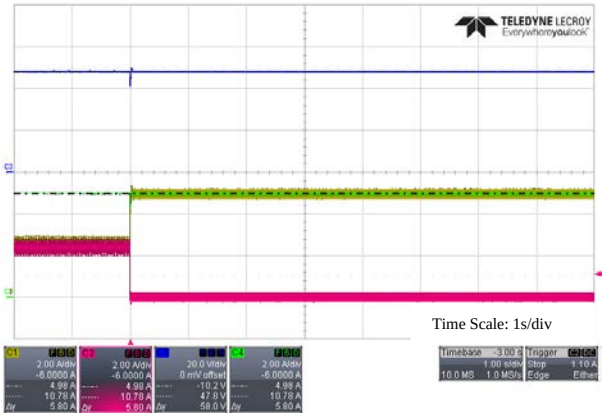

Figure 7.61: Paralleled Buck Converters – CVD
– Buck 1 and Buck 2 Operating → Buck 2 Switching Off
– Resistive Load R_{load} = 9.6Ω

Figure 7.62: Paralleled Buck Converters – CVD
– Buck 1 Switching Off
– Resistive Load R_{load} = 9.6Ω

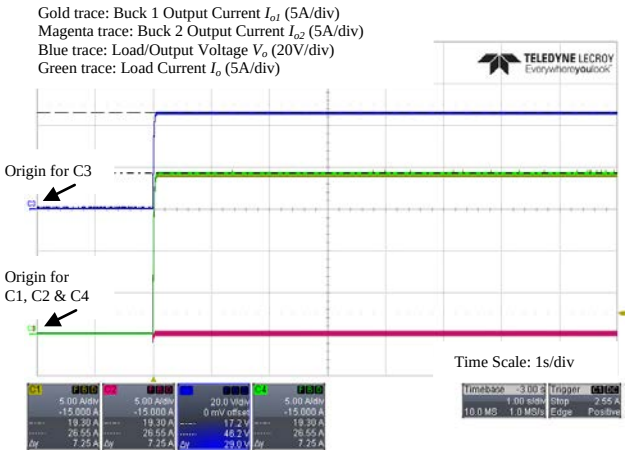

Figure 7.63: Paralleled Buck Converters – CVD
– Buck 1 Switching On
– Resistive Load R_{load} = 2.4Ω

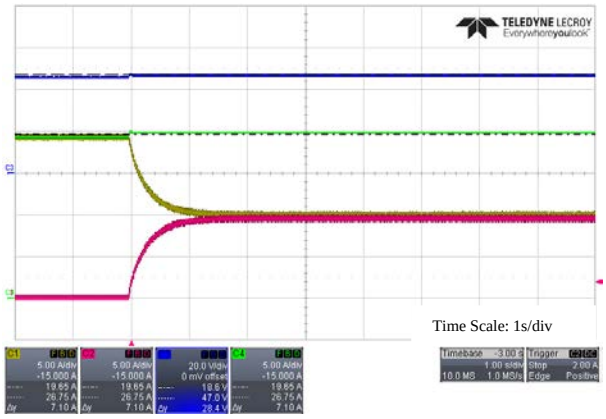

Figure 7.64: Paralleled Buck Converters – CVD
– Buck 1 Operating → Buck 2 Switching On
– Resistive Load R_{load} = 2.4Ω

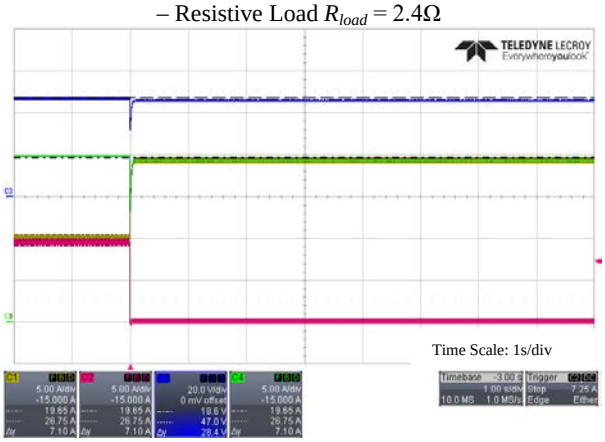

Figure 7.65: Paralleled Buck Converters – CVD
– Buck 1 and Buck 2 Operating → Buck 2 Switching Off
– Resistive Load R_{load} = 2.4Ω

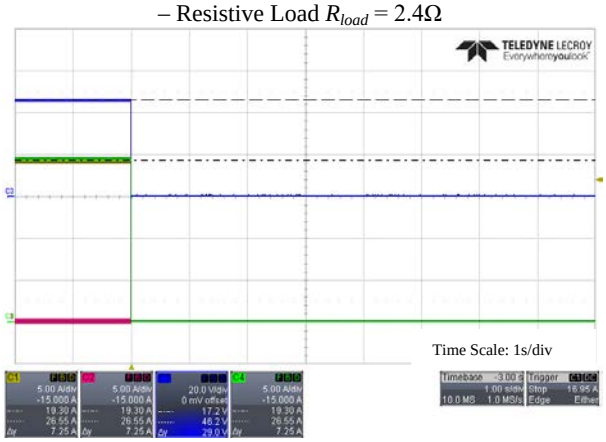

Figure 7.66: Paralleled Buck Converters – CVD
– Buck 1 Switching Off
– Resistive Load R_{load} = 2.4Ω

Table 7.3 lists the results obtained from the experimental tests performed with two parallel-connected Buck converters sharing a common resistive load using the CVD control method. The input voltage V_{in} for both Buck converters was 100V and the

voltage reference V_{ref} for the voltage controller was set to 48V. Tests were conducted with load resistances of 9.6Ω and 2.4Ω.

***k* term of CVD = 1/0.092Ω for both Buck Converters**								
R_{load}	**Expected** I_{out} **(**I_{load}**) Total**	**Expected** I_{out} **Buck 1**	**Expected** I_{out} **Buck 2**	**Expected** V_{out}	V_{out}	I_{out} **Buck 1**	I_{out} **Buck 2**	I_{out} **(**I_{load}**) Total**
9.6Ω	4.98A	2.49A	2.49A	47.77V	48.19V	2.50A	2.42A	4.99A
2.4Ω	19.62A	9.81A	9.81A	47.1V	46.83V	9.83A	9.68A	19.77A
Measurements taken from LeCroy Oscilloscope using differential voltage probe and current probes.								

Table 7.3: CVD Method Results

The results demonstrated very good current sharing performance. With a 9.6Ω resistive load, the individual Buck converters' output currents resulted to be around the expected 2.49A for each converter, for an expected total load current of 4.98A at 47.77V. Similarly good results were also obtained with a 2.4Ω resistive load, where the output currents from the Buck converters resulted around the expected 9.81A for each converter, for an expected total load current of 19.62A at 47.1V. Small differences in the output currents were expected to result, which are mainly due to differences between the two converters. The proposed CVD method, which is a modified I-V droop method, mitigated the oscillations experienced when using the I-V droop method, and also provided stability to the control system. In both test cases, the load current with load resistances of 9.6Ω and 2.4Ω, was successfully shared in less than 2s. This compares well with the simulation results documented in subsection 7.1.3.1. The simulation was performed using a load resistance of 0.92Ω to obtain the full load current of the Buck converter (2.5kW with 48V, 52.1A), which reached load sharing steady state in ≈3.5s. This meant that according to simulation the maximum expected sharing time between the two Buck converters was 3.5s. In practice the experimental results show that current sharing for load resistances of 9.6Ω and 2.4Ω was obtained in less than 2s, which is well within the maximum expected sharing time, demonstrating correct operation of the CVD control method.

7.3.4 Comparison of Droop Control Methods

In the previous subsections the results obtained from experimental testing using three droop methods were presented. The three droop control methods tested were V-I droop, I-V droop, and the new proposed CVD method. All droop control methods utilized the same droop coefficient; R_d = 0.092Ω for the V-I droop method and k = 1/0.092 for both I-V droop and CVD. This means that all methods caused the same droop voltage deviations in the output voltage, allowing the three droop methods to be compared to each other.

The experimental results confirmed what was observed during simulation testing. V-I droop control provided correct current sharing capability with good results as was expected, however its response was slower than CVD control.

When considering the experimental tests which were attempted with I-V droop, the results were also as expected, that is the control system was unstable. This instability was caused by the high gain and bandwidth of the voltage control loop, which is practically fixed according to the droop multiplier k used. In I-V droop, the voltage controller is effectively a proportional gain term equal to the droop multiplier k ($1/0.092 \approx 10.87$), which provided a voltage closed loop bandwidth of approximately 2.42kHz at full load (refer to Chapter 5 subsection 5.4.1.4). This high bandwidth interacted with the 2.5kHz anti-aliasing filter in the output voltage feedback path. In practice the anti-aliasing filter is needed to prevent aliasing when sampling by an ADC to implement the control system using a microcontroller. This means that I-V droop can be problematic for practical implementation with certain converter setups and using certain droop multiplier values.

In this research the new CVD method was proposed, which provided stability, eliminated any start-up oscillations, and provided very good response. The CVD method is a modified I-V droop control method which provides the ability to adjust the bandwidth of the voltage loop by the use of the pole and zero of the CVD controller (see Chapter 5 subsection 5.2.3). The voltage closed loop bandwidth with the CVD controller at full load was set to 4.26Hz (see Chapter 5 subsection 5.4.1.5). As one can note from the experimental results this droop method provided fast response without any oscillations and stability issues.

7.4 Conclusion

This chapter covered the simulations performed in Simulink/Matlab to test the Buck and Bidirectional converters connected in parallel, while sharing a common resistive load. It also covered the experimental results obtained from tests performed on the two Buck converters, while connected in parallel and sharing a resistive load. The droop control method was used to obtain load sharing between parallel-connected converters. Simulations and experiments were performed to test three droop control methods: V-I droop, I-V droop, and the proposed combined voltage and droop (CVD) method.

From the simulations carried out, all the three droop methods offered correct current sharing capabilities, as can be observed from the results in section 7.1. The I-V droop method offered faster sharing response when compared with V-I droop, however caused large oscillations during start-up due to high gain and bandwidth. Another issue when using I-V droop is the interaction with the anti-aliasing filter in the output voltage feedback path, which would lead to difficulties to apply in practice. The proposed CVD method mitigated the start-up oscillations by providing the ability to adjust the bandwidth of the voltage loop, which provided stability and very good response. From the simulation results obtained with two parallel-connected Buck converters with a common resistive load of 0.92Ω (52.1A at 48V), equal load sharing was obtained in less than 3s when the CVD method was used, while approximately 13s were needed when V-I droop was utilized. Subsection 7.1.4 provides a comparison of the three droop methods. Voltage restoration control was also tested with simulations. The voltage restoration control loop is an outer loop common to all converters within the DC microgrid. It is used to correct any voltage deviations created by droop control in the DC-bus voltage, thus restoring the DC-bus voltage to the desired value. Simulations with voltage restoration were performed with two paralleled Buck converters using V-I droop, I-V droop, and the CVD method. Another simulation was performed with paralleled Buck and Bidirectional converters using V-I droop. Voltage restoration was successfully attained with all the droop methods, restoring the DC-bus voltage to the desired 48V in approximately 20s, as can be observed from the results in section 7.2. A summary and comments on the voltage restoration simulations can be found in subsection 7.2.5.

Experimental testing of droop control with two Buck converters operated in parallel while sharing a resistive load was carried out with the three different droop control methods. All droop control methods utilized the same droop coefficient; R_d = 0.092Ω for the V-I droop method and k = 1/0.092 for both I-V droop and CVD. Therefore, all methods caused the same droop voltage deviations in the output voltage, allowing the three droop methods to be compared to each other.

The experimental results agreed very closely with the results obtained in the simulations of section 7.1. The results achieved showed that the V-I droop method provided good and accurate current sharing, however with slower response than the CVD method. When the two Buck converters were connected in parallel while sharing the current for load resistances of 9.6Ω and 2.4Ω, load current sharing was

obtained in less than 8s using V-I droop and in less than 2s using the CVD method. Attempts to perform experimental tests with I-V droop proved to be difficult, since the control system resulted to be unstable. This was expected since it was already observed during simulation testing. The control system instability was caused by the interaction of the voltage control loop and the anti-aliasing filter in the output voltage feedback path. A solution was found to overcome this unstable operation by means of the new proposed CVD method. Using the CVD method the bandwidth of the voltage loop can be adjusted using the pole and zero of the CVD controller. In fact the voltage closed loop bandwidth with the CVD controller at full load was set to 4.26Hz, which successfully obtained fast sharing response, very good sharing accuracy, and importantly no oscillations or stability issues.

Chapter 8 Simulation and Experimental Tests of the DC Microgrid

The DC microgrid consists of two Buck converters, a Bidirectional converter, resistive loads, and a battery storage system. Simulations were performed on the DC microgrid model in Simulink, to simulate the complete system including also a battery management system (BMS). Experimental tests were conducted on the experimental DC microgrid setup consisting of the two Buck converters, the Bidirectional converter connected to a battery bank, and resistive loads. This chapter presents the results obtained from these simulations and experimental tests.

8.1 DC Microgrid Simulations

Simulations were carried out to test the Buck and Bidirectional converters operating in a DC microgrid configuration, including also a BMS. The simulation model of the DC microgrid shown in Figure 8.1 consists of two 2.5kW Buck converters and a 1.5kW Bidirectional converter connected in parallel, together with resistive loads. The Bidirectional converter connects a 24V 120Ah battery bank to the DC microgrid. The DC microgrid bus voltage was set to 48V. The parameters used for the Buck and Bidirectional converters were the same as those used for the simulation models in Chapter 7, shown in Table 7.1. The Buck converters had a fixed input voltage of 100V and provided an output voltage of 48V at the DC-bus. The Bidirectional converter operated between the 48V of the DC-bus and the 24V of the battery bank, since this converter operated as a Boost when sharing the resistive load and as a Buck when charging the battery bank. The mode of operation of the Bidirectional converter was controlled by the BMS, which controlled when to share the load with the other converters and when to charge the battery bank. The BMS operation followed the algorithm documented by the flowchart in Chapter 5.

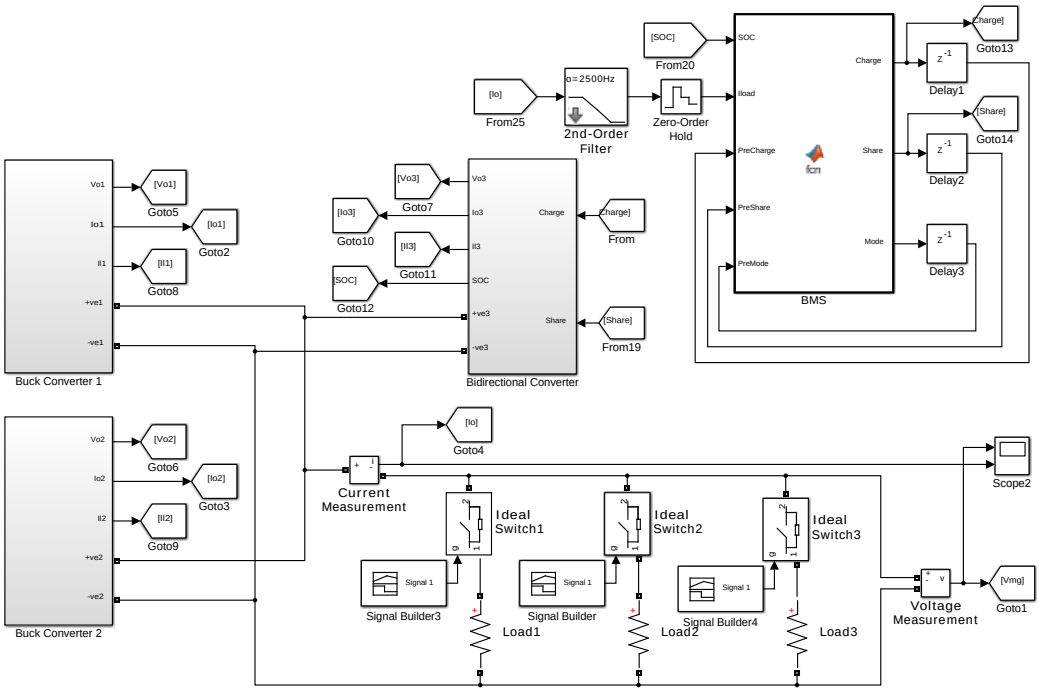

Figure 8.1: DC Microgrid Model and BMS in Simulink

8.1.1 Simulation of the DC Microgrid with the Bidirectional Converter Operating in Different Modes of Operation

The first simulation carried out using the DC microgrid model consisted in operating the two Buck converters in parallel, together with the Bidirectional converter operating in both battery charging mode and load sharing/supplying mode, to test the converters under the two different scenarios. The control system for the Buck converters consists of nested current and voltage discretized PI controllers with V-I droop, as shown in Figure 8.2. The control system for the Bidirectional converter consists of a current discretized PI controller when charging the battery, and nested current and voltage discretized PI controllers with V-I droop when sharing the load. The Bidirectional converter control system has been modified to enable the selection of the mode of operation, as shown in Figure 8.3. For this simulation the BMS was not used, and the modes of operation of the Bidirectional converter were changed using a controlled profile.

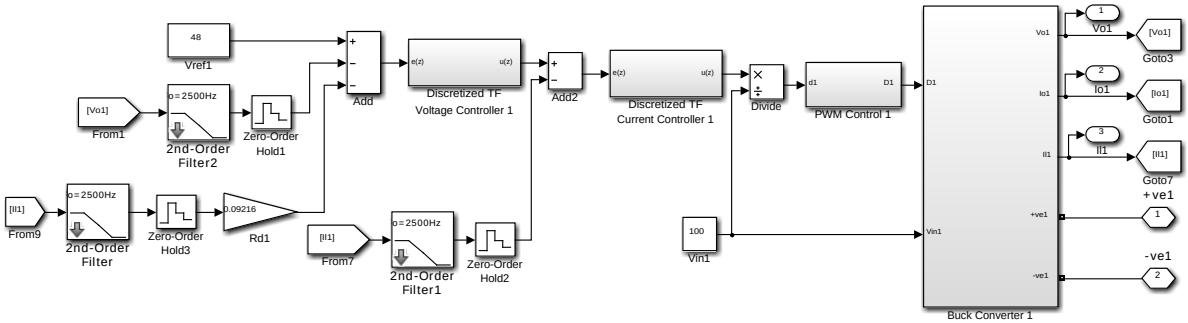

Figure 8.2: Buck Converter with Control System – Discrete System

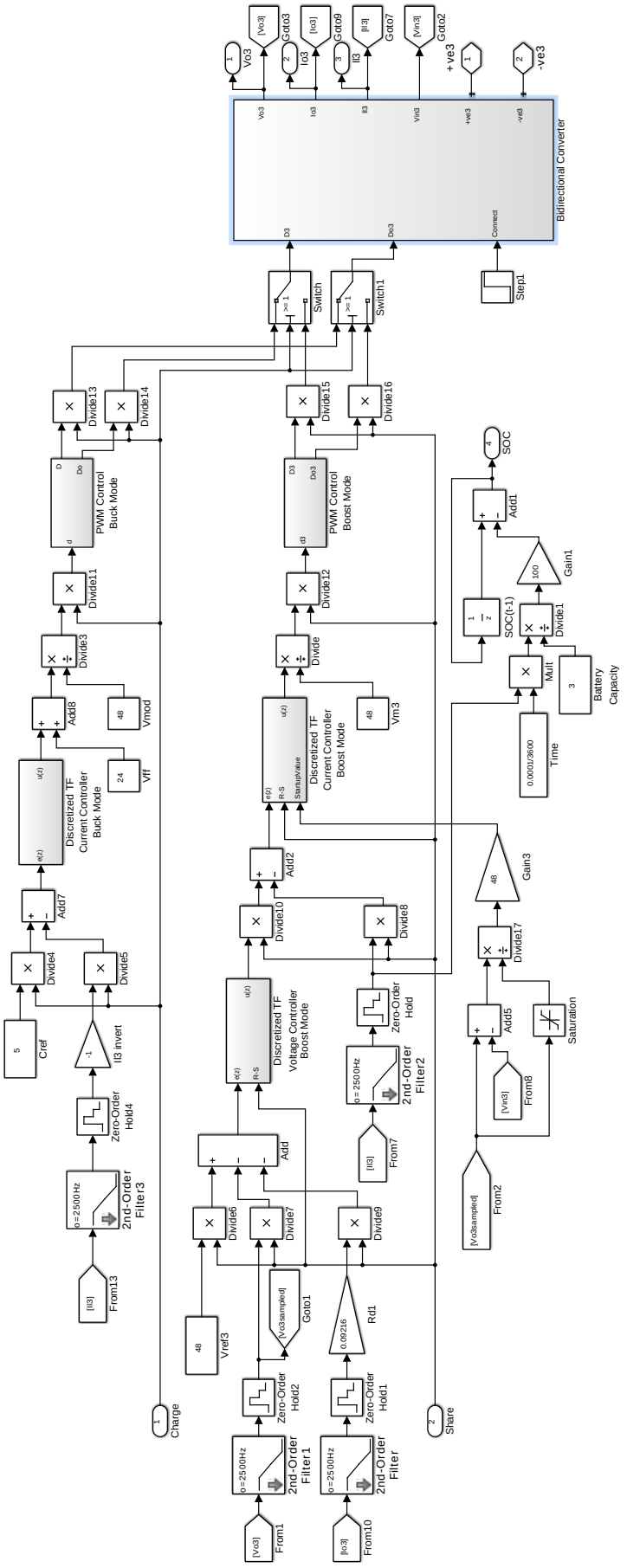

Figure 8.3: Bidirectional Converter with Charging and Sharing Control System – Discrete System

The droop resistance R_d was set to 0.092Ω for all converters to obtain equal load sharing (see Chapter 5 subsection 5.4.1.3). The battery bank connected to the Bidirectional converter was set to 24V with a capacity of 120Ah. The starting SOC of the battery was set to 80%. The simulation at t = 0s starts with the two Buck converters sharing a resistive load of 2.4Ω. At t = 5s the Bidirectional converter enters load sharing/supplying mode and starts to share the load with the other converters. At t = 15s the Bidirectional converter enters idle mode, and at t = 20s the mode of operation is changed to battery charging mode.

Figures 8.4 to 8.8 show the results obtained from the simulation. Figures 8.4 and 8.6 show the output current from each converter (I_{oBuck1}, I_{oBuck2}, and I_{oBiDir}) and the load current (I_{load}), during the changes in mode of operation, while Figures 8.5 and 8.7 show the output/DC-bus voltage (V_o). Figure 8.8 shows the SOC of the battery bank. For the first 5s the two Buck converters shared the load current between them. At t = 5s the Bidirectional converter entered load sharing/supplying mode operating as a Boost converter, started sharing the load current with the two Buck converters, and the three converters reached equal current sharing in approximately 5s. The SOC of the battery decreased from 80% to approximately 78.9%. At t = 15s the Bidirectional converter entered idle mode, where the two Buck converters took over the supply of the load current between them. At t = 20s the Bidirectional converter entered battery charging mode operating as a Buck converter, where the battery bank started to be charged with a constant current of 5A. The two Buck converters supplied between them the load current and the Bidirectional converter input current, reaching equal sharing in approximately 0.25s. The SOC of the battery increased from 78.9% to approximately 79.35%.

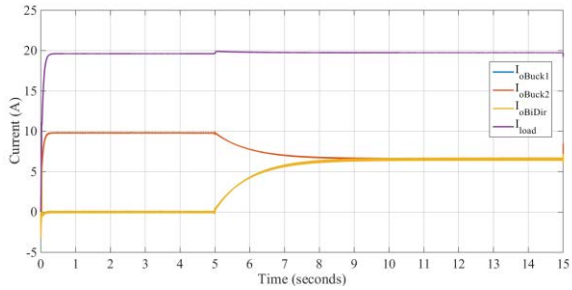

Figure 8.4: Output and Load Currents
- Buck converters Sharing
- Bidirectional converter in Load Sharing/Supplying Mode

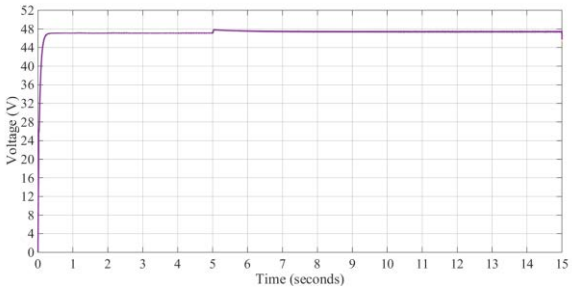

Figure 8.5: DC-Bus Voltage
- Buck converters Sharing
- Bidirectional converter in Load Sharing/Supplying Mode

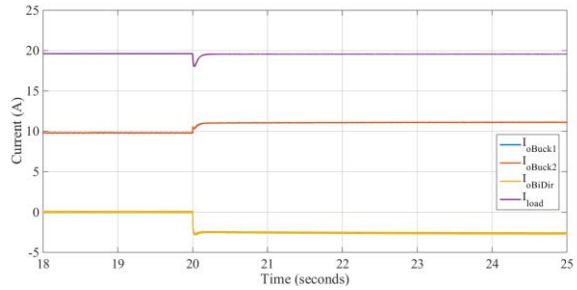

Figure 8.6: Output and Load Currents
- Buck converters Sharing
- Bidirectional converter in Battery Charging Mode

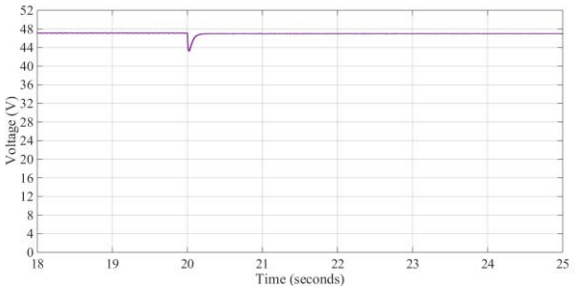

Figure 8.7: DC-Bus Voltage
- Buck converters Sharing
- Bidirectional converter in Battery Charging Mode

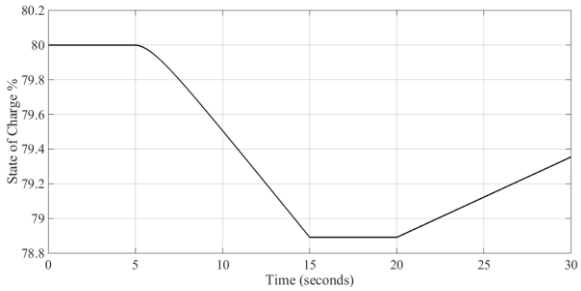

Figure 8.8: Battery State of Charge % – DC Microgrid – Different Modes of Operation

8.1.2 Simulation of the DC Microgrid with Step Load Changes

The second simulation carried out using the DC microgrid model consisted in varying the resistive loads in step changes to test current sharing between the three converters, and battery charging as controlled by the BMS. Although large step changes in load are not a common real life situation in DC microgrids, it provides a worst case scenario for testing purposes.

Similar to the previous simulation, the control system for the Buck converters consists of nested current and voltage discretized PI controllers with V-I droop. The control system for the Bidirectional converter consists of a current discretized PI controller when charging the battery, and nested current and voltage discretized PI controllers with V-I droop when sharing the load. The BMS controls the mode of operation of the Bidirectional converter, changing the mode between charging, sharing, or idle mode, according to the BMS algorithm (see Chapter 5). The mode of operation depends on the load current and the SOC of the battery bank.

The droop resistance R_d was set to 0.092Ω for all converters to obtain equal load sharing (see Chapter 5 subsection 5.4.1.3). For this simulation the battery bank connected to the Bidirectional converter was set to 24V with a capacity of only 3Ah, so that within a short time, the converter enters both the sharing, charging, and idle modes. The starting SOC of the battery was set to 80%.

The simulated load profile is as follows: The load resistance at t = 0s was set to 4.8Ω. At t = 5s the load resistance was reduced to 1.6Ω, while at t = 10s it was increased back to 4.8Ω. At t = 30s the load resistance changes to 9.6Ω.

Figures 8.9 to 8.11 show the results obtained from the simulation. Figure 8.9 shows the output current from each converter (I_{oBuck1}, I_{oBuck2}, and I_{oBiDir}) and the load current (I_{load}), while Figure 8.10 shows the output/DC-bus voltage (V_o). Figure 8.11 shows the SOC of the battery bank. For the first 5s the two Buck converters shared the load current between them. Since the load current was below 20A and the SOC of the battery was lower than 82%, the Bidirectional converter was in the charging mode, operating as a Buck converter charging the battery bank. Therefore, the two Buck converters in addition to the load current also supplied the input current of the Bidirectional converter. Between t = 5s and t = 10s the load current increased more than 20A, so the Bidirectional converter entered the sharing mode, operating as a Boost converter. All three converters shared the load current between them. After 10s the load current decreased under 18A so the Bidirectional converter changed mode to charging mode and continued charging the battery bank, while the Buck converters supplied all the load current and the input current for the Bidirectional converter. At t = 30s the load current decreases again. The Buck converters continued to supply the load current and the input current for the Bidirectional converter, while the Bidirectional converter remained in the charging mode until the SOC reached 82% at t = 68.7s. At an SOC of 82% the battery bank was fully charged, so the Bidirectional converter entered in idle mode, since the load current was below 20A.

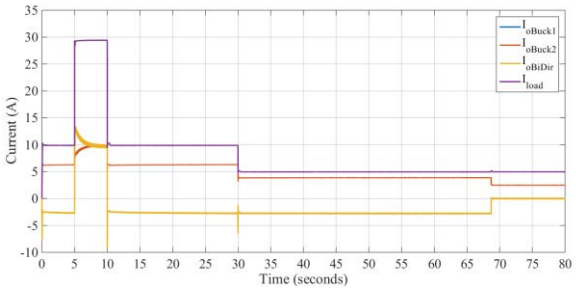

Figure 8.9: Output and Load Currents – with Step Load Changes

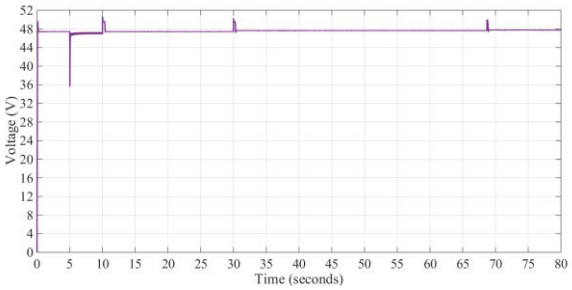

Figure 8.10: DC-Bus Voltage – with Step Load Changes

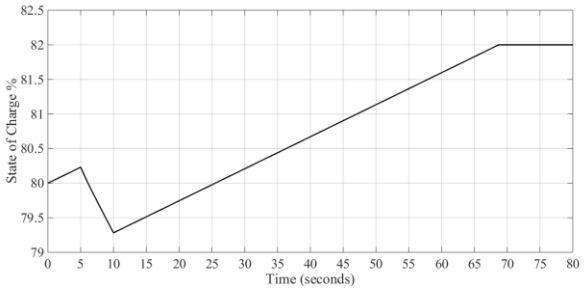

Figure 8.11: Battery State of Charge % – with Step Load Changes

8.1.3 Simulation of the DC Microgrid with Domestic Load (R_d = 0.092Ω for all Converters)

The third simulation carried out using the DC microgrid model consisted in simulating a typical domestic load situation. In this case a 24 hour load profile was used as the load for the DC microgrid. The load profile was obtained from logged power data of a typical Maltese house, showing complete 24h electrical power consumption during night and day times, with logging intervals of 30s. The data was logged as part of another research, during which the electrical power consumption of a domestic environment was monitored for a number of months [47].

Since this simulation had a period of 24 hours, the DC microgrid model was modified from a switched model to an average model, to reduce the simulation run time. The average model involved replacing all switching operations of the converters (PWM modulation block, IGBTs, and diodes) in the switched model with their averaged mathematical representation as obtained from mathematical modelling analysis in Chapter 4. The DC microgrid model with the BMS is shown in Figure 8.12. The power load profile is shown in Figure 8.13, and it was converted to a resistive load as can be observed in the DC microgrid model. This model also includes voltage restoration, however for this simulation this was not enabled. Figures 8.14 and 8.15 show the control systems for the Buck converters and the Bidirectional converter, respectively, which were modified to control the averaged converter models. Figures 8.16 and 8.17 show the averaged models for the Buck converter and Bidirectional converter, respectively. The droop resistance R_d was set to 0.092Ω for all converters to obtain equal load sharing. The battery bank connected to the Bidirectional converter was set to 24V with a capacity of 120Ah. The starting SOC of the battery was set to 68%. For this simulation the two Buck converters were assumed to be connected to stable 100V supplies.

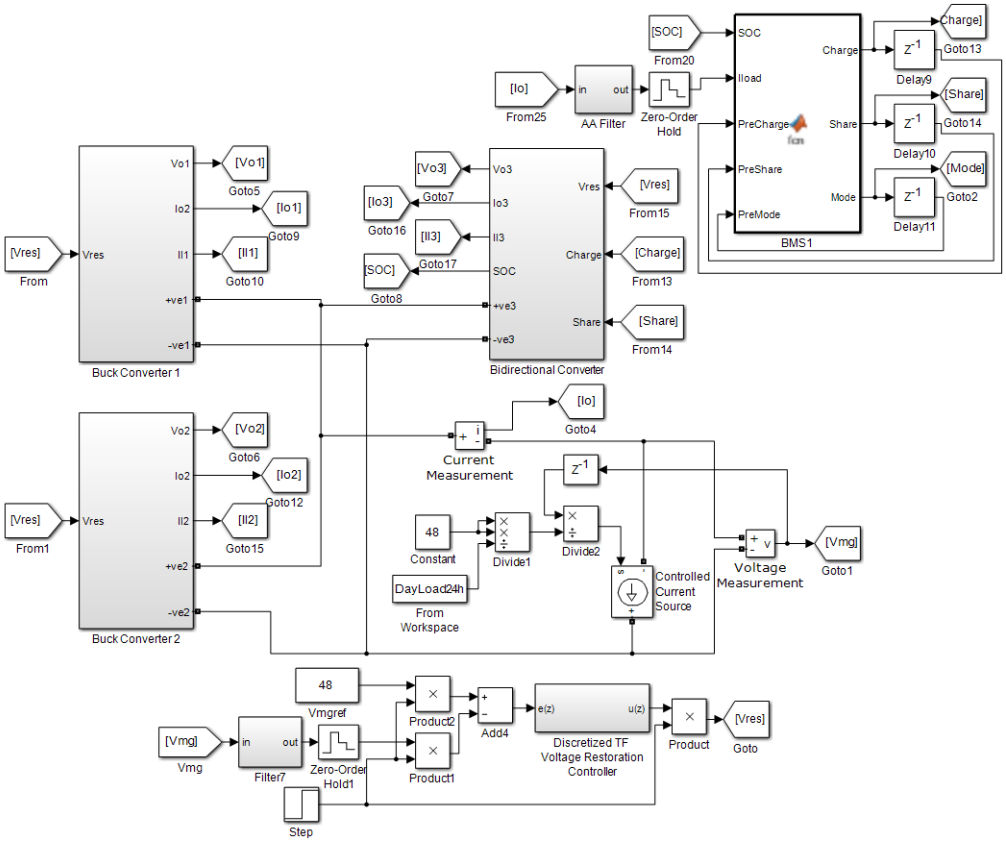

Figure 8.12: DC Microgrid Model with BMS and Load Profile

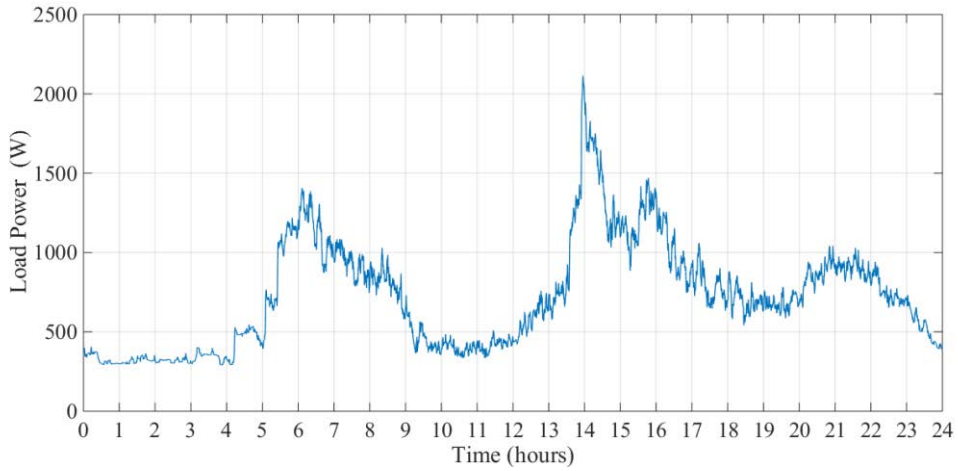

Figure 8.13: 24 Hour Domestic Power Load Profile

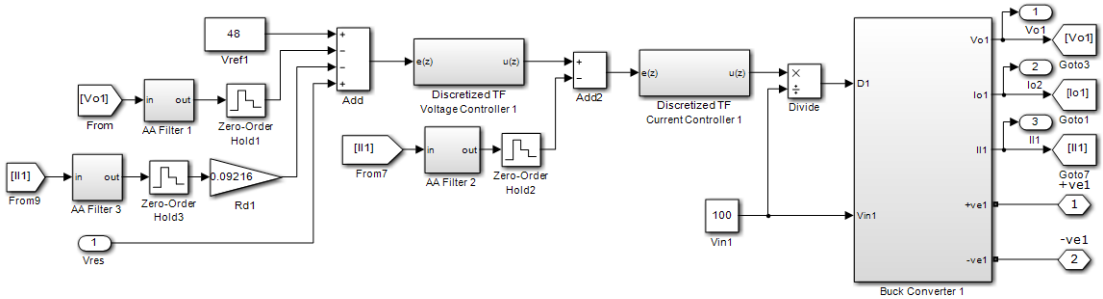

Figure 8.14: Control System for Averaged Buck Converter Model

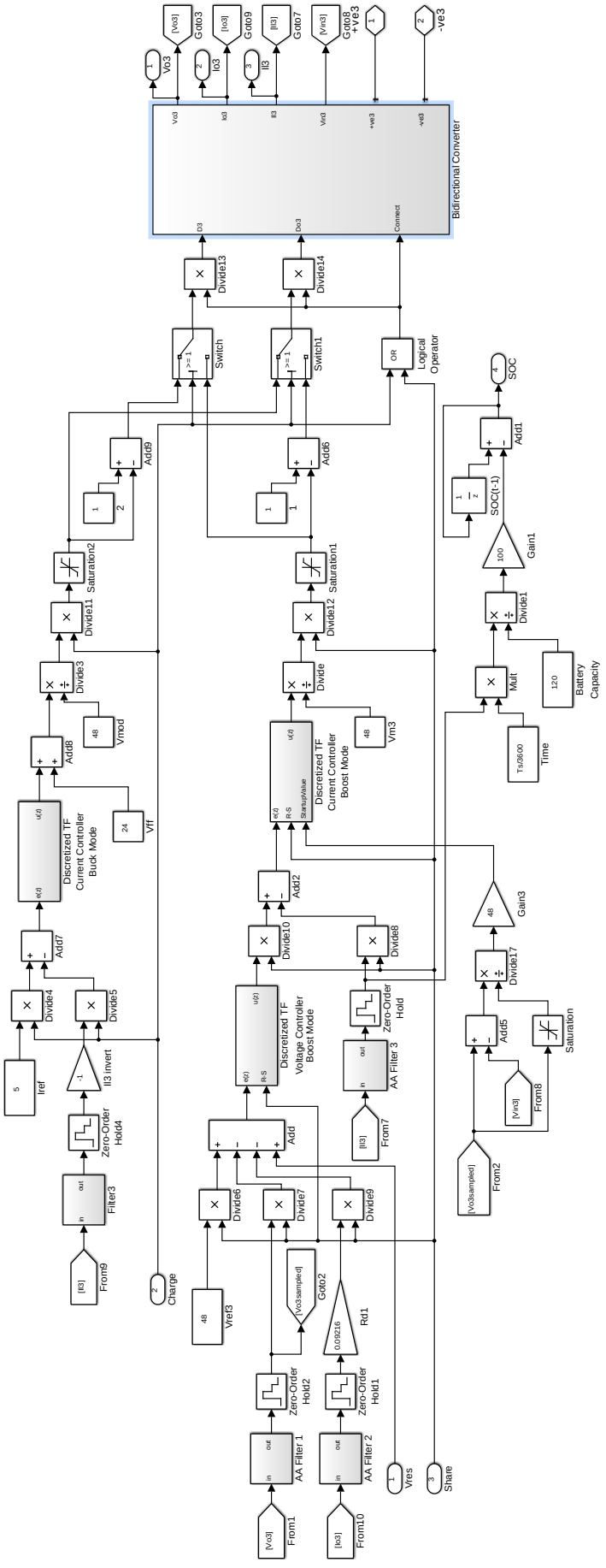

Figure 8.15: Control System for Averaged Bidirectional Converter Model

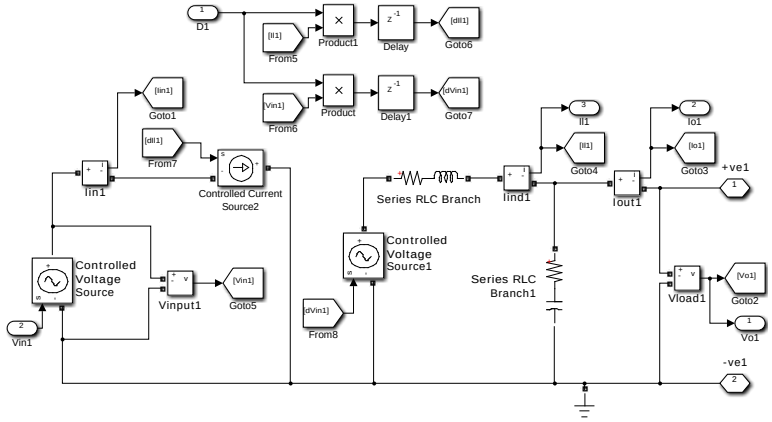

Figure 8.16: Averaged Buck Converter in Simulink

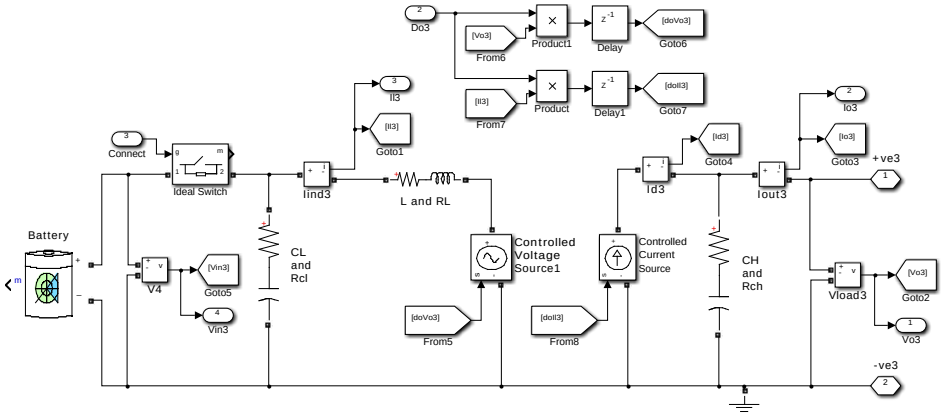

Figure 8.17: Averaged Bidirectional Converter in Simulink

Figures 8.18 to 8.20 show the results obtained from the simulation. Figure 8.18 shows the output current from each converter (I_{oBuck1}, I_{oBuck2}, and I_{oBiDir}) and the load current (I_{load}), while Figure 8.19 shows the output/DC-bus voltage (V_o). Figure 8.20 shows the SOC of the battery bank. From the simulation results one can note that the load current demand went over the 20A threshold on a number of occasions during the day, which induced the Bidirectional converter to aid the Buck converters with the load current. There were also a number of instances where the Bidirectional converter had time to charge the batteries, however although starting from an SOC of 68%, by the end of the 24 hours the SOC was at 62%. One can also observe that the DC-bus voltage has swell and dip disturbances caused by load variations and converter transitions, which give cause to further research to finding ways to mitigate these disturbances. The DC-bus voltage varies through the 24 hours due to droop control, according to the load current. Voltage restoration would help to correct this voltage variation to the desired 48V DC-bus voltage.

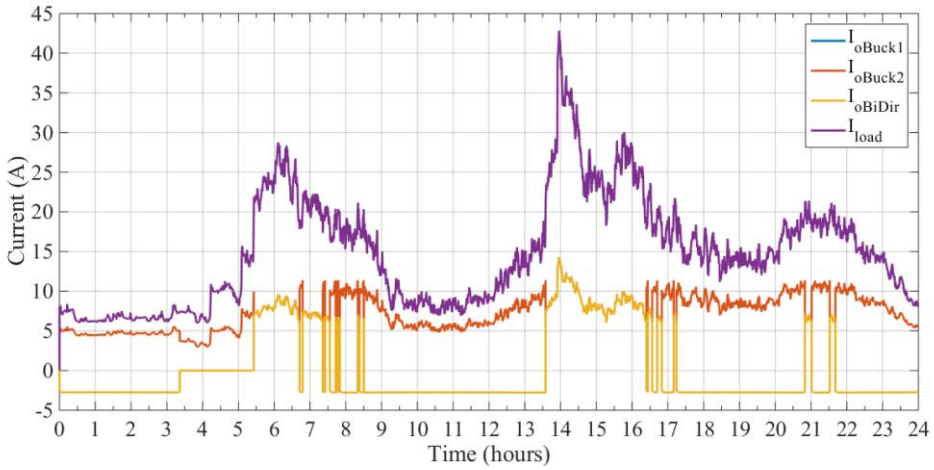

Figure 8.18: Output and Load Currents – 24h (R_d = 0.092Ω all Converters)

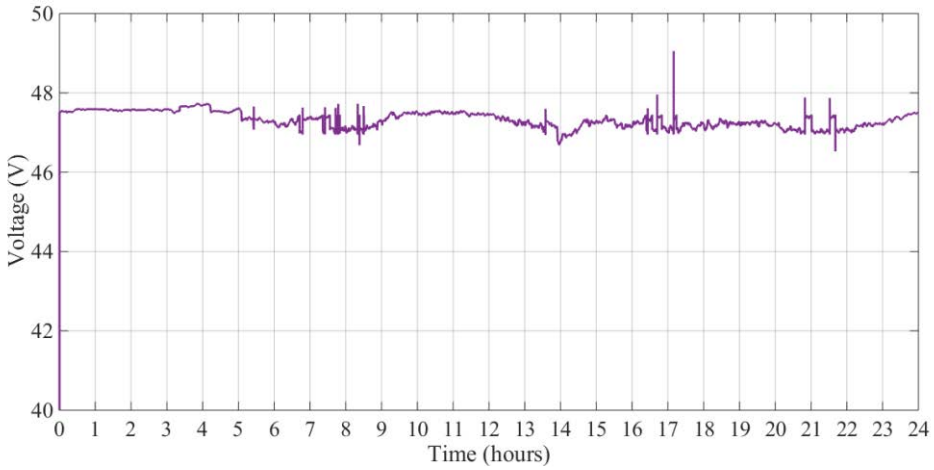

Figure 8.19: DC-Bus Voltage – 24h (R_d = 0.092Ω all Converters)

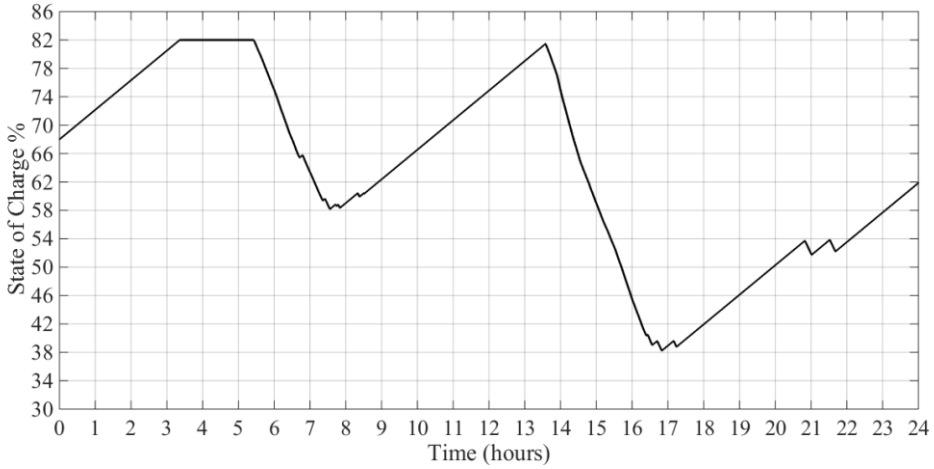

Figure 8.20: Battery State of Charge % – 24h (R_d = 0.092Ω all Converters)

8.1.4 Simulation of the DC Microgrid with Domestic Load (R_d = 0.24Ω for Buck Converters and R_d = 0.48Ω for Bidirectional Converter)

The fourth simulation carried out using the DC microgrid model consisted in repeating the simulation in subsection 8.1.3 with the 24 hour domestic load, but with different droop virtual resistances. In the previous simulation the droop resistance R_d

was set to 0.092Ω for all converters obtaining equal load sharing. For this simulation, the droop resistances were changed to 0.24Ω for both the Buck converters and 0.48Ω for the Bidirectional converter. This was done to reflect more the real current limitation in the hardware setup, which is limited to 20A output current from each Buck converter, and 10A output current from the Bidirectional converter, which corresponds to about 20A battery current. This limitation was caused by the 20A maximum current rating of the DC contactors, which were used within the converters.

As for the previous simulation, the same 24h load profile was used with the averaged DC microgrid model. The battery bank connected to the Bidirectional converter was set to 24V with a capacity of 120Ah and with a starting SOC of 68%. The two Buck converters were assumed to be connected to stable 100V supplies.

Figures 8.21 to 8.23 show the results obtained from the simulation. Figure 8.21 shows the output current from each converter (I_{oBuck1}, I_{oBuck2}, and I_{oBiDir}) and the load current (I_{load}), while Figure 8.22 shows the output/DC-bus voltage (V_o). Figure 8.23 shows the SOC of the battery bank. From the simulation results one can note that although the 24h load profile was not changed from the previous simulation, in this case the battery bank managed to get fully charged at a final SOC of 82%. With this setting of droop ratios, the Buck converters supplied a larger portion of the load current, leaving more time to the Bidirectional converter to charge the batteries. Similar to the simulation results in subsection 8.1.3, one can note that the DC-bus voltage contains swell and dip disturbances caused by sudden load variations and converter transitions. Large disturbances, such as the 9V (18.75%) dip before t = 21h, can cause damage to the loads and converters connected within the DC microgrid, therefore further research is needed to mitigate these disturbances.

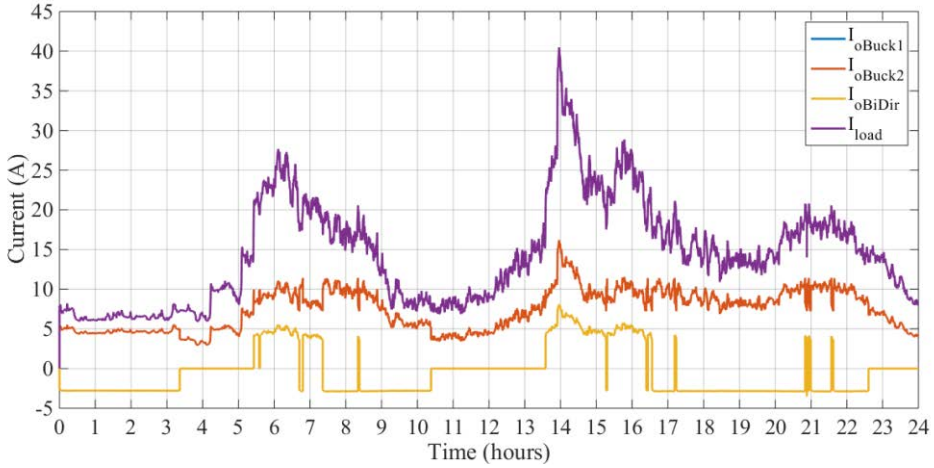

Figure 8.21: Output and Load Currents – 24h (R_d = 0.24Ω Buck Converters) (R_d = 0.48Ω Bidirectional Converter)

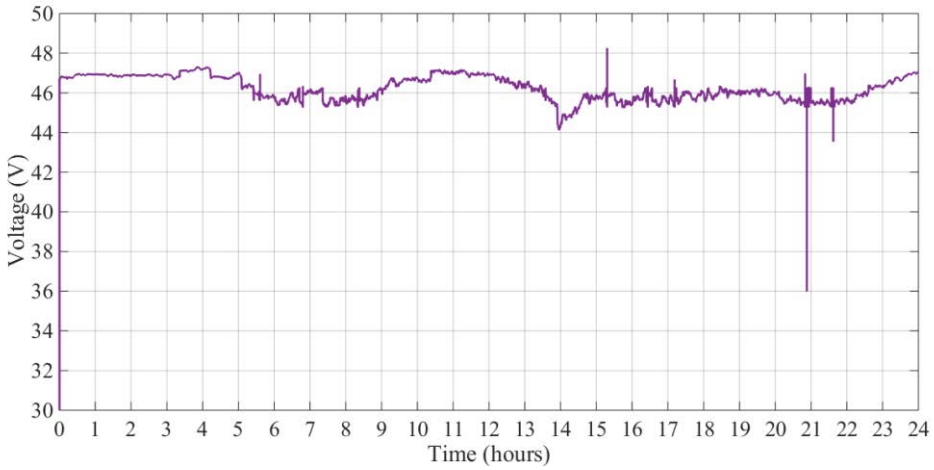

Figure 8.22: DC-Bus Voltage – 24h (R_d = 0.24Ω Buck Converters) (R_d = 0.48Ω Bidirectional Converter)

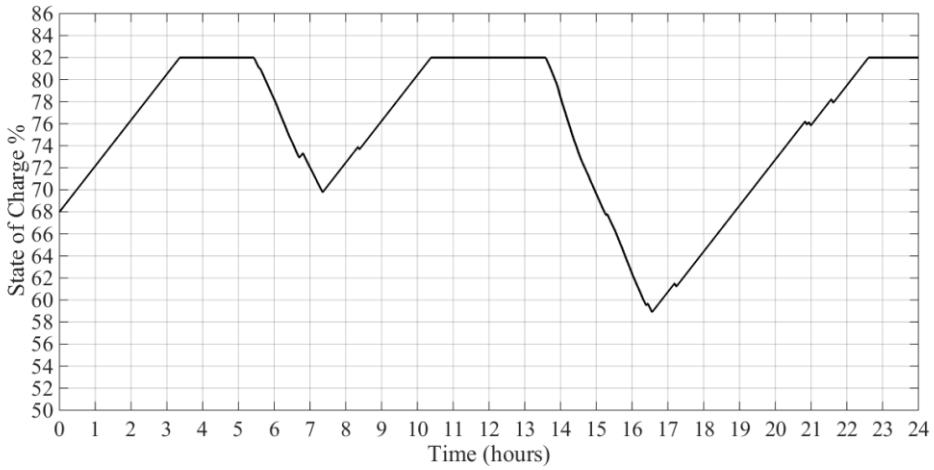

Figure 8.23: Battery State of Charge % – 24h (R_d = 0.24Ω Buck Converters) (R_d = 0.48Ω Bidirectional Converter)

8.1.5 Simulation of the DC Microgrid with Domestic Load including Voltage Restoration (R_d = 0.092Ω for all Converters)

The fifth simulation carried out using the DC microgrid model consisted in repeating the simulation from subsection 8.1.3 with the 24 hour domestic load, however this time with the control system including voltage restoration. The droop resistance R_d was set to 0.092Ω for all converters obtaining equal load sharing. The averaged DC microgrid model was again used for this simulation. The battery bank connected to the Bidirectional converter was set to 24V with a capacity of 120Ah and the SOC was set to 68%. The two Buck converters were assumed to be connected to stable 100V supplies.

Figures 8.24 to 8.26 show the results obtained from the simulation. Figure 8.24 shows the output current from each converter (I_{oBuck1}, I_{oBuck2}, and I_{oBiDir}) and the load current (I_{load}), while Figure 8.25 shows the output/DC-bus voltage (V_o). Figure 8.26 shows the SOC of the battery bank. In this case using voltage restoration control the DC-bus voltage was restored back to the desired 48V. This increase in DC-bus voltage caused

an increase in the load current, thus the Bidirectional converter shared a higher current, which in turn caused higher discharge in the batteries. This resulted in a lower battery SOC of approximately 48.8% at the end of the 24h, when compared to the SOC of 62% from the simulation results in subsection 8.1.3. As observed in the previous simulation results, the DC-bus voltage contains swell and dip disturbances caused by load variations and converter transitions, which should be mitigated to prevent damage to equipment.

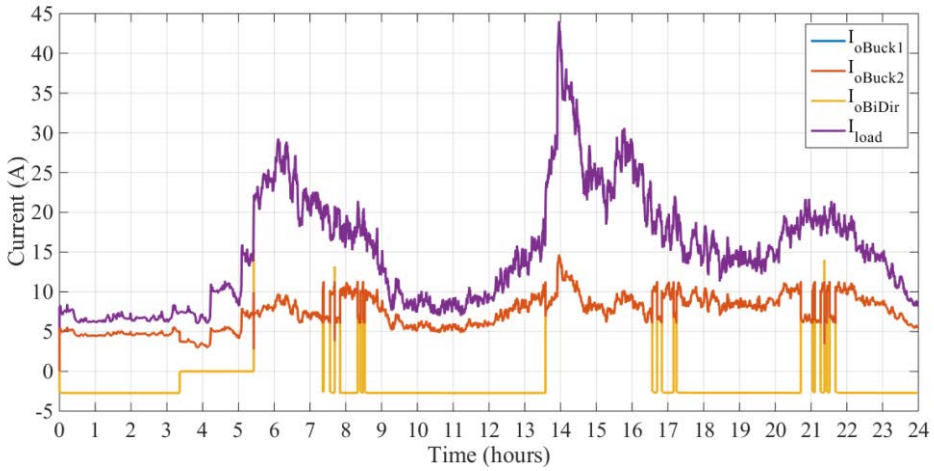

Figure 8.24: Output and Load Currents – 24h (R_d = 0.092Ω all Converters) – with Voltage Restoration

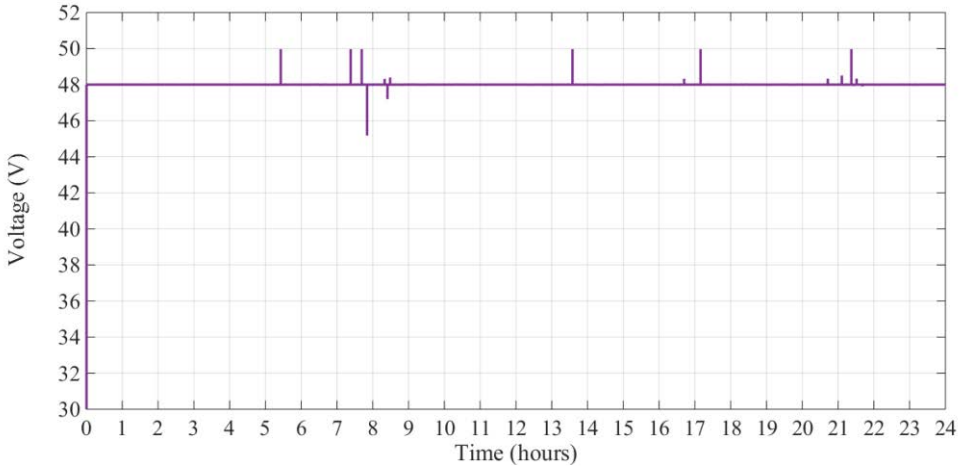

Figure 8.25: DC-Bus Voltage – 24h (R_d = 0.092Ω all Converters) – with Voltage Restoration

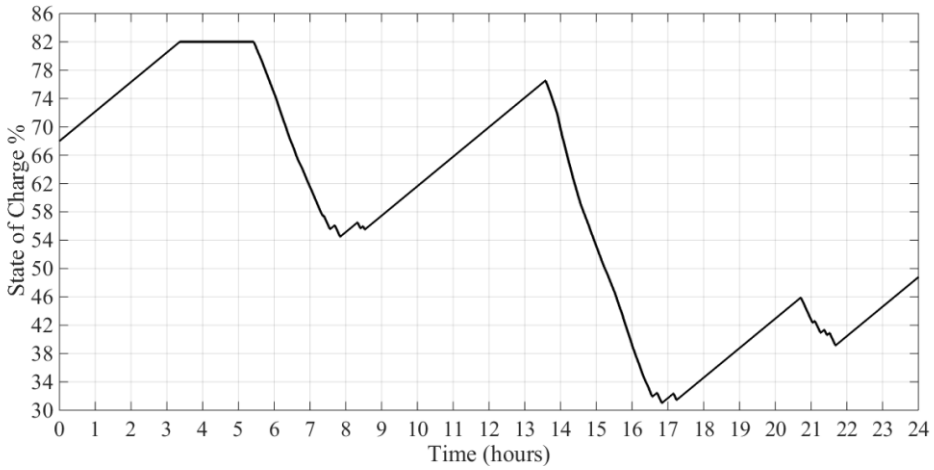

Figure 8.26: Battery State of Charge % – 24h (R_d = 0.092Ω all Converters) – with Voltage Restoration

8.1.6 Simulation of the DC Microgrid with Domestic Load including Voltage Restoration (R_d = 0.24Ω for Buck Converters and R_d = 0.48Ω for Bidirectional Converter)

The sixth simulation carried out using the DC microgrid model consisted in repeating the simulation from subsection 8.1.4 with the 24 hour domestic load, however this time with the control system including voltage restoration. The droop resistance R_d was set to 0.24Ω for both the Buck converters and 0.48Ω for the Bidirectional converter. The averaged DC microgrid model was again used for this simulation. The battery bank connected to the Bidirectional converter was set to 24V with a capacity of 120Ah and the SOC was set to 68%. The two Buck converters were assumed to be connected to stable 100V supplies.

Figures 8.27 to 8.29 show the results obtained from the simulation. Figure 8.27 shows the output current from each converter (I_{oBuck1}, I_{oBuck2}, and I_{oBiDir}) and the load current (I_{load}), while Figure 8.28 shows the output/DC-bus voltage (V_o). Figure 8.29 shows the SOC of the battery bank. Similar to the previous simulation, using voltage restoration control the DC-bus voltage was restored back to the desired 48V. This increase in DC-bus voltage caused an increase in the load current, thus the Bidirectional converter shared a higher current, which in turn caused higher discharge in the batteries. This resulted in a lower battery SOC of approximately 76% at the end of the 24h, when compared to the full charge SOC at 82% from the simulation results in subsection 8.1.4. As observed in the previous simulation results, the DC-bus voltage contains swell and dip disturbances caused by load variations and converter transitions, which should be mitigated to provide a more constant DC-bus voltage.

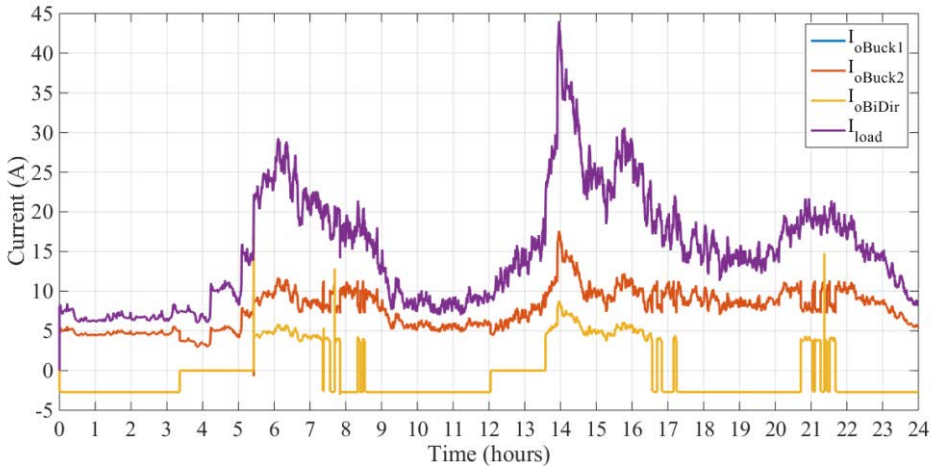

Figure 8.27: Output and Load Currents – 24h (R_d = 0.24Ω Buck Converters) (R_d = 0.48Ω Bidirectional Converter) – with Voltage Restoration

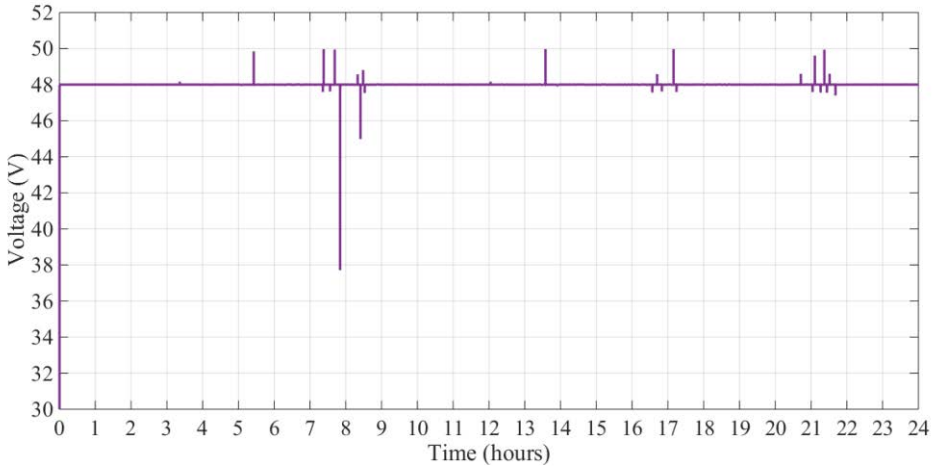

Figure 8.28: DC-Bus Voltage – 24h (R_d = 0.24Ω Buck Converters) (R_d = 0.48Ω Bidirectional Converter) – with Voltage Restoration

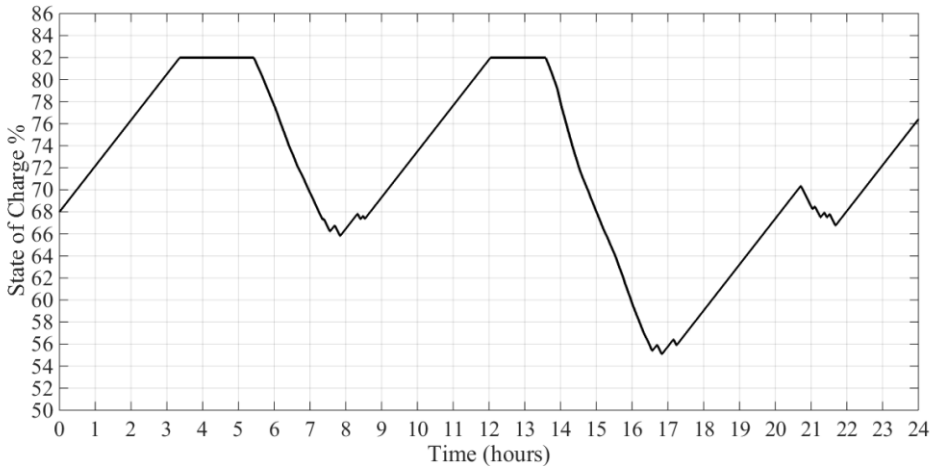

Figure 8.29: Battery State of Charge % – 24h (R_d = 0.24Ω Buck Converters) (R_d = 0.48Ω Bidirectional Converter) – with Voltage Restoration

8.1.7 Simulation of the DC Microgrid with Domestic Load (R_d = 0.24Ω for the first Buck Converter, PV Supply for the second Buck Converter, and R_d = 0.48Ω for Bidirectional Converter)

The final simulation carried out using the DC microgrid model consisted in operating one of the Buck converters (Buck 2) from a photovoltaic (PV) source. A 24 hour PV power profile was obtained from logged power data of a typical 1kW PV system in Malta during spring, with logging intervals of 30s. The data was logged as part of another research [47]. The 24 hour domestic load profile was again used to provide the resistive load for the DC microgrid. The averaged DC microgrid model was again used for this simulation. The droop resistance R_d was set to 0.24Ω for the first Buck converter and 0.48Ω for the Bidirectional converter. Buck converter 1 was assumed to be connected to a stable 100V supply. Buck converter 2 was supplied from the PV source, with the power profile shown in Figure 8.30. The control system for Buck converter 2 consisted of a current control loop, controlling the inductor current. The current reference for the current control loop was calculated from the PV power profile. Figure 8.31 shows the averaged control system for the PV-connected Buck converter 2. The battery bank connected to the Bidirectional converter was set to 24V with a capacity of 120Ah and the SOC was set to 68%.

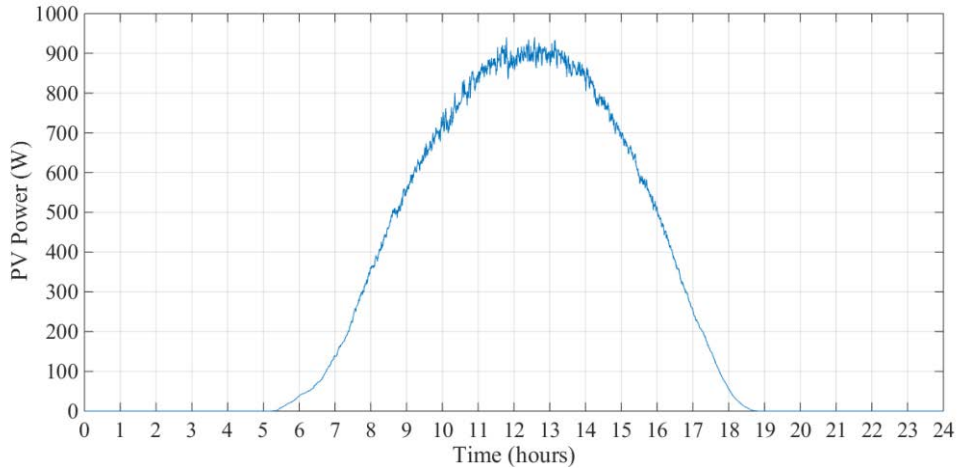

Figure 8.30: PV Power Profile

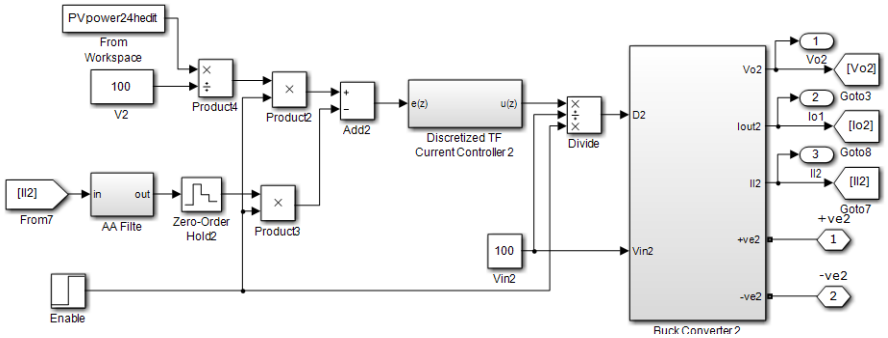

Figure 8.31: Control System for Averaged PV-Connected Buck Converter 2 Model

Figures 8.32 to 8.34 show the results obtained from the simulation. Figure 8.32 shows the output current from each converter (I_{oBuck1}, I_{oBuck2}, and I_{oBiDir}) and the load current (I_{load}), while Figure 8.33 shows the output/DC-bus voltage (V_o). Figure 8.34 shows the SOC of the battery bank. In this case the PV-connected Buck converter supplied all available power from the PV to the DC-bus. This meant that at certain times Buck converter 1 supplied all the load current, including the input current taken by the Bidirectional converter to charge the batteries. The PV-connected Buck converter 2 took over around 9:00, taking over the supply of the load from the other converters, although in the afternoon all the converters had to contribute to supply the load current. The DC-bus voltage varied between 43V and 48V during the 24 hours, which can be mitigated with voltage restoration. With regards to the battery bank SOC, although starting at 68%, the batteries ended the 24 hours with full charge at an SOC of 82%.

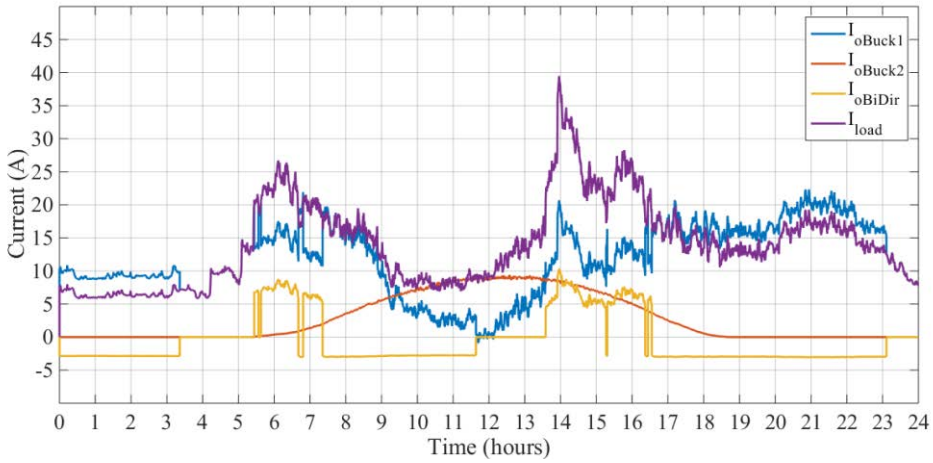

Figure 8.32: Output and Load Currents – 24h (R_d = 0.24Ω Buck Converter 1) (PV Connected Buck Converter 2) (R_d = 0.48Ω Bidirectional Converter)

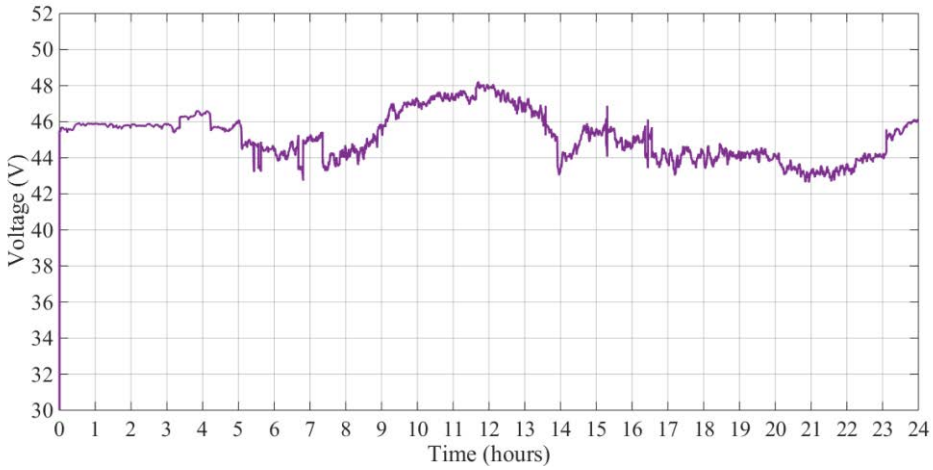

Figure 8.33: DC-Bus Voltage – 24h (R_d = 0.24Ω Buck Converter 1) (PV Connected Buck Converter 2) (R_d = 0.48Ω Bidirectional Converter)

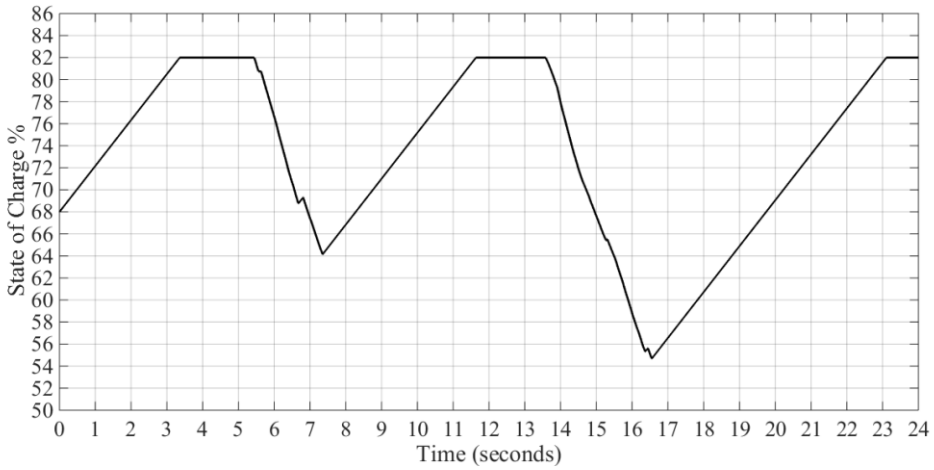

Figure 8.34: Battery State of Charge % – 24h (R_d = 0.24Ω Buck Converter 1) (PV Connected Buck Converter 2) (R_d = 0.48Ω Bidirectional Converter)

8.1.8 Summary of DC Microgrid Simulations

A 48V DC microgrid was modelled in Simulink/Matlab consisting of two Buck converters and a Bidirectional converter connected in parallel while sharing a resistive load. A 24V 120Ah battery bank was connected to the DC microgrid by means of the Bidirectional converter whose mode of operation was controlled by a battery management system (BMS). A number of simulations were performed with this DC microgrid model. The initial simulation tested the operation of the converters during two different scenarios: (1) when all the converters were sharing the load current between them, and (2) when the Buck converters were sharing the load current and the input current of the Bidirectional converter, while the Bidirectional converter was charging the battery bank.

The DC microgrid was also simulated under a worst case load change scenario with large step changes in load. Other simulations involved the operation of the DC microgrid with a typical 24 hour domestic load profile. For these simulations the DC microgrid was simulated for a 24 hour period, testing the operation of the converters, charging and discharging of the battery bank, and the operation of the BMS. All simulations confirmed the correct operation of the BMS algorithm, converter control system, and the converters connected in a DC microgrid configuration.

8.2 DC Microgrid Experimental Tests

A lab-based experimental DC microgrid was set up consisting of two Buck converters and a Bidirectional converter connected in parallel, together with resistive loads. The DC microgrid bus voltage was set to 48V. The Buck converters had an input voltage of 100V and provided an output voltage of 48V at the DC-bus. The Bidirectional converter operated between the 48V of the DC-bus and the 24V 120Ah battery bank. The Bidirectional converter operated as a Boost converter when sharing the resistive load and as a Buck converter when charging the battery bank. A block diagram of the DC microgrid setup is shown in Figure 8.35.

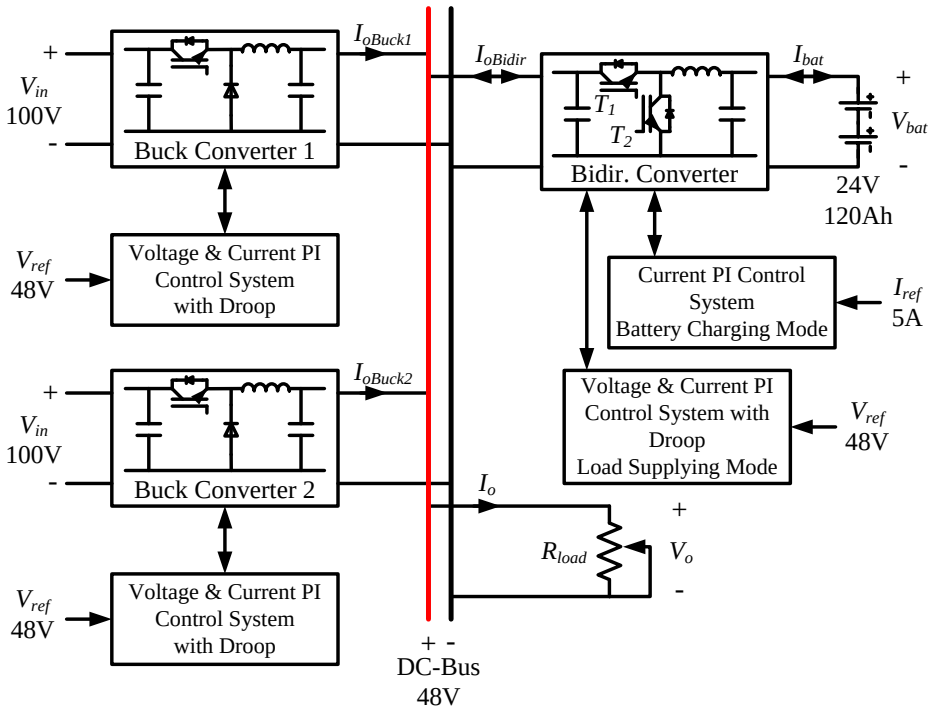

Figure 8.35: Block Diagram – Test Setup – Experimental DC Microgrid

Experimental tests with the DC microgrid setup consisted in two scenarios: the first scenario having the resistive load shared between the three converters (battery bank used as a source), and the second scenario having the Bidirectional converter charging the battery bank with the Buck converters supplying the resistive load and the input current required by the Bidirectional converter to charge the batteries. This section presents the results obtained from these experimental tests.

8.2.1 Scenario 1: Load Sharing between All Converters

In this case the Bidirectional converter is operated as a Boost converter in the load supplying/sharing mode. The control system for the Buck converters and the Bidirectional converter consisted of nested current and voltage PI controllers with the

V-I droop loop. The droop resistance R_d was set to 0.092Ω (Chapter 5 subsection 5.4.1.3), for all converters to obtain equal load sharing. The voltage reference for the voltage controllers was set to 48V. The resistive load was set to 2.4Ω (20A at 48V).

The Buck converters were switched on, one at a time, sharing equally the load current for a load resistance of 2.4Ω. Next, the Bidirectional converter was switched on to share the load with the Buck converters, obtaining equal current sharing between the three converters.

Figures 8.36 and 8.37 show the experimental results obtained from the DC microgrid, with the converters sharing a resistive load of 2.4Ω while operated with V-I droop control. The traces in Figure 8.36 are the output current of Buck 1 (I_{o1}), the output current of Buck 2 (I_{o2}), the output current of the Bidirectional (I_{oBidir}), and the total/load current (I_o). The traces in Figure 8.37 are the load/DC-bus voltage (V_o), the battery voltage (V_{bat}), and the battery current (I_{bat}).

Figure 8.36 shows the Bidirectional converter starting to share the load with the two Buck converters, until the three converters reach equal current sharing. Figure 8.37 shows the battery current being supplied to the Bidirectional converter.

Gold trace: Buck Converter 1 Output Current I_{oBuck1} (5A/div)
Magenta trace: Buck Converter 2 Output Current I_{oBuck2} (5A/div)
Blue trace: Bidirectional Converter Output Current I_{oBidir} (5A/div)
Green trace: Load Current I_o (5A/div)

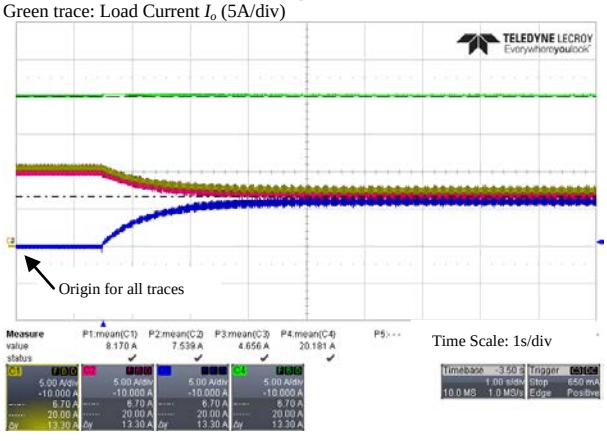

Figure 8.36: DC Microgrid – V-I Droop
– Buck 1 and 2 Converters Supplying Load
– Bidirectional Converter Switching On
– Resistive Load R_{load} = 2.4Ω

Gold trace: Load/DC-Bus Voltage V_o (20V/div)
Magenta trace: Battery Voltage V_{bat} (20V/div)
Blue trace: Battery Current - Input to Bidirectional Converter I_{bat} (5A/div)

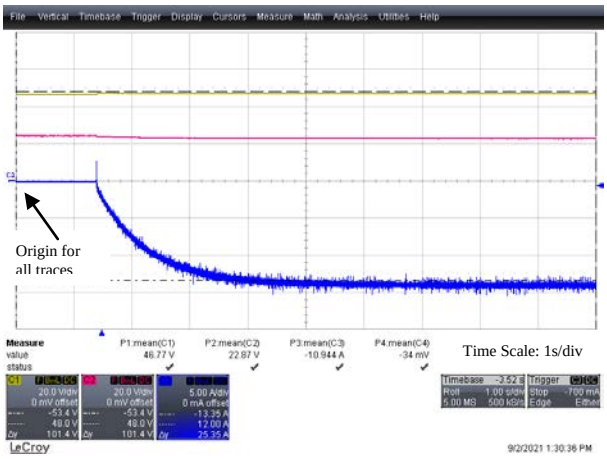

Figure 8.37: DC Microgrid – V-I Droop
– Buck 1 and 2 Converters Supplying Load
– Bidirectional Converter Switching On
– Battery Bank Side – Resistive Load R_{load} = 2.4Ω

Table 8.1 lists the results obtained from the experimental tests performed with the DC microgrid when the Bidirectional converter was operated as a Boost converter in load supplying/sharing mode. All converters used V-I droop control to share the load

current between them, with an equal value of R_d to obtain equal load sharing. The resistive load was set to set 2.4Ω (20A at 48V). The input voltage V_{in} for both Buck converters was 100V. The Bidirectional converter was connected to a 24V 120Ah battery bank. The voltage reference for the voltage controllers was set to 48V.

R_d = 0.092Ω for all Converters								
Target I_o	**R_{load}**	**Buck 1 I_{oBuck1}**	**Buck 2 I_{oBuck2}**	**Bidir. I_{oBidir}**	**Load I_o**	**Load V_o**	**Battery I_{bat}**	**Battery V_{bat}**
≈20A	2.4Ω	6.99A	6.77A	6.63A	20.2A	46.81V	15.60A	22.22V
Measurements taken from LeCroy Oscilloscope using differential voltage probe and current probes.								

Table 8.1: DC Microgrid Result – Load Sharing All Converters

The results demonstrate correct operation of the converters in a DC microgrid configuration. The converters showed the capability to equally share the load current between them with output currents around the expected 6.58A for each converter, for an expected total load current of 19.75A at 47.39V. Small differences in the output currents were expected, which are mainly due to differences between the converters. The load current of ≈20A was successfully shared in approximately 4s, matching the sharing time obtained from the simulation covered in subsection 8.1.1.

8.2.2 Scenario 2: Buck Converters Sharing the Current Required by Load and Bidirectional Converter (Charging Batteries)

In this case the Bidirectional converter is operated as a Buck converter in the battery charging mode. The control system for the Bidirectional converter consisted of a current PI controller, while the control system for the two Buck converters consisted of nested current and voltage PI controllers with the V-I droop loop. The droop resistance R_d was set to 0.092Ω (Chapter 5 subsection 5.4.1.3), for both Buck converters to obtain equal load sharing. The voltage reference for the voltage controllers within the Buck converters' control systems was set to 48V. The current reference for the current controller within the Bidirectional converter's control system was set to 5A. The test was performed with two values of resistive loads, set to 9.6Ω (5A at 48V) and 2.4Ω (20A at 48V).

The Buck converters were switched on, one at a time, sharing equally the resistive load. Next, the Bidirectional converter was switched on, to start charging the battery bank. The input current to the Bidirectional converter was supplied by the two Buck converters.

Figures 8.38 to 8.41 show the experimental results obtained from the DC microgrid, with the Buck converters operated with V-I droop control to supply a common

resistive load (9.6Ω and 2.4Ω), and the Bidirectional converter charging the battery bank. The traces in Figures 8.38 and 8.40 are the output current of Buck 1 (I_{o1}), the output current of Buck 2 (I_{o2}), the input current of the Bidirectional (I_{oBidir}), and the load current (I_o). The traces in Figures 8.39 and 8.41 are the load/DC-bus voltage (V_o), the battery voltage (V_{bat}), and the battery current (I_{bat}).

Figure 8.38 shows the two Buck converters sharing the load current for a resistive load of 9.6Ω, and the Bidirectional converter starts charging the batteries. The Buck converters increase their output current to supply the resistive load and the additional Bidirectional converter input current. Figure 8.39 shows the Bidirectional converter charging the battery bank with a current of 5A. Figures 8.40 and 8.41 show the same as explained above but with the resistive load changed to 2.4Ω.

Gold trace: Buck Converter 1 Output Current I_{oBuck1} (2A/div)
Magenta trace: Buck Converter 2 Output Current I_{oBuck2} (2A/div)
Blue trace: Bidirectional Converter Input Current I_{oBidir} (2A/div)
Green trace: Load Current I_o (2A/div)

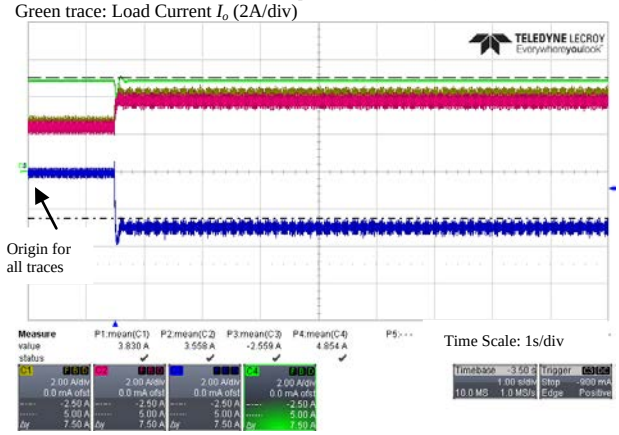

Figure 8.38: DC Microgrid – V-I Droop
– Buck 1 and 2 Converters Supplying Load & Bidirectional Converter Input Current
– Bidirectional Converter Switching On Charging Batteries
– Resistive Load R_{load} = 9.6Ω

Gold trace: Load/DC-Bus Voltage V_o (20V/div)
Magenta trace: Battery Voltage V_{bat} (20V/div)
Blue trace: Battery Current – Output from Bidirectional Converter I_{bat} (5A/div)

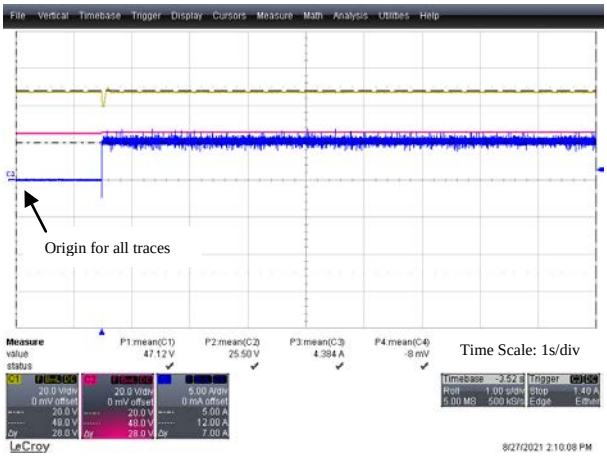

Figure 8.39: DC Microgrid – V-I Droop
– Buck 1 and 2 Converters Supplying Load & Bidirectional Converter Input Current
– Bidirectional Converter Switching On Charging Batteries
– Battery Bank Side – Resistive Load R_{load} = 9.6Ω

Gold trace: Buck Converter 1 Output Current I_{oBuck1} (5A/div)
Magenta trace: Buck Converter 2 Output Current I_{oBuck2} (5A/div)
Blue trace: Bidirectional Converter Input Current I_{oBidir} (5A/div)
Green trace: Load Current I_o (5A/div)

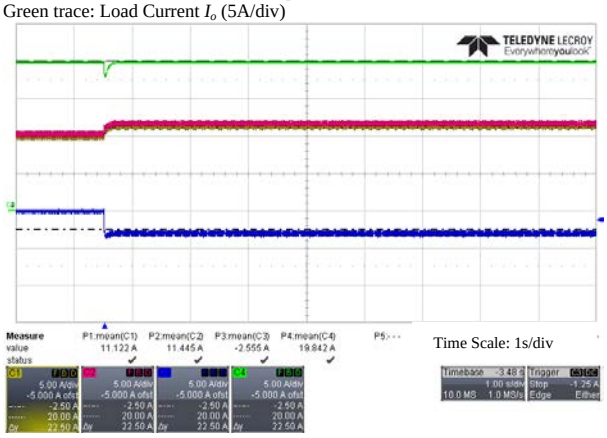

Figure 8.40: DC Microgrid – V-I Droop
– Buck 1 and 2 Converters Supplying Load & Bidirectional Input Current
– Bidirectional Converter Switching On Charging Batteries
– Resistive Load R_{load} = 2.4Ω

Gold trace: Load/DC-Bus Voltage V_o (20V/div)
Magenta trace: Battery Voltage V_{bat} (20V/div)
Blue trace: Battery Current – Output from Bidirectional Converter I_{bat} (5A/div)

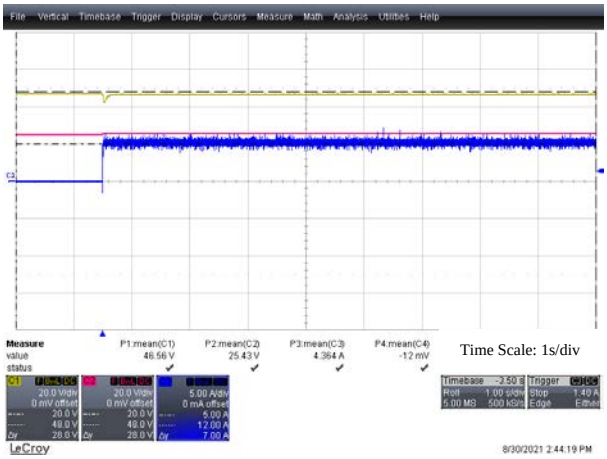

Figure 8.41: DC Microgrid – V-I Droop
– Buck 1 and 2 Converters Supplying Load & Bidirectional Input Current
– Bidirectional Converter Switching On Charging Batteries
– Battery Bank Side – Resistive Load R_{load} = 2.4Ω

Table 8.2 lists the results obtained from the experimental tests performed with the DC microgrid when the Bidirectional converter was operated as a Buck converter in battery charging mode. The two Buck converters used V-I droop control with an equal value of R_d, to obtain equal load sharing. The Bidirectional converter charged the batteries at 5A. The test was performed with resistive loads of 9.6Ω (5A at 48V) and 2.4Ω (20A at 48V). The input voltage V_{in} for both Buck converters was 100V. The Bidirectional converter was connected to a 24V 120Ah battery bank. The voltage reference for the voltage controllers was set to 48V.

R_d = 0.092Ω for the Buck Converters								
Target I_o	**R_{load}**	**Buck 1 I_{oBuck1}**	**Buck 2 I_{oBuck2}**	**Bidir. I_{oBidir}**	**Load I_o**	**Load V_o**	**Battery I_{bat}**	**Battery V_{bat}**
≈5A	9.6Ω	3.96A	3.82A	-2.85A	4.94A	47.59V	4.91A	25.98V
≈20A	2.4Ω	11.5A	11.62A	-2.94A	19.68A	46.68V	5.04A	25.75V
Measurements taken from LeCroy Oscilloscope using differential voltage probe and current probes.								

Table 8.2: DC Microgrid Result – Buck Converters Load Sharing – Bidirectional Converter Battery Bank Charging

The results demonstrate correct operation of the converters in a DC microgrid used to supply power to a resistive load and to charge a battery bank at the same time. For both test cases, the two Buck converters successfully shared the load current and Bidirectional converter input current, with approximate equally shared current. Small differences in the output currents were expected, which are mainly due to differences between the converters. In both test cases the Bidirectional converter successfully charged the battery bank with a charging current of ≈5A, and the input current to the Bidirectional converter of ≈2.5A was successfully supplied and divided between the two Buck converters. For the test with the 2.4Ω resistive load, the two Buck

converters reached equal current sharing in approximately 0.25s, matching the sharing time obtained from the simulation covered in subsection 8.1.1.

8.2.3 Summary of DC Microgrid Tests

The previous subsections presented the results obtained from experimental testing with the DC microgrid setup. The 48V DC microgrid setup consists of two Buck converters, a Bidirectional converter connected to a 24V battery bank, and a resistive load bank. Two scenarios were tested: the first scenario when the three converters shared the resistive load between them, and the second scenario when the two Buck converters shared the load and the Bidirectional converter charged the battery bank.

For the first scenario the Bidirectional converter was operated as a Boost converter. All converters used V-I droop with a droop resistance R_d set to 0.092Ω to obtain equal load sharing. A resistive load of 2.4Ω (20A at 48V) was connected to the DC microgrid. The results showed that the converters successfully shared the load current approximately equally between them with output currents around the expected 6.58A for each converter, for an expected total load current of 19.75A at 47.39V. The load current of ≈20A was successfully shared in approximately 4s, in agreement with the sharing time obtained from the simulation in subsection 8.1.1.

For the second scenario the Bidirectional converter was operated as a Buck converter and charged the battery bank. The two Buck converters used V-I droop with a droop resistance R_d set to 0.092Ω to obtain equal load sharing. Testing was carried out using two values of load resistances; 9.6Ω (5A at 48V) and 2.4Ω (20A at 48V). The results showed that for both test cases the two Buck converters successfully shared the load current and Bidirectional input current approximately equally between them. In both test cases the Bidirectional converter successfully charged the battery bank with a charging current of ≈5A. The input current of ≈2.5A to the Bidirectional converter was supplied and divided between the two Buck converters. For the test carried out with a load resistance of 2.4Ω, the two Buck converters reached equal current sharing in approximately 0.25s, agreeing with the sharing time obtained from the simulation covered in subsection 8.1.1.

The experimental results obtained from both test scenarios show correct operation of the three converters in a DC microgrid configuration, which were also verified with matching simulation results.

8.3 Conclusion

This chapter covered the simulations performed in Simulink/Matlab to test the Buck and Bidirectional converters, connected together with the control systems needed by the converters to operate within a DC microgrid configuration. This chapter also presented the results obtained from the experimental tests performed on the Buck and Bidirectional converters, which were connected together to form a DC microgrid. The lab-based DC microgrid consisted of two Buck converters (Buck 1 and Buck 2) and a Bidirectional converter, connected to a resistive load bank and battery bank.

A DC microgrid with a DC-bus voltage of 48V was simulated using a model consisting of two Buck converters and a Bidirectional converter connected in parallel while sharing a common resistive load. The Bidirectional converter connected a 24V 120Ah battery bank to the DC microgrid, and its mode of operation was controlled by a battery management system (BMS). The first simulation with the DC microgrid tested the operation of the converters during two different scenarios: the first scenario when all the converters were sharing the load current between them, and the second scenario when the Buck converters were sharing the load current and the input current of the Bidirectional converter, while the Bidirectional converter was charging the battery bank. Another simulation was performed with large step changes in load to simulate the DC microgrid under a worst case load change. Other DC microgrid simulations were performed with a typical 24 hour domestic load profile, testing the operation of the converters, charging and discharging of the battery bank, and the operation of the BMS. The BMS was used to control the Bidirectional converter by selecting its mode of operation between load sharing, charging, and idle operation. The simulations provided very good results, demonstrating correct operation of the converters and their controller systems when connected in a DC microgrid configuration. The BMS can be used to optimizing energy flow in the DC microgrid. These simulation results can be observed in section 8.1.

To perform the experimental testing, the two Buck converters and the Bidirectional converter prototypes were all connected in parallel together with a resistive load bank, to form an experimental lab-based 48V DC microgrid. Two scenarios were presented and tested: the first scenario consisted in having all the converters sharing the load between them and the second scenario consisted in having the Buck converters

sharing the load and the Bidirectional converter charging the 24V battery bank. Considering the first scenario, a resistive load of 2.4Ω was connected to the DC microgrid and the three converters used V-I droop control to share the load current between them, with an equal value of R_d to obtain equal load sharing. During this test the Bidirectional converter was operating as a Boost converter in load supplying/sharing mode, sharing the load with the other converters, while being supplied from the battery bank. The Buck converters were supplied from power supplies. The experimental results showed that all converters successfully shared the load current approximately equally between themselves, achieving a total load current of ≈20A, which was successfully shared in approximately 4s. Considering the second scenario, resistive loads of 9.6Ω and 2.4Ω were connected to the DC microgrid and the two Buck converters used V-I droop control to share the load current between them, with an equal value of R_d to obtain equal load sharing. During these two tests the Bidirectional converter operated as a Buck converter in battery charging mode and charged the battery bank with a charging current of 5A. Therefore, the two Buck converters supplied equal current to the resistive load and also shared the Bidirectional converter input current. The Buck converters successfully shared the supplied total load currents of ≈5A and ≈20A for the two tests performed with resistive loads of 9.6Ω and 2.4Ω, respectively, together with the ≈2.5A Bidirectional converter input current. For the test with the 2.4Ω resistive load, the two Buck converters reached equal sharing in approximately 0.25s.

The experimental results have confirmed the correct operation of all the converters connected together in a DC microgrid setup. The system was tested successfully at various load levels. This experimental setup will also serve as a basis for further research in the field of DC microgrids.

Chapter 9 Conclusion

The research presented involved the implementation of an experimental laboratory-based DC microgrid, including the formulation and design of algorithms to control the converters within the DC microgrid. The setting up of the experimental DC microgrid involved the design, building, and testing of three DC-DC converters, including energy storage. Two 2.5kW Buck converters and a 1.5kW Bidirectional converter made up the DC microgrid setup. The two Buck converters were used as power sources which in practice could be fed by renewable energy sources. The Bidirectional converter was used to connect a 24V battery bank. The DC microgrid was designed for a 48V DC-bus voltage, which was identified as an ideal voltage level for domestic use in a research study [15]. The two Buck converters were operated from a 100V input voltage to provide a 48V output voltage, while the Bidirectional converter was built to operate between 48V on the DC-bus-side and 24V on the battery-bank-side.

9.1 Summary of Main Contributions and Attainments

A literature search in the field of DC microgrids was conducted, with special focus on converter modelling and design, and the control systems needed to operate converters within a DC microgrid. Three areas of interest were identified: converter modelling, droop control, and battery management.

The selection of the converters and the control systems in use is very important for proper operation of the DC microgrid. Thus, having proper understanding of the converters and the control system is a must. In this regards, a detailed modelling exercise on the Buck and Boost converters used for the experimental DC microgrid setup was performed, in order to properly design the control system for these converters. The small signal models for both the Buck and the Boost converters were derived, modelling both converters in the continuous conduction mode (CCM) and in the discontinuous conduction mode (DCM). From these models, transfer functions were derived which were used to design the control system for the converters.

Droop control has been found to be the most suitable method used to obtain load sharing between paralleled converters. From literature it was found that the Impedance (V-I) droop method was the most commonly used, and one can find a

number of adaptive droop methods based on this. In other literature the Admittance (I-V) droop method was adopted. I-V droop can offer higher bandwidth speeds than V-I droop, thus providing faster response to changes and transitions in the DC microgrid. However, testing the I-V droop control method by simulation and also by experiments resulted in unacceptable start-up overshoots and oscillations, including stability problems. I-V droop can be problematic to apply in practice due to bandwidth interactions with other parts of the control loop such as the anti-aliasing filters. These interactions can lead to instability as observed in the results. During this research work an innovative alternative modified I-V droop method called Combined Voltage and Droop (CVD) method was developed, which solved the mentioned issues with I-V droop. Chapter 7 covered the simulation results and the experimental results obtained with this novel method, showing its successful implementation and operation. The innovation of this new droop control method provided one of the two main contributions in this thesis.

Literature shows that a lot of research work has been carried out on energy management systems and battery management. Some authors focus on obtaining utmost efficiency from the battery banks, others focus on obtaining highest energy throughput from renewable energy sources, while others try to take a holistic approach on the efficiency of the complete DC microgrid setup, which can make the control system complicated and difficult to implement in a practical installation. The need was felt to develop a BMS that would be simple to implement within a DC microgrid, but at the same time open for further development and expansion. During this work a BMS was developed as a high-level control for the Bidirectional converter, allowing it to share the load with the other microgrid converters or charge the battery bank when required. The BMS was presented in Chapter 5 and simulation results were presented in Chapter 8. This BMS algorithm provided another main contribution in this thesis. The implementation of the experimental setup for the BMS consists of both hardware and firmware which take time to implement. During this research work the hardware part was partially completed, however more time was needed for the complete implementation and testing. Therefore, due to time restrictions the proposed BMS was only implemented and tested by simulations. Eventually the proposed BMS system will be built providing a simple but effective control of the Bidirectional converter.

9.2 Summary of Research Work and Results

Following the literature review it was decided to model, design, and build a DC microgrid consisting of two Buck converters and a Bidirectional converter.

The design of the converters and their control systems was initially tested using simulations, which provided successful results, as reported in Appendix A. Simulations were performed to test the primary control system consisting of nested current and voltage control loops. Three methods of droop control were tested using simulations: V-I droop, I-V droop, and the proposed CVD method. Secondary control was also tested by simulations, where voltage restoration was applied to compensate for voltage deviations on the DC-bus caused by the droop. The simulations provided satisfactory results, confirming correct design and operation, as was reported in the results of Chapter 7.

Experimental testing followed, where each converter was tested on its own, to confirm the correct operation of the power electronics unit, sensing and control circuitry, as well as the firmware code. The Buck and Bidirectional converters were initially tested as an open converter to have better access to hardware testing points. The Buck converter was tested up to an output current of 42A at an output voltage of 48V. Effects of inductor saturation were observed starting at a current of approximately 30A. Removing the inductor from its metal housing mitigated slightly the saturation effects allowing the converter to work up to over 42A. However, it was decided to operate the inductors in earthed metal housing to reduce any EMI issues that might result. This decision was also taken due to the fact that the converters were going to be operated with a maximum current of 20A, limited by the DC contactors' maximum current rating.

Once the operation of the Buck and Bidirectional converters was successfully confirmed, the converters were installed in enclosures, each of the three converters in its own enclosure. This setup provided plug-and-play converter prototype units, which facilitated the setting up of the DC microgrid, and provided a setup open to further expansion. The enclosed converter prototypes shall allow for potential future work, also possibly with the manufacturing industry.

Further tests with the Buck converters consisted in testing the converters both in CCM and DCM, as well as testing with step load changes from 5A to 20A and vice-versa. This was done to observe the converter's performance under extreme load changes. The Bidirectional converter was tested in its two modes of operation: in load

supplying mode as a Boost converter and in battery charging mode as a Buck converter. All testing produced successful operation with satisfactory performance, as reported in Appendix B.

The three droop methods: V-I droop, I-V droop, and the CVD method, were tested experimentally, using two paralleled Buck converters with a common resistive load. From the results presented in Chapter 7, it was shown that the innovative CVD method produced very good results. This method was shown to be faster than the V-I droop method and at the same time it overcame the stability issues that resulted with the I-V droop method.

For the final experimental tests, the laboratory-based experimental DC microgrid was set up with all three converters connected in parallel, together with a resistive load. The first test with the complete DC microgrid was performed with all three converters sharing the load current among them using V-I droop. In the next test, the Buck converters shared the load while the Bidirectional converter charged the battery bank. The input current for the Bidirectional converter was supplied and shared by the two Buck converters. In both test cases successful results were obtained, as documented in Chapter 8.

The BMS was formulated and tested via simulations with the model of the DC microgrid. Various simulations were performed testing the DC microgrid with a 24hr domestic load profile. This provided a view on how the proposed BMS would work. The BMS was connected to the Bidirectional converter, and sensed the microgrid load current and the battery current. The battery current was used to calculate the state-of-charge (SOC) of the batteries. According to the load current and the SOC, the BMS controls the mode of operation of the Bidirectional converter, sharing the load with the other converters when the load current is over 20A and charging the batteries when the load current is below 20A. The 20A was selected since it is the maximum current rating of each converter. However, the Bidirectional converter enters idle mode if the batteries are discharged (SOC < 20%) or the batteries are fully charged (SOC > 82%) and the load current is below 20A. Very promising results were obtained from the simulations performed with the DC microgrid including the BMS. These are shown in Chapter 8. Further testing with the experimental DC microgrid would include the proposed BMS to evaluate its performance.

9.3 Further Work

The experimental DC microgrid setup has shown to operate correctly and robustly, and in this respect it can be used for further research work concerning DC microgrids. In addition, the setup was designed and built to be easily expanded with additional converters. Further research could be directed towards:

- Practical implementation of the voltage restoration loop

The voltage restoration loop controller was designed in Chapter 5, and simulations were performed to test the design. The results are shown in Chapter 7. However, there was no time during this research work to actually implement voltage restoration in the experimental DC microgrid. Further work can be done on this aspect.

- Mitigate voltage and current disturbances during large load changes

During step load transitions, especially large step load changes, large voltage disturbances occur, which also affect the current. In fact from the results obtained, it can be noted that the step transition from 5A to 20A caused a large voltage sag of around 28V, which also causes the load current to sag. The step transition from 20A to 5A caused a large voltage swell, again also affecting the current. This caused the anti-windup of the current controller to operate, holding the voltage at 55V and preventing a larger spike in the voltage. These disturbances are mainly caused by the dynamics of the system, and the slowness in the response of the voltage control loop. There is a limit on the bandwidth of the outer voltage control loop, since it has to be slower than the inner current control loop. Possibly these disturbances can be mitigated by the introduction of a Bidirectional converter using supercapacitors in the DC microgrid system. Further research can be done on this aspect.

- Current sharing discrepancy between droop controlled paralleled converters

Parallel-connected converters with a droop control system should share the current load equally between them if the droop coefficient (droop resistance) is equal. However, in practice this precise equal sharing is difficult to obtain due to differences in the converters, and differences in the line resistances between the converter, the DC-bus, and the load/s. The unequal load sharing can also result due to calibration differences in the converters' sensing circuitry. These current differences can be observed in the experimental results obtained when testing the converters using droop

control. Further work and research can be carried out to formulate a compensation technique to correct these current differences at a primary and/or secondary control level.

- Adaptive droop control to connect converters with photovoltaic sources

A converter with a photovoltaic (PV) source can be connected to a DC microgrid using a maximum power point tracking (MPPT) system to feed all power available from the PV to the DC-bus. In an islanded DC microgrid, if the loads connected are not enough to absorb the energy generated by the PV source, operational issues would result. A possible alternate control system can be designed using an adaptive droop control method for the PV source converter. This way the PV source converter could share the loads connected in the DC microgrid with other droop controlled converters, but with a droop controlled output voltage and current. A control system like this would offer more control on the converter's load share.

- Further BMS development

The BMS developed can be further enhanced to provide high-level control to various converters within the DC microgrid, to utilize the energy available as efficiently as possible. For example, in a DC microgrid containing a PV source, the battery charging process can be controlled to charge the batteries when the PV is operating at its maximum power output. Further work can be done on this aspect, extending the BMS to obtain better energy utilization within the DC microgrid.

References

[1] R. H. Lasseter, “Microgrids”, IEEE Power Engineering Society Winter Meeting, pp. 305-308, 2002.

[2] R. H. Lasseter and P. Paigi, “Microgrid: A Conceptual Solution”, IEEE 35th Annual Power Electronics Specialists Conference (PESC 04), pp. 4285-4290, 2004.

[3] L. Mariam, M. Basu, and M. F. Conlon, “A Review of Existing Microgrid Architectures”, Hindawi Journal of Engineering, Vol. 2013, Article ID 937614, 14 April 2013.

[4] H. Jiayi, J. Chuanwen, and X. Rong, “A review on Distributed Energy Resources and Microgrid”, Elsevier Renewable and Sustainable Energy Reviews, Vol. 12, Issue 9, December 2008, pp. 2472-2483, 30 July 2007.

[5] T. Dragicevic, X. Lu, J. C. Vasquez, and J. M. Guerrero, “DC Microgrids – Part I: A Review of Control Strategies and Stabilzation Techniques”, IEEE Transactions on Power Electronics, Vol. 31, Issue 7, pp. 4876 – 4891, July 2016.

[6] T. Dragicevic, X. Lu, J. C. Vasquez, and J. M. Guerrero, “DC Microgrids – Part II: A Review of Power Architectures, Applications and Standardization Issues”, IEEE Transactions on Power Electronics, Vol. 31, Issue 5, pp. 3528 - 3549, May 2016.

[7] F. Gao, Y. Gu, S. Bozhko, G. Asher, and Pat Wheeler, “Analysis of Droop Control Methods in DC Microgrids”, IEEE 2014 16th European Conference on Power Electronics and Applications (EPE'14-ECCE Europe), 26-28 August 2014, Lappeenranta, Finland.

[8] Y. Han, X. Ning, P. Yang, and L. Xu, “Review of Power Sharing, Voltage Restoration and Stabilization Techniques in Hierarchical Controlled DC Microgrids”, IEEE Access, Vol. 7, pp. 149202 – 149223, 11 October 2019.

[9] K. M. Bhargavi, N. S. Jayalakshmi, D. N. Gaonkar, A. Shrivastava, and V. K. Jadoun, “A Comprehensive Review on Control Techniques for Power Management of Isolated DC Microgrid System Operation”, IEEE Access, Vol. 9, pp. 32196 – 32228, 19 February 2021.

[10] A. Alassi and O. Ellabban, “Design of an Intelligent Energy Management System for Standalone PV/Battery DC Microgrid”, IEEE 2nd International Conference on Smart Grid and Renewable Energy (SGRE), Doha, Qatar, 19-21 November 2019.

[11] K. N. C. Jayasena, D.K.J.S. Jayamaha, N. W. A. Lidula, and A. D. Rajapakse, “SOC Based Multi-Mode Battery Energy Management System for DC Microgrids”, IEEE Moratuwa Engineering Research Conference (MERCon), Moratuwa, Sri Lanka, 3-5 July 2019.

[12] M. Sechilariu, B. C. Wang, and F. Locment, “Supervision Control for Optimal Energy Cost Management in DC Microgrid: Design and Simulation”, Elsevier Journal of Electrical Power and Energy Systems, Vol. 58, pp. 140-149, June 2014.

[13] A. C. Luna, N. L. Diaz, L. Meng, M. Graells, J. C. Vasquez, and J. M. Guerrero, “Generation-Side Power Scheduling in a Grid-Connected DC Microgrid”, IEEE First International Conference on DC Microgrids (ICDCM), Atlanta, GA, USA, 7-10 June 2015.

[14] S. Ali, Z. Zheng, M. Aillerie, J. P. Sawicki, M. C. Péra, and D. Hissel, “A Review of DC Microgrid Energy Management Systems Dedicated to Residential Applications”, Energies, Vol. 14, Issue 14, 17 July 2021.

[15] S. Anand and B. G. Fernandes, "Optimal Voltage Level for DC Microgrids," presented at the 36th Annual Conference (IECON 2010), IEEE Industrial Electronics Society, November 2010.

[16] J. M. Guerrero, J. C. Vasquez, J. Matas, L. G. de Vicuna, and M. Castilla, "Hierarchical Control of Droop-Controlled AC and DC Microgrids – A General Approach Toward Standardization," IEEE Transactions on Industrial Electronics, vol. Vol. 58, January 2011.

[17] Q. Shafiee, T. Dragicevic, J. C. Vasquez, and J. M. Guerrero, "Hierarchical Control for Multiple DC-Microgrids Clusters," IEEE Transactions on Energy Conversion, vol. Vol. 29, December 2014.

[18] Q. Shafiee, T. Dragicevic, J. C. Vasquez, and J. M. Guerrero, "Modeling, Stability Analysis and Active Stabilization of Multiple DC-Microgrid Clusters," presented at the Energycon 2014, Dubrovnik, Croatia, May 2014.

[19] S. Peyghami-Akhuleh, H. Mokhtari, P. Davari, P. C. Loh, and F. Blaabjerg, "A New Secondary Control Approach for Voltage Regulation in DC Microgrids," presented at the 8th Annual IEEE Energy Conversion & Exposition, Milwaukee, WL, United States, September 2016.

[20] P. Karlsson and J. Svensson, "Voltage Control and Load Sharing in DC Distributed Systems," presented at the European Power Electronics Conference (EPE 2003), Toulouse, France, September 2003.

[21] Z. Jin, L. Meng, R. Han, J. M. Guerrero, and J. C. Vasquez, "Admittance-type RC-Mode Droop Control to Introduce Virtual Inertia in DC Microgrids," presented at the IEEE Energy Conversion Congress and Exposition (ECCE), Cincinnati, Ohio, United States, October 2017.

[22] S. Peyghami, H. Mokhtari, and F. Blaabjerg, "Decentralized Load Sharing in a Low-Voltage Direct Current Microgrid With an Adaptive Droop Approach Based on a Superimposed Frequency," IEEE Journal of Emerging and Selected Topics in Power Electronics, vol. Vol. 5, pp. 1205-1215, September 2017.

[23] S. Peyghami, H. Mokhtari, P. C. Loh, P. Davari, and F. Blaabjerg, "Distributed Primary and Secondary Power Sharing in a Droop-Controlled LVDC Microgrid with Merged AC and DC Characteristics", IEEE Transactions on Smart Grid, Vol. 9, No. 3, pp. 2284 - 2294, May 2018.

[24] S. Peyghami, H. Mokhtari, and F. Blaabjerg, "Autonomous Power Management in LVDC Microgrids based on a Superimposed Frequency Droop", IEEE Transactions on Power Electronics, Vol. 33, No. 6, pp. 5341 – 5350, June 2018.

[25] X. Lu, J. M. Guerrero, K. Sun, and J. C. Vasquez, "An Improved Droop Control Method for DC Microgrids Based on Low Bandwidth Communication With DC Bus Voltage Restoration and Enhanced Current Sharing Accuracy", IEEE Transactions on Power Electronics, Vol. 29, No. 4, April, 2014.

[26] L. Gao, Y. Liu, H. Ren, and J. M. Guerrero, "A DC Microgrid Coordinated Control Strategy Based on Integrator Current-Sharing", *Energies* **2017**, *10*, 1116. https://doi.org/10.3390/en10081116.

[27] T. Dragicevic, J. M. Guerrero, J. C. Vasquez, and D. Skrlec, "Supervisory Control of an Adaptive-Droop Regulated DC Microgrid With Battery Management Capability," IEEE Transactions on Power Electronics, vol. Vol. 29, pp. Pages 695-706, February 2014.

[28] X. Lu, K. Sun, J. M. Guerrero, J. C. Vasquez, and L. Huang, "State-of-Charge Balance Using Adaptive Droop Control for Distributed Energy Storage Systems in DC Microgrid Applications," IEEE Transactions on Industrial Electronics, vol. Vol. 61, June 2014.

[29] X. Lu, K. Sun, J. M. Guerrero, J. C. Vasquez, and L. Huang, "Droop-Control-Based State-of-Charge Balancing Method for Charging and Discharging Process in Autonomous DC Microgrids," presented at the IEEE 23rd International Symposium on Industrial Electronics (ISIE 2014), Istanbul, Turkey, June 2014.

[30] X. Lu, K. Sun, J. M. Guerrero, J. C. Vasquez, and L. Huang, "Double-Quadrant State-of-Charge-Based Droop Control Method for Distributed Energy Storage Systems in Autonomous DC Microgrids," IEEE Transactions on Smart Grid, vol. Vol. 6, pp. Pages 147-157, January 2015.

[31] S. Subham, M. Sukumar, J. Shatakshi, and S. Bhim, "A Cooperative Adaptive Droop Based Energy Management and Optimal Voltage Regulation Scheme for DC Microgrids", IEEE Transactions on Industrial Electronics, Vol. 67, No. 4, April 2020.

[32] R. F. Bastos, T. Dragicevic, J. M. Guerrero, and R. Q. Machado, "Decentralized Control for Renewable DC Microgrid with Composite Energy Storage System and UC Voltage Restoration Connected to the Grid," presented at the 42nd Annual Conference of IEEE Industrial Electronics Society (IECON2016), Florence, Italy, October 2016.

[33] F. Zhang, Y. Yang, C. Ji, W. Wei, Y. Chen, C. Meng, Z. Jin, and G. Zhang, "Power Management Strategy Research for DC Microgrid with Hybrid Storage System," presented at the IEEE First International Conference on DC Microgrids (ICDCM 2015), Atlanta, GA, USA, June 2015.

[34] M. A. Jarrahi, F. Roozitalab, M. M. Arefi, M. S. Javadi, and J. P. S. Catalao, "DC Microgrid Energy Management System Containing Photovoltaic Sources Considering Supercapacitors and Battery Storage", International Conference on Smart Energy Systems and Technologies (SEST 2020), Istanbul, Turkey, 7-9 Sept. 2020.

[35] N. Mohan, T. M. Undeland, and W. P. Robbins, Power Electronics: Converters, Applications, and Design, 3rd Edition, Wiley, 2002.
[36] R. W. Erickson and D. Maksimovic, Fundamentals of Power Electronics, Second Edition, Springer, 2001.
[37] R. W. Erickson, Course Notes: Introduction to Power Electronics, University of Colorado Boulder and Coursera, 2016.
[38] M. Murnane and A. Ghazel, 'A Closer Look at State of Charge (SOC) and State of Health (SOH) Estimation Techniques for Batteries', Technical Article, Analog Devices.
[39] W. Y. Chang, 'The State of Charge Estimating Methods for Battery: A Review', Hindawi, ISRN Applied Mathematics, Vol. 2013, Article ID 953792, 2013.
[40] K. Movassagh, A. Raihan, B. Balasingam, and K. Pattipati, 'A Critical Look at Coulomb Counting Approach for State of Charge Estimation in Batteries', Energies, Vol.14, Issue 14, 2021.
[41] S. L. Wang, X. Xiong, C. Y. Zou, L. Chen, C. Jiang, Y. X. Xie, and D. I. Stroe, 'An Improved Coulomb Counting Method Based on Dual Open-Circuit Voltage and Real-Time Evaluation of Battery Discharge Capacity Considering Temperature and Battery Aging', Wiley International Journal of Energy Research, Vol. 45, Issue 12, pp. 17609-17621, 2021.
[42] LEM, Voltage Transducer LV25-P Datasheet.
[43] LEM, Current Transducer LA55-P/SP1 Datasheet.
[44] Semikron Semidriver SKHI 10/12 (R) High Power IGBT Driver Datasheet, Semikron, 2006.
[45] Semikron Skyper 32 Pro R IGBT Driver Core, Rev. 5, Semikron, 2018.
[46] Semikron Board 1 SKYPER 32PRO R Adaptor board, Rev. 2, Semikron, 2010.
[47] Jessica Settino, Research Work at University of Malta, 2016.
[48] Adam Chidley, 'Understanding ESR in Electrolytic Capacitors', https://www.avnet.com/wps/portal/abacus/resources/article/understanding-esr-in-electrolytic-capacitors/, 2017.

Appendix A Buck and Bidirectional Converters Simulation Results

The Buck and Bidirectional converters were modelled in Simulink/Matlab to test and simulate their functionality and operation. The converters were initially simulated on their own to test the operation of their respective control system. The Buck converter was simulated in the continuous conduction mode (CCM) as well as in the discontinuous conduction mode (DCM), using a resistive load. The Bidirectional converter was simulated while operating as a Boost converter in the load sharing/supplying mode and as a Buck converter in the battery charging mode. This appendix covers these simulation tests and the results obtained.

A.1 Buck Converter Simulations

Simulations were performed to test the model of the Buck converter controlled by nested current and voltage PI controller loops. Figure A.1 shows the simulation model of the control system with PI controllers in the s-domain, and Figure A.2 shows the model of the Buck converter. The current loop controls the inductor current I_L and the voltage loop controls the output voltage V_o. The reference voltage for the voltage loop was set to 48V.

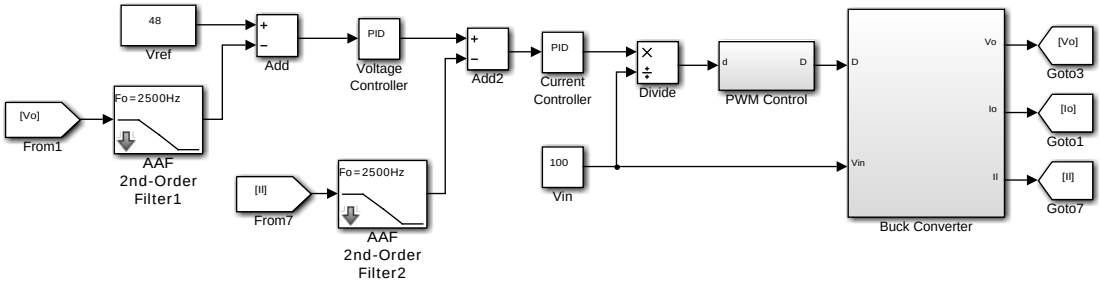

Figure A.1: Buck Converter with Current and Voltage PI Controllers in s-Domain

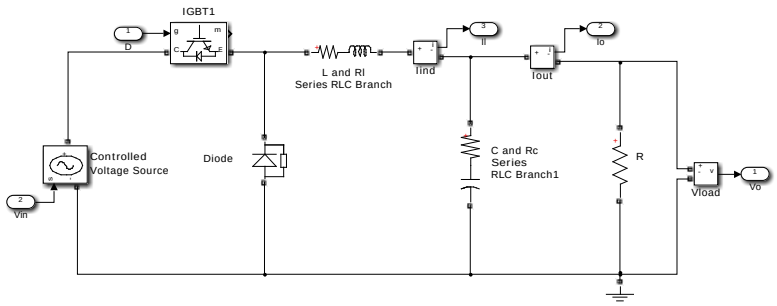

Figure A.2: Buck Converter in Simulink

Table A.1 lists the parameters used in the Buck converter simulation model.

Input Voltage V_{in}	100V
Output Voltage V_o	48V
Switching Frequency f_s	10kHz
Inductor L	479μH
Inductor Resistance R_L	2mΩ
Capacitor C	270μF
ESR R_c	2.1mΩ
Current PI K_P	1.144
Current PI K_I	880
Voltage PI K_P	0.0644
Voltage PI K_I	4.6

Table A.1: Buck Converter - Simulation Parameters

Three simulations were performed: the first simulation was performed with the Buck converter operating in the continuous conduction mode (CCM), the second simulation was performed with the Buck converter operating in the discontinuous conduction mode (DCM), and the third simulation was performed with step changes in resistive load. These simulations were performed in both the continuous and discrete time domain, with similar results, therefore only the results obtained in the continuous time domain are documented in this thesis.

A.1.1 Buck Converter in CCM

For the first simulation the Buck converter was operated in CCM, with a load resistance of 0.92Ω, to obtain an output current of 52.1A at an output voltage of 48V (full load power of 2.5kW).

Figures A.3 to A.7 show the simulation results obtained when the Buck converter was operated in CCM. Figure A.3 shows the inductor current during start-up and at steady state. Figure A.4 focuses on the inductor current ripple with a peak-to-peak magnitude of 5.2A, matching the desired value according to the design of the inductor covered in Chapter 3. The output voltage successfully reached a steady state value of 48V, as shown in Figure A.5. Figure A.6 shows the output voltage ripple with a peak-to-peak magnitude of 0.24V, matching the desired value according to the output capacitor calculation in Chapter 3. The output current reached a steady state value of 52.1A, as shown in Figure A.7. The settling times for the inner current closed loop and the voltage closed loop with a 2% settling band were approximately 7ms and 0.96s, respectively, matching the desired settling times (6.9ms and 0.96s) as designed in Chapter 5 (subsection 5.4.1.1 and 5.4.1.2).

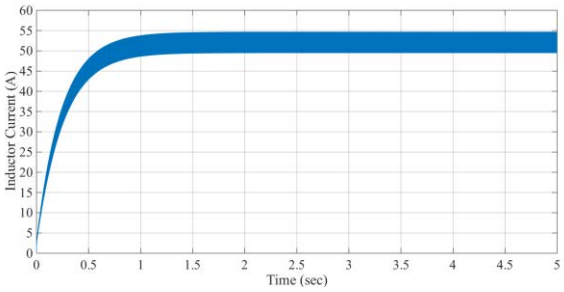

Figure A.3: Inductor Current (CCM) – Buck

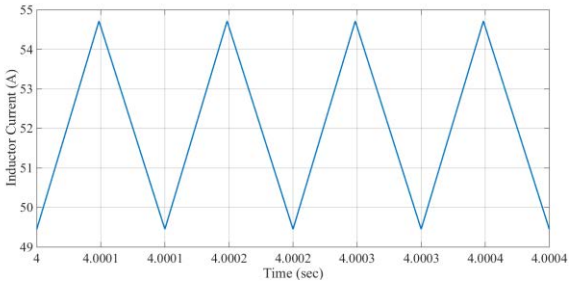

Figure A.4: Inductor Current – Ripple (CCM) – Buck

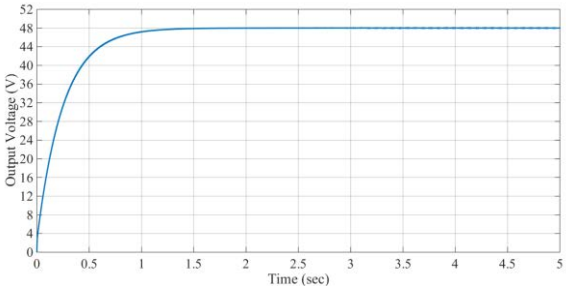

Figure A.5: Output Voltage (CCM) – Buck

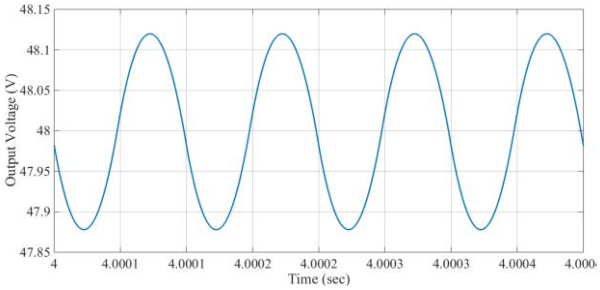

Figure A.6: Output Voltage – Ripple (CCM) – Buck

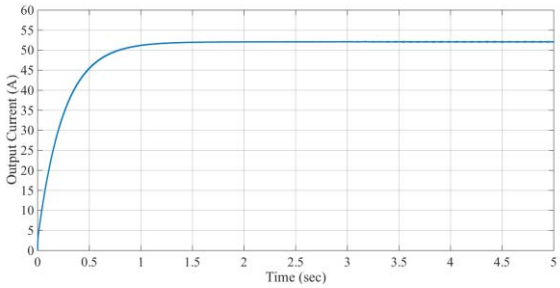

Figure A.7: Output Current (CCM) – Buck

A.1.2 Buck Converter in DCM

For the second simulation the Buck converter was operated in DCM, with a load resistance of 48Ω, to obtain an output current of 1A at an output voltage of 48V.

Figures A.8 to A.12 show the simulation results obtained when the Buck converter was operated in DCM. Figure A.8 shows the inductor current during start-up and at steady state. Figure A.9 focuses on the inductor current ripple, showing DCM operation. The inductor current ripple has a peak of approximately 3.25A, staying below the CCM peak-to-peak inductor current ripple magnitude of 5.2A. The output voltage successfully reached a steady state value of 48V, as shown in Figure A.10. Figure A.11 shows the output voltage ripple with a peak-to-peak magnitude of 0.18V, which is below the CCM peak-to-peak output voltage ripple of 0.24V. The output current reached a steady state value of 1A, as shown in Figure A.12.

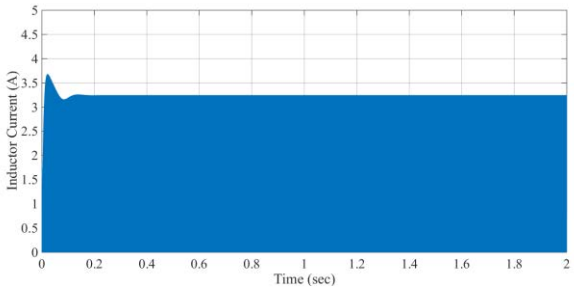

Figure A.8: Inductor Current (DCM) – Buck

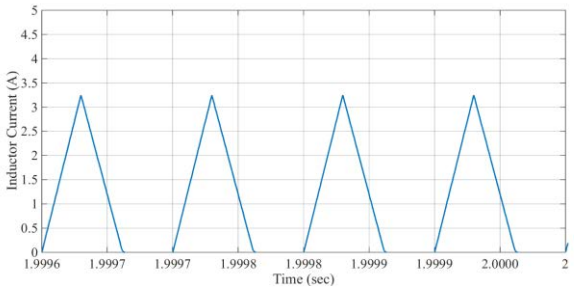

Figure A.9: Inductor Current – Ripple (DCM) – Buck

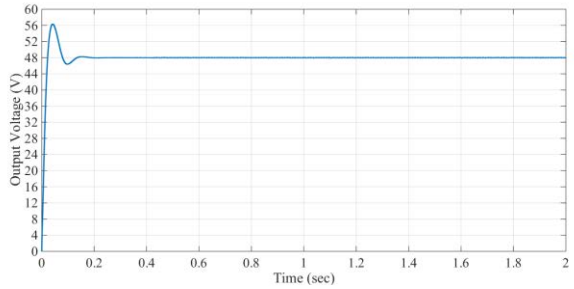

Figure A.10: Output Voltage (DCM) – Buck

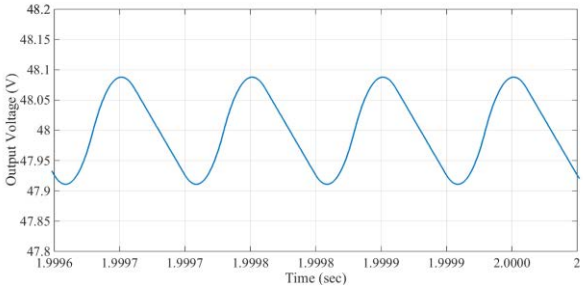

Figure A.11: Output Voltage – Ripple (DCM) – Buck

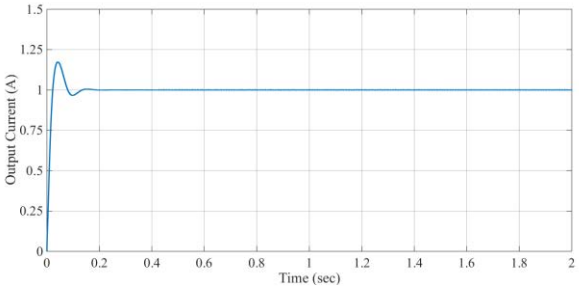

Figure A.12: Output Current (DCM) – Buck

A.1.3 Buck Converter with Load Change

For the third simulation the Buck converter was tested with a load step change. The Buck converter started at t = 0s with a load resistance of 2.4Ω, at t = 3s the resistance changed to 2Ω, and at t = 7s the load resistance changed back to 2.4Ω.

For this simulation the model of the Buck converter was modified as shown in Figure A.13, to apply load steps to the converter.

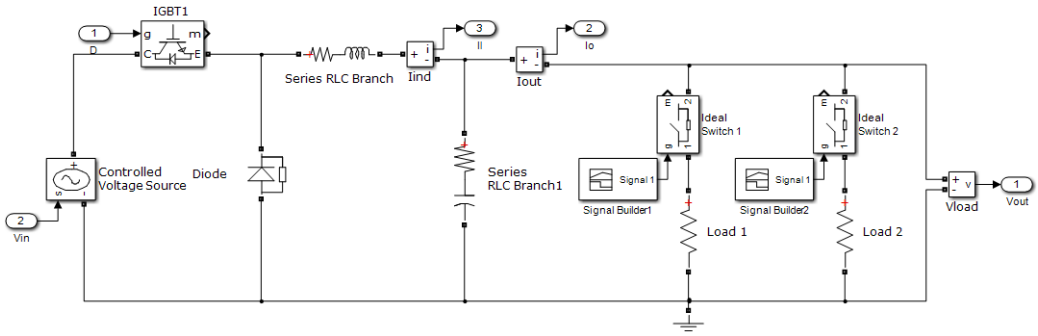

Figure A.13: Buck Converter in Simulink including Load Steps

Figures A.14 to A.16 show the simulation results obtained from the Buck converter with a change in load resistance from 2.4Ω to 2Ω and vice-versa. Figures A.14, A.15, and A.16 show the inductor current, the output voltage, and the output current,

respectively, during start-up and during the load changes. From Figure A.15, one can note that the change in load caused a dip and a swell in the output voltage. The larger the load change, the larger the disturbance in the voltage. During the 20% (4A) load changes, there was a 6.5V dip at t = 3s and a 7.5V swell at t = 7s in the output voltage. These voltage disturbances also caused spikes in the output current as can be observed in Figure A.16. These disturbances are caused by the dynamics of the system, and the slowness in the response of the voltage control loop. There is a limit on the bandwidth of the outer voltage control loop, since it has to be slower than the inner current control loop. The bandwidth of the voltage control loop is also limited by the anti-aliasing filter in the output voltage feedback path. The swell at t = 7s can be limited by the use of an anti-windup feature within the PI controllers.

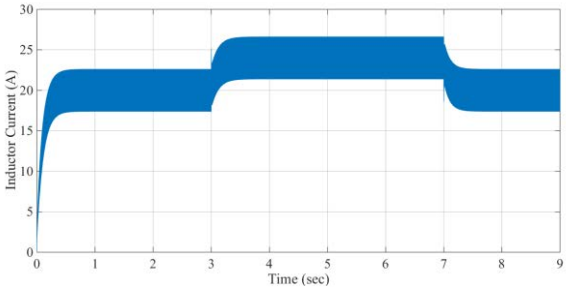

Figure A.14: Inductor Current – Buck – Load Change 2.4Ω - 2Ω

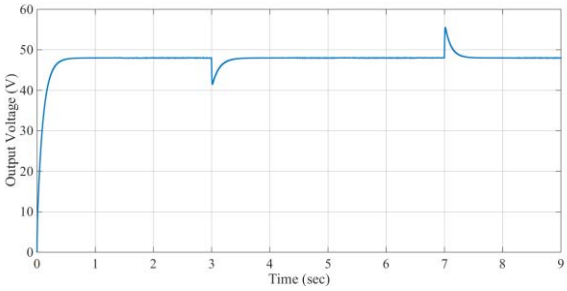

Figure A.15: Output Voltage – Buck – Load Change 2.4Ω - 2Ω

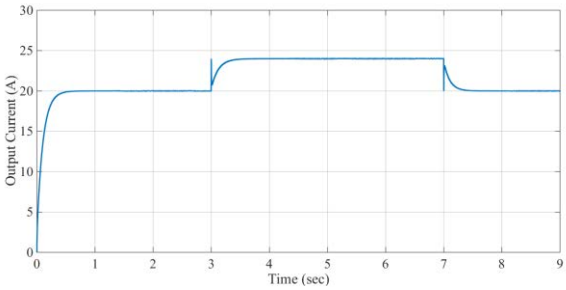

Figure A.16: Output Current – Buck – Load Change 2.4Ω - 2Ω

A.2 Bidirectional Converter Simulations

Simulations were also performed to test the modelled Bidirectional converter (Synchronous Buck converter) and its control system. The control system can be divided in two parts: one part takes care of battery charging and the other part takes care of load sharing/supplying. At this stage these two parts of the control system were considered on their own for ease of testing, and to focus on the two separate modes of operation. Eventually these two parts were combined to form a joint control system.

Figure A.17 (a) shows the simulation model of the control system with a current PI controller, which controls the converter during battery charging (battery charging mode). In this case the converter is operated as a Buck converter, reducing the input voltage from 48V to approximately 24V (depending on the charging current and battery bank voltage) to charge the batteries. Figure A.17 (b) shows the simulation model of the control system with nested current and voltage PI controllers, which controls the converter when supplying a load (load supplying mode). In this case the converter is operated as a Boost converter, supplying a load at 48V from the 24V battery bank. Figure A.18 shows the model of the Bidirectional converter: (a) connected for battery charging, and (b) connected to supply a resistive load. Since the voltage sources at both ends of the converter can be both inputs and outputs, to reduce confusion these were labelled as higher-side voltage V_H for the 48V side and lower-side voltage V_L for the 24V battery side. The battery model used for the simulations was set to represent a 24V 120Ah AGM Lead Acid type battery bank.

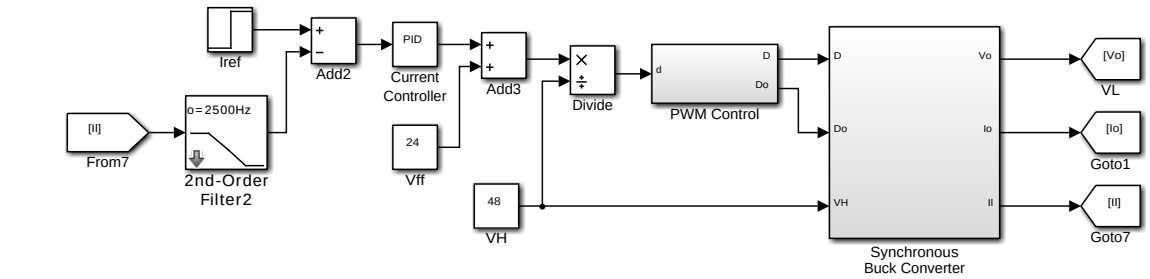

(a)

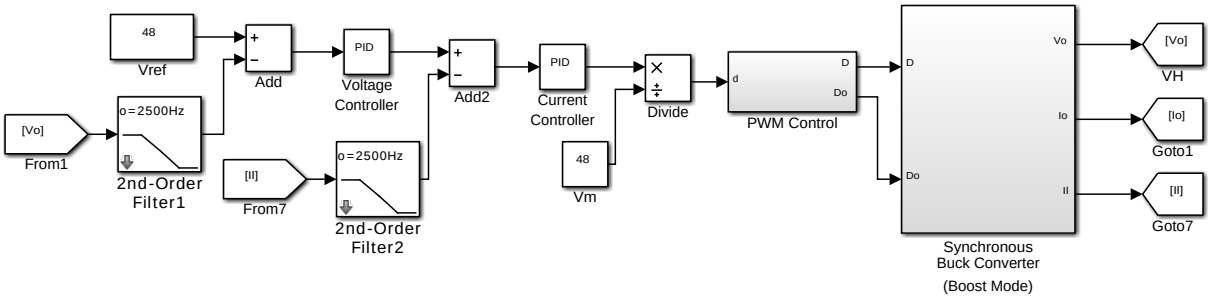

(b)

Figure A.17: Bidirectional Converter Control System in s-Domain
(a) Battery Charging (b) Load Connected

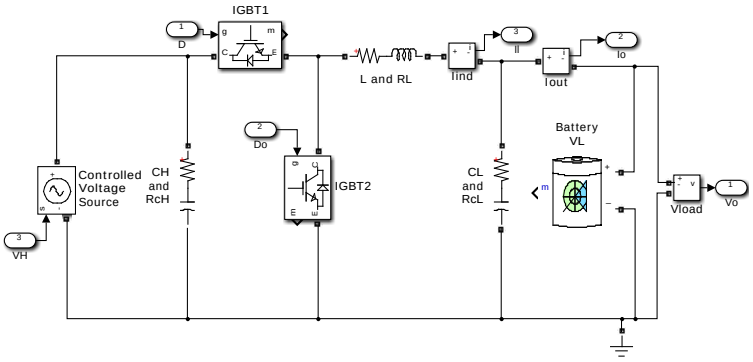

(a) Battery Charging (Buck Mode)

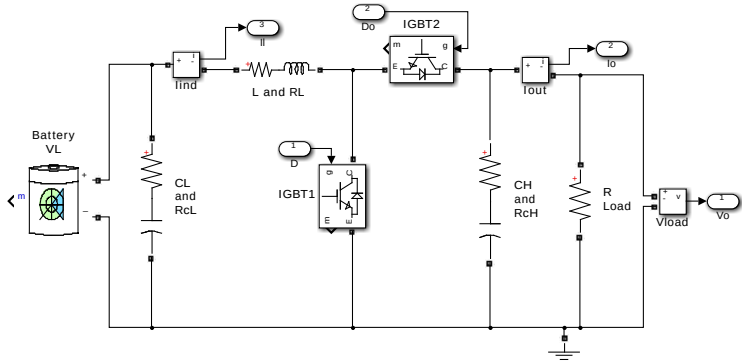

(b) Load Connected (Boost Mode)

Figure A.18: Bidirectional Converter in Simulink

Table A.2 lists the parameters used in the Bidirectional converter simulation model.

Lower-Side Voltage V_L	24V
Higher-Side Voltage V_H	48V
Switching Frequency f_s	10kHz
Inductor L	192µH
Inductor Resistance R_L	2mΩ
Lower-voltage-side Capacitor C_L	680µF
Lower-voltage-side Capacitor ESR R_{cL}	0.03Ω
Higher-voltage-side Capacitor C_H	1500µF
Higher-voltage-side Capacitor ESR R_{cH}	0.03Ω
Buck-Mode Current PI K_P	0.75777
Buck-Mode Current PI K_I	871
Boost-Mode Current PI K_P	0.6426
Boost-Mode Current PI K_I	378
Boost-Mode Voltage PI K_P	0.72
Boost-Mode Voltage PI K_I	80

Table A.2: Bidirectional Converter - Simulation Parameters

Two simulations were performed with the Bidirectional converter operated as a Buck converter: the first simulation was performed with the converter supplying a resistive load, and the second simulation was performed with the converter charging the battery bank. Three simulations were performed with the Bidirectional converter operated as a Boost converter: the first simulation was performed with the converter operated

from a 24V voltage source to supply a resistive load, the second simulation was performed with the converter operated from a 24V battery bank to supply a resistive load, and the third simulation was performed with step changes in resistive load. These simulations were performed in both the continuous and discrete time domain, with similar results, therefore only the results obtained in the continuous time domain are documented in this thesis.

A.2.1 Bidirectional Converter in Buck Mode - Supplying a Resistive Load

The first simulation was performed with the converter supplying a load resistance of 1.2Ω (instead of the battery) to test the current PI controller with resistive load. The higher-side voltage source V_H (input voltage source) was set to 48V. The reference current for the current loop was set to 20A.

Figures A.19 to A.23 show the results from the simulation with the Bidirectional converter operating as a Buck converter while connected to a 1.2Ω resistive load. Figure A.19 shows the inductor current during start-up and at steady state. Figure A.20 focuses on the inductor current ripple with a peak-to-peak magnitude of 6.25A, matching the desired value according to the design of the inductor covered in Chapter 3. The output voltage reached a steady state value of 24V, as shown in Figure A.21. Figure A.22 shows the output voltage ripple with a peak-to-peak magnitude of approximately 0.18V, 0.06V larger than the designed value of 0.12V. This resulted due to the ESR of the capacitor which reduces filtering effectiveness [48]. The output current reached a steady state value of 20A, as shown in Figure A.23. The settling time for the current closed loop with a 2% settling band was approximately 9.8ms.

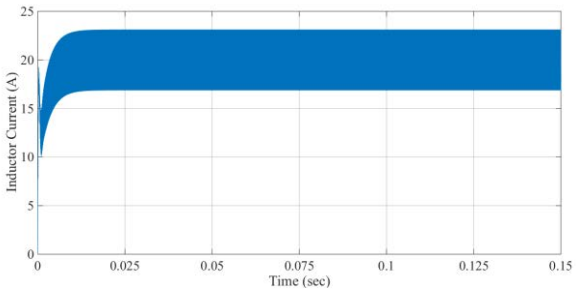

Figure A.19: Inductor Current – Bidirectional – Buck Mode

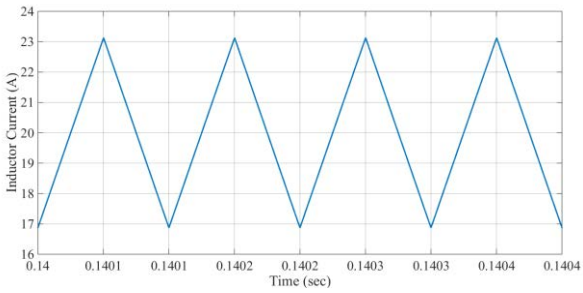

Figure A.20: Inductor Current – Ripple – Bidirectional – Buck Mode

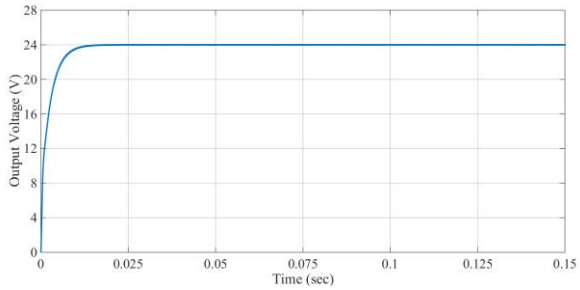

Figure A.21: Output Voltage – Bidirectional – Buck Mode

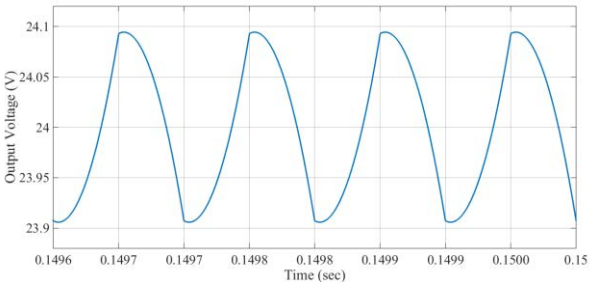

Figure A.22: Output Voltage – Ripple – Bidirectional – Buck Mode

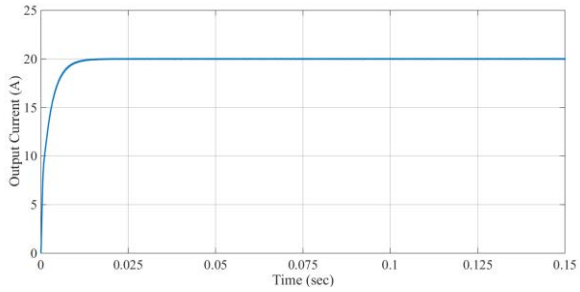

Figure A.23: Output Current – Bidirectional – Buck Mode

A.2.2 Bidirectional Converter in Buck Mode – Battery Charging

The second simulation was performed with the converter charging the battery with a charging current of 20A. The state of charge (SOC) of the battery was set to 80%. For this simulation test, a feed-forward voltage of 24V was added to the output of the current PI controller to reduce back-flowing current from the battery to the input voltage source during start-up of the converter. The input higher-side voltage source V_H was set to 48V. The reference current for the current loop was set to 20A.

Figures A.24 to A.27 show the results from the simulation with the Bidirectional converter operating as a Buck converter while charging the battery. Figure A.24 shows the inductor current during start-up and at steady state. Figure A.25 shows the output current / charging current successfully reaching a steady state value of 20A. Figure A.26 shows the output voltage / battery voltage during start-up and charging, while Figure A.27 shows a zoomed output voltage / battery voltage which can be observed to increase due to charging. The peak at start-up was caused due to the 24V feed-forward to the output of the controller, which started the PWM generator by this value. From the charging current in Figure A.25 it can be observed that the battery reduced the capacitor's ability to filter out the current ripple. This is due to the internal impedance/resistance of the battery which effectively changes the plant and the dynamics of the system, thus affecting the ripple. The SOC of the battery was 80% at start-up with minimal increase till the end of the simulation (t = 0.15s). The settling time for the current closed loop with a 2% settling band was approximately 2.4ms,

approximately matching the 2.5ms settling time as designed in Chapter 5 subsection 5.4.3.1.

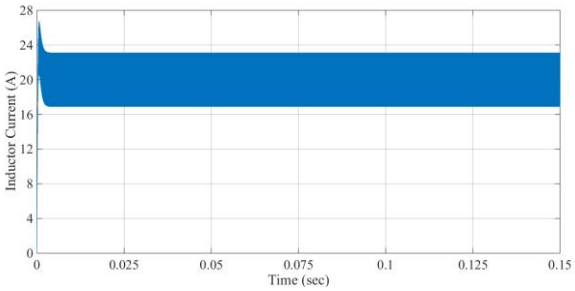

Figure A.24: Inductor Current – Bidirectional – Buck Mode – Battery Charging

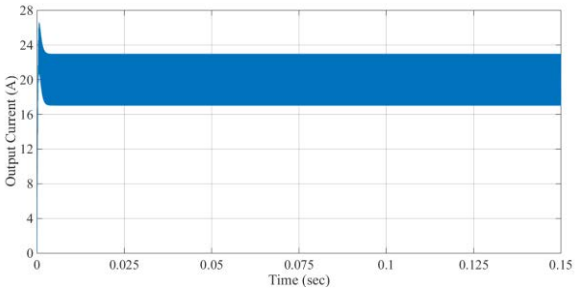

Figure A.25: Output Current / Charging Current – Bidirectional – Buck Mode – Battery Charging

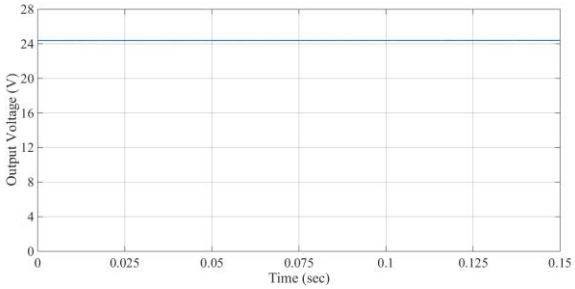

Figure A.26: Output Voltage / Battery Voltage – Bidirectional – Buck Mode – Battery Charging

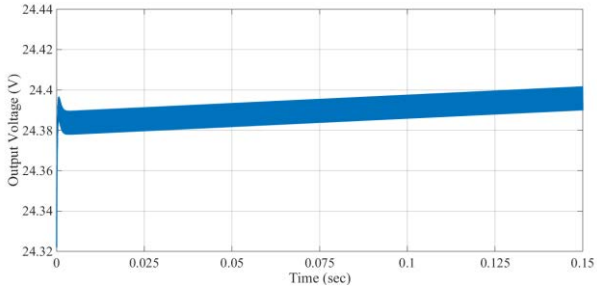

Figure A.27: Output Voltage / Battery Voltage – Increasing – Bidirectional – Buck Mode – Battery Charging

A.2.3 Bidirectional Converter in Boost Mode - Supplying a Resistive Load

In this simulation the converter supplied a load resistance of 1.536Ω at 48V, to obtain full load current (31.25A), therefore, an output power of 1.5kW. The input source in this case was a voltage source of 24V. The reference voltage for the voltage loop was set to 48V.

Figures A.28 to A.32 show the results from the simulation with the Bidirectional converter operating as a Boost converter with a 24V input voltage source and a 1.536Ω resistive load. Figure A.28 shows the inductor current during start-up and at steady state. Figure A.29 focuses on the inductor current ripple with a peak-to-peak magnitude of 6.25A, matching the desired value according to the design of the inductor covered in Chapter 3. The output voltage successfully reached a steady state value of 48V, as shown in Figure A.30. Figure A.31 shows the output voltage ripple with a peak-to-peak magnitude of approximately 2.8V, which is 1.8V larger than the designed value of 1V. This resulted due to the ESR of the capacitor which reduces filtering effectiveness [48]. The output current reached a steady state value of 31.25A, as shown in Figure A.32. The settling times for the inner current closed loop and the voltage closed loop with a 2% settling band were approximately 6.7ms and 0.146s,

respectively, matching the desired settling times (6.7ms and 0.146s) as designed in Chapter 5 (subsection 5.4.3.2 and 5.4.3.3).

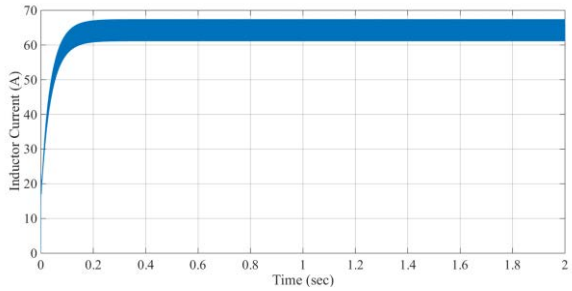

Figure A.28: Inductor Current – Bidirectional – Boost Mode

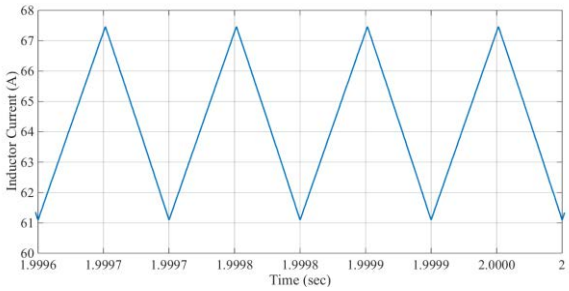

Figure A.29: Inductor Current – Ripple – Bidirectional – Boost Mode

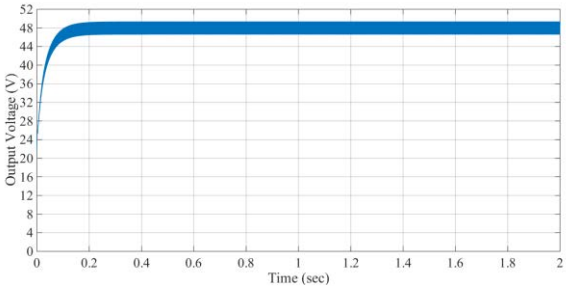

Figure A.30: Output Voltage – Bidirectional – Boost Mode

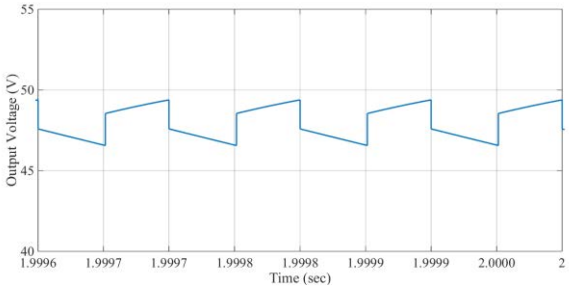

Figure A.31: Output Voltage – Ripple – Bidirectional – Boost Mode

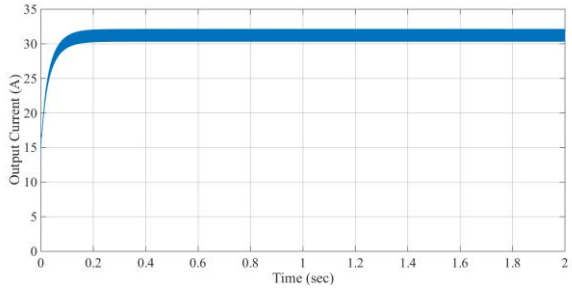

Figure A.32: Output Current – Bidirectional – Boost Mode

A.2.4 Bidirectional Converter in Boost Mode - Supplying a Resistive Load with the Battery as the Source

In this simulation the converter supplied a resistance of 2.4Ω at 48V, to obtain a load current of 20A. The input voltage source in this case was the battery at 24V, with a starting state of charge (SOC) of 100%. The reference voltage for the voltage loop was set to 48V.

Figures A.33 to A.35 show the results from the simulation with the Bidirectional converter operating as a Boost converter with a 24V battery source and a 2.4Ω resistive load. Figure A.33 shows the inductor current during start-up and at steady state. The output voltage successfully reached a steady state value of 48V, as shown in Figure A.34, while the output current reached a steady state value of 20A, as shown in Figure A.35. From Figure A.33 one can note that the inductor current is increasing with time. This is due to the battery discharging, reducing the battery voltage, which

in turn causes the control system to request more input current to keep the converter's output voltage and current at the required values. Starting at 100%, the SOC of the battery reduced to approximately 99.98% after 2s, at the end of the simulation. The settling times for the inner current closed loop and the voltage closed loop with a 2% settling band were approximately 6.7ms and 0.146s, respectively, matching the desired settling times (6.7ms and 0.146s) as designed in Chapter 5 (subsection 5.4.3.2 and 5.4.3.3).

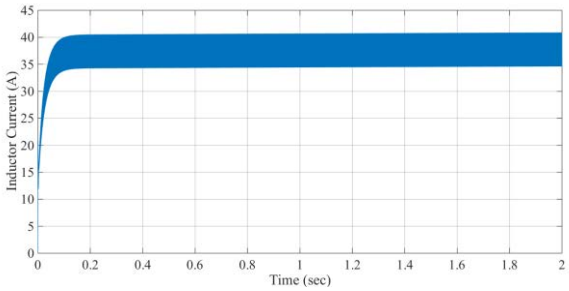

Figure A.33: Inductor Current – Bidirectional – Boost Mode – Battery Source

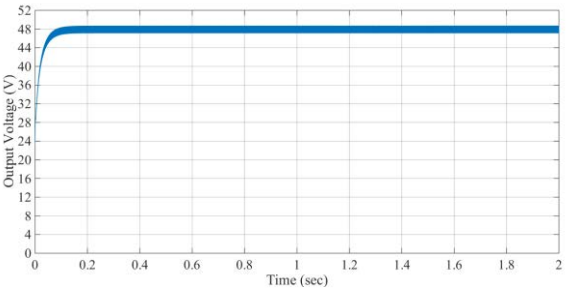

Figure A.34: Output Voltage – Bidirectional – Boost Mode – Battery Source

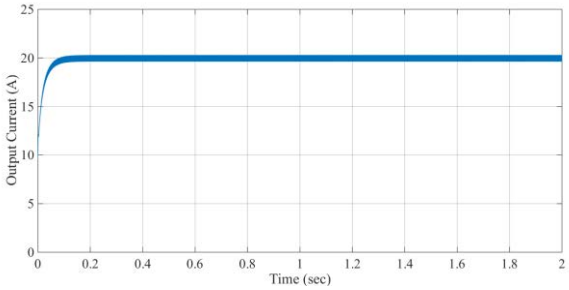

Figure A.35: Output Current – Bidirectional – Boost Mode – Battery Source

A.2.5 Bidirectional Converter in Boost Mode - Resistive Load Change with the Battery as the Source

In this simulation, the converter started with a load resistance of 2.4Ω, at t = 3s the resistance changed to 2Ω, and at t = 7s the load resistance was changed back to 2.4Ω. The converter was operating as a Boost converter, with a 24V battery source. The starting SOC of the battery was set to 100%. The model of the Bidirectional converter in Boost mode was modified as shown in Figure A.36, to enable load steps with different load resistance values.

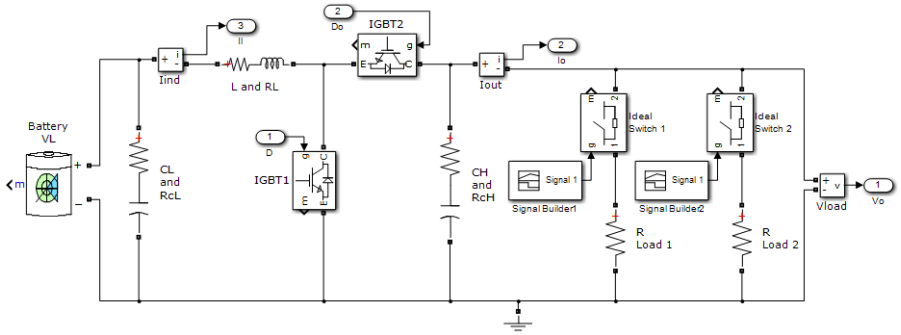

Figure A.36: Bidirectional Converter in Simulink (Boost Mode) including Load Changing

Figures A.37 to A.39 show the simulation results obtained from the Bidirectional converter, with the load resistance changing from 2.4Ω to 2Ω and vice-versa. This change in load resistance provided a 20% change in the output current, from 20A to 24A and vice-versa, at an output voltage of 48V. Figures A.37, A.38, and A.39 show the inductor current, the output voltage, and the output current, respectively, during start-up and load step changes. Small disturbances in the output voltage can be observed at the load change transitions at t = 3s and t = 7s, with similar spikes also resulting in the output current. However, the control system successfully managed to control the output voltage back to 48V.

Similar to the previous simulation, the inductor current increased with time, due to the battery discharging, thus reducing the battery voltage, which in turn causes the control system to request more input current to keep the converter's output voltage and current at the required values. Starting at 100%, the SOC of the battery reduced to approximately 99.92% after 9s, at the end of the simulation.

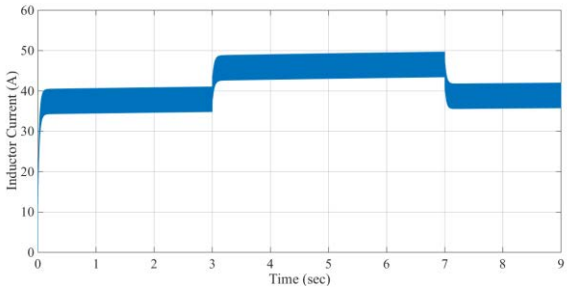

Figure A.37: Inductor Current – Bidirectional – Boost Mode – Battery Source – Load Change 2.4Ω - 2Ω

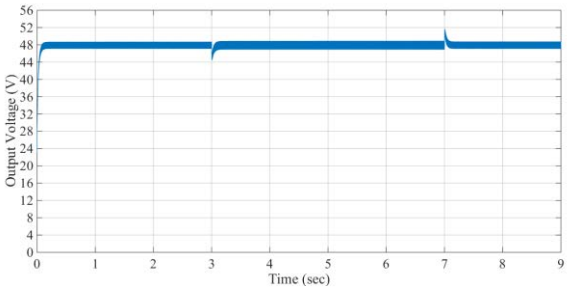

Figure A.38: Output Voltage – Bidirectional – Boost Mode – Battery Source – Load Change 2.4Ω - 2Ω

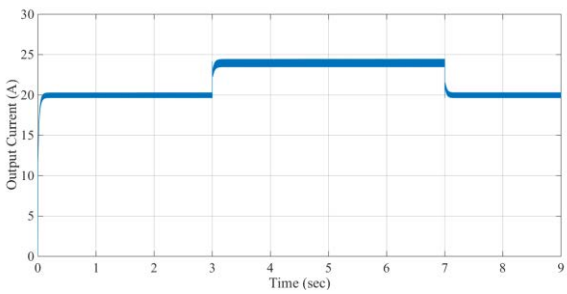

Figure A.39: Output Current – Bidirectional – Boost Mode – Battery Source – Load Change 2.4Ω - 2Ω

A.3 Conclusion

This chapter covered the simulations performed in Simulink/Matlab to test the designed Buck and Bidirectional converters, together with the control systems needed by the converters to operate within a DC microgrid. At first simulations were performed with the modelled Buck and Bidirectional converters on their own. The control system for the Buck converters consists of nested current and voltage control loops using PI controllers that controlled the inductor current and output voltage, respectively. The Buck converter was simulated in both the continuous conduction mode (CCM) and in discontinuous conduction mode (DCM). The control system for the Bidirectional converter is divided in two parts: one part takes care of battery charging where the converter is operated as a Buck converter (battery charging mode), and another part takes care of load supplying/sharing where the converter is operated as a Boost converter (load supplying/sharing mode). The simulation results obtained were very satisfactory, confirming correct operation of the designed converters and their control systems, as can be observed in sections A.1 and A.2 for the Buck converter and the Bidirectional converter, respectively.

Appendix B Buck and Bidirectional Converters Experimental Results

This chapter presents the results obtained from the experimental tests carried out on the individual converters. Initially the Buck and Bidirectional converters were tested while operating on their own. Starting from the Buck converter, it was at first tested as an open prototype on a test bench, to test the operation of the power stage and the PCBs built to provide the IGBT switching control system. Once the converter was successfully tested, two Buck converters were built within their own enclosure to provide two standalone Buck converters. Each enclosed Buck converter was tested on its own. The control system for the Buck converters consisted of nested current and voltage control loops using PI controllers, controlling the inductor current and output voltage, respectively. The Buck converters were tested in both the continuous conduction mode (CCM), as well as in discontinuous conduction mode (DCM). The Buck converters were also tested with step changes in load, to observe the behaviour during these transitions.

A similar procedure was followed for the Bidirectional converter, which was initially tested as an open prototype on a test bench. Once testing was successful, the Bidirectional converter was built within its own enclosure, providing a standalone unit, which was then tested on its own. The control system for the Bidirectional converter consisted in two parts depending on the operating mode of the converter. When the Bidirectional converter was operated in the load sharing/supplying mode, it operated as a Boost converter with the control system consisting of nested current and voltage control loops using PI controllers, which controlled the inductor current and output voltage, respectively. When the Bidirectional converter was operated in the battery charging mode, it operated as a Buck converter with the control system consisting of a current loop using a PI controller, which controlled the inductor current.

B.1 Buck Converter Tests

Two Buck converters were built to form part of the experimental DC microgrid. These were designed and built to operate with an input voltage in the range 70V – 120V and an output voltage of 48V. The Buck converters were operated with a recommended input voltage of 100V during testing. The finished converters were

enclosed in their own enclosure so as to be operated as standalone units (see Chapter 6 - Experimental Setup). These were labelled Buck 1 and Buck 2. The individual Buck converters were tested in the continuous conduction mode (CCM) and in the discontinuous conduction mode (DCM). Testing involved operating the converters with different resistive load values, using a controlled resistive load bank. The converters were also tested with changing loads, to test the behaviour during load transitions.

Since the results obtained from the tests performed with Buck 1 and Buck 2 were very similar, only the results obtained with Buck 1 are presented and discussed in this thesis.

The Buck converter was initially tested with a fixed duty cycle, to verify the operation of the power stage and driving electronics. Once this was confirmed, testing was performed with the Buck converter controlled using nested current and voltage PI controllers as designed in Chapter 5 - Converter Control. The nested current and voltage PI controllers controlled the inductor current and the output voltage, respectively.

B.1.1 Experimental Testing of the Buck Converter Prototype with Resistive Loads in CCM

The initial tests carried out using the Buck converter were performed on an open prototype unit, on a test bench without any enclosure, to make probing easier and to perform tests with the inductor with and without a metal housing. These tests served to confirm the correct operation of the Buck converter with the control system, and provided an observation of the effects of the inductor's metal enclosure on the inductor saturation.

The experimental test consisted in operating the Buck converter prototype with a controlled resistive bank. The Buck converter was controlled using nested current and voltage PI controllers, with the voltage reference for the voltage controller set to 48V. The input voltage to the Buck converter was set to 100V, which was supplied by a DC power supply. During these tests the inductor was enclosed in a metal housing to reduce EMI issues. Figure B.1 shows a block diagram of the test setup.

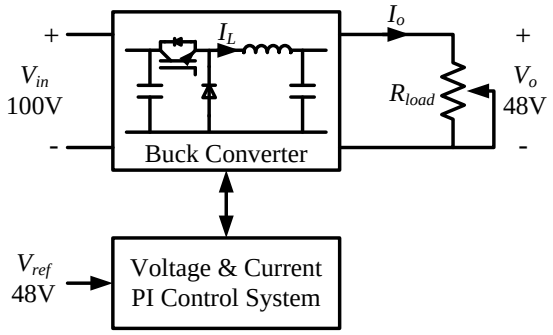

Figure B.1: Block Diagram – Test Setup – Buck Converter – Variable Resistive Load

Figures B.2 to B.12 show the experimental results obtained when the Buck converter (open prototype) using nested current and voltage control was operated with a resistive load. Figure B.2 shows the inductor current I_L, output current I_o, output voltage V_o, and the PWM output from the microcontroller during steady state with an 8Ω resistive load set for an output current of 6A. Figure B.3 shows the start-up of the Buck converter with an 8Ω resistive load to obtain an output current of 6A. Similarly, Figures B.4 to B.12 show the results obtained with resistive loads of 4Ω, 2.7Ω, 2Ω, 1.6Ω, and 1.3Ω, where the output current was increased from 12A to 36A to test the converter operation.

From the results obtained with a load resistance of 1.6Ω, at an output current of 30A, inductor saturation started to occur, observed by the distortion in the inductor current ripple. In fact reducing the load resistance further to 1.3Ω, caused the Buck converter to go unstable due to very large inductor ripple, which caused the protection to kick-in, tripping and switching off the converter due to high inductor current, as can be seen in Figure B.12. It must be pointed out that the Buck converter inductor (design covered in Chapter 3 subsection 3.2.1) was enclosed in an earthed metal housing to reduce EMI emissions which would affect nearby circuitry. The magnetic field of the inductor was affected by the housing which reduced the effectiveness of the gap in the ferrite core, thus causing the inductor to reach saturation before expected.

Figure B.2: Buck Converter – Open Prototype – Steady State
R_{load} = 8Ω, I_o = 6A

Figure B.3: Buck Converter – Open Prototype – Start-Up
R_{load} = 8Ω, I_o = 6A

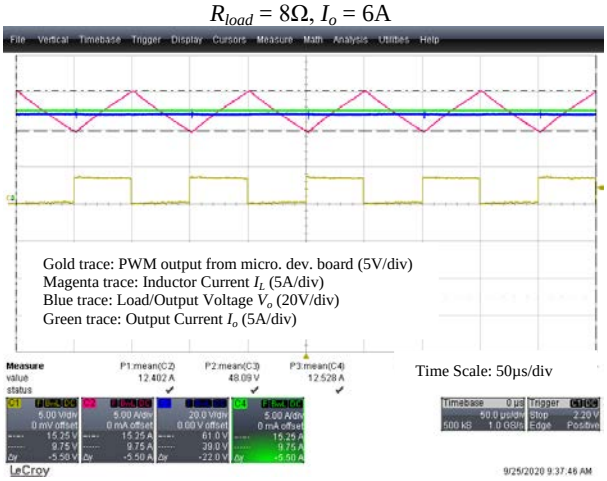

Figure B.4: Buck Converter – Open Prototype – Steady State
R_{load} = 4Ω, I_o = 12A

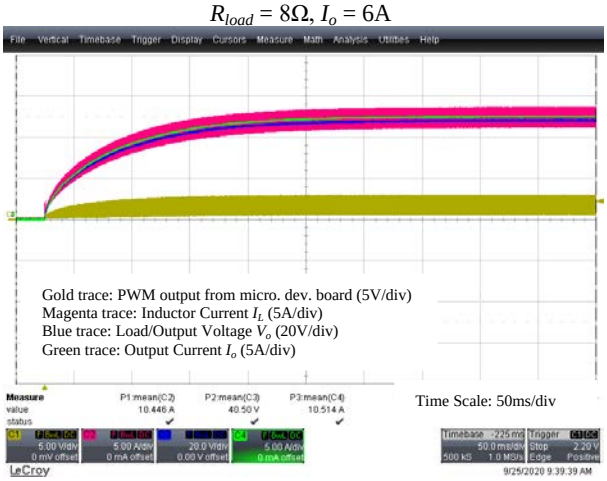

Figure B.5: Buck Converter – Open Prototype – Start-Up
R_{load} = 4Ω, I_o = 12A

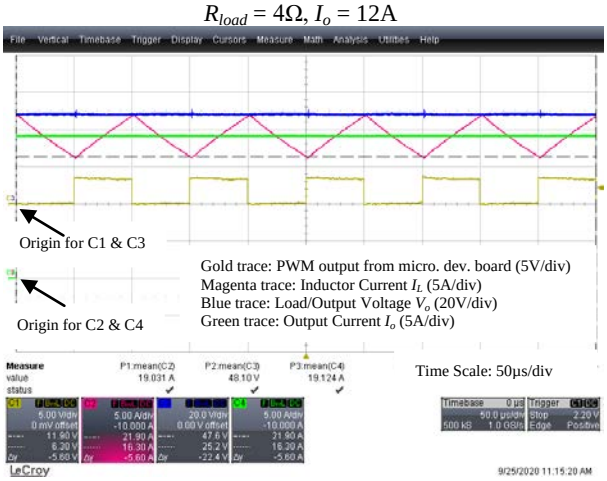

Figure B.6: Buck Converter – Open Prototype – Steady State
R_{load} = 2.7Ω, I_o = 18A

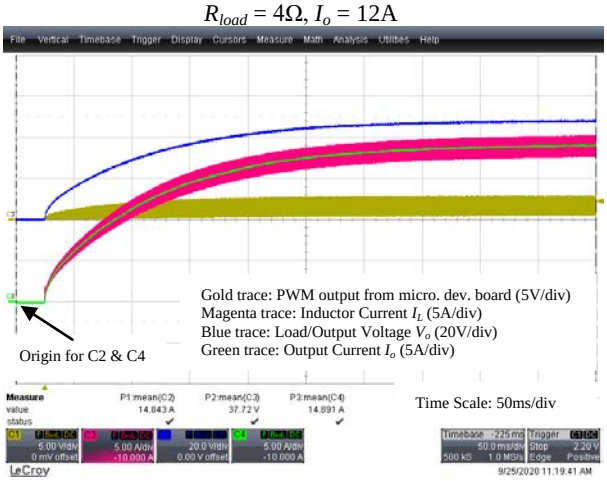

Figure B.7: Buck Converter – Open Prototype – Start-Up
R_{load} = 2.7Ω, I_o = 18A

Figure B.8: Buck Converter – Open Prototype – Steady State
R_{load} = 2Ω, I_o = 24A

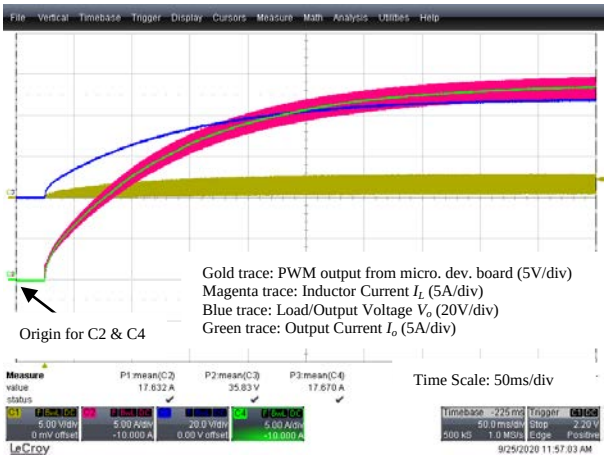

Figure B.9: Buck Converter – Open Prototype – Start-Up
R_{load} = 2Ω, I_o = 24A

Figure B.10: Buck Converter – Open Prototype – Steady State
R_{load} = 1.6Ω, I_o = 30A

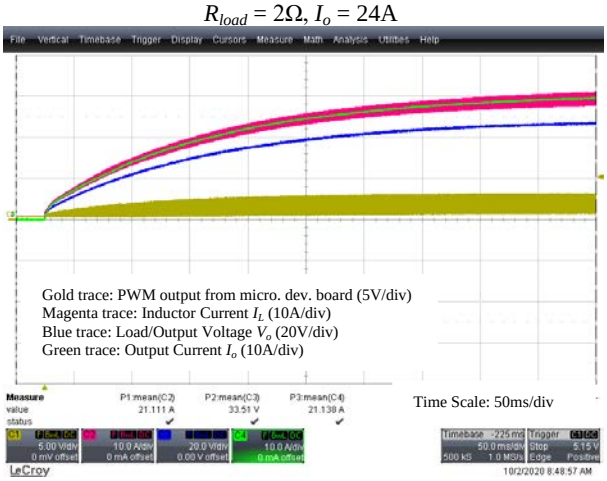

Figure B.11: Buck Converter – Open Prototype – Start-Up
R_{load} = 1.6Ω, I_o = 30A

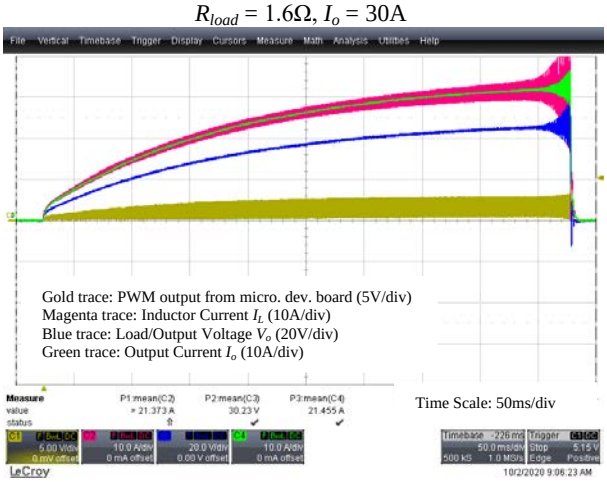

Figure B.12: Buck Converter – Open Prototype – Start-Up
R_{load} = 1.3Ω, I_o = 36A (High Inductor Current Trip)

To investigate the saturation and instability issue further, the inductor was removed from the metal enclosure and tested again. The Buck converter was retested with 1.6Ω to obtain 30A output current, and also with further reduction in resistive load to go further up in output current.

Figures B.13 to B.20 show the experimental results obtained when the Buck converter (open prototype) using nested current and voltage control was operated with load resistances of 1.6Ω, 1.3Ω, 1.2Ω, and 1.14Ω, with the inductor removed from the metal enclosure. Figures B.13 and B.14 show the steady state operation and the start-up of the Buck converter with a 1.6Ω to obtain an output current of 30A. From the results and current shape, it can be observed that without the metal enclosure inductor saturation did not occur at this output level. In fact operating the Buck converter with a resistive load of 1.3Ω, to get an output current of 36A, did not cause a tripping condition, as can be seen from Figures B.15 and B.16. Further reduction of the load resistance to 1.2Ω, to get an output current of 40A, resulted in signs of saturation in the inductor current ripple, as observed in Figure B.17, although from Figure B.18 it can be noted that the start-up of the converter was successful. The load resistance was reduced further to 1.14Ω, obtaining an output current of 42A, with a successful start-up but with the inductor current showing distorted ripple, observed from Figures B.19 and B.20. This was the maximum operating point without the converter tripping due to high inductor current, caused by the large ripple distortion.

Figure B.13: Buck Converter – Open Prototype – Steady State
R_{load} = 1.6Ω, I_o = 30A

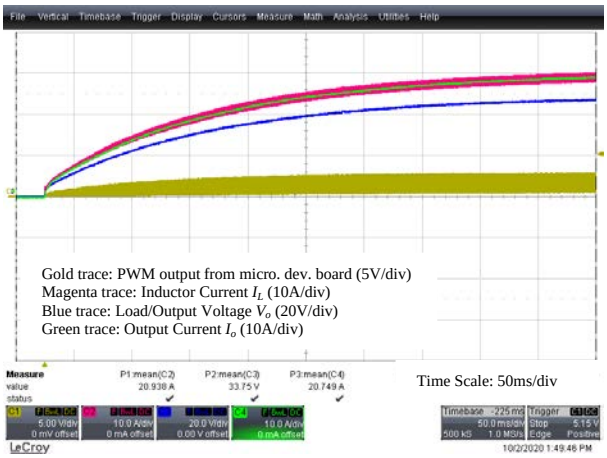

Figure B.14: Buck Converter – Open Prototype – Start-Up
R_{load} = 1.6Ω, I_o = 30A

Figure B.15: Buck Converter – Open Prototype – Steady State
R_{load} = 1.3Ω, I_o = 36A

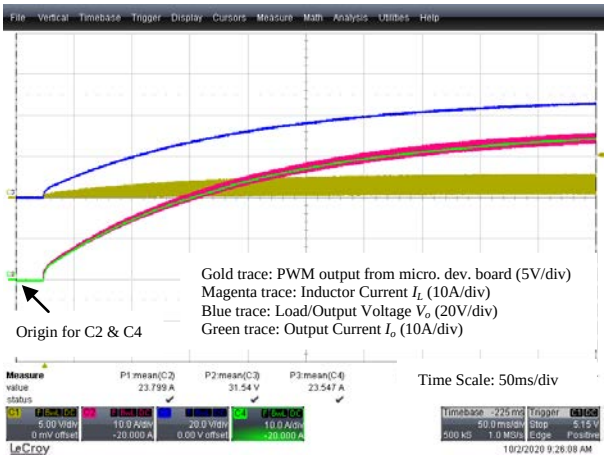

Figure B.16: Buck Converter – Open Prototype – Start-Up
R_{load} = 1.3Ω, I_o = 36A

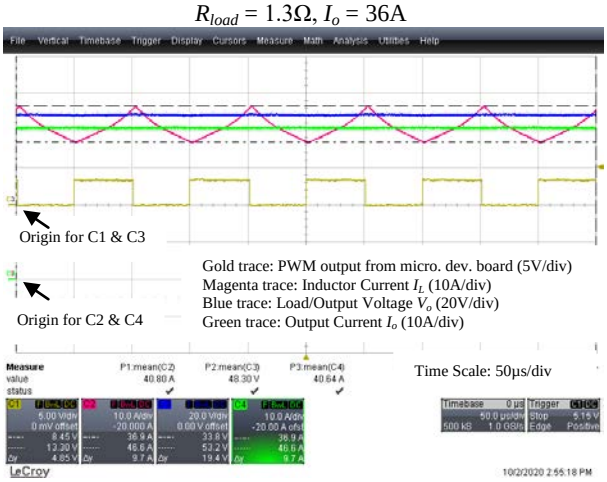

Figure B.17: Buck Converter – Open Prototype – Steady State
R_{load} = 1.2Ω, I_o = 40A

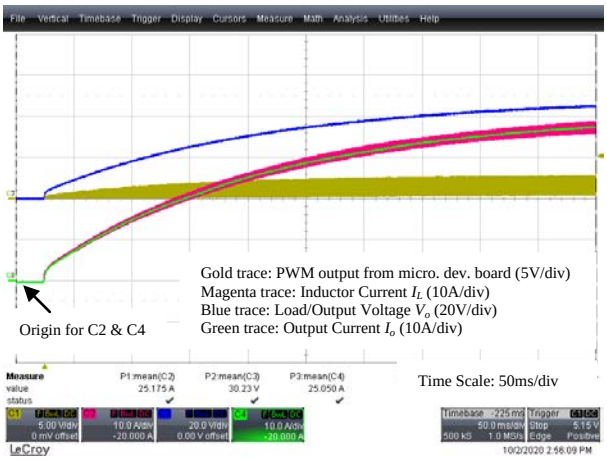

Figure B.18: Buck Converter – Open Prototype – Start-Up
R_{load} = 1.2Ω, I_o = 40A

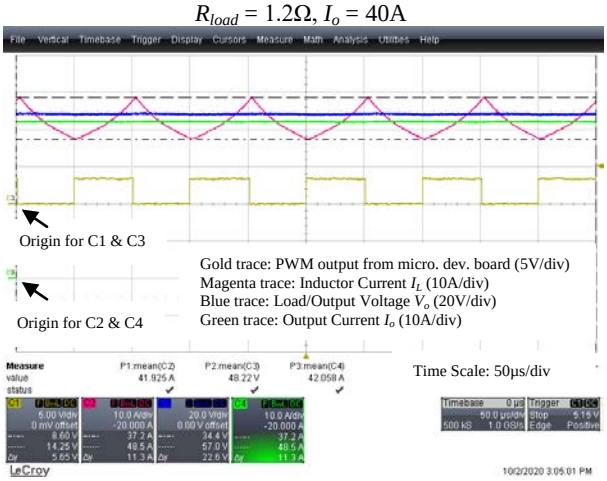

Figure B.19: Buck Converter – Open Prototype – Steady State
R_{load} = 1.14Ω, I_o = 42A

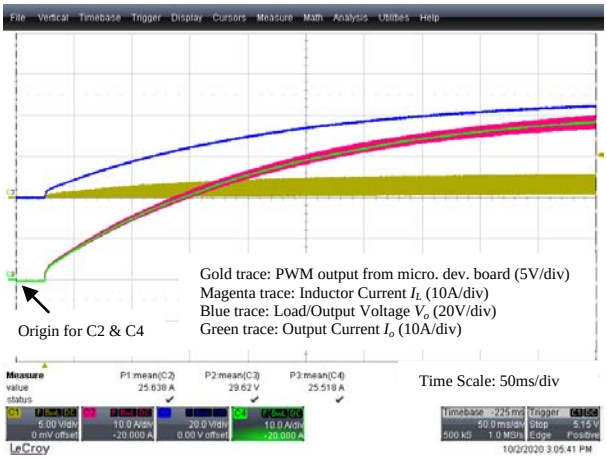

Figure B.20: Buck Converter – Open Prototype – Start-Up
R_{load} = 1.14Ω, I_o = 42A

Table B.1 lists the results obtained from the experimental tests performed with the open prototype of the Buck converter. During these experiments the Buck converter was tested with various resistive load values to obtain an output current in the range

between 6A up to 42A. The voltage reference for the control system V_{ref} was set to 48V. The Buck converter was supplied by an input voltage V_{in} of 100V.

Target I_o	R_{load}	I_{in}*	V_o**	I_o**
6A	8Ω	2.9A	48.11V	6.14A
12A	4Ω	5.85A	48.09V	12.53A
18A	2.66Ω	8.94A	48.1V	19.12A
24A	2Ω	11.96A	48.08V	23.85A
30A	1.6Ω	15.1A	48.53V	30.03A
36A	1.3Ω	18.17A	48.31V	36.06A
40A	1.2Ω	20.08A	48.3V	40.64A
42A	1.14Ω	21.04A	48.22V	42.06A
* Measurements taken using Fluke Current Clamp Meter. ** Measurements taken from LeCroy Oscilloscope using differential voltage probe and current probes.				

Table B.1: Buck Converter (Open Prototype) Results

From the results obtained it was concluded that the Buck converter was operating correctly and as expected, obtaining the expected output voltage of 48V, and reaching a maximum output power of 2kW. By analysing the inductor current ripple from the results obtained when there was no effect of inductor saturation, the peak-to-peak magnitude resulted to be around 5.2A, matching the designed value as calculated in Chapter 3 subsection 3.2.1, thus confirming correct design of the inductor.

The tests involving the inductor metal housing gave an insight on the effects of the metal housing on the inductor operation and its saturation. It was concluded that for the enclosed Buck converter prototype, the best solution for the inductor was to be enclosed in the metal housing, so as to limit EMI issues. This conclusion was reached from the fact that the effect of the metal housing started to be observed at around an output current of 30A. The enclosed Buck converters were going to be operated with a maximum output current of 20A due to limitations in the contactors used within the unit, as explained in Chapter 6. Therefore, within the operating range of the Buck converters, saturation would not be experienced.

Once the previous group of tests confirmed proper operation of the Buck converter, two converters were built and enclosed in their own enclosure so as to be operated as standalone units, and were labelled Buck 1 and Buck 2. The individual converters were tested again under similar conditions as in subsection B.1.1. The Buck converters were controlled using nested current and voltage PI controllers, which controlled the inductor current and output voltage, respectively. The voltage reference for the voltage controller was set to 48V. The input voltage to the Buck converters

was set to 100V, supplied from a DC power supply. The enclosed Buck converters were tested with a maximum output current of 20A due to current handling limitations in the contactors used within the converter units. Having obtained similar results from both enclosed Buck converters, only results from Buck 1 are presented here.

The Buck converters were tested with different resistive load values while operating in CCM. The resistive loads were set to 9.6Ω, 4.8Ω, and 2.4Ω, using a resistive load bank, to obtain an output current of 5A, 10A, and 20A, respectively. The test setup can be represented by the block diagram shown in Figure B.1.

Figures B.21 to B.26 show the experimental results obtained when the Buck converter (Buck 1) was operated with load resistances of 9.6Ω, 4.8Ω, and 2.4Ω. Figures B.21, B.23, and B.25 show steady state operation of the Buck converter with 9.6Ω, 4.8Ω, and 2.4Ω loads, obtaining output currents of 5A, 10A, and 20A, respectively. Figures B.22, B.24, and B.26 show the start-up of the Buck converter with the three load resistances.

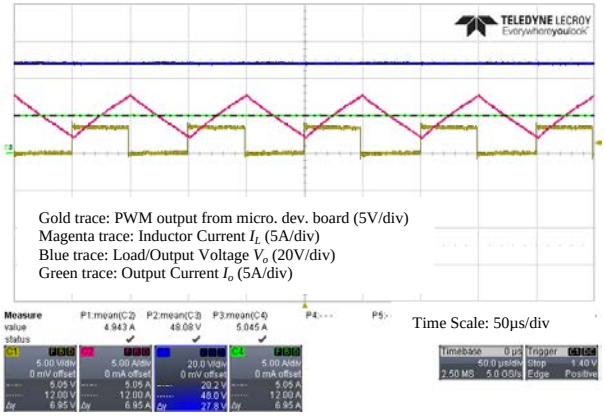

Figure B.21: Buck Converter – Buck 1 – Steady State
R_{load} = 9.6Ω, I_o = 5A

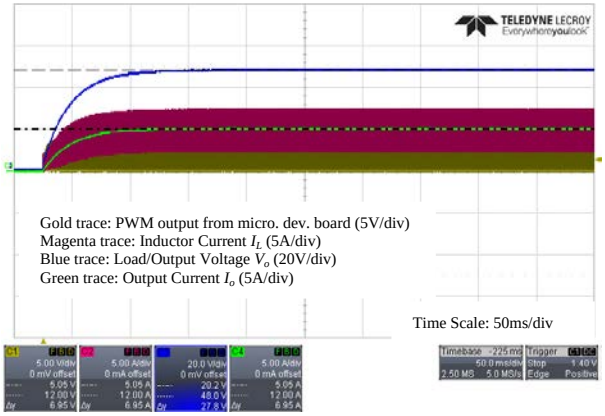

Figure B.22: Buck Converter – Buck 1 – Start-Up
R_{load} = 9.6Ω, I_o = 5A

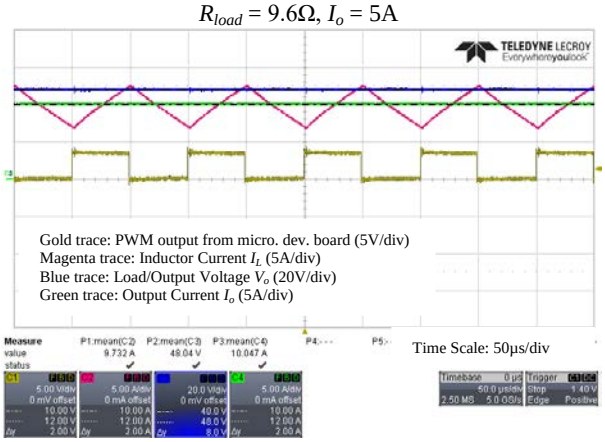

Figure B.23: Buck Converter – Buck 1 – Steady State
R_{load} = 4.8Ω, I_o = 10A

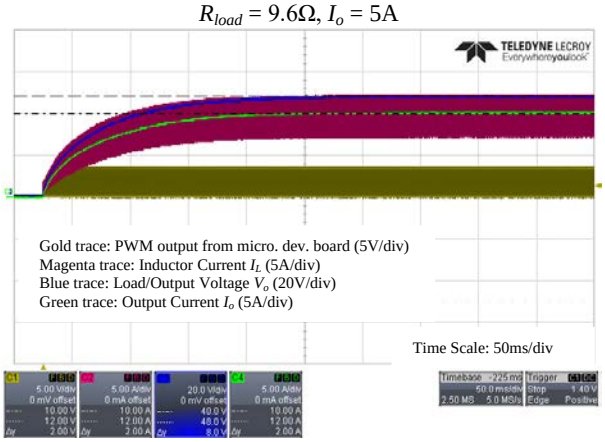

Figure B.24: Buck Converter – Buck 1 – Start-Up
R_{load} = 4.8Ω, I_o = 10A

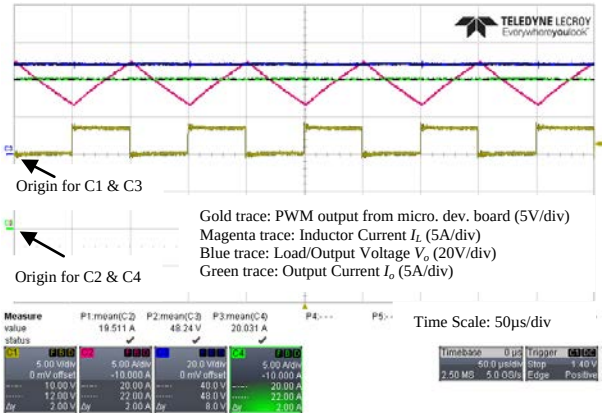

Figure B.25: Buck Converter – Buck 1 – Steady State
R_{load} = 2.4Ω, I_o = 20A

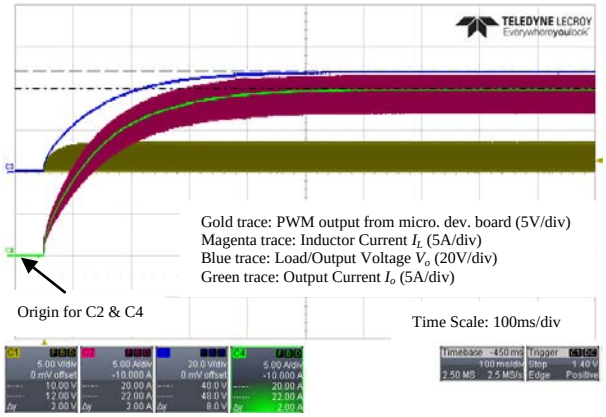

Figure B.26: Buck Converter – Buck 1 – Start-Up
R_{load} = 2.4Ω, I_o = 20A

Table B.2 lists the results obtained from the experimental tests performed with the Buck converter (Buck 1) in the continuous conduction mode (CCM). During these experiments the Buck converter was tested with resistive load values of 9.6Ω, 4.8Ω, and 2.4Ω, obtaining output currents of 5A, 10A, and 20A, respectively, with an output voltage of 48V. In this case, since the unit under test was the enclosed prototype Buck converter (Buck 1), no tests above 20A were performed so that the maximum current handling of the contactors was not exceeded. The voltage reference for the control system V_{ref} was set to 48V. The Buck converter was supplied by an input voltage V_{in} of 100V.

Target I_o	**R_{load}**	**I_{in}***	**V_o****	**I_o****	**Settling Time (approx.)**
5A	9.6Ω	2.9A	48.08V	5.05A	80ms
10A	4.8Ω	5.4A	48.04V	10.05A	150ms
20A	2.4Ω	10.6A	48.24V	20.03A	350ms
* Measurements taken using Fluke Current Clamp Meter. The value includes the current taken by the control circuits and contactor coils (0.23A). ** Measurements taken from LeCroy Oscilloscope using differential voltage probe and current probes.					

Table B.2: Buck Converter (Buck 1) CCM Results

The settling times (2% band) expected from the design of the voltage closed loop in Chapter 5 are in the range of 95ms to 0.96s, for a load current varying between 10% to 100% full load current (5.21A – 52.1A). If the load current values of 5A, 10A, and 20A are taken into consideration, by calculation using the voltage closed loop transfer function in Matlab the expected settling times would be 89.5ms, 199ms, and 385ms for load currents of 5A, 10A, and 20A, respectively. From the experimental tests the approximate settling times resulted to be 80ms, 150ms, and 350ms for the same load currents. Comparing the settling times of these experimental results with the expected values from the design, one can note that these are very similar, which continue to demonstrate the successful operation of the designed Buck converters.

B.1.2 Experimental Testing of the Buck Converter Prototype with Resistive Loads in DCM

The Buck converters were also tested with resistive loads while operating in DCM. For the converter to operate in DCM, a low current needs to flow such that the inductor current ripple reaches zero for part of the switching period. DCM operation was obtained by relatively high resistive loads of 48 Ω and 24Ω to obtain an output current of 1A and 2A, respectively. These resistive loads were set using a resistive load bank. The test setup can be represented by the block diagram shown in Figure B.1. The Buck converter was controlled using nested current and voltage PI controllers. As for the previous tests, the voltage reference for the voltage controller was set to 48V and the input voltage to the Buck converter was set to 100V.

Figures B.27 and B.28 show the steady state operation and the start-up of the Buck converter (Buck 1) with a 48Ω load and an output current of 1A. Figures B.29 and B.30 show the steady state operation and the start-up of the Buck converter (Buck 1) with a 24Ω load and an output current of 2A.

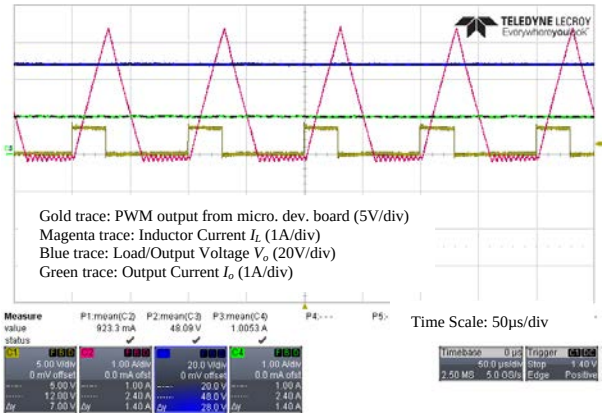

Figure B.27: Buck Converter – Buck 1 – Steady State
R_{load} = 48Ω, I_o = 1A

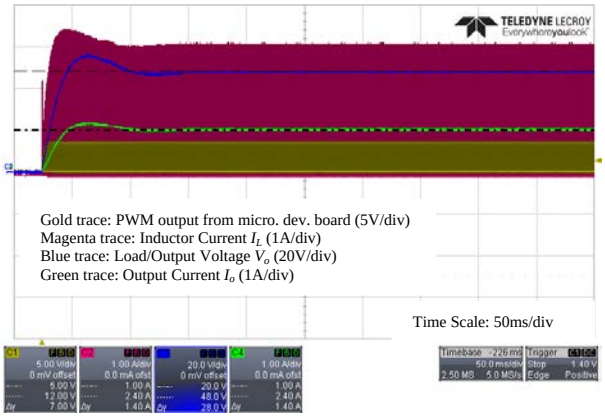

Figure B.28: Buck Converter – Buck 1 – Start-Up
R_{load} = 48Ω, I_o = 1A

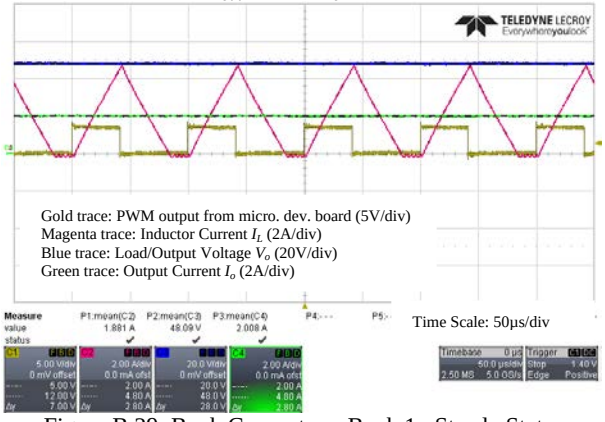

Figure B.29: Buck Converter – Buck 1– Steady State
R_{load} = 24Ω, I_o = 2A

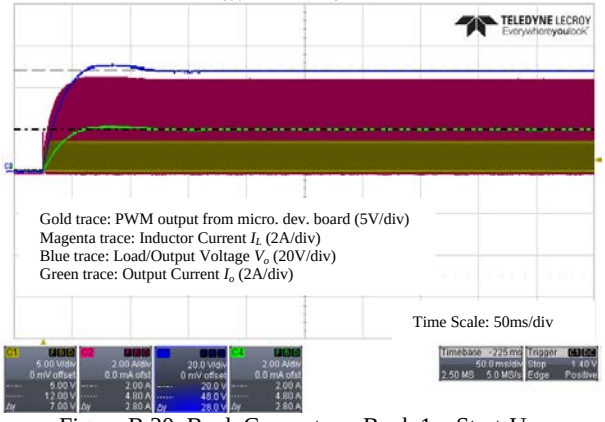

Figure B.30: Buck Converter – Buck 1 – Start-Up
R_{load} = 24Ω, I_o = 2A

Table B.3 lists the results obtained from the experimental tests performed with the Buck converter (Buck 1) in the discontinuous conduction mode (DCM). During these experiments the Buck converter was tested with resistive load values of 48Ω and 24Ω, obtaining output currents of 1A and 2A, respectively, with an output voltage of 48V. The voltage reference for the control system V_{ref} was set to 48V. The Buck converter was supplied by an input voltage V_{in} of 100V.

Target I_o	**R_{load}**	**I_{in}^***	**V_o^{**}**	**I_o^{**}**
1A	48Ω	0.8A	48.09V	1A
2A	24Ω	1.3A	48.09V	2A
* Measurements taken using Fluke Current Clamp Meter. The value includes the current taken by the control circuits and contactor coils (0.23A). ** Measurements taken from LeCroy Oscilloscope using differential voltage probe and current probes.				

Table B.3: Buck Converter (Buck 1) DCM Results

B.1.3 Experimental Testing of the Buck Converter Prototype with Resistive Loads Changes

Experimental tests with the Buck converters also involved testing with step change in resistive load, to observe the behaviour during the transition. The resistive loads were set to 9.6Ω and 2.4Ω, to obtain an output current of 5A and 20A, respectively. The first transition was a load change from 5A to 20A, and the second was a load change from 20A to 5A. The test setup can be represented by the block diagram shown in Figure B.31. The Buck converter was controlled using nested current and voltage PI controllers. Anti-windup protection was used with the integrators of the current and voltage PI controllers, which were set at a limit value of 55V for the current PI and at a limit value of 70A for the voltage PI. The voltage reference for the voltage controller was set to 48V and the input voltage to the Buck converter was set to 100V.

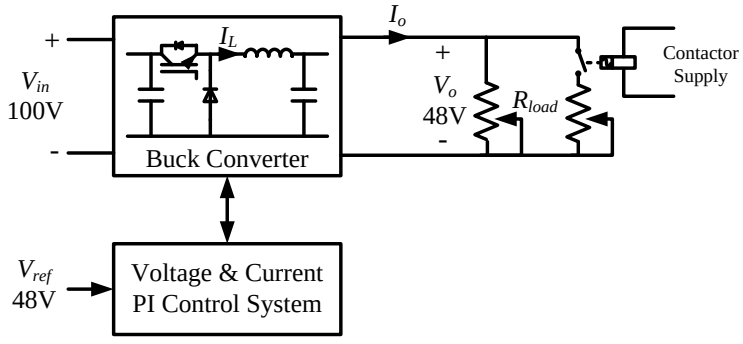

Figure B.31: Block Diagram – Test Setup – Buck Converter – Resistive Load Change

Figure B.32 shows the result obtained from the Buck converter with a change in load resistance from 9.6Ω to 2.4Ω, causing a step load transition from 5A to 20A.

Figure B.33 shows the transition from 2.4Ω to 9.6Ω, causing a step load transition from 20A to 5A.

The results show that the step transition from 5A to 20A caused a voltage sag of around 28V (58.3%) affecting also the current. The step transition from 20A to 5A caused a voltage swell affecting also the current, and causing the anti-windup of the current controller to operate and hold the voltage at 55V, preventing a larger voltage spike. These disturbances are mainly caused by the dynamics of the system, and the slowness in the response of the voltage control loop. Although such a large step in load is not a common occurrence during normal operation of a converter, it was used to test the Buck converters for the worst case scenario.

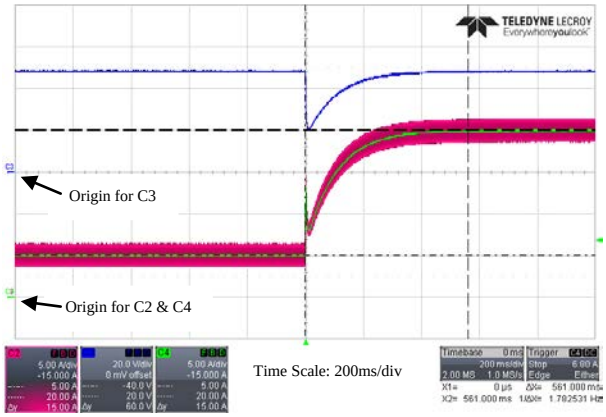

Figure B.32: Buck Converter – Buck 1 – Transition
R_{load1} = 9.6Ω, I_{o1} = 5A → R_{load2} = 2.4Ω, I_{o2} = 20A
(with measured current values)
Magenta trace: Inductor Current I_L (5A/div)
Blue trace: Load/Output Voltage V_o (20V/div)
Green trace: Output Current I_o (5A/div)

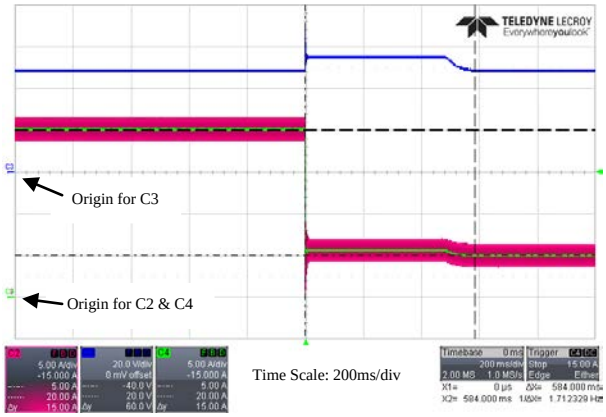

Figure B.33: Buck Converter – Buck 1 – Transition
R_{load1} = 2.4Ω, I_{o1} = 20A → R_{load2} = 9.6Ω, I_{o2} = 5A
(with measured current values)
Magenta trace: Inductor Current I_L (5A/div)
Blue trace: Load/Output Voltage V_o (20V/div)
Green trace: Output Current I_o (5A/div)

Table B.4 lists the results obtained from the experimental tests performed with the Buck converter (Buck 1) with a change in load current between 5A and 20A, and vice-versa. The voltage reference for the control system V_{ref} was set to 48V. The Buck converter was supplied by an input voltage V_{in} of 100V. The results obtained show that the control system successfully managed to control the converter even with a load step of 400%. The output voltage reached the desired value of 48V, in transition times of less than 600ms.

Target I_o	**R_{load}**	**Transition Time (till steady state)**
5A → 20A	9.6Ω → 2.4Ω	~561ms
20A → 5A	2.4Ω → 9.6 Ω	~584ms

Table B.4: Buck Converter (Buck 1) Resistive Load Change Results

B.1.4 Summary of Experimental Testing with the Buck Converters

The results that were presented in this section were obtained from experimental tests performed on the Buck converter. The first tests were conducted on an open Buck converter prototype to make testing and probing easier. This prototype was also used to perform tests using the inductor with and without a metal housing. This setup was used to carry out testing with two main aims: to confirm the correct operation of the designed Buck converter with its control system before installing it in its enclosure, and to investigate the effect of the inductor's metal housing on the converter operation. The Buck converter was tested with a variable resistive load bank which was set at values varying in steps from 4Ω to 1.14Ω. This achieved a load current between 6A to 42A, at an output voltage of 48V. The initial tests were carried out with the Buck converter having a metal housed inductor. Effects of inductor saturation were observed to start at a load current of 30A, and the inductor current ripple started to get distorted. At a load current of 36A the distortion in the inductor current ripple increased to such as extent that the control system became unstable and consequently triggered a trip error in the converter. The inductor was removed from the metal enclosure and the Buck converter was retested from a load current of 30A up to 42A. This time at a load current of 30A no signs of inductor saturation were observed, and operation at 36A load current did not cause converter tripping. Effects in the current due to saturation were observed in the inductor current ripple at a load current of 40A. The load resistance was reduced further to obtain an output current of 42A, which resulted to be the maximum operating point of the converter without tripping due to high inductor current caused by large ripple distortion. These tests were carried out to investigate the effects of the metal housing on inductor saturation and the converter stability. It was determined that for correct operation the converter output current had to be limited to 30A, so that a metal-enclosed inductor is used to avoid any high electromagnetic radiation from interfering with other circuitry.

Once the designed Buck converter was confirmed to operate correctly, two enclosed Buck converters were built, and labelled Buck 1 and Buck 2. Both finalized converters were tested on their own, which showed identical operational behaviour. Therefore, only the results obtained from Buck 1 are documented in this thesis. Although the Buck converters had to be limited to 30A operation due to the use of metal-enclosed inductors, they were actually further limited to a maximum of 20A

due to current handling limitations in the DC contactors used within the converter units (see Chapter 6).

The Buck converters were tested with a resistive load bank, while operating in CCM and DCM. Testing in CCM consisted in operating the Buck converter with resistive loads of 9.6Ω, 4.8Ω, and 2.4Ω, obtaining output currents of 5A, 10A, and 20A, respectively, with an output voltage of 48V. Testing in DCM consisted in operating the Buck converter with resistive loads values of 48Ω and 24Ω, obtaining output currents of 1A and 2A, respectively, with an output voltage of 48V. The Buck converter was tested successfully in both modes of operation. The inductor current ripple measured from the results during CCM, had a peak-to-peak magnitude of around 5.2A, matching the desired value (see Chapter 3, subsection 3.2.1). Moreover the experimental results matched the simulation results documented in Appendix A, which verified that the experimental system achieved the performance observed in the modelled Buck converter. The settling times (2% band) obtained with load values of 5A, 10A, and 20A, resulted to be 80ms, 150ms, and 350ms, respectively, while the calculated settling times expected with the same load values were 89.5ms, 199ms, and 385ms, which are very close.

Further experimental testing with the Buck converters involved applying a step load change to observe the converters' operation during the transition. The resistive loads were set to 9.6Ω and 2.4Ω, to obtain a step in output current of 5A to 20A, and vice-versa, at an output voltage of 48V. The step transition from 5A to 20A caused a 58.3% voltage sag (28V), which caused a sag in the current. The step transition from 20A to 5A caused a voltage swell, which caused a swell in the current, and consequently caused the anti-windup of the current controller to operate and hold the voltage at 55V, preventing a larger voltage spike. These disturbances are mainly caused by the dynamics of the system, and the slowness in response of the voltage control loop. However, the control system of the Buck converter managed to recover and supply the load current successfully. These disturbances were observed also in the simulation test results covered in Appendix A, and further research is required to find ways to mitigate these spikes.

B.2 Bidirectional Converter Tests

The Bidirectional converter was built to connect a battery bank to the experimental DC microgrid setup. The Bidirectional converter operates with 48V at the DC-bus side and with 24V at the battery bank side. The finished converter was enclosed in its own enclosure so as to be operated as a standalone unit (see Chapter 6 - Experimental Setup). The Bidirectional converter can operate in two modes: in battery charging mode (Buck mode) and in load sharing/supplying mode (Boost mode), therefore it was tested in both modes. Testing involved operating the converter with different resistive load values, using a controlled resistive load bank in both Buck and Boost modes. Tests were also performed with the Bidirectional converter operating in Buck mode charging the battery bank, and in Boost mode supplying a resistive load from the battery bank as the source.

Initially the Bidirectional converter was tested with a fixed duty cycle, to verify the correct operation of the power stage and driving electronics. Once this was confirmed, testing was performed with the Bidirectional converter controlled using nested current and voltage PI controllers when operated in Boost mode and using a current PI controller when operated in Buck mode. The controller design was discussed in Chapter 5. In Boost mode the nested current and voltage PI controllers controlled the inductor current and output voltage, respectively. In Buck mode the current PI controller controlled the inductor current.

B.2.1 Experimental Testing of the Bidirectional Converter Prototype with Resistive Loads in Buck Mode

The initial tests carried out using the Bidirectional converter were performed on an open prototype unit, facilitating probing during testing. The Bidirectional converter prototype was tested in Buck mode connected to a resistive load. The resistive load was set to 4.8Ω and 2.4Ω, using a resistive load bank. The control system consisted of a current PI controller, which controlled the inductor current. Two tests were performed with the converter in this mode; one with the current reference of the current controller set to 5A and another with the current reference of the current controller set to 10A. The input voltage to the Bidirectional converter was set to 48V, which was supplied by a DC power supply. Figure B.34 shows a block diagram of the test setup.

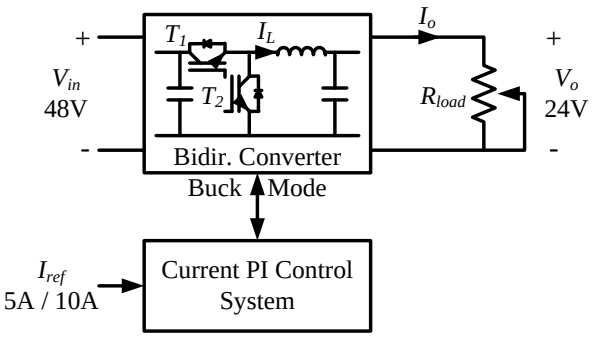

Figure B.34: Block Diagram – Test Setup – Bidirectional Converter (Buck Mode) – Resistive Load

Figures B.35 to B.40 show the results obtained when the Bidirectional converter was operated in Buck mode with resistive loads. Figures B.35 and B.36 show the steady state operation of the Bidirectional converter with a load resistance of 4.8Ω and a current reference of 5A, while the start-up is shown in Figure B.37. Figures B.38 and B.39 show the steady state operation of the Bidirectional converter with a load resistance of 2.4Ω and a current reference of 10A, while the start-up is shown in Figure B.40.

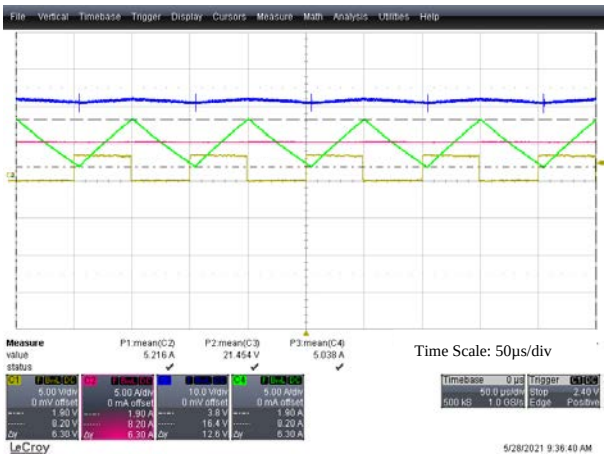

Figure B.35: Bidirectional Converter – Buck Mode – Steady State
R_{load} = 4.8Ω, I_o = 5A

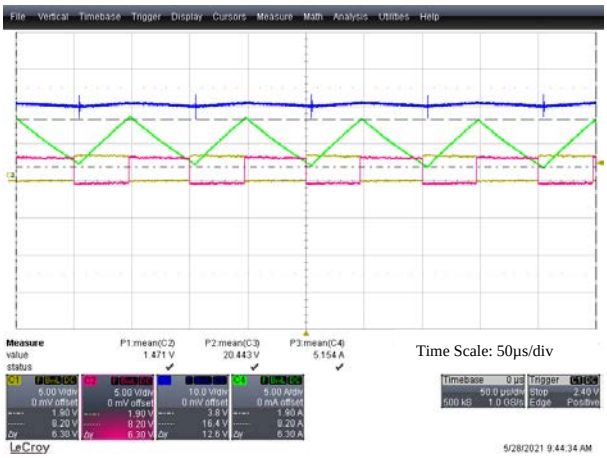

Figure B.36: Bidirectional Converter – Buck Mode – Steady State – both PWM waveforms shown
R_{load} = 4.8Ω, I_o = 5A

Figures B.35 and B.37:
Gold trace: PWM from microcontroller IGBT1 (PWM1A) (5V/div)
Magenta trace: Load/Output Current I_o (5A/div)
Blue trace: Load/Output Voltage V_o (10V/div)
Green trace: Inductor Current I_L (5A/div)

Figure B.36:
Gold trace: PWM from µcontroller IGBT1 (PWM1A) (5V/div)
Magenta trace: PWM from µcontroller IGBT2 (PWM1B) (5V/div)
Blue trace: Load/Output Voltage V_o (10V/div)
Green trace: Inductor Current I_L (5A/div)

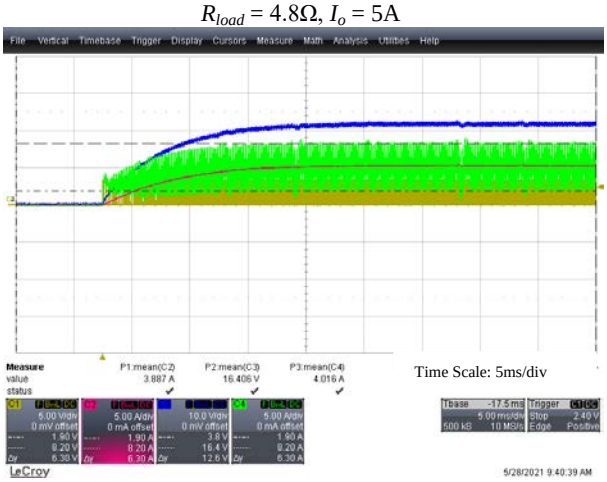

Figure B.37: Bidirectional Converter – Buck Mode – Start-Up
R_{load} = 4.8Ω, I_o = 5A

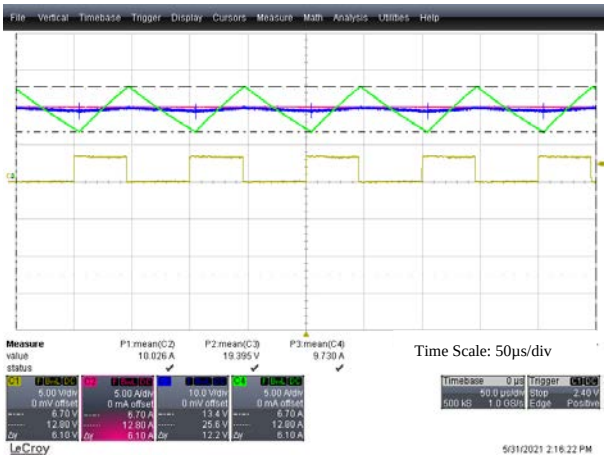

Figure B.38: Bidirectional Converter – Buck Mode – Steady State
R_{load} = 2.4Ω, I_o = 10A

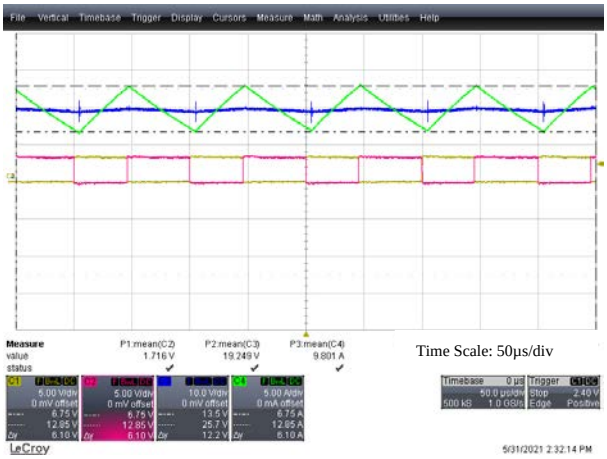

Figure B.39: Bidirectional Converter – Buck Mode – Steady State – both PWM waveforms shown
R_{load} = 2.4Ω, I_o = 10A

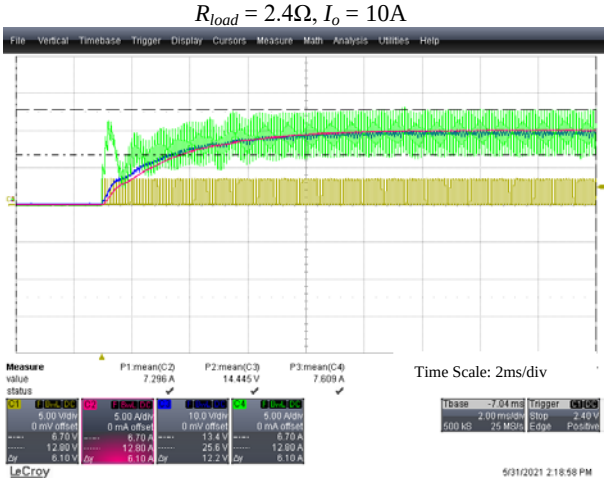

Figure B.40: Bidirectional Converter – Buck Mode – Start-Up
R_{load} = 2.4Ω, I_o = 10A

Figures B.38 and B.40:
Gold trace: PWM from µcontroller IGBT1 (PWM1A) (5V/div)
Magenta trace: Load/Output Current I_o (5A/div)
Blue trace: Load/Output Voltage V_o (10V/div)
Green trace: Inductor Current I_L (5A/div)

Figure B.39:
Gold trace: PWM from µcontroller IGBT1 (PWM1A) (5V/div)
Magenta trace: PWM from µcontroller IGBT2 (PWM1B) (5V/div)
Blue trace: Load/Output Voltage V_o (10V/div)
Green trace: Inductor Current I_L (5A/div)

Table B.5 lists the results obtained from the experimental tests performed with the open Bidirectional converter prototype, operated as a Buck converter with resistive load values of 4.8Ω and 2.4Ω. Two tests were performed: one with the current reference of the current controller set to 5A and another with the current reference of the current controller set to 10A. The input voltage to the Bidirectional converter was set to 48V. The results demonstrate correct operation of the Bidirectional converter and the control system, successfully obtaining the desired output currents of 5A and 10A.

I_{ref}	R_{load}	V_o^*	I_o^*
5A	4.8Ω	21.45V	5.22A
10A	2.4Ω	19.4V	10.03A
* Measurements taken from LeCroy Oscilloscope using differential voltage probe and current probes.			

Table B.5: Bidirectional Converter (Open Prototype) – Buck Mode with Resistive Loads Results

B.2.2 Experimental Testing of the Bidirectional Converter Prototype with Resistive Loads in Boost Mode

Experimental tests were performed with the open Bidirectional converter prototype operated as a Boost converter with a resistive load. The resistive load was set to 9.6Ω and 4.8Ω, using a resistive load bank, to obtain an output current of 5A and 10A, respectively. The Bidirectional converter in Boost mode was controlled using nested current and voltage PI controllers, which controlled the inductor current and output voltage, respectively. The voltage reference of the voltage PI controller was set to 48V. The input voltage to the Bidirectional converter was set to 24V, which was supplied by a DC power supply. Figure B.41 shows a block diagram of the test setup.

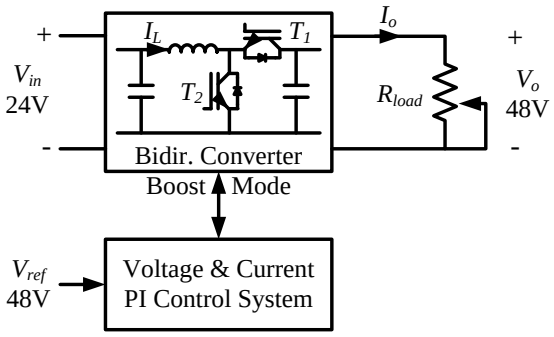

Figure B.41: Block Diagram – Test Setup – Bidirectional Converter (Boost Mode) – Resistive Load

Figures B.42 to B.47 show the results obtained when the Bidirectional converter was operated as a Boost converter with resistive loads. Figures B.42 and B.43 show the steady state operation of the Bidirectional converter with a load resistance of 4.8Ω, obtaining an output current of 5A at 48V, while the start-up is shown in Figure B.44. Figures B.45 and B.46 show the steady state operation of the Bidirectional converter with a load resistance of 2.4Ω, obtaining an output current of 10A at 48V, while the start-up is shown in Figure B.47.

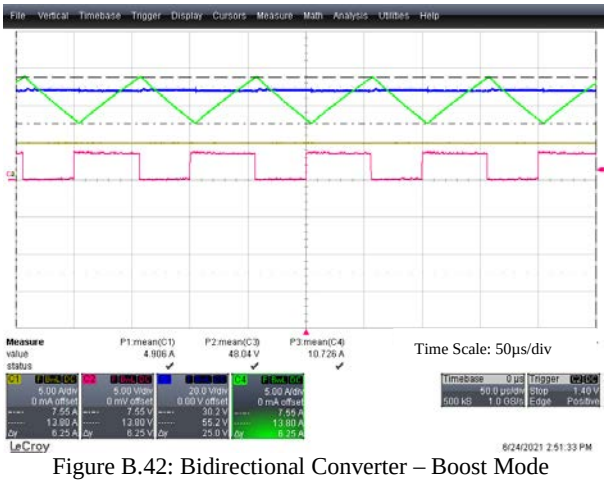

Figure B.42: Bidirectional Converter – Boost Mode – Steady State
R_{load} = 4.8Ω, I_o = 5A

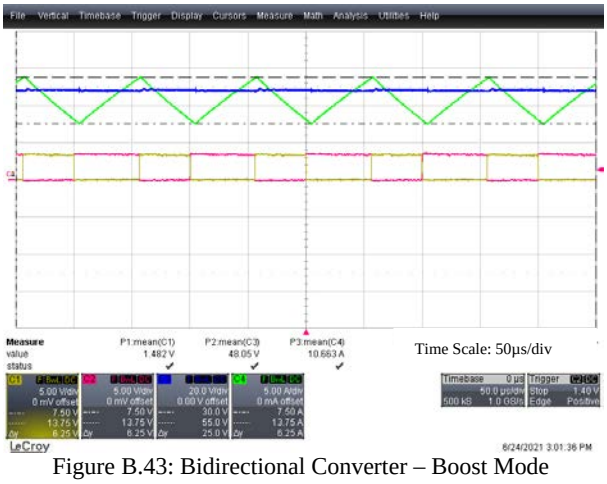

Figure B.43: Bidirectional Converter – Boost Mode – Steady State – both PWM waveforms shown
R_{load} = 4.8Ω, I_o = 5A

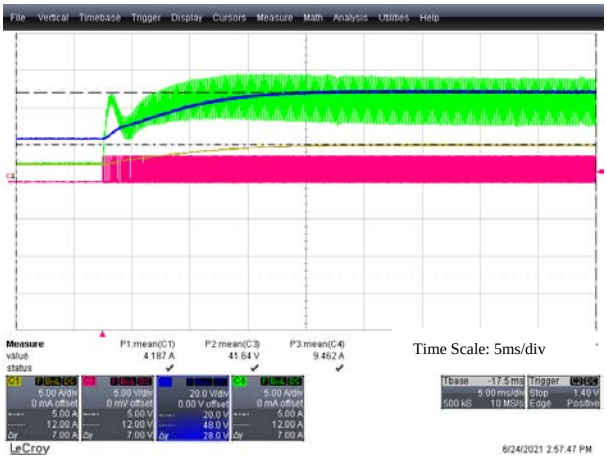

Figure B.44: Bidirectional Converter – Boost Mode – Start-Up
R_{load} = 4.8Ω, I_o = 5A

Figures B.42 and B.44:
Gold trace: Load/Output Current I_o (5A/div)
Magenta trace: PWM from µcontroller IGBT2 (PWM1B) (5V/div)
Blue trace: Load/Output Voltage V_o (20V/div)
Green trace: Inductor Current I_L (5A/div)

Figure B.43:
Gold trace: PWM from µcontroller IGBT1 (PWM1A) (5V/div)
Magenta trace: PWM from µcontroller IGBT2 (PWM1B) (5V/div)
Blue trace: Load/Output Voltage V_o (20V/div)
Green trace: Inductor Current I_L (5A/div)

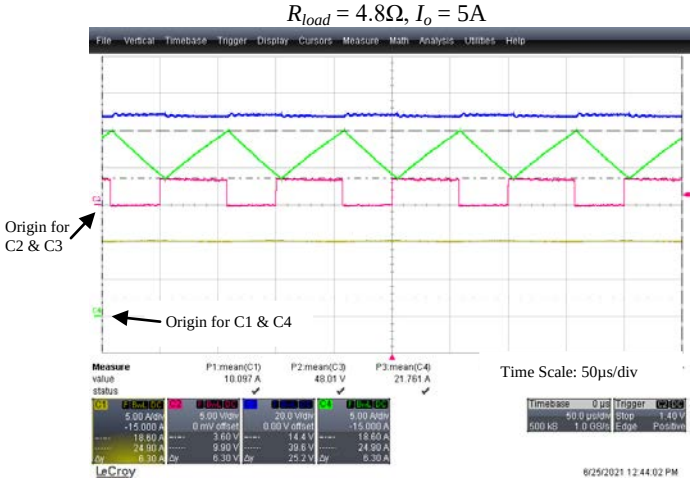

Figure B.45: Bidirectional Converter – Boost Mode – Steady State
R_{load} = 2.4Ω, I_o = 10A

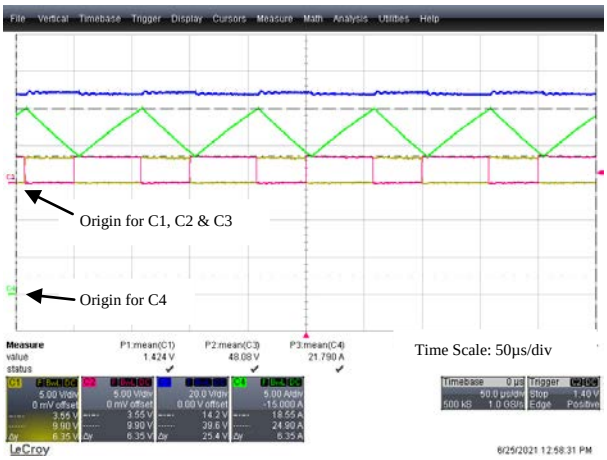

Figure B.46: Bidirectional Converter – Boost Mode – Steady State – both PWM waveforms shown
R_{load} = 2.4Ω, I_o = 10A

Figures B.45 and B.47:
Gold trace: Load/Output Current I_o (5A/div)
Magenta trace: PWM from µcontroller IGBT2 (PWM1B) (5V/div)
Blue trace: Load/Output Voltage V_o (20V/div)
Green trace: Inductor Current I_L (5A/div)

Figure B.46:
Gold trace: PWM from µcontroller IGBT1 (PWM1A) (5V/div)
Magenta trace: PWM from µcontroller IGBT2 (PWM1B) (5V/div)
Blue trace: Load/Output Voltage V_o (20V/div)
Green trace: Inductor Current I_L (5A/div)

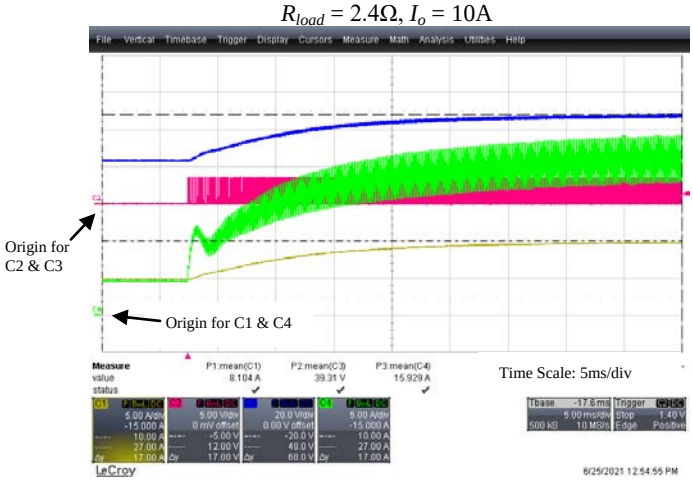

Figure B.47: Bidirectional Converter – Boost Mode – Start-Up
R_{load} = 2.4Ω, I_o = 10A

Table B.6 lists the results obtained from the experimental tests performed with the open Bidirectional converter prototype, operated as a Boost converter with resistive load values of 9.6Ω and 4.8Ω, to obtain output currents of 5A and 10A, respectively,

at an output voltage of 48V. The output voltage reference for the voltage controller was set to 48V and the input voltage of the Bidirectional converter was 24V.

Target I_o	**R_{load}**	**V_o***	**I_o***	**Settling Time** ** **(approx.)**
5A	9.6Ω	48.04V	4.91A	15ms
10A	4.8Ω	48.01V	10.1A	35ms
* Measurements taken from LeCroy Oscilloscope using differential voltage probe and current probes. ** Starting at 24V.				

Table B.6: Bidirectional Converter (Open Prototype) – Boost Mode with Resistive Loads Results

The results obtained confirmed that both the converter and the control system were operating correctly, obtaining the expected output voltage of 48V. The inductor current ripple measured from the results had a peak-to-peak magnitude of around 6.25A, matching the desired value, as designed in Chapter 3, subsection 3.2.2.

The settling times (2% band) expected from the design of the voltage closed loop in Chapter 5 are in the range of 37.7ms to 146ms, for a load current varying between 10% to 100% full load current (3.13A – 31.25A). If the load current values of 5A and 10A are taken into consideration, by calculation using the voltage closed loop transfer function in Matlab the expected settling times would be 19ms and 52.7ms for load currents of 5A and 10A, respectively. It must be pointed out that when the 24V input voltage was connected to the Bidirectional converter, the 24V resulted on the load without the converter being switched. This is due to the Boost converter topology, where the input voltage results on the load through the forward biased diode within the IGBT. This affected the settling times measured from the experimental results, since start-up started from an output voltage of 24V not from 0, thus resulting in a shorter settling time. By simulating with a similar condition in Matlab the settling times result to be ≈15ms and ≈38ms for load currents of 5A and 10A, respectively. From the experimental tests the approximate settling times resulted to be ≈15ms and ≈35ms for the same load currents. Comparing the settling times of these experimental results with the values from the simulation, one can note that these are very similar, which demonstrates that the operation of the Bidirectional converter agrees with its simulation model.

B.2.3 Experimental Testing of the Bidirectional Converter Prototype in Buck Mode – Battery Charging

Following the previous conducted tests, from the results obtained it was concluded that the Bidirectional converter was operating successfully as expected in both modes of operation. Therefore, the Bidirectional converter was built in its own enclosure so

as to be operated as a standalone unit (see Chapter 6 - Experimental Setup). The finalized Bidirectional converter was tested in both Buck and Boost mode to confirm proper operation of the converter, while connected to a resistive load bank and using a controlled power supply as the input source. The enclosed Bidirectional converter when operated as a Boost converter was tested with a maximum output current of 10A, since this corresponds to around 20A input current, which is the maximum current handling of the contactors in use within the converter unit (as explained in Chapter 6). Once correct operation was confirmed, tests were performed with the Bidirectional converter connected to the battery bank.

Tests were performed with the Bidirectional converter operated as a Buck converter to charge the battery bank (Battery Charging Mode). During these tests the Bidirectional converter was connected to a 24V 120Ah battery bank made up of two 12V batteries connected in series. The input voltage to the Bidirectional converter was set to 48V, which was supplied by a DC power supply. The Bidirectional converter was controlled using a current PI controller, which controlled the inductor current. The converter was operated with two current controller references of 5A and 10A. A feed-forward voltage of 24V was applied to the current controller to reduce back flowing current from the battery during converter start-up. The test setup can be represented by the block diagram shown in Figure B.48.

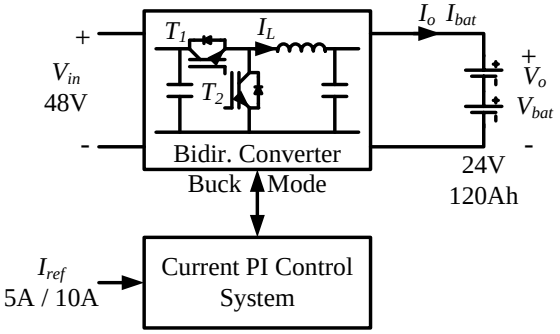

Figure B.48: Block Diagram – Test Setup – Bidirectional Converter (Buck Mode) – Battery Charging

Figures B.49 to B.54 show the results obtained when the Bidirectional converter was operated as a Buck converter to charge the battery bank. Figures B.49 and B.50 show the steady state operation of the Bidirectional converter, successfully charging the batteries with a current of 5A, while the start of charging is shown in Figure B.51. Figures B.52 and B.53 show the steady state operation of the Bidirectional converter, successfully charging the batteries with a current of 10A, while the start of charging is shown in Figure B.54.

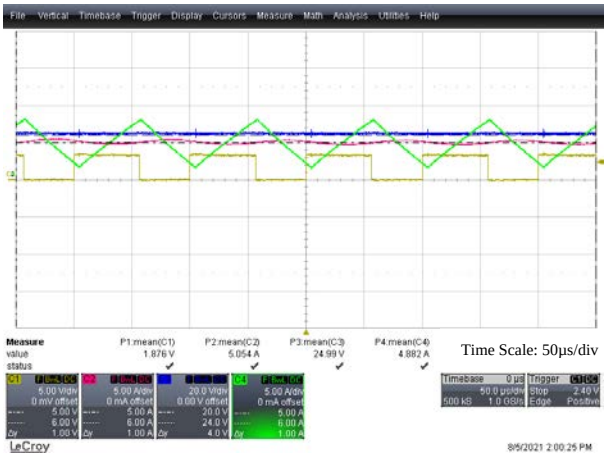

Figure B.49: Bidirectional Converter – Buck Mode – Steady State – Battery Charging I_{bat} = 5A

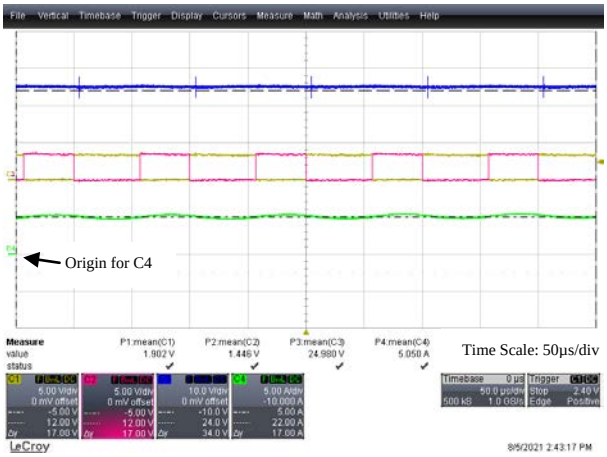

Figure B.50: Bidirectional Converter – Buck Mode – Steady State – both PWM waveforms shown – Battery Charging I_{bat} = 5A

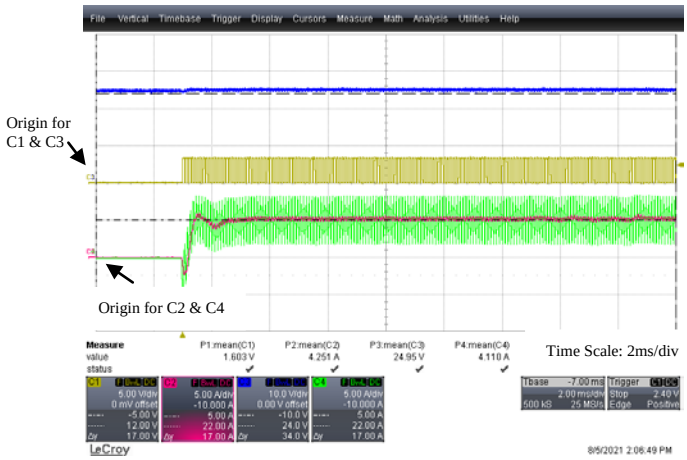

Figure B.51: Bidirectional Converter – Buck Mode – Start-Up – Battery Charging I_{bat} = 5A

Figures B.49 and B.51:
Gold trace: PWM from µcontroller IGBT1 (PWM1A) (5V/div)
Magenta trace: Battery/Output Current I_{bat} (5A/div)
Blue trace: Battery/Output Voltage V_{bat} (20V/div)
Green trace: Inductor Current I_L (5A/div)

Figure B.50:
Gold trace: PWM from µcontroller IGBT1 (PWM1A) (5V/div)
Magenta trace: PWM from µcontroller IGBT2 (PWM1B) (5V/div)
Blue trace: Battery/Output Voltage V_{bat} (10V/div)
Green trace: Battery/Output Current I_{bat} (5A/div)

Figure B.52: Bidirectional Converter – Buck Mode – Steady State – Battery Charging I_{bat} = 10A

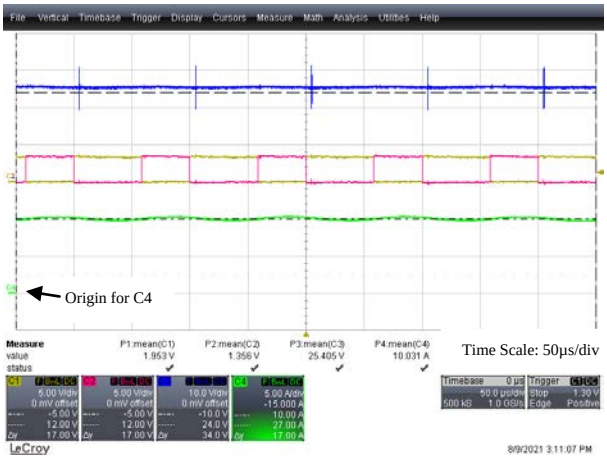

Figure B.53: Bidirectional Converter – Buck Mode – Steady State – both PWM waveforms shown – Battery Charging I_{bat} = 10A

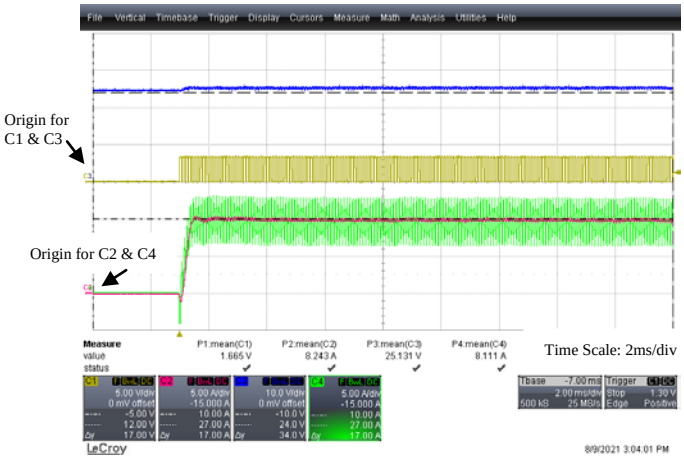

Figures B.52 and B.54:
Gold trace: PWM from µcontroller IGBT1 (PWM1A) (5V/div)
Magenta trace: Battery/Output Current I_{bat} (5A/div)
Blue trace: Battery/Output Voltage V_{bat} (10V/div)
Green trace: Inductor Current I_L (5A/div)

Figure B.53:
Gold trace: PWM from µcontroller IGBT1 (PWM1A) (5V/div)
Magenta trace: PWM from µcontroller IGBT2 (PWM1B) (5V/div)
Blue trace: Battery/Output Voltage V_{bat} (10V/div)
Green trace: Battery/Output Current I_{bat} (5A/div)

Figure B.54: Bidirectional Converter – Buck Mode – Start-Up – Battery Charging I_{bat} = 10A

Table B.7 lists the results obtained from the experimental tests performed with the Bidirectional converter, operated as a Buck converter to charge the 24V battery bank. Tests were conducted with two charging currents of 5A and 10A. The input voltage to the Bidirectional converter was set to 48V.

I_{ref}	V_o^* (V_{bat})	I_o^* (I_{bat})
5A	24.99V	5.05A
10A	25.72V	10.08A
* Measurements taken from LeCroy Oscilloscope using differential voltage probe and current probes.		

Table B.7: Bidirectional Converter – Battery Charging Mode (Buck Mode) Results

The results show successful operation of the Bidirectional converter and the control system where the batteries were successfully charged with the demanded reference current.

B.2.4 Experimental Testing of the Bidirectional Converter Prototype with Resistive Load in Boost Mode – Battery Bank Input

Experimental tests were also performed with the Bidirectional converter operating as a Boost converter, supplying a resistive load with the battery bank as the input source (Load Sharing/Supplying Mode). The Bidirectional converter was connected to load resistances of 9.6Ω and 4.8Ω, to obtain load currents of 5A and 10A, respectively, at an output voltage of 48V. As for the previous test, the 24V 120Ah battery bank was used. The Bidirectional converter was controlled using nested current and voltage PI controllers, which controlled the inductor current and output voltage, respectively. The voltage reference for the voltage controller was set to 48V. The test setup can be represented by the block diagram shown in Figure B.55.

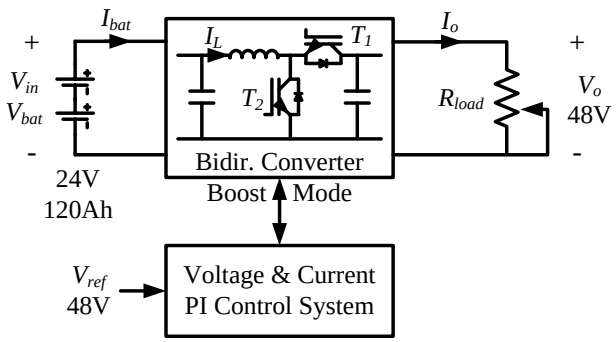

Figure B.55: Block Diagram – Test Setup – Bidirectional Converter (Boost Mode) – Load Supplying

Figures B.56 to B.61 show the results obtained when the Bidirectional converter was operated as a Boost converter with resistive loads and the battery bank as the input source. Figures B.56 and B.57 show the steady state operation of the Bidirectional converter with a resistive load of 9.6Ω, obtaining an output current of 5A at 48V, while start-up is shown in Figure B.58. Figures B.59 and B.60 show the steady state operation of the Bidirectional converter with a resistive load of 4.8Ω, obtaining an output current of 10A at 48V, while start-up is shown in Figure B.61.

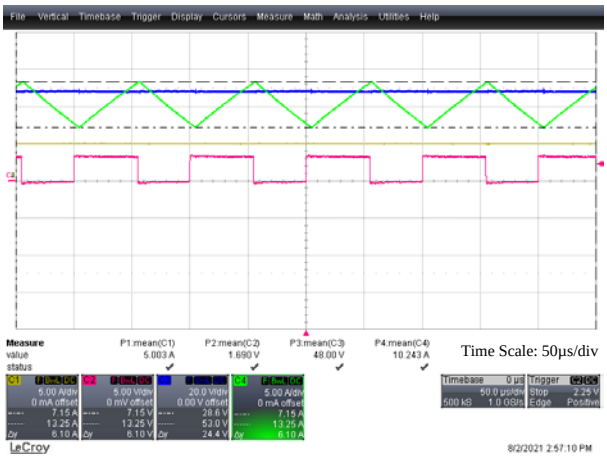

Figure B.56: Bidirectional Converter – Boost Mode – Steady State – Battery Supply – Load Supplying R_{load} = 9.6Ω, I_o = 5A

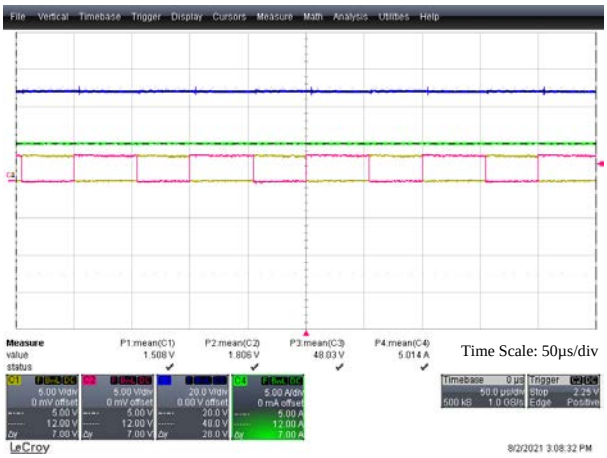

Figure B.57: Bidirectional Converter – Boost Mode – Steady State – Battery Supply – both PWM waveforms shown – Load Supplying R_{load} = 9.6Ω, I_o = 5A

Figures B.56 and B.58:
Gold trace: Load/Output Current I_o (5A/div)
Magenta trace: PWM from µcontroller IGBT2 (PWM1B) (5V/div)
Blue trace: Load/Output Voltage V_o (20V/div)
Green trace: Inductor Current I_L (5A/div)

Figure B.57:
Gold trace: PWM from µcontroller IGBT1 (PWM1A) (5V/div)
Magenta trace: PWM from µcontroller IGBT2 (PWM1B) (5V/div)
Blue trace: Load/Output Voltage V_o (20V/div)
Green trace: Load/Output Current I_o (5A/div)

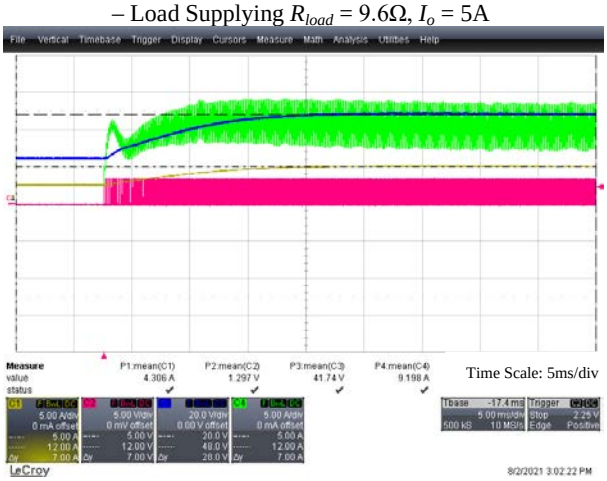

Figure B.58: Bidirectional Converter – Boost Mode – Start-Up – Battery Supply – Load Supplying R_{load} = 9.6Ω, I_o = 5A

Figure B.59: Bidirectional Converter – Buck Mode – Steady State – Battery Supply – Load Supplying R_{load} = 4.8Ω, I_o = 10A

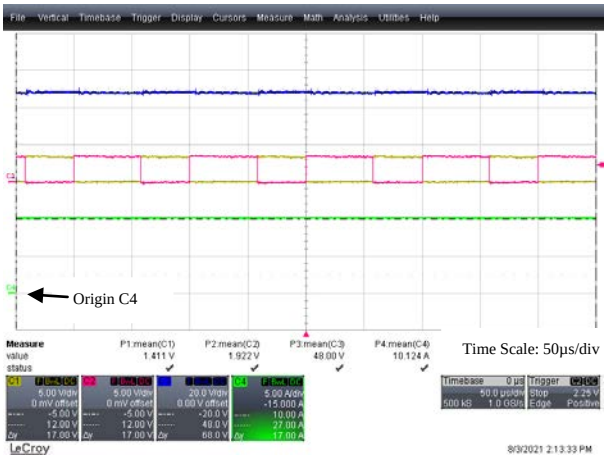

Figure B.60: Bidirectional Converter – Buck Mode – Steady State – Battery Supply – both PWM waveforms shown – Load Supplying R_{load} = 4.8Ω, I_o = 10A

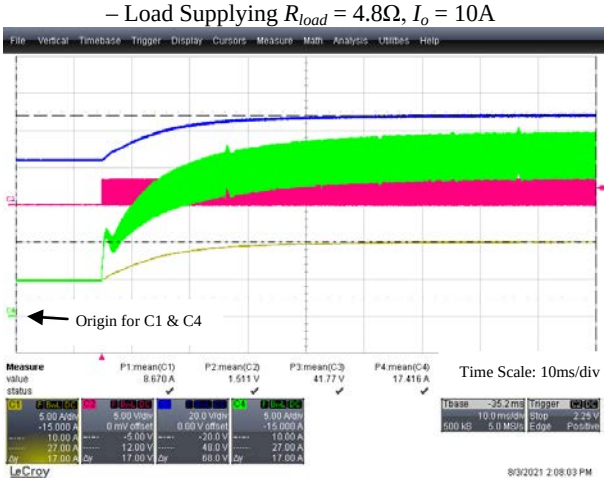

Figure B.61: Bidirectional Converter – Buck Mode – Start-Up – Battery Supply – Load Supplying R_{load} = 4.8Ω, I_o = 10A

Figures B.59 and B.61:
Gold trace: Load/Output Current I_o (5A/div)
Magenta trace: PWM from µcontroller IGBT2 (PWM1B) (5V/div)
Blue trace: Load/Output Voltage V_o (20V/div)
Green trace: Inductor Current I_L (5A/div)

Figure B.60:
Gold trace: PWM from µcontroller IGBT1 (PWM1A) (5V/div)
Magenta trace: PWM from µcontroller IGBT2 (PWM1B) (5V/div)
Blue trace: Load/Output Voltage V_o (20V/div)
Green trace: Load/Output Current I_o (5A/div)

Table B.8 lists the results obtained from the experimental tests performed with the Bidirectional converter, operated as a Boost converter with resistive loads and using the 24V battery bank as the input source. Tests were conducted with resistive load values of 9.6Ω and 4.8Ω, to obtain output currents of 5A and 10A, respectively, at an output voltage of 48V. The voltage reference for the voltage controller was set to 48V.

Target I_o	**R_{load}**	**V_o***	**I_o***	**Settling Time** ** **(approx.)**
5A	9.6Ω	48V	5A	15ms
10A	4.8Ω	48.07V	10A	35ms
* Measurements taken from LeCroy Oscilloscope using differential voltage probe and current probes. ** Starting at 24V				

Table B.8: Bidirectional Converter – Load Supplying Mode (Boost Mode) (Battery Input Supply) Results

The results obtained confirmed that both the converter and the control system were operating correctly, successfully obtaining the expected output voltage of 48V. The inductor current ripple measured from the results had a peak-to-peak magnitude of around 6.25A, matching the desired value, as designed in Chapter 3, subsection 3.2.2.

The settling times (2% band) obtained from the experimental results are practically the same as the settling times obtained from simulations performed in Matlab using the model of the Bidirectional converter operated as a Boost converter under similar conditions and with the same load values. From the simulations the settling times result to be ≈15ms and ≈38ms for load currents of 5A and 10A, respectively, while from the experimental tests the approximate settling times resulted to be ≈15ms and ≈35ms for the same load currents.

B.2.5 Summary of Experimental Testing with the Bidirectional Converter

The results that were presented in this section were obtained from experimental tests performed on the Bidirectional converter. Initially the tests were conducted on an open Bidirectional converter prototype to make testing and probing easier. The open Bidirectional converter prototype was tested in both Buck and Boost modes. In Buck mode, the Bidirectional converter was tested with resistive loads of 4.8Ω and 2.4Ω, where using current control, load currents of 5A and 10A were successfully obtained. In Boost mode, the Bidirectional converter was tested with resistive loads of 9.6Ω and 4.8Ω, where using nested current and voltage control, load currents of 5A and 10A were successfully obtained at an output voltage of 48V. The inductor current ripple measured from the results when the Bidirectional converter was operated as a Boost converter, had a peak-to-peak magnitude of around 6.25A, matching the desired value, as designed in Chapter 3. This verified correct inductor design. For all tests the inductor was enclosed in a metal housing to limit the effect of EMI on adjacent circuitry.

Once the designed Bidirectional converter was confirmed to operate correctly, an enclosed Bidirectional converter was built and tested to a maximum current of 20A. This current limit was due to the current rating of the DC contactors used within the unit. Further testing on the Bidirectional converter was conducted using the enclosed finalized converter. Tests were performed with the Bidirectional converter operated as a Buck converter to charge a 24V 120Ah battery bank (Battery Charging Mode). In battery charging mode the Bidirectional converter, using current control, successfully charged the battery bank with charging currents of 5A and 10A. Tests were also performed with the Bidirectional converter operating as a Boost converter, supplying a resistive load, with the 24V 120Ah battery bank as the input source (Load

Sharing/Supplying Mode). In load sharing/supplying mode the Bidirectional converter was connected to load resistances of 9.6Ω and 4.8Ω, where using nested current and voltage control, load currents of 5A and 10A were successfully obtained, at an output voltage of 48V.

The operation of the experimental Bidirectional converter was compared with that observed in the simulations of Appendix A. With the Bidirectional converter operated as a Boost converter, the settling times (2% band) obtained with load values of 5A and 10A, resulted to be ≈15ms and ≈35ms, respectively. The settling times obtained from simulations performed with the model of the Bidirectional converter operated as a Boost converter under similar conditions and with the same load values were ≈15ms and ≈38ms. Therefore, the very close settling time values obtained from the experimental results and the simulations verified the correct controlled operation of the Bidirectional converter.

B.3 Conclusion

This chapter presented the results obtained from the experimental tests performed on the Buck and Bidirectional converters.

The Buck converters were tested on their own, to confirm proper operation of the converters and their control system. The control system for the Buck converters consists of nested current and voltage control loops using PI controllers that control the inductor current and output voltage, respectively. The Buck converters were operated in both the continuous conduction mode (CCM) and in the discontinuous conduction mode (DCM). At first the Buck converter was built as an open prototype. The Buck converter was tested in CCM using a resistive load bank to obtain load currents in the range of 6A to 42A at 48V for a maximum output power of about 2kW. Inductor saturation prevented further testing with higher load currents, due to large inductor current ripple which tripped the protection circuit of the converter. Once proper operation of the designed Buck converter was confirmed, two Buck converters were assembled in their own enclosure to operate as separate units. The finalized Buck converters were also tested in CCM, successfully obtaining load currents of 5A, 10A, and 20A, at an output voltage of 48V. The output current for the enclosed Buck converters was limited to 20A due to the current rating of the DC contactors used within the units. The settling times (2% band) obtained from the experimental results for Buck converter 1 with load current values of 5A, 10A, and

20A, were 80ms, 150ms, and 350ms, respectively. These agreed very well with the calculated settling times expected for the same load values, which were 89.5ms, 199ms, and 385ms. The Buck converters were also tested in DCM using a resistive load bank, successfully obtaining load currents of 1A and 2A, at an output voltage of 48V. The Buck converters were also tested with step changes in load of 5A to 20A, and vice-versa. The results show that with load step changes of 400%, the control system successfully managed to control the converter and re-establish the output voltage of 48V, in transition times of less than 600ms.

Similar to the Buck converters, the Bidirectional converter was tested on its own, to confirm proper operation of the converter and its control system. The control system for the Bidirectional converter consists in two parts depending on the operating mode of the converter. When the Bidirectional converter is operated in the load supplying mode, it operates as a Boost converter with the control system consisting of nested current and voltage control loops using PI controllers, which control the inductor current and output voltage, respectively. When the Bidirectional converter is operated in the battery charging mode, it operates as a Buck converter with the control system consisting of a current loop using a PI controller, which controls the inductor current. At first the Bidirectional converter was built as an open prototype. The Bidirectional converter was tested successfully operating as a Buck converter with load currents of 5A and 10A. It was also tested as a Boost converter successfully obtaining output currents of 5A and 10A, at an output voltage of 48V. Once proper operation of the designed Bidirectional converter was confirmed, it was assembled in its own enclosure to operate as a separate unit. The finalized Bidirectional converter was tested successfully operating as a Buck converter to charge the 24V 120Ah battery bank with charging currents of 5A and 10A. The Bidirectional converter was also tested operating as a Boost converter using the 24V battery bank as the input source, successfully obtaining output currents of 5A and 10A, at an output voltage of 48V. The settling times (2% band) obtained from the experimental results for the Bidirectional converter operating as a Boost converter with load current values of 5A and 10A, were 15ms and 35ms, respectively. These agreed very well with the settling times obtained from the simulations with the same conditions and same load values, which were 15ms and 38ms.